Mechanochemical strategies for synthesis and modification of functional metal-organic frameworks

Martinez, Valentina

Doctoral thesis / Doktorski rad

2024

Degree Grantor / Ustanova koja je dodijelila akademski / stručni stupanj: **University of Zagreb, Faculty of Chemical Engineering and Technology / Sveučilište u Zagrebu, Fakultet kemijskog inženjerstva i tehnologije**

Permanent link / Trajna poveznica: https://urn.nsk.hr/urn:nbn:hr:149:573978

Rights / Prava: In copyright/Zaštićeno autorskim pravom.

Download date / Datum preuzimanja: **2025-02-06**

Repository / Repozitorij:

Repository of Faculty of Chemical Engineering and Technology University of Zagreb

University of Zagreb

Faculty of Chemical Engineering and Technology

Valentina Martinez

Mechanochemical strategies for synthesis and modification of functional metal-organic frameworks

DOCTORAL DISSERTATION

Zagreb, 2024

Kandidatkinja   **Valentina Martinez**

predala je dana: <u>8. svibnja 2024.</u> doktorski rad izrađen pod mentorstvom dr. sc. Krunoslava Užarevića, znan. savj., Institut Ruđer Bošković, Zagreb i izv. prof. dr. sc. Igora Dejanovića, Sveučilište u Zagrebu Fakultet kemijskog inženjerstva i tehnologije.

Povjerenstvo za ocjenu doktorskog rada u sastavu:
1. prof. dr. sc. Ernest Meštrović, Sveučilište u Zagrebu Fakultet kemijskog inženjerstva i tehnologije
2. doc. dr. sc. Petar Kassal, Sveučilište u Zagrebu Fakultet kemijskog inženjerstva i tehnologije
3. prof. dr. sc. Mirta Rubčić, Sveučilište u Zagrebu Prirodoslovno-matematički fakultet

pozitivno je ocijenilo doktorski rad doktorandice Valentine Martinez, a Fakultetsko vijeće Sveučilišta u Zagrebu Fakulteta kemijskog inženjerstva i tehnologije na sjednici održanoj dana <u>1. srpnja 2024.</u> prihvatilo je ocjenu i odobrilo obranu doktorskog rada pred istim povjerenstvom.

Obrana doktorskog rada održana je dana   <u>12. srpnja 2024.</u>

D e k a n

prof. dr. sc. Ante Jukić

University of Zagreb

Faculty of Chemical Engineering and Technology

Valentina Martinez

Mechanochemical strategies for synthesis and modification of functional metal-organic frameworks

DOCTORAL DISSERTATION

Krunoslav Užarević, Scientific Adviser, PhD
Assoc. Prof. Igor Dejanović, PhD

Zagreb, 2024

Sveučilište u Zagrebu

Fakultet kemijskog inženjerstva i tehnologije

Valentina Martinez

Mehanokemijske strategije za sintezu i modifikaciju funkcionalnih metalo-organskih mreža

DOKTORSKI RAD

dr. sc. Krunoslav Užarević, znanstveni savjetnik
izv. prof. dr. sc. Igor Dejanović

Zagreb, 2024

Bibliographic page

Bibliographic data:

❖ UDK: 544.1:547.1-19(043.3)=111

❖ Scientific area: Natural sciences

❖ Scientific field: Chemistry

❖ Scientific branch: Inorganic chemistry

❖ Institution: Ruđer Bošković Institute, Division of Physical Chemistry, Laboratory for Applied and Sustainable Chemistry

❖ Supervisors: Krunoslav Užarević, Scientific Adviser, PhD

                         Assoc. Prof. Igor Dejanović, PhD

❖ Number of pages: 141

❖ Number of figures: 8

❖ Number of tables: -

❖ Number of references: 80

❖ Date of defence: July 12, 2024

❖ Reviewers:

   ❖ Prof. Ernest Meštrović, PhD, University of Zagreb, Faculty of Chemical Engineering and Technology

   ❖ Assist. Prof. Petar Kassal, PhD, University of Zagreb, Faculty of Chemical Engineering and Technology

   ❖ Prof. Mirta Rubčić, PhD, University of Zagreb, Faculty of Science, Department of Chemistry

   ❖ Replacement: Trpimir Ivšić, PhD, Research Associate, Ruđer Bošković Institute

❖ Dissertation is stored in:

National and University Library in Zagreb, Hrvatske bratske zajednice 4, 10000 Zagreb

Library of the Faculty of Chemical Engineering and Technology, Zagreb, Marulićev trg 20, 10000 Zagreb

Ruđer Bošković Institute Library, Bijenička cesta 54, 10000 Zagreb

Information about mentors

Krunoslav Užarević, Scientific Adviser, PhD

Krunoslav Užarević, PhD is a Scientific Adviser and the Head of the Laboratory for Sustainable and Applied Chemistry at the Department of Physical Chemistry of the Ruđer Bošković Institute in Zagreb. He earned his doctoral degree in 2009 under the supervision of Prof. Marina Cindrić, PhD (Department of Chemistry, Faculty of Science, University of Zagreb). He supervised two doctoral dissertations and over 10 master's and undergraduate thesis. He has initiated numerous international collaborations and led several research projects. In 2014, he received a Marie Curie Fellowship and spent two years in the Group of Prof Tomislav Friščić (Department of Chemistry, McGill University, Montreal, Canada). He is a scientific expert specialised in the development of mechanochemical processes for the synthesis of various classes of functional materials, from supramolecular receptors and organic compounds to highly porous functional materials, inorganic materials and organometallic compounds. His work in the field of mechanochemistry has positioned him as a leading expert, particularly in the development of new unconventional MOF materials. He co-authored over 50 papers, which have been cited over 4000 times. He has received multiple awards. Most recently, he received the Croatian Academy of Sciences and Arts (HAZU) Award for 2023 in the field of mathematical, physical, and chemical sciences. This award recognises his outstanding contributions to sustainable mechanochemical synthesis and his work in the mechanochemical and controlled synthesis of unconventional porous coordination materials of the fourth generation as potent catalysts and spintronic materials. Currently, a particular part of his research includes designing new, advanced devices that introduce other forms of energy into mechanochemical synthesis.

Assoc. Prof. Igor Dejanović, PhD

Igor Dejanović, PhD is an Associate Professor at the Faculty of Chemical Engineering and Technology, University of Zagreb. He earned his doctoral degree in 2010 under the joint supervision of Prof. Ljubica Matijašević, PhD (Faculty of Chemical Engineering and Technology, University of Zagreb) and Prof. Žarko Olujić, PhD (TU Delft, Netherlands). In 2011, he was awarded the "Vera Johanides" Young Scientist Award. He is employed at the Department of Reaction Engineering, and his area of research is industrial separation processes, with an emphasis on thermal separation processes. He is a scientific expert with many years of experience in the field of process systems engineering with numerous collaborations with industry partners. He is the author of numerous scientific papers, cited over 1500 times. Of great importance for the field of presented doctorate stands out the experience in the development of mechanochemical reactions on larger scales, which is essential for the preparation of these materials for industrial applications. He was a mentor of one doctoral dissertation and over 40 master's and undergraduate thesis. He is the president of the Section for Chemical Engineering of the Croatian Society of Chemical Engineers (CSCE) and an active member of the Working Party in Fluid Separations at the European Federation of Chemical Engineering (EFCE).

The topic of the dissertation was accepted at the 9th regular session of the University of Zagreb, Faculty of Chemical Engineering and Technology in the 354th academic year 2022/2023, held on September 25, 2023, and approved at the 4th regular session of the Senate of the University of Zagreb in the 355th academic year 2023/2024, held on January 23, 2024.

Acknowledgements

SAŽETAK

MEHANOKEMIJSKE STRATEGIJE ZA SINTEZU I MODIFIKACIJU FUNKCIONALNIH METALO-ORGANSKIH MREŽA

Valentina Martinez
Institut Ruđer Bošković, Bijenička cesta 54, 10000 Zagreb

Metalo-organske mreže (MOF) među najistraživanim su poroznim materijalima zbog prilagodljivosti njihovih fizikalno-kemijskih svojstava kroz modifikacije u strukturi i širokog potencijala primjene. Mehanokemijska sinteza MOF-ova održiva je i često nadmoćnija alternativa otopinskoj sintezi MOF-ova. Stoga je cilj ovog rada bio unaprijediti mehanokemijske strategije sinteze i modifikacije MOF-ova kao i njihovih nekonvencionalnih derivata, korištenjem dvije dobro istražene grupe MOF-ova, ZIF-8 i MOF-74. To je uključivalo razvoj kontrolirane mehanokemijske sintetske strategije za enkapsulaciju funkcionalnih gostiju u MOF-ove, koristeći enkapsulaciju Buckminsterfullerena u ZIF-8 kao modelni sustav. Nadalje, istraživana je priprema kristalnih i amorfnih faza multivarijantnih MOF-ova, bimetalnih cink-bakarnih MOF-74 materijala različitim sintetskim putevima, uključujući mehanokemijsku amorfizaciju. Rezultati su pokazali da odabir odgovarajuće sintetske strategije značajno utječe na fizikalna i kemijska svojstva te na moguću primjenu istraženih MOF-ova.

Ključne riječi: amorfizacija/ enkapsulacija/ funkcionalni materijali/ mehanokemija/ multivarijantni MOF

ABSTRACT

MECHANOCHEMICAL STRATEGIES FOR SYNTHESIS AND MODIFICATION OF FUNCTIONAL METAL-ORGANIC FRAMEWORKS

Valentina Martinez
Ruđer Bošković Institute, Bijenička cesta 54, 10000 Zagreb

Metal-organic frameworks (MOF) are among the most researched porous materials due to the tunability of their physico-chemical properties through structural changes and broad application potential. Mechanochemical MOF synthesis is a sustainable and often superior alternative to solution MOF synthesis. Therefore, this work aimed to advance mechanochemical strategies for the synthesis and modification of MOFs and their unconventional derivatives by using two well-investigated MOF classes, ZIF-8 and MOF-74. It involved the development of the controllable mechanochemical synthetic strategy for the encapsulation of functional guests into MOFs, using the encapsulation of Buckminsterfullerene into ZIF-8 as a model system. Moreover, it explored the preparation of both crystalline and amorphous phases of multivariate MOFs, bimetallic zinc-copper MOF-74 materials through diverse synthetic pathways, including mechanochemical amorphisation. The results have demonstrated that the selection of an appropriate synthetic strategy significantly affects the physical and chemical characteristics and the possible applications of explored MOFs.

Keywords: amorphisation/ encapsulation/ functional materials/ mechanochemistry/ multivariate MOF/

Table of contents

§ 1. INTRODUCTION

Mechanochemistry is an interdisciplinary field of science that studies chemical reactions initiated by mechanical forces, typically through shearing, stretching, and grinding, thus generating reactive sites. With its roots in ancient times, mechanochemistry has evolved into an indispensable tool for modern synthetic chemists in less than thirty years. Its ability to overcome the limitations of traditional solvent-based synthesis methods, coupled with technological advancements, has broadened its applicability and efficiency in the synthesis of novel materials.[1] Mechanochemical synthesis has proven its value for preparing porous materials, such as zeolites, porous carbons, metal-organic frameworks (MOFs), and others. In the last 20 years, it has advanced notably in the field of metal-organic frameworks (MOFs), a class of materials that offer a unique combination of properties. MOFs are assembled of metal and organic components, termed nodes and linkers. Metal nodes are cations or complex metal-oxo clusters, while linkers are typically mono-, di-, tri-, or tetravalent organic molecules that bridge metal nodes. Due to their permanent porosity, design possibilities through metal coordination preferences, organic linker size, geometry, and connectivity, and due to vast and diverse application potential, MOFs are widely studied.[2] In 2019, IUPAC included metal-organic frameworks and mechanochemistry in the Top Ten Emerging Technologies in Chemistry, with the potential to make our planet more sustainable.[3]

Generally, MOFs are synthesised using the solvothermal method. However, this method presents several challenges. Typically, it requires high boiling point solvents and heating to high temperatures (120 °C) for extended periods, ranging from 12 hours to several days.[4] The high temperatures needed in the solvothermal synthesis are energy-consuming. Moreover, the metal precursor and organic linker must be relatively soluble when the mixture reaches the target temperature, which limits the choice of metal precursors to more soluble and potentially corrosive salts. The reaction temperature, time, solvent, reagent concentration, pH, and nature of the precursors are all parameters that can be systematically varied, and these variations can affect the topology, crystal size, and phase composition of the resulting MOF. Achieving the desired topology, size, and phase control is not straightforward. Alternative methods, such as mechanochemical synthesis, are emerging as promising alternatives to the solvothermal synthesis of MOFs. These methods address some of the challenges associated with the

solvothermal method and offer new possibilities for better control over the topology, size, and phase composition of MOFs.[5]

This dissertation explores the potential of mechanochemical synthesis and transformation of functional metal-organic frameworks with the ability to exhibit distinct properties potentially useful for numerous applications. To achieve this, it explores two archetypical MOF classes, ZIFs and MOF-74. Zeolitic-imidazolate frameworks (ZIFs) are a subclass of metal-organic frameworks that bear a structural resemblance to zeolites. They are composed of metal ions (M) with tetrahedral coordination, typically Zn(II) or Co(II), coordinated to nitrogen atoms from imidazolate linkers. The similarity between ZIFs and zeolites is attributed to the M-Im-M angle of 145°, which closely approximates the Si-O-Si angle commonly observed in zeolites[6] Zeolitic-imidazolate frameworks of sodalite topology, namely ZIF-8, are characterised by large pores with small openings. They are suitable for encapsulating and immobilising various functional guests, bringing new functionalities to ZIFs. Guest encapsulation in solvent-based approaches has challenges and lacks control.[7] Thus, this dissertation aims to develop a mechanochemical strategy for controlled guest molecule encapsulation into ZIF-8 and to determine the effect of the encapsulated guests on ZIF-8 properties. Furthermore, it explores the MOF-74 family, that is, MOFs constructed from 2,5-dihydroxyterephthalic acid and the various divalent metal cations, typically transition or alkaline-earth metal cations. MOF-74 frameworks is characterised by hexagonal channel pores that extend along the crystallographic axis *c* and contain open metal sites at their corners. These unsaturated metal coordination sites act as Lewis acidic centres that can strongly interact with incoming molecules, making them suitable for storage and catalytic applications.[8–10] This work examines the effect of heterometal or defect introduction into the MOF-74 structure on their properties and applicability. Including heterometals in the framework creates a new chemical environment due to the synergistic action of metals, and these new features open new application opportunities. Main synthetic strategies again rely on mechanochemistry as solvent-based approaches are generally inefficient, metal type dependent, and result in inhomogeneous metal distribution.[11]

It is hypothesised that the guest molecules' encapsulation by mechanochemistry can be controlled and that the encapsulated guests will improve the properties of ZIF-8. Equally important, it is hypothesised that the properties of bimetallic MOF-74 materials should differ depending on the mechanochemical synthetic route used. Among the routes, amorphisation, a mechanochemical transformation, is hypothesised to give amorphous MOF-74 materials with improved properties compared to crystalline ones.

§ 2. STATE OF THE ART

2.1. Mechanochemistry

2.1.1. The evolution of mechanochemistry

Mechanochemistry is a branch of chemistry that studies physico-chemical transformations initiated by mechanical energy generated by mechanical stress compression, extrusion, shearing, and friction, among others. A material subjected to mechanical treatment can undergo significant geometric and electronic distortions at the molecular or atomic level. Mechanical stimuli cause chemical species within the material to approach each other at high velocities, which can ultimately lead to the formation of covalent bonds. In other instances, this force can influence intermolecular non-covalent interactions or cause structural defects, which can modify crystal packing and alter the physico-chemical properties of the bulk material.[12] These transformations occur either without solvents or with minimal amounts of solvents. Therefore, mechanochemical methods are more sustainable and efficient than the classical solution methods as they do not depend on the reactants' and products' solubility in often harmful solvents needed for solution syntheses. This also enables using reactants in a stoichiometrical ratio rather than in excess.[13] All of this makes them more efficient.

The first documented use of mechanochemistry dates to ca. 300 BC. In the short booklet titled "On Stones", Theophrastus of Eresus described the reduction of cinnabar (HgS) to mercury by grinding with a small amount of vinegar in copper mortar. In the next 2000 years, milling and grinding have been used to process minerals, grains, and medicine and prepare chemicals for further processing. In his early papers from 1820, M. Faraday termed the method a "dry way" of reaction induction. His and other references to the technique suggest that it was common knowledge that grinding in a mortar can occasionally introduce some chemical action between solids. However, there has been no extensive study on the chemical effects of mechanical action. Mechanochemistry slowly began to gain recognition in the 1880s when W. Spring established geological mechanochemistry. Following that, in the 1890s, M. Carey Lea carried out the first systematic studies on the chemical effect of mechanical action, and A.R. Ling and J. L. Baker researched mechanochemical reactions in organic systems. Their work marked the beginning of systematic research in mechanochemistry. Then, in 1919, Ostwald officially recognised mechanochemistry as a separate branch of chemistry by including it in his chemical systematics alongside photochemistry, thermochemistry, and electrochemistry.[13]

State of the art

The development of lab-scale mills and related technological advancements have played a crucial role in facilitating the broader implementation of mechanochemistry. Initially, mechanochemical research primarily focused on minerals, inorganic compounds, and polymers. It was in the 1980s that supramolecular and organic chemistry were systematically explored and incorporated into the field, thanks to the research of F. Toda, M. C. Etter, and W. Jones, among others. Their work paved the way for modern mechanochemistry, which has proven superior to solution synthesis in many ways.[13]

Nowadays, it is used to prepare new organic and inorganic materials, discover new synthetic pathways and intermediates, and produce products otherwise inaccessible by solution methods. Mechanochemistry has the potential to offer innovative solutions across scientific disciplines and present exciting breakthroughs in the future. In this context, mechanochemical processing is often accompanied by direct reaction monitoring, which enables a rational understanding of observed transformations and provides the necessary information to develop models of mechanochemical reactivity and optimise reaction conditions.[14,15] Furthermore, newly developed experimental setups combine mechanochemistry with other energy sources, including heat, light, sound, and electrical impulses, further advancing the field.[1]

2.1.2. An overview of mechanochemical equipment and techniques

Mechanochemical processes involve a range of variables, both external and internal. External variables are related to the physical setup of the mechanochemical process. They include the type of milling equipment used (e.g., mortar and pestle, mixer mill, planetary mill, twin-screw extruder), the composition and size of the milling vessel (e.g., polymethylmethacrylate, stainless steel, zirconia oxide, Teflon), the characteristics of the grinding balls (composition, size and number of balls amongst others), and the duration and frequency of milling. (Figure 1) The researcher can control and adjust these variables to optimise the process. They can use batch or continuous mechanochemical approaches depending on the specific needs. The batch processes include mortar-and-pestle grinding and milling in various mills, such as mixer, planetary, eccentric, and Simoloyer mills. The resulting batch sizes can range from milligrams for a mixer mill to kilograms for a Simoloyer mill.

Conversely, a continuous process utilising a single- or twin-screw extruder allows for multiple throughputs, from $g\,min^{-1}$ to $kg\,min^{-1}$, without requiring the equipment to scale up with the amounts of the material that can be processed. In addition, resonant acoustic mixing is a novel upscaling mechanochemical technology based on agitation that eliminates the need for milling media, such as balls. While not a new technology per se, resonant acoustic mixing is a valuable new addition to mechanochemistry.[16]

Figure 1. Standard equipment used for mechanochemical reactions. Left to right: mortar and pestle; mixer mill with milling vessels (Teflon, stainless steel, PMMA) and balls (ZrO_2, stainless steel); planetary mill with stainless steel milling vessel; twin-screw extruder.

Internal variables are inherent to the chemical environment and the reagents used. These variables are typically dictated by the nature of the materials being processed and the specific reactions taking place. They include the solid-state structure of the reagents or the use of additives, which will be further discussed below.[17] Neat grinding (NG) represents the most rudimentary form of mechanochemical synthesis, in which solid reactants undergo grinding without any solvent. This dry grinding is commonly used to avoid solvent coordination and insertion or solvate formation, but it can often result in incomplete reactions or amorphisation of the product. The other commonly used form of grinding that solves these issues is liquid-assisted grinding (LAG). It uses a minimal quantity of liquid during the grinding process, and this liquid serves dual purposes: it functions as a lubricant and can also participate directly in the reactions, influencing the reaction pathway and product distribution.[18] The defining parameter for LAG is η, which represents the ratio of the volume of liquid (in μL) to the combined weights of the solid reactants (in mg). This parameter was first explored for cocrystal synthesis[19] but has also proved applicable for other systems with slight η-scale modifications.[17] Figure 2.a illustrates a parameter η scale suitable for most explored systems.

In addition to neat and liquid-assisted grinding, variations of mechanochemical grinding exist that involve additives other than solvents, some of which are displayed in Figure 2.b. Appropriate additives can enhance both reaction selectivity and product quality. Others can slow down or prevent specific chemical reactions. Additives have a complex role in a system, even when added in small amounts. They can stabilise certain solid forms, enhance particle diffusion and partial dissolution of reactants, and activate specific reactions. One such method is ion- and liquid-assisted grinding (ILAG), where a liquid and an ionic compound are added to the grinding process. These additives are usually used to promote the dissolution of solid reactants, creating a homogeneous reaction mixture, which enhances the reactivity of the reactants and thus improves the efficiency of the grinding process. It is worth noting that these grinding forms can be integrated so that the reaction initiates as neat-grinding, and additives are added after the initial pre-milling.[20,21]

Two less common mechanochemical grinding forms are seeding-assisted grinding (SEAG) and polymer-assisted grinding (POLAG). SEAG involves grinding in the presence of seed crystals of the desired product polymorph to obtain the desired polymorph of a compound.[22] Grinding with macromolecules, such as polyethylene glycol polymers (PEGs), as solid or liquid additives in POLAG provides advantages over conventional liquid-assisted grinding. It eliminates the risk of undesirable solvate formation while also allowing control of the resulting particle size or high yield for some specific organic reactions.[23–26]
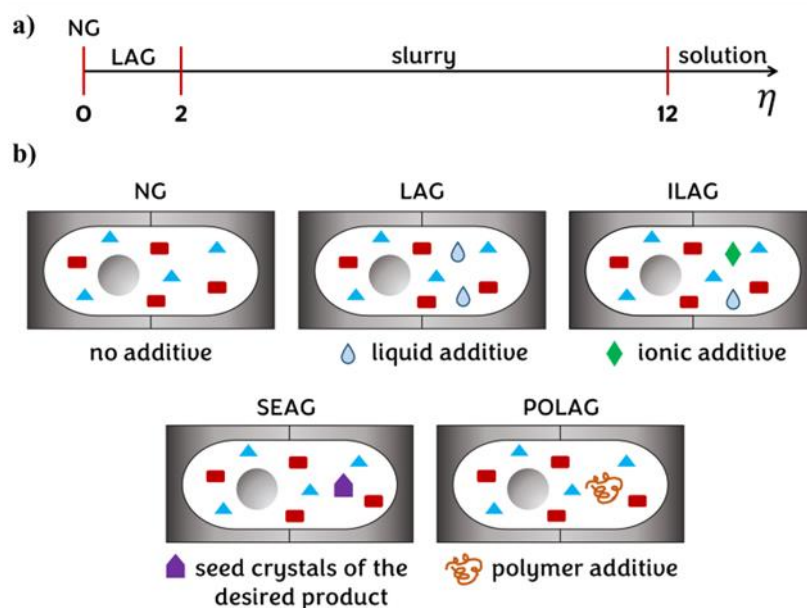
6

Figure 2 a) Scale of parameter *η*, which represents the ratio of the volume of liquid (in μL) to the combined weights of the solid reactants (in mg) and defines LAG. b) Various forms of mechanochemical grinding (NG - neat grinding, LAG - liquid-assisted grinding, ILAG - ion- and liquid-assisted grinding, SEAG seeding-assisted grinding, POLAG polymer-assisted grinding)

Real-time in-situ monitoring methods are another significant advancement in modern-day mechanochemistry.[27] They are crucial in providing insights into the kinetics and mechanisms of mechanochemical reactions. Among these methods, synchrotron X-ray diffraction and Raman spectroscopy have proven effective in detecting reaction intermediates, metastable phases, and compounds that may change at ambient conditions of ex-situ measurement and for determining kinetic models. The measurements are conducted in excellent time resolution (e.g., ten scans per second), thereby enabling the kinetics of mechanochemical reactions to be determined accurately without interrupting or perturbing the chemical processes.[14,15]

Combinations of miscellaneous energy sources with mechanochemistry also show significant potential, with heat and light currently being the most explored. The rate of a mechanochemical reaction, the formation of products, and the overall efficiency of the process can be significantly influenced by variations in temperature.[28–30] Temperature monitoring is a crucial aspect of many chemical processes that involve controlled heating. It ensures that the temperature remains within acceptable limits so that the process proceeds as intended. However, heat may sometimes be generated due to exothermic reactions or friction and mechanical action. In such situations, temperature monitoring helps to obtain information about

7

the nature of the reaction. Light can drive reactions by creating radical or excited-state species. Therefore, a combination of mechanical- and photo-activation can provide new synthetic possibilities. However, specific prerequisites must be met. The milling vessel must be transparent to the incident light source, and the appropriate light source must be chosen according to its intended use. In this context, irradiation with ultraviolet light is still challenging due to the opaque materials commonly used for milling jars.[31] In contrast, the situation with visible light is much simpler because many materials suitable for milling jars are transparent in this wavelength range. Photo-mechanochemistry can speed up reaction times, reduce the amount of catalyst required,[32] or even eliminate the need for a catalyst.[33] With continued research and development, thermo- and photo-mechanochemistry can transform synthetic chemistry and lead to new and impactful discoveries.

.

2.2.   Advancements in MOF mechanochemistry

2.2.1. *The emergence of mechanochemistry in MOF synthesis*

Conventional solvothermal MOF synthesis involves mixing a metal salt with a multitopic organic linker in a high boiling point solvent (e.g., *N*, *N*-diethylformamide (DEF), *N*, *N*-dimethylformamide (DMF), dimethylsulfoxide, (DMSO)). The mixture is then heated, typically for 12 to 48 hours, with the prerequisite that the precursors are at least slightly soluble at the target temperature. This type of MOF synthesis can be susceptible to synthesis conditions and precursor changes, so reproducibility requires profuse optimisation.[4] Unlike solution-based methods, which predominantly use excess precursors and vast amounts of solvent to produce sub-gram quantities of MOF, mechanochemistry uses precursors in stoichiometric ratios and avoids large amounts of solvent, thus preventing waste. Therefore, it is not surprising that following the first report on the use of mechanochemistry in MOF preparation in 2006,[34] the field of MOF mechanochemistry evolved and grew.

In the following sections, some significant advancements in MOF mechanochemistry will be discussed. The scope of metal precursors used for MOF preparation is expanding to more sustainable options such as metal oxides and carbonates. This is possible because mechanochemistry does not require bulk solvent, which means that reactions can occur irrespective of the solubility of starting materials. Furthermore, LAG and ILAG techniques showed great value in MOF synthesis. These techniques typically improve the reactivity and yield of some reactions and accelerate the others. Specifically, in MOF synthesis, the liquid or ionic additive can direct a reaction to a specific MOF polymorph. In recent years, the use of direct time-resolved in-situ reaction monitoring has brought about a significant transformation to the field of mechanochemistry. Through the implementation of time-resolved in-situ techniques for reaction monitoring, we have gained a better understanding of MOF formation and have been able to optimise some reactions. This approach has also allowed us to identify reaction intermediates not previously observed by conventional solution synthesis. Due to the increasing complexity of their composition and properties, new strategies for synthesising MOFs are constantly being developed. Mechanochemistry offers a sustainable and rapid approach to MOF preparation, allowing for precise control of the chemical composition within the framework and, together with reaction monitoring methods, provides new insights into the framework formation process.[5]

2.2.2. *Grinding with benign metal precursors and milling additives*

Remarkable advances in the mechanochemistry of MOFs have been achieved thanks to their capability to employ metal oxides, hydroxides, and other metal precursors of low solubility in MOF preparation. The merit of utilising such materials is that they usually produce water as the reaction's only byproduct, making it environmentally friendly and atom-efficient. Besides that, water originating from hydrate salts or as a byproduct of said reaction can enhance the reaction rate and crystallinity in solvent-free reactions. At an early stage of MOF mechanochemistry, zinc oxide (ZnO) was recognised as a valuable compound among the metal oxides. As such, it has been used to synthesise various coordination polymers and MOFs.[20,35,36] Recently, Thorne et al. investigated the efficiency of different ZIF-62 synthesis routes. Their study of ZIF-62 synthesis showed the supremacy of the mechanochemical synthetic route over the solvothermal one in terms of atom economy. The mechanochemical route that used ZnO and appropriate organic linkers displayed a high atom economy of 92.2%. In comparison, the solvothermal route had an atom economy of 2.2% owing to the vast excess of the used organic linker.[37]

Not every mechanochemical reaction can be initiated in solvent-free conditions; thus, the field of preparative mechanochemistry flourished substantially in the early 2000s with the introduction of liquid (solvents) and solid (ionic salts) additives into mechanochemical procedures. This extended to MOF mechanochemistry as well. Two strategies, LAG with liquid additives and ILAG with liquid and ionic additives combine acid-base reactions and self-assembly to facilitate the framework construction. Further investigations have shown that the choice of liquid and ionic additive can determine the type of MOF product.

Using different liquid additives, Yuan et al. constructed three different MOFs from the same ZnO and 1,4-benzene dicarboxylic acid mixture (Figure 3.a). Water as a liquid additive gave one-dimensional $[Zn(bdc)(H_2O)_2]$, DMF gave two-dimensional $[Zn(bdc)(H_2O)] \cdot DMF$, and methanol (MeOH) gave three-dimensional $[Zn(bdc)(H_2O)]$ material.[38] Similarly, Karadeniz et al. demonstrated that depending on the use of a liquid additive (MeOH, DMF or DEF) and a zirconium precursor (Zr_6 or Zr_{12} oxo-cluster), milling can selectively produce polymorphic porphyrinic zirconium MOFs, MOF-525 or PCN-223 MOF. (Figure 3.b). While polar protic liquid additive MeOH enabled the formation of MOF-525, polar aprotic liquid additives DMF and DEF facilitated the formation of PCN-223. Notably, the solution-based synthesis of these materials did not exhibit such solvent-dependent selectivity.[39]

Furthermore, Friščić et al. investigated the impact of different ionic additives, specifically nitrates ($NaNO_3$, NH_4NO_3, KNO_3) and sulphates (Na_2SO_4, $(NH_4)_2SO_4$, K_2SO_4) salts, on the final topology of a pillared MOF $[Zn_2(bdc)_2(DABCO)]$ (Figure 3.c). They observed that nitrate

additives governed the reaction toward cubic MOF topology, while sulphate additives favoured the formation of a hexagonal MOF topology.[20] This impact of ionic additives was further explored on other MOFs, including ZIFs. Beldon et al. reported that ammonium salts as ionic additives directed the mechanochemical MOF formation toward three different MOF topologies with varying porosities: *rho* topology with $(NH_4)_2SO_4$, *qtz* topology with NH_4NO_3 g and *ana* topology with $NH_4CH_3SO_3$ (Figure 3.d).[36] All of the above examples demonstrate the versatility of mechanochemical reactions while maintaining sustainability.
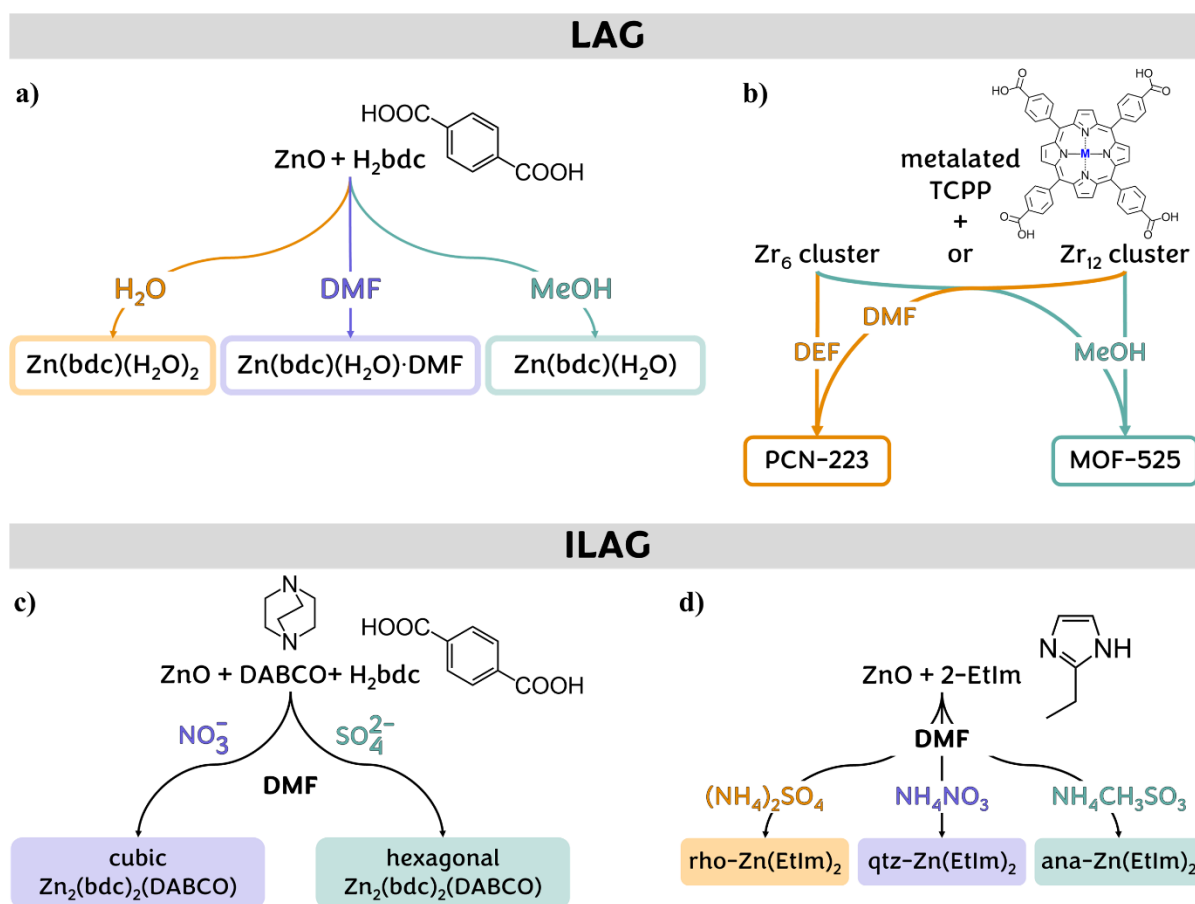

Figure 3 Diversity of metal-organic frameworks (MOFs) achieved through different liquid(a, b) or ionic (c, d) additives.

2.2.3. Time-resolved in-situ monitoring of mechanochemical reactions

As described in the following paragraphs, the introduction of real-time in-situ reaction monitoring techniques has significantly improved the understanding of mechanochemical processes and provided valuable insight into the mechanisms of MOF formation. Here, high-energy synchrotron X-rays pass through the reaction vessel, diffracting on the present materials and allowing for uninterrupted monitoring of dynamic crystalline phase changes with the resolution in seconds (Figure 4.a).[14] Real-time reaction monitoring enabled the discovery of simple, intermediate phases, such as discrete or polymeric metal−organic complexes,[40] intermediate phases of MOF transformation,[41] and others. Also, it gave insight into reaction progress depending on the solvent or the milling duration.[40] Usually, a more prolonged milling leads solely to better conversion. Still, in some cases, it can affect MOF type by reducing the porosity and crystallinity of the MOF, giving more dense or amorphous phases.[5]

Friščić et al. have provided novel insights into the mechanosynthesis of zinc imidazolate frameworks. Their study examined how the type and quantity of liquid or ionic additive (solvent and salt additive) affect the formation of different $Zn(HIm)_2$, $Zn(MeIm)_2$, and $Zn(EtIm)_2$ phases.[42] The research yielded several interesting findings. In the case of the HIm reaction with ZnO, salt additives accelerated product formation and increased yield, and different solvent additives stabilised different $Zn(HIm)_2$ topologies (*zni*, ZIF-4, ZIF-6). At the same time, NG resulted in a non-porous polymer. The study also demonstrated the importance of ionic additives (simple ammonium salts) for the rapid completion of the ZIF-8 ($Zn(MeIm)_2$) synthesis. Moreover, the synthesis of $Zn(EtIm)_2$ following the rho→ana→qtz topologies transformation can be influenced by both ionic and liquid additives, with no reaction occurring with additive-free LAG or NG. The salt and solvent additive type affects the phase transformation rate and stabilises a specific topology.

Katsenis et al. made a fascinating observation while monitoring the mechanochemical synthesis of ZIF-8 using synchrotron in-situ powder X-ray diffraction. They noticed that after the preparation of ZIF-8 sod-polymorph, further milling led to amorphisation. Following that, an unexpected recrystallisation occurred. In repeated experiments, recrystallisation led either to previously unreported *kat* polymorph and subsequently to non-porous *dia* polymorph or went directly to *dia*. These observations suggest that the mechanochemical process ends in a thermodynamically more stable phase.[41] (Figure 4.b) A similar thing was observed with the previously mentioned porphyrinic zirconium MOFs, where prolonged milling converted MOF-525 to a more thermodynamically stable PCN-223 phase.[39]

In another instance, Beamish-Cook et al. used synchrotron in-situ powder X-ray diffraction to investigate the mechanism of mechanochemical synthesis of the Zn-MOF-74, which led to the identification of four reaction intermediates.[43] It displayed how mechanochemical synthesis can be complex, and parameters must be closely monitored and optimised to ensure the desired outcome. In this case, DMF as a liquid additive governs the reaction through a mechanism different from the previously reported for the analogous mechanochemical synthesis of Zn-MOF-74 with water as a liquid additive (Figure 4.c). This once again confirmed the significance of the careful selection of liquid additives depending on the desired outcome.[40]
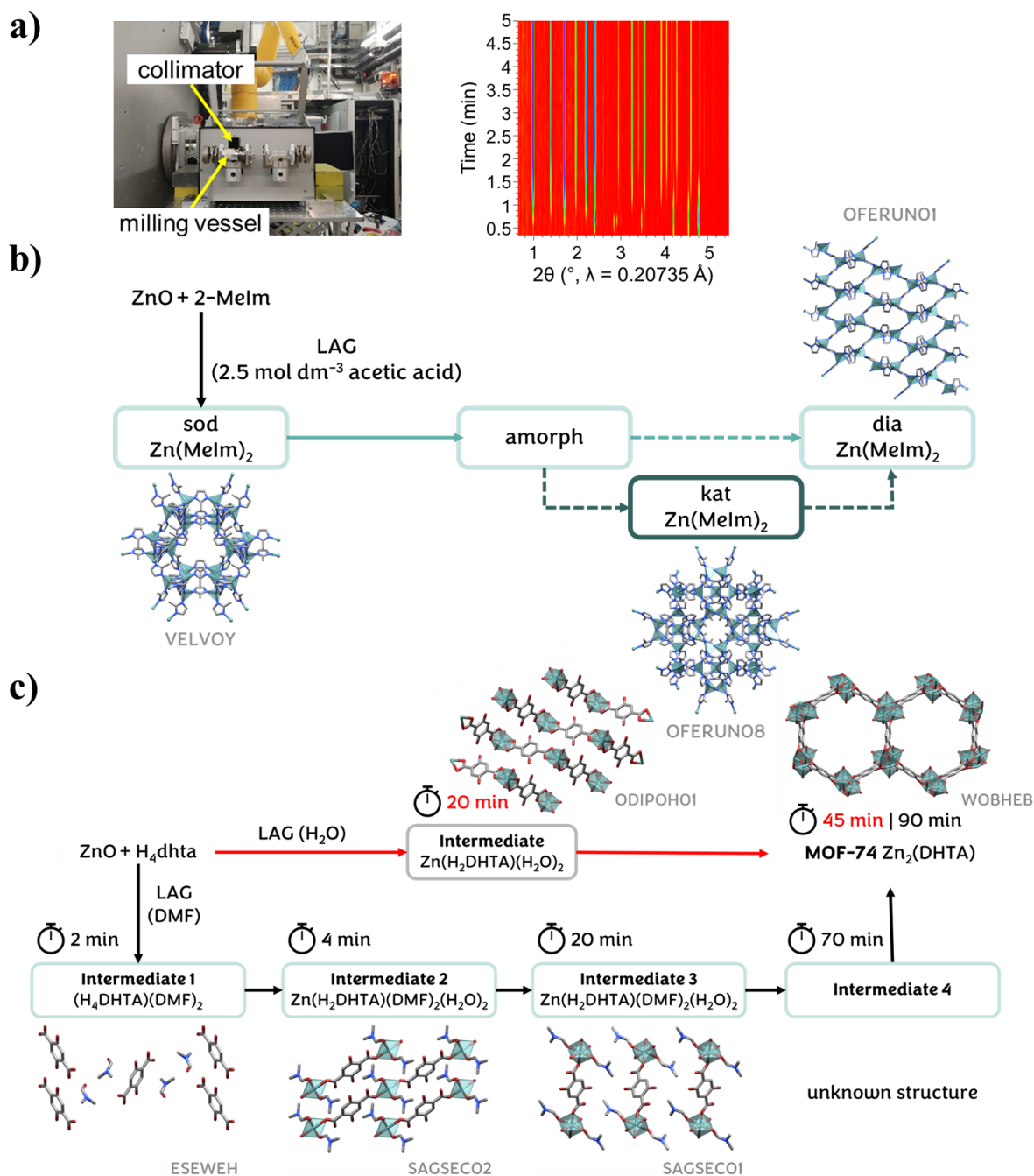
Figure 4 In-situ synchrotron XRD monitoring a) Setup for mechanochemical reactions, with an example of time-resolved diffractograms illustrating the reactants-to-products phase transformation. b) The sequence of solid-state transformations observed in the LAG (2.5 mol dm^{-3} acetic acid) reaction of ZnO and 2-MeIm (1:2 ratio) in ref 41. c) Illustration of the observed phase evolution during the mechanochemical reaction between ZnO and H$_4$DHTA (2:1 ratio) in the presence of DMF (ref 43) or H$_2$O (ref 40) liquid additives. Displayed structures were acquired from CCDC,[44] and their refcodes are shown in the figure. Hydrogen atoms are omitted for clarity.

2.2.4. Multivariate MOFs (4th generation MOFs)

Another significant advancement in the mechanochemistry of MOFs came with the introduction of functional MOFs. In the context of metal-organic frameworks, the term functional refers to the ability of MOFs to exhibit specific properties that are useful for various applications. There is a constant development in the complexity of frameworks and their properties. The first-generation MOFs had a structure that collapsed upon solvent removal. The second generation of MOFs overcame this issue and could survive the removal of the guests, leading to a substantial increase in the complexity of MOF chemistry and potential applications. The third generation introduced flexible MOFs that can adapt their crystal and electronic structure in response to the guests and the environment. The latest fourth generation brought about a notable increase in the complexity of metal-organic frameworks, considering factors such as their constituents, guests, and defects. This has resulted in the creation of multifunctional materials, significantly broadening the MOF's field of application.[45]

The rise in complexity of fourth-generation MOFs is particularly evident in multivariate MOFs, which comprise at least two distinct organic linkers or metal nodes.[46] These complex materials often display superb catalytic or selective properties compared to their homogeneous counterparts.[47–49] While MOFs with diverse organic linkers featuring equivalent node-linker connectivity but differing functional groups are frequently studied, those with diverse metal nodes are significantly less explored. This can be attributed to the challenges associated with their solution synthesis. The linker multivariance relies primarily on linkers of comparable length that can achieve equivalent node-linker connectivity and, therefore, MOFs of comparable structures regardless of linkers' additional features. However, the extension of this concept to metal nodes and the synthesis of heterometallic MOFs with structure and topology comparable to those of analogous monometallic MOFs presents a formidable challenge. The control of the distribution of metal with varying ionic radii, polarising power, acidity, or coordination geometries within the framework and their respective ratios is much more complex.[50] This is arguably why linker multivariance in MOFs is often approached via direct synthesis, while metal multivariance has necessitated the development of alternative synthetic strategies, not necessarily solution-based ones. Mechanochemistry has proven to be a straightforward and dependable method for heterometallic MOF synthesis.

Panda et al. have demonstrated that mechanochemical alloying can successfully be used to produce bimetallic MOFs. They tested this method on three representative MOF groups: Al-ndc, ZIF-8, and MOF-74. To do this, they first prepared two monometallic MOFs they planned to mix, such as Al-ndc and Ga-ndc or Zn-MOF-74 and Co-MOF-74, then mixed them in

different molar ratios. These mixtures were then subjected to ball milling, which caused amorphisation. The powders were then exposed to saturated water or methanol vapour at 25°C for three days, producing bimetallic crystalline materials with varying properties that are isostructural to their parent MOFs. Furthermore, the researchers investigated several metal combinations and found that bimetallic MOFs typically formed when metals of similar atomic radii were combined. For some of the investigated MOFs, mechanical milling was the only successful method for synthesising bimetallic MOF material, as conventional solution-based syntheses failed to provide the crystalline bimetallic MOF material.[51]

In a recent study, mechanochemistry was once again proven more effective than solution-based syntheses. Xu et al. used mechanochemical synthesis to create a high-entropy zeolitic imidazole framework (HE-ZIF) of sodalite topology inspired by high-entropy alloys (HEAs). The new material consisted of five metal ions, namely Zn(II), Co(II), Cd(II), Ni(II), and Cu(II), coordinated to 2-methylimidazole linkers and randomly dispersed in the ZIF lattice. Even though Cd(II), Ni(II), and Cu(II) have a different usual coordination mode than Zn(II) and Co(II), which are known to solely form sodalite ZIF frameworks, ZIF-8(Zn) and ZIF-67(Co), the HE-ZIF was successfully assembled with the desired metal ratio and distribution. HE-ZIF showed enhanced catalytic properties compared to single-metal ZIF materials or their physical mixture, likely due to the synergistic effect of the five metal ions. On the other hand, solution synthesis was unable to provide the HE-ZIF.[52]

Ayoub et al. have proposed a two-step mechanochemical synthesis strategy for fabricating bimetallic MM'-MOF-74 materials (M, M' – alkaline earth or divalent transition metal), which is rational, fast, and efficient. In the first step, a simple coordination complex (M(DHTA) or M'(DHTA)), termed intermediate, is constructed using 2,5-dihydroxyterephtalic acid (DHTA) and corresponding metal salt (oxide, hydroxide or acetate) in a 1:1 stoichiometric ratio. In the second step, this intermediate is combined with the corresponding metal salt to produce the final MM'-MOF-74 material, which has a 1:1 molar ratio of the two metals.[53] The concept behind this process is known as template-directed synthesis. This approach involves using a 1D metal-organic polymer with well-defined binding sites within its structure as a template for incorporating a secondary metal, which converts it into an open 3D structure, metal-organic framework.[54] Interestingly, the 1D metal-organic polymer $Zn(H_2O)_2(H_2DHTA)$ (intermediate) phase used in the Ayoub et al. study was first observed by Julien et al. during the in-situ monitoring of the Zn-MOF-74 formation thus confirming the importance of reactive intermediates in MOF mechanosynthesis.[40]

Expanding the mechanochemical approach to other valuable MOFs, Thorne et al. researched mixed metal glass-forming zeolitic imidazolate framework (ZIF-62) materials. They discovered that the mechanosynthetic route allowed precise control over metal dopant content and could incorporate up to 20% Co(II) into the framework. This resulted in a melting temperature (T_m) decrease compared to the pure Zn analogue. The findings suggest that this discovery has the potential to broaden the operational scope of ZIF liquids.[37]

This section explores heterometallic MOFs, which feature distinct metals as the primary building blocks (metal nodes). However, it is important to highlight that this classification also encompasses MOFs that involve supplementary metals integrated into the organic linker (such as those found in porphyrin rings) or those that have them included in the structure in some other capacity and have garnered increased attention in recent years.[50,55]

Metal-organic frameworks have proven to be excellent host matrices for encapsulating various guest molecules. Guest encapsulation into MOFs primarily relies on solution-based methods, which are dependent on the solubility, MOF pore size, and aperture size. However, the main challenge associated with this approach is the limited control over the encapsulation process, primarily stemming from the competition of guest molecules with solvent molecules for MOF pore inhabitation.[7,56] Although limited attention has been devoted to the mechanochemical preparation of guest@MOF composites, it emerged as an attractive strategy that may facilitate the expansion of guest encapsulation to unexplored MOFs.[57–59]

Li et al. have developed a sustainable and straightforward mechanochemical approach for encapsulating metal nanoparticles (MNPs) into MOFs.[60] MNPs@MOF composites are formed by direct mechanochemical transformation of solid metal precursor-supported MNPs hybrids (e.g. ZnO with palladium MNPs). This approach does not require MNPs stabilising agents, usually used in solution synthesis, and overcomes other drawbacks of solution synthesis. MNPs in synthesised MNPs@MOFs are well-entrapped in the MOF matrices and mainly distributed near the surface of the MOFs, which is beneficial for their catalytic selectivity and activity. Furthermore, the MNPs@MOF composites can be easily synthesised on a gram scale, indicating their potential for industrial applications.

In another instance, Wei et al. demonstrated the encapsulation of enzymes into MOFs using ball milling.[61] Careful tuning of pH and synthesis planning enabled the successful encapsulation of chosen enzymes into MOFs (ZIF-8, UiO-66-NH$_2$ and MOF-74) with controlled enzyme loading and even distribution throughout the MOF. To evaluate the efficacy of enzyme@MOF composites, they were incubated with peptidase, demonstrating the shielding ability of MOFs, which enabled the enzyme to retain its activity.

Furthermore, the introduction of structural defects in metal-organic frameworks (MOFs) can lead to the emergence of new functionalities. There are various approaches to introduce such defects, both pre- and post-synthetically.[62] However, mechanochemical defect introduction usually results in amorphous MOFs. Amorphous MOFs usually retain their crystalline counterparts' structural units and connectivity but lack long-range order. Their amorphous nature presents numerous exciting possibilities for practical applications, either as novel functional materials or as mediators of other processes.[63]

Muratović et al. explored the amorphisation of MOF-74 materials. They prepared amorphous phases of Zn-MOF-74 and Ni-MOF-74 by the mechanochemical treatment of dehydrated Zn-MOF-74 and Ni-MOF-74. It was observed that amorphous Ni-MOF-74 displays significantly lower bulk magnetisation compared to its crystalline counterpart due to changes in the coordination sphere of nickel occurring upon mechanical action, resulting in the spin crossover (from $S = 1$ to $S = 0$).[64]

Moreover, Cao et al. first explored mechanochemical amorphisation of ZIF-8, which is a process that irreversibly transforms the crystalline to amorphous ZIF-8.[65] Subsequent studies revealed that heating the resulting amorphous phase under argon leads to the formation of qtz-ZIF-8, a crystalline polymorph of ZIF-8.[66] Additionally, it was discovered that mixed ligand zeolitic-imidazolate framework, ZIF-62, can also be mechanochemically amorphised and can directly produce glass when melt-quenched.[67] This provides a novel route to a wider variety of glass-forming systems and removes the requirement for melt-quenching only crystalline materials. These findings underscore the crucial role of amorphous phases of MOFs as metastable intermediates in the formation of crystalline or glassy phases.

§ 3. DISCUSSION

3.1. Preface

Because of their remarkable properties, MOFs are continuously and extensively studied in academic research groups and industry. As already demonstrated in the *State of the art*, the mechanochemistry of 4th generation MOFs is still largely unexplored. However, significant advances have been achieved in recent years. This dissertation makes a valuable contribution to the advancement of functional MOFs through the development of guest@MOF and multivariate MOF synthetic strategies. It investigates the mechanochemical synthesis and transformation of functional metal-organic frameworks (MOF) development, focusing on two archetypal MOF classes, ZIF-8 and MOF-74.[68–70]

The primary objective of this study was to develop a mechanochemical method for the controlled encapsulation of guest molecules into ZIF-8 and to evaluate the impact of the encapsulated guests on the properties of the given MOF. The study utilised Buckminsterfullerene, a spherical C_{60} fullerene, as a guest molecule due to its great potential for enhancing the properties of the materials in which it is integrated or enclosed.[68] Moreover, it explored the impact of heterometal or defect introduction into the MOF-74 structure on their characteristics and potential applications.[69,70] To achieve these goals, the primary synthetic approaches rely on mechanochemistry, as solvent-based methods tend to be ineffective, metal type dependent, and result in uneven metal distribution.

The synthesis of target MOF materials was carried out following the principles of green chemistry. Metal oxides and hydroxides were used as reactants for synthesis to avoid the harmful environmental effects of nitrates, sulphates, or chlorides. Furthermore, green solvents were prioritised as liquid additives for synthesis, where the solvent amount was minimal. The synthesised materials were thoroughly characterised by a range of spectroscopic (FTIR, NMR, UV-Vis, EPR), microscopic (TEM, SEM), and diffraction (PXRD) techniques. The magnetic properties of particular MOFs were investigated using an EPR spectrometer and a SQUID magnetometer. Additionally, in-situ monitoring was conducted using diffraction of synchrotron X-ray radiation to understand better the course of mechanochemical synthesis of bimetallic MOF materials and improve the synthesis process. Certain materials were also tested for their catalytic activity. Through these analyses, we established that introducing guests, heterometals, or defects into the structure changes and, in most cases, enhances MOFs' properties.

3.2. Development of a mechanochemical method for the controlled guest@MOF encapsulation

Our exploration of functional metal-organic framework preparation and transformation started with developing a method for controlled synthesis of composite guest@MOF materials, with C_{60}@ZIF-8 as a model system(Appendix I).[68] Generally, functional materials with fullerenes or fullerene derivatives embedded in their structure exhibit enhanced stability, conductivity, magnetism, or catalytic activity compared to their constituents.[7] Since metal-organic frameworks have proven to be excellent matrices for encapsulating guest molecules,[59,71] and the mechanochemical approach of guest encapsulation is superior to the solution approach,[57,58,60,61] the development of here described method is of great importance for the further development of functional guest@MOF materials. Selecting a suitable MOF host for the encapsulation and immobilisation of guests is critical for successfully implementing various applications. In this regard, ZIF-8 has emerged as the preferred choice due to its optimal pore size, geometry, and hydrophobicity. With a pore diameter of 11.6 Å and pore aperture diameter of only 3.4 Å, ZIF-8 is particularly well-suited for accommodating and immobilising C_{60} fullerene, which has a diameter of about 6.8 Å (Figure 5.a).[6,72] We have aimed to prepare four C_{60}@ZIF-8 materials containing 15, 30, 60, and 100 mol% of fullerene relative to the maximum available ZIF-8 pores. In order to determine the best approach for C_{60}@ZIF-8 preparation and assess the encapsulation efficacy of the approaches, we utilised mechanochemical synthesis, solvothermal synthesis, and post-synthetic modification.

Mechanochemical synthesis of C_{60}@ZIF-8 materials was carried out in a stepwise manner, beginning with the 10-minute milling of stoichiometric amounts of zinc oxide (ZnO) and 2-methylimidazole (2-MeIm) with fullerene C_{60}. This aimed to ensure reactive components are well mixed; no crystalline MOF was prepared at this stage (Figure S2, Appendix II). After that, ethanol (EtOH) and ammonium nitrate (NH_4NO_3) were added, and milling resumed for 45 minutes, resulting in purple-coloured materials; the colour of the materials darkened with the increase in the fullerene content (Figure 1, Appendix I). The mechanochemical synthesis was conducted in the described manner to ensure the assembly of the ZIF-8 framework around the fullerene and its efficient entrapment (Figure 5.b). Before further analyses, all ground materials were washed with toluene to remove potential excess of C_{60} from the crystallite surface. Even in high target ratios, the successful inclusion of fullerene guests was confirmed by colourless wash-out (Figure S1, Appendix II). (note: Traces of C_{60} fullerene in the toluene are easily observable as they colour the solution intensive purple.)

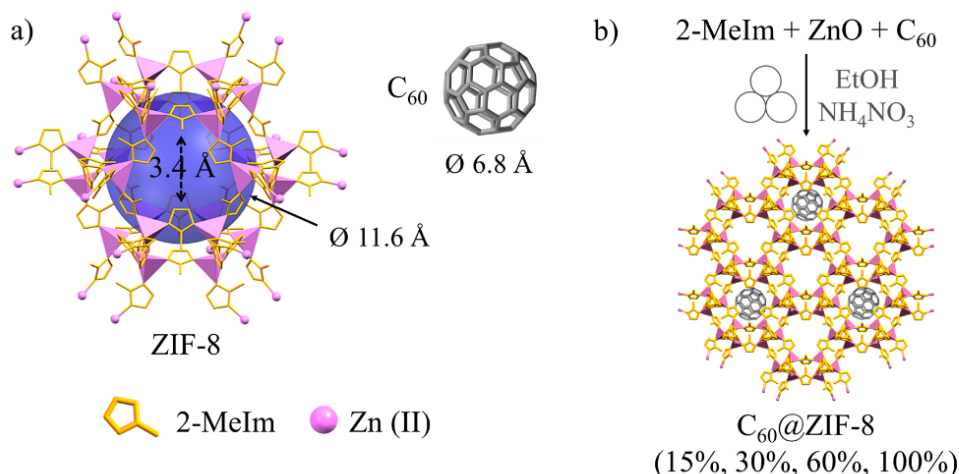**Figure 5** a) Sodalite topology ZIF-8 pore (11.6 Å) and aperture (3.4 Å) diameter size in comparison to that of C_{60} fullerene (6.8 Å) b) C_{60}@ZIF-8 materials synthesis scheme

PXRD analysis confirmed that ball milling successfully generated phase-pure C_{60}@ZIF-8 materials. Interestingly, the relative peak intensity in the PXRD of C_{60}@ZIF-8 materials varied depending on the amount of fullerene encapsulated. This feature was then used to estimate the extent of C_{60} encapsulation (Figure 2, Appendix I). The Bragg reflection most suitable for this purpose is (110), as the changes in its intensity are the most pronounced. This can be ascribed to the inclusion of hollow C_{60}, which modifies the electronic density in the ZIF-8 cages, significantly reducing the intensity of the (110) mirror plane located at the centre of the pore. To confirm this finding, we have constructed the ZIF-8 3×3×3 unit cell with varying amounts of C_{60} in the pores using the atomic simulation environment.[73] The PXRD of simulated structures shows excellent agreement with the experimentally observed PXRD data (Figure 6), thus confirming that the reduction of the (110) peak intensity is a direct result of guest inclusion.
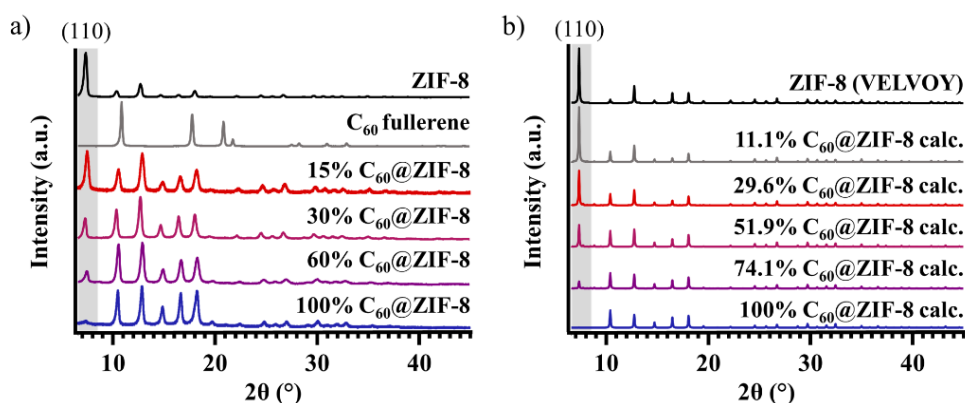
Figure 6 Experimental (a) and calculated (b) PXRD data for the ZIF-8 and the C_{60}@ZIF-8 composites

Discussion

Furthermore, guest-free ZIF-8 was prepared as a white microcrystalline solid through the above-described ILAG procedure without adding the fullerene. Milling prepared ZIF-8 with C_{60} resulted in a low degree of encapsulation, as evidenced by the colour of the products and PXRD and IR spectroscopic analysis (Figures S3 and S8, Appendix II). The solid products of the mechanochemical post-synthetic encapsulation attempts remained almost colourless after the washing, whereas the wash-outs were deep purple. These findings confirmed that for the inclusion of the C_{60} fullerene guests into sodalite MOFs, the mechanochemical formation of the framework around the C_{60} template is more appropriate. Additional experiments were conducted to exclude the presence of any C_{60}-2MeIm complex species that may play a role in moderating encapsulation (Figures S5 and S15, Appendix II).

Additionally, the attempt to prepare C_{60}@ZIF-8 from the solution post-synthetically by immersing the guest-free ZIF-8 in an oversaturated toluene solution of C_{60} resulted in low fullerene loading. After a week of soaking, only a small amount of fullerene was encapsulated, evident from the sample's pale beige colour and the PXRD and IR analyses (Figures S4 and S8, Appendix II). A similar outcome was observed with the solvothermal synthesis attempt in the DMF-toluene mixture at 120 °C. (Figure S4, Appendix II). The low efficiency in the encapsulation for solution-based syntheses may be attributed to the solvation and competition of fullerene with the solvent molecules for the ZIF-8 pore. This is supported by the IR spectroscopic analyses of the products (see Section S3, Appendix II).

Moreover, computational simulations of molecular dynamics (MD) were conducted to study the nature of C_{60} encapsulation into ZIF-8 and better understand this behaviour. According to the density-functional based tight-binding (DFTB) molecular dynamics (MD) simulation, the transport of fullerene molecules from pore to pore is found to be a challenging task that requires simultaneous rotation of all six imidazole rings on the aperture to enable C_{60} to move to the next pore. Such a low-probability event in ZIF-8 may account for the low loading of C_{60} in the standard soaking approach (see Figure 7, Appendix I; Section S5, Appendix II).

As noted earlier, quantitative IR spectroscopic analysis was carried out as a straightforward method to evaluate the success of C_{60} encapsulation. Pellets of standard samples were prepared and analysed parallel to mechanochemically synthesised samples to determine the amount of encapsulated fullerene. The experimentally observed amount of the encapsulated C_{60} was then compared with the theoretically expected amount to assess the efficiency and controllability of the encapsulation process.

Discussion

The IR spectrum of C_{60} fullerene is characterised by four distinctive bands. Of these, two bands at 577 and 528 cm^{-1} are attributed to the radial motion of carbon atoms, while the other two, at 1428 and 1182 cm^{-1}, are attributed to the tangential motion of carbon atoms. The latter two significantly overlap with ZIF-8 bands in the IR spectra of prepared C_{60}@ZIF-8 samples (Figure S8, Appendix II). However, the radial-motion bands do not and serve as markers for further analysis of C_{60}@ZIF-8 (Figure 3a, Appendix I and Figure S9, Appendix II). The IR spectrum of ZIF-8 is in good agreement with previous reports. The IR spectra of C_{60}@ZIF-8 samples were evaluated concerning varying loadings of fullerene C_{60} (detailed in Section S3, Appendix II). At low C_{60} loadings, the IR spectrum of ZIF-8 remains largely unaffected. However, higher C_{60} loadings result in more prominent spectral changes. Specifically, the spectral envelope, attributed to ethanol confined in the ZIF-8 cages between 1280 and 1200 cm^{-1}, disappears for 30% and higher loadings. (detailed in Figure 3a, Appendix I and Figure S12, Appendix II). The imidazole stretching bands at 1425 and 1458 cm^{-1}, respectively, change their relative intensity (Figure S10, Appendix II). Moreover, the in-plane deformation band at 1380 cm^{-1} experiences a substantial increase in intensity, though less prominent for loadings over 30% (Figure S11, Appendix II). As expected, upon C_{60} encapsulation, the imidazole ring deformation bands change. Specifically, the 780−720 cm^{-1} spectral envelope is composed of two bands, namely 760 cm^{-1} and 750 cm^{-1}. While the in-plane imidazole ring deformation band at 750 cm^{-1} remains unaffected, the out-of-plane deformation band at 760 cm^{-1} significantly increases in intensity (Figure S13, Appendix II). This indicates that, although free-standing inside the pore, the encapsulated C_{60} molecule affects the dynamics of the imidazole linkers and the MOF framework. Furthermore, the zinc-nitrogen stretching band and the above-mentioned Buckminsterfullerene radial motion bands slightly shift (Figure S14, Appendix II).

The efficiency of C_{60} encapsulation was quantified by analysing the 528 and 577 cm^{-1} fullerene bands. (detailed in Section S.3.2, Appendix II). The intensities and other spectral parameters related to the C_{60} molar ratio were determined by individually fitting the 528 and 577 cm^{-1} bands. The corresponding bands for an equivalent amount of the C_{60} standards are considered in the same spectral ranges. The mechanochemical approach described in this study allowed efficient C_{60} encapsulation, achieving up to 95% efficiency for 100%C_{60}@ZIF-8. Conversely, the post-synthetic process, which involved milling of fullerene and ZIF-8 and soaking it in toluene solution with an excess of fullerene as well as solvothermal synthesis, resulted in low loading (< 2.0 %) (Figure 4, Appendix I).

Discussion

Since the mechanochemical approach was most successful, we attempted to make 30% C_{60}@ZIF-8 material at the 10-milligram scale, as one of the initial motivations for this work was developing a procedure for efficient encapsulation of endofullerenes (commonly available in sub-milligram amount). The scaled-down synthesis was successful, and toluene filtrates were again colourless, proving the efficiency of the mechanochemical procedure regardless of the synthesis scale (Figure S6 and S16, Appendix II).

Furthermore, the materials underwent various analyses to investigate the influence of the encapsulated fullerene on the physicochemical properties of the ZIF-8. Electron paramagnetic resonance (EPR) spectroscopy determined that C_{60} in the framework was intact, as there were no changes in the spectra upon C_{60} encapsulation (Figures S21 and S22, Appendix II). High-angle annular dark-field scanning transmission electron microscopy (HAADF-STEM) and high-resolution transmission electron microscopy (HRTEM) were used to examine the fullerene position in the pore of ZIF-8 (Figure 6 Appendix I). Although its position was not unambiguously uncovered, we have seen the structure of ZIF-8 and discovered that C_{60}@ZIF-8 materials have better stability under electron radiation than empty ZIF-8, which loses its crystallinity upon the same dose. UV-Vis spectroscopy was used to examine the effect of the guest on the material's electronic properties. It was determined that encapsulation of C_{60} into the framework drastically reduces interactions between the C_{60} molecules and isolates them properly, and spectra of C_{60}@ZIF-8 resemble the one from diluted C_{60} solution (Figure 5, Appendix I, Figures S19 and S20, Appendix II). The inclusion of C_{60} did not significantly improve the thermal stability of ZIF-8 material (Figures S23 and S24, Appendix II). Finally, the chemical stability of C_{60}@ZIF-8 composites in acidic (0.5 mol dm^{-3} HCl (aq)) and basic (1 mol dm^{-3} KOH (aq)) environments was also examined. C_{60}@ZIF-8 samples were submerged in HCl or KOH water solutions and layered with toluene. Upon sonication, the sample in the basic solution remained unharmed, and the one in the acidic solution showed the release of C_{60} evidenced by characteristic toluene colouration. (Figure 8, Appendix I). These observations prove that mechanochemically encapsulated C_{60} is efficiently captured in the ZIF-8 framework and gets released only after framework destruction.

3.3. Strategies for bimetallic zinc-copper MOF-74 materials synthesis and modification

The next objective of our research was to advance bimetallic MOF synthesis. We investigated the mechanochemical synthesis of bimetallic zinc-copper MOF-74 materials to evaluate the impact of introducing heterometals on the framework through the MOF-74 materials' magnetic properties.[69] MOF-74 was chosen due to its chemical stability and tunable properties. This MOF is characterised by large hexagonal channel pores with 12 Å in diameter that extend along the crystallographic axis *c*. These channels are made of divalent metal cations (M^{2+}) ordered in 1D metal-oxo chains bridged by 2,5-dihydroxy-1,4-terephthalate anion ($DHTA^{4-}$), forming the M_2DHTA framework (Figure 1a, Appendix III). MOF-74 class is highly modular, with several monometallic MOFs known and multiple applications investigated.[8–10] This modularity also allows for the preparation of mixed metal phases with unique properties that stem from the synergistic effect between the two metals coupled closely in the 1D oxometallic chain.[74]

The controllable introduction of specific heterometallic combinations into the oxometallic chain of MOF through solution-based procedures remains a formidable challenge. As outlined in the *State of the art*, mechanochemical procedures offer a unique level of selectivity, stoichiometric control, and the ability to create unique products. One such example is the bimetallic MOFs. The efficient mechanochemical preparation of bimetallic MOFs can be achieved by two main approaches, either by combining already synthesised MOFs by mechanochemical alloying [51] or by stepwise synthesis starting from inorganic sources and organic ligands, thus enabling control over the metal stoichiometric ratio and minimising solvent consumption.[53] The latter approach in MOF-74 synthesis exploits the different binding capabilities of carboxylic and phenolic functional groups of H_4DHTA, which allow for the selective and controllable binding of target metals to a specific position. In the first step, this approach produces a 1D metal-organic polymer with well-defined binding sites within its structure that serve as a template for incorporating a secondary metal, which converts the structure into an open 3D metal-organic framework.

Here, we present three distinct bimetallic MM-MOF-74 materials containing zinc (II) and copper (II) nodes in a 1:1 ratio. These materials were synthesised using various mechanochemical approaches and polymeric precursors (Figure 1b, Appendix III). In order to determine the magnetic properties of the monometallic Cu-MOF-74 and to see how copper dilution and distribution within the bimetallic framework affect the magnetic properties of MOF-74 materials, we prepared Cu-MOF-74 by milling $Cu(OH)_2$ with DHTA in 2:1 ratio.

Discussion

Next, we prepared three zinc-copper MOF-74 materials following different reaction pathways inspired by the ones in the previous paragraph.[51,53] The ZnCu-MOF-74 material was prepared in two steps following a previously described technique.[53] In the first step, ZnO and DHTA were milled together to form the zinc intermediate phase, followed by the introduction of $Cu(OH)_2$ in the second step. The mechanochemical synthesis of the CuZn-MOF-74 material was designed analogously, preparing the Cu-INT in the first step and adding ZnO in the second step, resulting in CuZn-MOF-74 material. Zn/Cu-MOF-74-alloyed material was prepared by mixing Zn-MOF-74 and Cu-MOF-74 in a 1:1 ratio. The mixture of the two materials was milled, dried and then amorphised. The crystalline Zn/Cu-MOF-74-alloyed phase was obtained by exposing the amorphous mixture to methanol vapours (accelerated ageing).[75] The synthesis details can be found in Section 1.1 of Appendix IV. Three prepared zinc-copper MOF-74 materials are phase pure (Figures S2-S5 and S10-13, Appendix IV), indistinguishable by PXRD, and their FTIR spectra closely match (Figure 7 and Figure 2, Appendix III). Established based on flame atomic absorption spectroscopy (AAS) and scanning electron microscopy-energy dispersive X-ray analysis (SEM-EDAX), the molar ratio of the two metals in bimetallic zinc-copper MOF-74 materials is approximately 1:1 (Section S2.4. Appendix IV).
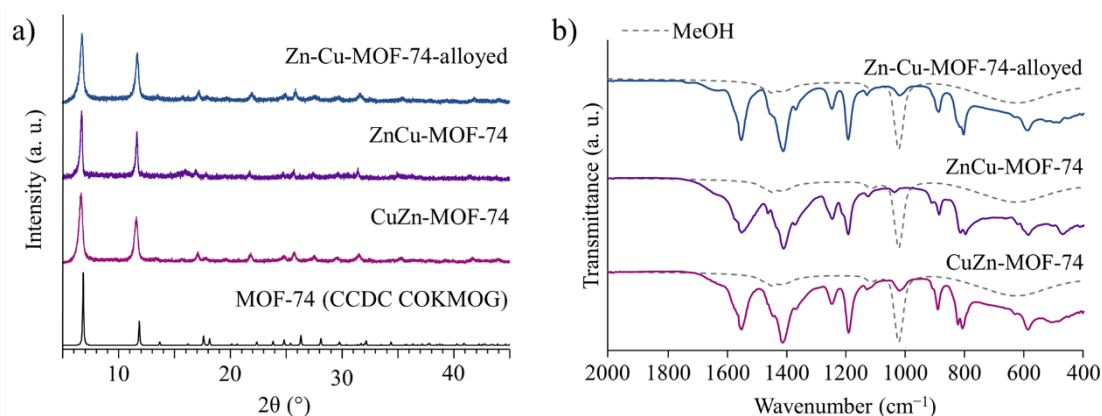
Figure 7 Mechanochemically synthesised zinc-copper MOF-74 a) PXRD patterns compared to the simulated pattern of MOF-74 (CCDC code: COKMOG), and b) FTIR spectra. Additional bands in the spectra originate from residual methanol (dashed line).

To study the differences that heterometal introduction brings, we examined the magnetic properties of prepared zinc-copper MOF-74 materials and compared them with Cu-MOF-74. Electron paramagnetic resonance (EPR) spectroscopy and superconducting quantum interference device (SQUID) analysis are powerful tools for investigating spin dynamics and magnetic properties that can provide detailed information on magnetic and electronic states.

26

Here, EPR analysis was applied to investigate local structural and magnetic properties, and subsequent SQUID analysis gave a more precise interpretation of EPR data and clarified bulk MOF-74 magnetic behaviour. X-band-EPR and HF-EPR spectra of Cu-MOF-74 are shown in Figure 3 in Appendix III. HF-EPR spectral shape analysis reveals two contributions, one corresponding to noninteracting, paramagnetic spin species and the other to magnetically coupled spin species. SQUID revealed that Cu-MOF-74 contains antiferromagnetic copper chains with weak interchain ferromagnetic interaction (Figure 4, Appendix III). X-band-EPR and HF-EPR spectra of zinc-copper MOF-74 materials are shown in Figure 5, Appendix III.

The HF-EPR spectrum of ZnCu-MOF-74 exhibits a typical pattern with a peak and a shoulder, and the spectra of CuZn-MOF-74 and Zn/Cu-MOF-74-alloyed are single Lorentzian-shaped lines pointing at the presence of noteworthy antiferromagnetic interactions. The narrower line of Zn/Cu-MOF-74-alloyed indicates a stronger antiferromagnetic interaction than in CuZn-MOF-74. The SQUID data for bimetallic MOF-74 materials exhibit distinct differences when compared among them and to monometallic Cu-MOF-74. The introduction of non-magnetic zinc to dilute magnetic copper leads to an increase in the number of paramagnetic spins and higher magnetisation in bimetallic MOFs. Figure 6 in Appendix III illustrates diverse magnetisation curves that do not overlap, indicating different types of spin clustering based on the synthetic route. This is also evident in the differences in magnetic susceptibility. CuZn-MOF-74 exhibits a combination of isolated paramagnetic copper species and long copper−copper associations. It is similar to Cu-MOF-74 but shows reduced intrachain coupling and ferromagnetic interchain interaction. ZnCu-MOF-74 displays a combination of well-isolated paramagnetic copper species and short copper dimers. Finally, Zn/Cu-MOF-74-alloyed, according to magnetic and other data, seems to be a physical mixture of Cu-MOF-74 and Zn-MOF-74. More details are in Appendix III and Sections S2.5 and S2.6 of Appendix IV).

To complement EPR and SQUID results, we used solid-state nuclear magnetic resonance (ssNMR). The ^{13}C MAS NMR spectra of bimetallic MOFs, CuZn-MOF-74, ZnCu-MOF-74, and Zn-Cu-MOF-74-alloyed were compared to the spectra of neat Cu-MOF-74 and Zn-MOF-74 (detailed in Appendix III). All bimetallic samples have methanol remnants in pores, indicated by a sharp signal at about 50 ppm and many broad framework-related signals with isotropic shifts, ranging from about −100 to 700 ppm. The absence of signals at shifts characteristic for monometallic copper and zinc MOF-74 indicates that carbon nuclei within both CuZn-MOF-74 and ZnCu-MOF-74 samples experience diverse environments, which implicates that functional groups of DHTA linkers of the MOF-74 framework connect to metal nodes of different types. In contrast, the ^{13}C MAS NMR spectrum of Zn/Cu-MOF-74-alloyed

suggests that this sample is either a mixture of monometallic copper and zinc MOF-74 or has large monometallic copper- and zinc-based domains (Figure 7, Appendix III).

Time-resolved in-situ PXRD reaction monitoring has revealed mechanisms beyond diverse copper-zinc MOF-74 formation. The transformation of Zn-INT to ZnCu-MOF-74 occurs through a multistep process that includes a short-lived UTSA-74 phase[76] (Figure 8a, Appendix III). This reaction does not involve any observable transformation of the Zn-INT to Cu-INT phase, indicating that copper does not exchange zinc from the carboxylate sites; it is incorporated at available free metal sites. The transformation of Cu-INT to CuZn-MOF-74 exhibits different dynamics. The consumption of ZnO in the synthesis of CuZn-MOF-74 occurs slowly (Figures 8b, Appendix III and S18, Appendix IV). This observation implies that Cu-INT undergoes partial conversion to Cu-MOF-74, as observed in the solution (Figure S1, Appendix IV), and that zinc incorporates at vacant metal sites, leading to reduced copper dilution, determined through magnetic measurements. The higher reactivity of the copper (II) with the DHTA ligand is further supported by the monitoring of the formation of the bimetallic framework MOF-74 using DHTA, ZnO, and $Cu(OH)_2$, where different copper intermediate phases are formed before the final MOF-74 (Figures 8c, Appendix III, and S19, Appendix IV). The observed differences in reactivity and affinity of the two metals for the functional groups of DHTA ligand, along with the crystal structure of the Cu-INT, which is being reported for the first time in this study (details in Section S2.2, Appendix IV),[44,69] may explain the variations in the distribution of metals in the oxometallic chains and the magnetic properties of three copper-zinc MOFs. The higher reactivity of copper compared to zinc, even towards phenolic groups, rationalises the formation of longer copper chains in the CuZn-MOF-74 and the efficient dispersion of copper nodes in the ZnCu-MOF-74 suggested by magnetic measurements.

3.4. Effects of defect and heterometal introduction on catalytic properties of MOF-74 materials

The final objective of our research was to explore the effects of mechanical amorphisation on MOF properties in the context of catalytic applications.[70] MOFs' distinct characteristics and considerable catalytic capacity have made them a focal point in the ongoing quest for novel catalysts. Their qualities arise from their porous structure and the nature of the metal nodes and organic linkers that comprise them.[2] This is emphasised after the recent synthetic advances in heterometallic MOF catalyst preparation, which display enhanced stability and applicability potential compared to their monometallic analogues.[61] A particularly exciting class of MOFs in this context is MOF-74, a family of MOF whose mechanochemical synthesis and structure is described in detail in Section 3.3. Moreover, it was recently shown that introducing traces of other metals into the oxometallic chain of MOF-74 could increase the activity and stability of the resulting heterometallic material.[53] Ball milling can be used for the stoichiometry-controlled formation of bimetallic zinc-copper MOF-74 materials with a 1:1 Zn: Cu molar ratio (Figure 1, Appendix V). Here, we explored the catalytic properties of ZnCu-MOF-74 upon mechanochemical amorphisation. Among potential zinc-copper MOF-74 materials, we chose this one as analyses showed it has the best copper distribution and dilution in the framework.[69]

The proximity of Zn and Cu cations gives rise to complex interactions that may have practical implications in catalytic reactions. This study aimed to investigate the potential of such an arrangement in ZnCu-MOF-74, coupled with its high porosity, for hydrogenating CO_2 to methanol. Recent research has demonstrated that metal-organic frameworks (MOFs) can effectively support active nanocatalysts, improving selectivity in methanol synthesis.[77,78] This work seeks to build upon this promising avenue of research by examining the catalytic performance of ZnCu-MOF-74.

We have prepared the crystalline ZnCu-MOF-74 (c-ZnCu-MOF-74) and compared its catalytic performance to the monometallic CuMOF-74 and the industrial $Cu/ZnO/Al_2O_3$ catalyst. Furthermore, we aimed to investigate the influence of mechanochemical amorphisation, which introduces defects and causes the collapse of the porous framework (Figure 8a),[79] on the solid-gas phase heterogeneous catalytic reaction by examining the catalytic performance of amorphous ZnCu-MOF-74 (a-ZnCu-MOF-74). As detailed below, the catalytic activity and selectivity of bimetallic MOF-74 are significantly influenced by the mechanochemical amorphisation, more so than by the high porosity and accessibility of Zn and Cu metal nodes in c-ZnCu-MOF-74.

Discussion

The mechanochemical incorporation of defects to ZnCu-MOF-74 leads to the fast collapse of the MOF-74 structure, as observed previously for Ni- and Zn-MOF-74.[64] This phenomenon is evident through a significant disparity in porosity between the crystalline and amorphous samples (Figures 2 and 3, Appendix V). The surface area and pore volume of a-ZnCu-MOF-74 are much lower than that of c-ZnCu-MOF-74, and the amorphised ZnCu-MOF-74 (a-ZnCu-MOF-74) displays a broad PXRD pattern without Bragg peaks characteristic of crystalline MOF-74 (Figure 8a).

FTIR spectra of c-ZnCu-MOF-74 show sharp signals that broaden and shift upon amorphisation (Figure 8b). The most notable difference in the spectra is the appearance of a new band corresponding to the stretching vibration of the uncoordinated carbonyl group, which was previously observed during the mechanochemical amorphisation of Ni-MOF-74.[64] The present evidence suggests that the amorphisation of ZnCu-MOF-74 is a result of the partial breakage of the metal-carboxylate bonds, forming a defective coordination sphere around copper and zinc metals. This claim is corroborated by a recent theoretical study that revealed the dynamic nature of metal-linker bonds in MOFs, which can break and reform under specific conditions.[80]
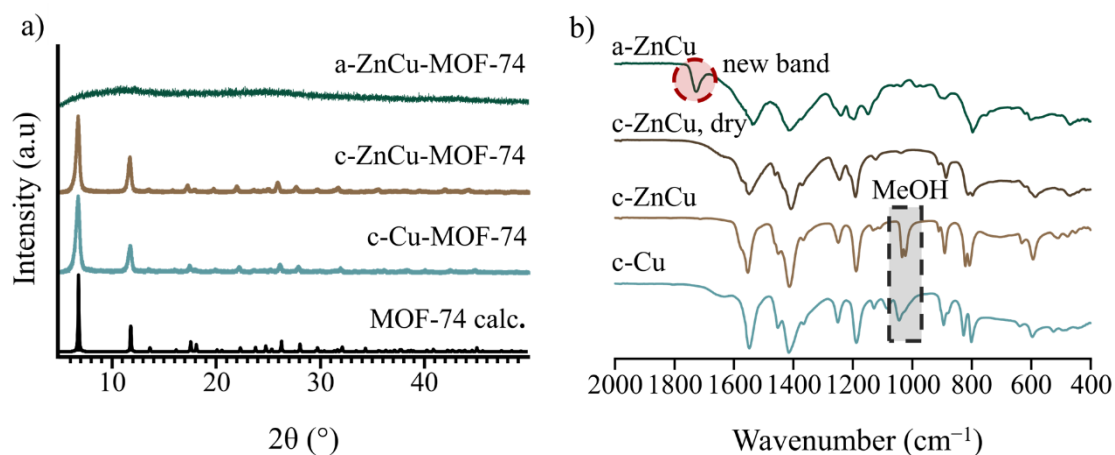
Figure 8 a) PXRD patterns of c-ZnCu-MOF-74 and a-ZnCu-MOF-74 compared to monometallic Cu-MOF-74 and simulated pattern of MOF-74 (CCDC code: COKMOG); (b) FTIR spectra of mechanochemically synthesised c-ZnCu-MOF-74 and a-ZnCu-MOF-74. A new band that appears upon amorphisation is circled. Additional bands in the spectra originate from residual methanol (dashed line square).

Cu-MOF-74, c-ZnCu-MOF-74 and a-ZnCu-MOF-74 exhibit similar decomposition profiles under the nitrogen flow within the temperature range of 400–900 °C (solvent-free MOF); see Figures S7 and S8, Appendix VI. This suggests that introducing a loss of long-range ordering does not significantly impact the thermal stability of MOF-74. To determine the local arrangement of metals in synthesised MOF-74 catalysts, we employed solid-state nuclear magnetic resonance spectroscopy (ssNMR).

As evident from Figure 4 in Appendix V, neither the ^{13}C MAS NMR spectrum of c-ZnCu-MOF-74 nor the spectrum of a-ZnCu-MOF-74 is a simple sum of the spectra of Zn-MOF-74 and Cu-MOF-74. This indicates that prepared bimetallic samples are new mixed metal phases. The ^{13}C MAS NMR spectra of c-ZnCu-MOF-74 and a-ZnCu-MOF-74 are rather similar but not identical to one another. They both exhibit several narrow signals in the range between 0 and 240 ppm and several broad signals in the range between 0 and 800 ppm. The narrow signals belong to carbon atoms in diamagnetic amorphous species. In the spectrum of a-ZnCu-MOF-74, the denoted signals belong to PMMA, an impurity introduced by milling, whereas the signals at 123, 155, and 170 ppm belong to domains of amorphous Zn-MOF-74. An additional narrow signal is present at about 213 ppm, which might correspond to the uncoordinated carbonyl group of the linker molecule. The broad signals are associated with carbon atoms near paramagnetic Cu centres. Strong hyperfine coupling between the unpaired electronic spins of copper ions and nuclear spins of ^{13}C nuclei results in significant shifts and broadening of these signals. The number, the positions, and the width of the broad signals of c-ZnCuMOF-74 and a-ZnCu-MOF-74 differ from those in the spectrum of the pure crystalline Cu-MOF-74. This suggests that Zn and Cu atoms are partially well-dispersed and "intimately" mixed within the two mixed-metal frameworks, giving rise to several different chemical environments for the nearby carbon atoms. In the spectrum of the crystalline material, we can notice a strong, sharp signal of MeOH. Moreover, the spectra of the two bimetallic samples exhibit differences in the broad signals resonating between 300 and 800 ppm. These findings are consistent with the results of the IR analysis, indicating that the connectivity of Zn and Cu within the frameworks of the crystalline and amorphous ZnCu-MOF-74 is rather different.

The mechanochemical synthesis resulted in ZnCu-MOF-74 particles of an irregular shape and size range of 10–80 nm, further decreasing to 5–30 nm upon amorphisation (Figure 5, Appendix V). Furthermore, SEM-EDAX analysis indicated homogeneous distribution and 1:1 Zn:Cu ratio in both the crystalline and amorphous ZnCu-MOF-74 materials (Figures S9-S11, Appendix VI).

Discussion

The catalytic performance of monometallic Cu-MOF-74 was found to be significantly improved by the incorporation of zinc. The bimetallic c-ZnCu-MOF-74 catalyst exhibited four to six times better catalytic activity towards methanol synthesis than Cu-MOF-74 material (Figure 6, Appendix V). This is attributed to the formation of additional active catalytic sites, which are facilitated by the lower activation energy towards methanol in the commercial Cu/ZnO/Al$_2$O$_3$ catalyst caused by zinc. The high surface area of active copper species in the Cu/ZnO/Al$_2$O$_3$ catalyst is achieved by the dispersion of copper in the ZnO/Al$_2$O$_3$ matrix, which led us to hypothesis that the activity of c-ZnCu-MOF-74 would be somewhat similar. However, it was observed that using a-ZnCu-MOF-74 was more beneficial, with a further increase in activity by four- to seven-fold after amorphisation (Figure 6, Appendix V).

The surface area of a-ZnCu-MOF-74 is much lower (~250 times) than the surface area of c-ZnCu-MOF-74. This observation indicates that introducing defects through amorphisation is instrumental in creating more active sites and, consequently, plays a more critical role in MeOH synthesis than the porosity of crystalline MOF. The impact of catalyst structure and composition on catalytic properties was evaluated using the Arrhenius plot (Figure 7, Appendix V). Moreover, Table 1 in Appendix V contains activation energy (E_a), preexponential factors (A), and the rates of MeOH and CO formation (r) for synthesised MOF-74 samples and Cu/ZnO/Al$_2$O$_3$ catalyst for MeOH and CO formation at 200 °C.

Together with catalytic activity, selectivity toward methanol was also examined. It was observed that adding zinc to the oxometallic chain in crystalline Cu-MOF-74 led to an almost five-fold (approx. 4.7) increase in MeOH synthesis selectivity (Figure 8, Appendix V). The amorphisation of c-ZnCu-MOF-74 reduced the surface area and particle size, changing the metal nodes' coordination sphere in MOF-74. These changes resulted in an increase in selectivity toward MeOH by a factor of 8.3 for amorphous ZnCu-MOF-74. In contrast, separated copper atoms or small copper clusters in the crystalline MOF tend to promote the competitive RWGS (reverse water-gas shift) reaction, with the rate of RWGS reaction of c-ZnCu-MOF-74 nearly reaching that of MeOH synthesis.

§ 4. CONCLUSIONS

The mechanochemical ILAG approach emerged as a highly efficient, sustainable, and precise method for preparing fulleretic materials with specific amounts of fullerene C_{60} guests. This method outperforms traditional solution synthetic and post-synthetic encapsulation procedures, as it resolves solvent-related issues such as solubility, solvation, and competition of the fullerene guest with solvent molecules for the MOF pores. Moreover, as hypothesised in the *Introduction*, the studied approach enables stoichiometrically controlled loading of the Buckminsterfullerene into ZIF-8. Additionally, the confinement of C_{60} in the ZIF-8 contributes to the enhanced properties of ZIF-8, as hypothesised, particularly in terms of rigidity and stability of ZIF-8 against electron dose radiation. DFTB-based molecular dynamics studies indicate that the hollow fullerene is accommodated in the middle of the cage, rationalising the changes in the IR and PXRD data observed upon encapsulation. Entrapped fullerene is immobilised and exhibits almost single-molecule properties. Transport of the fullerene through the framework is an energetically unfavourable process and requires substantial rearrangement in the aperture structure. The entrapped C_{60} are well isolated from one another, making ZIF-8 a suitable matrix for the efficient immobilisation of fullerene guests. The remarkable efficiency and scalability of the presented mechanochemical procedure suggest its potential extension to the entrapment of metallofullerenes, obtainable at a sub-milligram scale, to develop novel fulleretic materials with advanced functionalities.

Prepared mixed-metal MOF-74 materials are almost indistinguishable from PXRD and FTIR but have different magnetic behaviour. The presented magnetic analysis of zinc-copper MOF-74 materials shows that magnetically active nodes can be efficiently dispersed in the MOF-74 framework using mechanochemical synthesis, leading to different magnetic properties among them and compared to the monometallic Cu-MOF-74. Cu-MOF-74 possesses antiferromagnetic copper chains with weaker interchain ferromagnetic interaction. CuZn-MOF-74, obtained via the copper intermediate phase, combines isolated paramagnetic copper species and longer copper−copper associations with the reduced strength of intrachain coupling and ferromagnetic interchain interaction. Moreover, ZnCu-MOF-74, obtained via the zinc-intermediate phase, combines well-isolated paramagnetic copper species and short copper dimers. According to magnetic (EPR and SQUID), microscopic (SEM-EDAX), and spectroscopic (ssNMR) results, the alloyed sample was predominantly a physical mixture of

Conclusions

Cu-MOF-74 and Zn-MOF-74 domains. Besides that, real-time in-situ synchrotron PXRD monitoring uncovered that the difference between the materials stems from the different natures of the metal species and their affinity for the DHTA functional groups. In the present case, zinc is firmly bound to DHTA in Zn-INT, resulting in an efficient dispersion and isolation of paramagnetic copper nodes introduced in the second synthetic step. Contrarywise, the high reactivity of copper (II) with DHTA ligand leads to the formation of longer copper chains and different magnetic properties. This confirms the hypothesis that the properties of bimetallic MOF vary depending on the mechanochemical synthetic route used. Therefore, one should be cautious of the order in which two metals are combined, as small changes in spin states and magnetic anisotropy among synthesised materials lead to substantially different magnetic behaviours.

ZnCu-MOF-74, which showed the most uniform zinc-copper metal distribution of all zinc-copper MOF-74 materials, was further studied for catalysis. Unlike the monometallic Cu-MOF-74, bimetallic crystalline ZnCu-MOF-74, shows good catalytic activity for selective reduction of CO_2 to methanol. Mechanochemical amorphisation of the desolvated porous crystalline ZnCu-MOF-74 material results in the formation of amorphous and non-porous ZnCu-MOF-74 material with a similar distribution of heterometal nodes. The spectroscopic analyses show that the coordination sphere of the nodes is changed upon amorphisation, most likely due to the break of carboxylate−metal bonds. The catalytic activity of the amorphous catalysts significantly surpasses that of the crystalline ZnCu-MOF-74 counterpart due to the additional active sites formed during the amorphisation. This confirms the hypothesis that the amorphisation of MOF-74 yields amorphous materials with improved properties when compared to the crystalline MOF counterparts. Particularly noteworthy is the increase in the selectivity towards methanol formation following the amorphisation of the MOF. The amorphous ZnCu-MOF-74 exhibits selectivity comparable to that of the industrial $Cu/ZnO/Al_2O_3$. In the context of the methanol synthesis reaction, it becomes evident that the introduction of defects through amorphisation is more important than the initial catalyst porosity. This suggests that CO_2 reduction primarily occurs on the surface of the MOF catalyst.

The findings outlined in this work represent significant advancements in the development of mechanochemical synthetic strategies for the preparation of functional MOFs. Together, they shed light on how guest encapsulation and metal or defect introduction into the framework affect its structure and properties, providing better understanding and novel insights and paving the way for future research and development in the field of metal-organic frameworks.

§ 5. LIST OF ABBREVIATIONS, ACRONYMS, AND SYMBOLS

2-MeIm (or MeIm) - 2-methylimidazole

A - preexponential factor

a-ZnCu-MOF-74 – amorphous bimetallic zinc-copper MOF-74

AAS- atomic absorption spectroscopy

bdc - 1,4-benzene dicarboxylic acid

c-ZnCu-MOF-74 – crystalline bimetallic zinc-copper MOF-74

Cu-INT - copper intermediate

DABCO - 1,4-diazabicyclo[2.2.2]octane

DEF - *N, N*-diethylformamide

DHTA - 2,5-dihydroxyterephtalic acid or 2,5-dihydroxy-1,4-terephthalic acid*

DMF - *N, N*-dimethylformamide

DMSO – dimethylsulfoxide

E_a -activation energy

EPR - electron paramagnetic resonance

EtIm - ethyl-imidazole

EtOH - ethanol

FTIR-ATR - Fourier transform infrared spectroscopy – attenuated total reflectance

HAADF-STEM - high-angle annular dark-field scanning transmission electron microscopy

HE-ZIF - high-entropy zeolitic imidazolate framework

HEA - high-entropy alloy

HF-EPR - high-field electron paramagnetic resonance

HRTEM - high-resolution transmission electron microscopy

ILAG-ion-assisted grinding

HIm - imidazole

LAG - liquid-assisted grinding

MAS- magic-angle spinning

MD - molecular dynamics

MNP - metal nanoparticle

MOF - metal-organic framework

List of abbreviations, acronyms, and symbols

MeOH - methanol

η - parameter in mechanochemical synthesis, which represents the ratio of the volume of liquid (in μL) to the combined weights of the solid reactants (in mg) and defines LAG

NG - neat grinding

NMR - nuclear-magnetic resonance

NP - nanoparticle

PEG - polyethylene glycol polymers

PMMA- polymethylmethacrylate

POLAG – polymer-assisted grinding

PXRD - powder diffraction

r -reaction rate

RWGS - reverse water-gas shift

SEAG - seeding-assisted grinding

SEM-EDAX - scanning electron microscopy-energy dispersive X-ray analysis

ssNMR - solid-state nuclear magnetic resonance

TEM - transmission electron microscopy

TGA- thermogravimetric analysis

T_m – melting temperature

UV-Vis - ultraviolet-visible spectroscopy

ZIF - zeolitic imidazolate framework

*present also in half (H_2DHTA) or fully (H_4DHTA) protonated (abbreviated) form

§ 6. BIBLIOGRAPHY

(1) V. Martinez, T. Stolar, B. Karadeniz, I. Brekalo, K. Užarević, Advancing Mechanochemical Synthesis by Combining Milling with Different Energy Sources *Nat. Rev. Chem.* **7** (2022) 51–65.

(2) V. V. Butova, M. A. Soldatov, A. A. Guda, K. A. Lomachenko, C. Lamberti, Metal-Organic Frameworks: Structure, Properties, Methods of Synthesis and Characterization *Russ. Chem. Rev.* **85** (2016) 280–307.

(3) F. Gomollón-Bel, Ten Chemical Innovations That Will Change Our World: IUPAC Identifies Emerging Technologies in Chemistry with Potential to Make Our Planet More Sustainable *Chem. Int.* **41** (2019) 12–17.

(4) A. J. Howarth, A. W. Peters, N. A. Vermeulen, T. C. Wang, J. T. Hupp, O. K. Farha, Best Practices for the Synthesis, Activation, and Characterization of Metal-Organic Frameworks *Chem. Mater.* **29** (2017) 26–39.

(5) T. Stolar, K. Užarević, Mechanochemistry: An Efficient and Versatile Toolbox for Synthesis, Transformation, and Functionalization of Porous Metal-Organic Frameworks *CrystEngComm* **22** (2020) 4511–4525.

(6) K. S. Park, Z. Ni, A. P. Côté, J. Y. Choi, R. Huang, F. J. Uribe-Romo, H. K. Chae, M. O'Keeffe, O. M. Yaghi, Exceptional Chemical and Thermal Stability of Zeolitic Imidazolate Frameworks *Proc. Natl. Acad. Sci.* **103** (2006) 10186–10191.

(7) A. M. Rice, E. A. Dolgopolova, N. B. Shustova, Fulleretic Materials: Buckyball- and Buckybowl-Based Crystalline Frameworks *Chem. Mater.* **29** (2017) 7054–7061.

(8) W. L. Queen, M. R. Hudson, E. D. Bloch, J. A. Mason, M. I. Gonzalez, J. S. Lee, D. Gygi, J. D. Howe, K. Lee, T. A. Darwish, M. James, V. K. Peterson, S. J. Teat, B. Smit, J. B. Neaton, J. R. Long, C. M. Brown, Comprehensive Study of Carbon Dioxide Adsorption in the Metal-Organic Frameworks M_2(dobdc) (M = Mg, Mn, Fe, Co, Ni, Cu, Zn) *Chem Sci* **5** (2014) 4569–4581.

(9) K. Lee, J. D. Howe, L.-C. Lin, B. Smit, J. B. Neaton Small-Molecule Adsorption in Open-Site Metal-Organic Frameworks: A Systematic Density Functional Theory Study for Rational Design *Chem. Mater.* **27** (2015) 668–678.

(10) T. Xiao, D. Liu, The Most Advanced Synthesis and a Wide Range of Applications of MOF-74 and Its Derivatives *Microporous Mesoporous Mater.* **283** (2019) 88–103.

(11) C. Castillo-Blas, F. Gándara, Metal-Organic Frameworks Incorporating Multiple Metal Elements *Isr. J. Chem.* **58** (2018) 1036–1043.

(12) A. A. L. Michalchuk, E. V. Boldyreva, A. M. Belenguer, F. Emmerling, V. V. Boldyrev, Tribochemistry, Mechanical Alloying, Mechanochemistry: What Is in a Name? *Front. Chem.* **9** (2021) 685789.

(13) L. Takacs, The Historical Development of Mechanochemistry *Chem. Soc. Rev.* **42** (2013) 7649.

(14) I. Halasz, S. A. J. Kimber, P. J.; Beldon, A. M. Belenguer, F. Adams, V. Honkimäki, R. C. Nightingale, R. E. Dinnebier, T. Friščić, In Situ and Real-Time Monitoring of Mechanochemical Milling Reactions Using Synchrotron X-Ray Diffraction *Nat. Protoc.* **8** (2013) 1718–1729.

(15) S. Lukin, K. Užarević, I. Halasz, Raman Spectroscopy for Real-Time and in Situ Monitoring of Mechanochemical Milling Reactions. *Nat. Protoc.* **16** (2021) 3492–3521.

(16) J. F. Reynes, V. Isoni, F. García, Tinkering with Mechanochemical Tools for Scale Up. *Angew. Chem. Int. Ed.* **62** (2023) e202300819.

Bibliography

(17) L. E. Wenger, T. P. Hanusa, Synthesis without Solvent: Consequences for Mechanochemical Reactivity *Chem. Commun.* **59** (2023) 14210–14222.

(18) M. Arhangelskis, D. K. Bučar, S. Bordignon, M. R. Chierotti, S. A. Stratford, D. Voinovich, W. Jones, D. Hasa, Mechanochemical Reactivity Inhibited, Prohibited and Reversed by Liquid Additives: Examples from Crystal-Form Screens. *Chem. Sci.* **12** (2021) 3264–3269.

(19) T. Friščić, S. L. Childs, S. A. A. Rizvi, W. Jones, The Role of Solvent in Mechanochemical and Sonochemical Cocrystal Formation: A Solubility-Based Approach for Predicting Cocrystallisation Outcome. *CrystEngComm* **11** (2009) 418–426.

(20) T. Friščić, D. G. Reid, I. Halasz, R. S. Stein, R. E. Dinnebier, M. J. Duer, Ion- and Liquid-Assisted Grinding: Improved Mechanochemical Synthesis of Metal-Organic Frameworks Reveals Salt Inclusion and Anion Templating *Angew. Chem. Int. Ed.* **49** (2010) 712–715.

(21) J. L. Do, T. Friščić, Mechanochemistry: A Force of Synthesis. *ACS Cent. Sci.* **3** (2017) 13–19.

(22) D. Cinčić, I. Brekalo, B. Kaitner, Solvent-Free Polymorphism Control in a Covalent Mechanochemical Reaction *Cryst. Growth Des*. **12** (2012) 44–48.

(23) D. Hasa, G. Schneider Rauber, D. Voinovich, W. Jones Cocrystal Formation through Mechanochemistry: From Neat and Liquid-Assisted Grinding to Polymer-Assisted Grinding. *Angew. Chem. Int. Ed*. **54** (2015) 7371–7375.

(24) D. Hasa, E. Carlino, W. Jones, Polymer-Assisted Grinding, a Versatile Method for Polymorph Control of Cocrystallization. *Cryst. Growth Des*. **16** (2016) 1772–1779.

(25) V. Declerck, E. Colacino, X. Bantreil, J. Martinez, F. Lamaty, Poly(Ethylene Glycol) as Reaction Medium for Mild Mizoroki–Heck Reaction in a Ball-Mill *Chem. Commun*. **48** (2012) 11778.

(26) L. Konnert, M. Dimassi, L. Gonnet, F. Lamaty, J. Martinez, E. Colacino, Poly(Ethylene) Glycols and Mechanochemistry for the Preparation of Bioactive 3,5-Disubstituted Hydantoins. *RSC Adv.* **6** (2016) 36978–36986.

(27) A. A. L. Michalchuk, F. Emmerling, Time-Resolved In Situ Monitoring of Mechanochemical Reactions. *Angew. Chem. Int. Ed.* **61** (2022) e202117270.

(28) N. Cindro, M. Tireli, B. Karadeniz, T. Mrla, K. Užarević, Investigations of Thermally Controlled Mechanochemical Milling Reactions *ACS Sustain. Chem. Eng.* **7** (2019) 16301–16309.

(29) I. Brekalo, V. Martinez, B. Karadeniz, P. Orešković, D. Drapanauskaite, H. Vriesema, R. Stenekes, M. Etter, I. Dejanović, J. Baltrusaitis, K. Užarević, Scale-Up of Agrochemical Urea-Gypsum Cocrystal Synthesis Using Thermally Controlled Mechanochemistry *ACS Sustain. Chem. Eng.* **10** (2022) 6743–6754.

(30) J. Alić, I. Lončarić, M. Etter, M. Rubčić, Z. Štefanić, M. Šekutor, K. Užarević, T. Stolar, Direct in Situ Measurement of Polymorphic Transition Temperatures under Thermo-Mechanochemical Conditions *Phys. Chem. Chem. Phys.* **26** (2024) 4840–4844.

(31) J. Stojaković, B. S. Farris, L. R. MacGillivray, Vortex Grinding for Mechanochemistry: Application for Automated Supramolecular Catalysis and Preparation of a Metal-Organic Framework *Chem. Commun*. **48** (2012) 7958.

(32) A. N. Sokolov, D. Bučar, J. Baltrusaitis, S. X. Gu, L. R. MacGillivray, Supramolecular Catalysis in the Organic Solid State through Dry Grinding *Angew. Chem. Int. Ed*. **49** (2010) 4273–4277.

(33) J. G. Hernández, Mechanochemical Borylation of Aryldiazonium Salts; Merging Light and Ball Milling. Beilstein *J. Org. Chem.* **13** (2017) 1463–1469.

(34) A. Pichon, A. Lazuen-Garay, S. L. James, Solvent-Free Synthesis of a Microporous Metal-Organic Framework. *CrystEngComm* **8** (2006) 211.

Bibliography

(35) T. Friščić, L. Fábián, Mechanochemical Conversion of a Metal Oxide into Coordination Polymers and Porous Frameworks Using Liquid-Assisted Grinding (LAG). *CrystEngComm* **11** (2009) 743.

(36) P. J. Beldon, L. Fábián, R. S. Stein, A. Thirumurugan, A. K. Cheetham, T. Friščić, Rapid Room-Temperature Synthesis of Zeolitic Imidazolate Frameworks by Using Mechanochemistry *Angew. Chem. Int. Ed*. **49** (2010) 9640–9643.

(37) M. F. Thorne, M. L. R. Gómez, A. M. Bumstead, S. Li, T. D. Bennett, Mechanochemical Synthesis of Mixed Metal, Mixed Linker, Glass-Forming Metal-Organic Frameworks. *Green Chem.* **22** (2020) 2505–2512.

(38) W. Yuan, T. Friščić, D. Apperley, S. L. James, High Reactivity of Metal-Organic Frameworks under Grinding Conditions: Parallels with Organic Molecular Materials *Angew. Chem. Int. Ed.* **49** (2010) 3916–3919.

(39) B. Karadeniz, D. Žilić, I. Huskić, L. S. Germann, A. M. Fidelli, S. Muratović, I. Lončarić, M. Etter, R. E. Dinnebier, D. Barišić, N. Cindro, T. Islamoglu, O. K. Farha, T. Friščić, K. Užarević, Controlling the Polymorphism and Topology Transformation in Porphyrinic Zirconium Metal–Organic Frameworks via Mechanochemistry. *J. Am. Chem. Soc.* **141** (2019) 19214–19220.

(40) P. A. Julien, K. Užarević, A. D. Katsenis, S. A. J. Kimber, T. Wang, O. K. Farha, Y. Zhang, J. Casaban, L. S. Germann, M. Etter, R. E. Dinnebier, S. L. James, I. Halasz, T. Friščić, In Situ Monitoring and Mechanism of the Mechanochemical Formation of a Microporous MOF-74 Framework *J. Am. Chem. Soc.* **138** (2016) 2929–2932.

(41) A. D. Katsenis, A. Puškarić, V. Štrukil, C. Mottillo, P. A. Julien, K. Užarević, M.-H. Pham, T.-O. Do, S. A: J. Kimber, P. Lazić, O. Magdysyuk, R. E. Dinnebier, I. Halasz, T. Friščić, In Situ X-Ray Diffraction Monitoring of a Mechanochemical Reaction Reveals a Unique Topology Metal-Organic Framework *Nat. Commun.* **6** (2015) 6662.

(42) T. Friščić, I. Halasz, P. J. Beldon, A. M. Belenguer, F. Adams, S. A. J. Kimber, V. Honkimäki, R. E. Dinnebier, Real-Time and in Situ Monitoring of Mechanochemical Milling Reactions. *Nat. Chem*. **5** (2013) 66–73.

(43) J. Beamish-Cook, K. Shankland, C. A: Murray, P. Vaqueiro, Insights into the Mechanochemical Synthesis of MOF-74. *Cryst. Growth Des*. **21** (2021) 3047–3055.

(44) C. R. Groom, I. J. Bruno, M. P. Lightfoot, S. C. Ward, *The Cambridge Structural Database. Acta Crystallogr. Sect. B Struct. Sci. Cryst. Eng. Mater*. **72** (2016) 171–179.

(45) S. Kitagawa, Future Porous Materials. *Acc. Chem. Res.* **50** (2017) 514–516.

(46) A. Helal, Z. H. Yamani, K. E. Cordova, O. M. Yaghi, Multivariate Metal-Organic Frameworks *Natl. Sci. Rev*. **4** (2017) 296–298.

(47) L. Chen, H.-F. Wang, C. Li, Q. Xu, Bimetallic Metal–Organic Frameworks and Their Derivatives *Chem. Sci*. **11** (2020) 5369–5403.

(48) Y. Wang, H. Lv, E. S. Grape, C. A. Gaggioli, A. Tayal, A. Dharanipragada, T. Willhammar, A. K. Inge, X. Zou, B. Liu, Z. Huang, A Tunable Multivariate Metal-Organic Framework as a Platform for Designing Photocatalysts *J. Am. Chem. Soc*. **143** (2021) 6333–6338.

(49) K. T. Smith, K. C. Stylianou, Multivariate Metal–Organic Frameworks Generated through Post-Synthetic Modification: Impact and Future Directions *Dalton Trans*. **52** (2023) 16578–16585.

(50) J. Castells-Gil, N. Almora-Barrios, B. Lerma-Berlanga, N. M. Padial, C. Martí-Gastaldo, Chemical Complexity for Targeted Function in Heterometallic Titanium-Organic Frameworks *Chem. Sci*. **14** (2023), 6826–6840.

(51) T. Panda, S. Horike, K. Hagi, N. Ogiwara, K. Kadota, T. Itakura, M. Tsujimoto, S. Kitagawa, Mechanical Alloying of Metal-Organic Frameworks *Angew. Chem. Int. Ed*. **56** (2017) 2413–2417.

Bibliography

(52) W. Xu, H. Chen, K. Jie, Z. Yang, T. Li, S. Dai, Entropy-Driven Mechanochemical Synthesis of Polymetallic Zeolitic Imidazolate Frameworks for CO_2 Fixation. *Angew. Chem. Int. Ed.* **58** (2019), 5018–5022.

(53) G. Ayoub, B. Karadeniz, A. J. Howarth, O. K. Farha, I. Đilović, L. S. Germann, R. E. Dinnebier, K. Užarević, T. Friščić, Rational Synthesis of Mixed-Metal Microporous Metal-Organic Frameworks with Controlled Composition Using Mechanochemistry *Chem. Mater.* **31** (2019) 5494–5501.

(54) D. Kim, A. Coskun, Template-Directed Approach Towards the Realization of Ordered Heterogeneity in Bimetallic Metal-Organic Frameworks *Angew. Chem. Int. Ed.* **56** (2017) 5071–5076.

(55) L. Vujević, B. Karadeniz, N. Cindro, A. Krajnc, G. Mali, M. Mazaj, S. M. Avdoshenko, A. A. Popov, D. Žilić, K. Užarević, M. Kveder, Improving the Molecular Spin Qubit Performance in Zirconium MOF Composites by Mechanochemical Dilution and Fullerene Encapsulation *Chem. Sci.* 14 (2023) 9389–9399.

(56) F. G. Cirujano, F. X. Llabrés I Xamena, Metal-Organic Frameworks as Nanoreactors and Host Matrices for Encapsulation. in Samahe Sadjadi (ed) Organic Nanoreactors From Molecular to Supramolecular Organic Compounds, 1st ed, Elsevier, 2016; pp 305–340.

(57) P. Gao, X. Shi, X. Xu, W. Wei, Versatile and Efficient Mechanochemical Synthesis of Crystalline Guest⊂Zeolitic Imidazolate Framework Complexes by in Situ Host-Guest Nanoconfinement *Cryst. Growth Des.* **18** (2018) 5845–5852.

(58) S. A. Noorian, N. Hemmatinejad, J. A. R. Navarro, Bioactive Molecule Encapsulation on Metal-Organic Framework via Simple Mechanochemical Method for Controlled Topical Drug Delivery Systems. Microporous *Mesoporous Mater.* **302** (2020) 110199.

(59) W. Liang, P. Wied, F. Carraro, C. J. Sumby, B. Nidetzky, C.-K. Tsung, P. Falcaro, C. J. Doonan, Metal-Organic Framework-Based Enzyme Biocomposites *Chem. Rev.* **121** (2021), 1077–1129.

(60) X. Li, Z. Zhang, W. Xiao, S. Deng, C. Chen, N. Zhang, Mechanochemistry-Assisted Encapsulation of Metal Nanoparticles in MOF Matrices via a Sacrificial Strategy *J. Mater. Chem. A* **7** (2019) 14504–14509.

(61) T. H. Wei, S. H. Wu, Y. D. Huang, W. S. Lo, B. P. Williams, S. Y. Chen, H. C. Yang, Y. S. Hsu, Z. Y. Lin, X. H. Chen, P. E. Kuo, L. Y. Chou, C. K. Tsung, F. K. Shieh, Rapid Mechanochemical Encapsulation of Biocatalysts into Robust Metal-Organic Frameworks *Nat. Commun.* **10** (2019) 5002.

(62) A. K. Cheetham, T. D. Bennett, F. X. Coudert, A. L. Goodwin Defects and Disorder in Metal-Organic Frameworks *Dalton Trans.* **45** (2016) 4113–4126.

(63) T. D. Bennett, A. K. Cheetham, Amorphous Metal-Organic Frameworks *Acc. Chem. Res.* **47** (2014) 1555–1562.

(64) S. Muratović, B. Karadeniz, T. Stolar, S. Lukin, I. Halasz, M. Herak, G. Mali, Y. Krupskaya, V. Kataev, D. Žilić, K. Užarević, Impact of Dehydration and Mechanical Amorphization on the Magnetic Properties of Ni(II)-MOF-74 *J. Mater. Chem. C* **8** (2020) 7132–7142.

(65) S. Cao, T. D. Bennett, D. A. Keen, A. L. Goodwin, A. K. Cheetham, Amorphization of the Prototypical Zeolitic Imidazolate Framework ZIF-8 by Ball-Milling *Chem. Commun.* **48** (2012) 7805.

(66) M. F. Thorne, C. Castillo-Blas, L. N. McHugh, A. M. Bumstead, G. Robertson, A. F. Sapnik, C. S. Coates, F. N. Sayed, C. P. Grey, D. A. Keen, M. Etter, I. Da Silva, K. Užarević, T. D. Bennett, Formation of New Crystalline Qtz-[Zn(mIm)₂] Polymorph from Amorphous ZIF-8 *Chem. Commun.* **58** (2022) 11949–11952.

Bibliography

(67) M. F. Thorne, A. F. Sapnik, L. N. McHugh, A. M. Bumstead, C. Castillo-Blas, D. S. Keeble, M. Diaz Lopez, P. A. Chater, D. A. Keen, T. D. Bennett, Glassy Behaviour of Mechanically Amorphised ZIF-62 Isomorphs *Chem. Commun.* **57** (2021) 9272–9275.

(68) V. Martinez, B. Karadeniz, N. Biliškov, I. Lončarić, S. Muratović, D. Žilić, S. M. Avdoshenko, M. Roslova, A. A. Popov, K. Užarević, Tunable Fulleretic Sodalite MOFs: Highly Efficient and Controllable Entrapment of C_{60} Fullerene via Mechanochemistry *Chem. Mater.* **32** (2020) 10628–10640.

(69) S. Muratović, V. Martinez, B. Karadeniz, D. Pajić, I. Brekalo, M. Arhangelskis, M. Mazaj, G. Mali, M. Etter, T. Friščić, Y. Krupskaya, V. Kataev, D. Žilić, K. Užarević, Low-Dimensional Magnetism in Multivariate Copper/Zinc MOF-74 Materials Formed via Different Mechanochemical Methods *Inorg. Chem.* **61** (2022) 18181–18192.

(70) T. Stolar, A. Prašnikar, V. Martinez, B. Karadeniz, A. Bjelić, G. Mali, T. Friščić, B. Likozar, K. Užarević, Scalable Mechanochemical Amorphization of Bimetallic Cu-Zn MOF-74 Catalyst for Selective CO_2 Reduction Reaction to Methanol *ACS Appl. Mater. Interfaces* **13** (2021) 3070–3077.

(71) J. Juan-Alcañiz, J. Gascon, F. Kapteijn, Metal-Organic Frameworks as Scaffolds for the Encapsulation of Active Species: State of the Art and Future Perspectives *J. Mater. Chem.* **22** (2012) 10102.

(72) A. Goel, J. B. Howard, J. B. Vander Sande, Size Analysis of Single Fullerene Molecules by Electron Microscopy *Carbon* **42** (2004) 1907–1915.

(73) A. Hjorth Larsen, J. Jørgen Mortensen, J. Blomqvist, I. E. Castelli, R. Christensen, M. Dułak, J. Friis, M. N. Groves, B. Hammer, C. Hargus, E. D. Hermes, P. C. Jennings, P. Bjerre Jensen, J. Kermode, J. R. Kitchin, E. Leonhard Kolsbjerg, J. Kubal, K. Kaasbjerg, S. Lysgaard, J. Bergmann Maronsson, T. Maxson, T. Olsen, L. Pastewka, A. Peterson, C. Rostgaard, J. Schiøtz, O. Schütt, M. Strange, K. S. Thygesen, T. Vegge, L. Vilhelmsen, M. Walter, Z. Zeng, K. W. Jacobsen, The Atomic Simulation Environment—a Python Library for Working with Atoms. *J. Phys. Condens. Matter* **29** (2017) 273002.

(74) H. Kim, C. S. Hong, MOF-74-Type Frameworks: Tunable Pore Environment and Functionality through Metal and Ligand Modification. *CrystEngComm* **23** (2021) 1377–1387.

(75) M. J. Cliffe, C. Mottillo, R. S. Stein, D. K. Bučar, T. Friščić, Accelerated Aging: A Low Energy, Solvent-Free Alternative to Solvothermal and Mechanochemical Synthesis of Metal-Organic Materials *Chem. Sci.* **3** (2012) 2495–2500.

(76) F. Luo, C. Yan, L. Dang, R. Krishna, W. Zhou, H. Wu, X. Dong, Y. Han, T. L. Hu, M. O'Keeffe, L. Wang, M. Luo, R. B. Lin, B. Chen, UTSA-74: A MOF-74 Isomer with Two Accessible Binding Sites per Metal Center for Highly Selective Gas Separation. *J. Am. Chem. Soc.* **138** (2016) 5678–5684.

(77) B. An, J. Zhang, K. Cheng, P. Ji, C. Wang, W. Lin, Confinement of Ultrasmall Cu/ZnO$_x$ Nanoparticles in Metal-Organic Frameworks for Selective Methanol Synthesis from Catalytic Hydrogenation of CO_2 *J. Am. Chem. Soc.* **139** (2017) 3834–3840.

(78) H. Kobayashi, J. M. Taylor, Y. Mitsuka, N. Ogiwara, T. Yamamoto, T. Toriyama, S. Matsumura, H. Kitagawa, Charge Transfer Dependence on CO_2 Hydrogenation Activity to Methanol in Cu Nanoparticles Covered with Metal-Organic Framework Systems *Chem. Sci.* **10** (2019) 3289–3294.

(79) T. D. Bennett, T. K. Todorova, E. F. Baxter, D. G. Reid, C. Gervais, B. Bueken, B. Van De Voorde, D. De Vos, D. A. Keen, C. Mellot-Draznieks, Connecting Defects and Amorphization in UiO-66 and MIL-140 Metal-Organic Frameworks: A Combined Experimental and Computational Study *Phys. Chem. Chem. Phys.* **18** (2016) 2192–2201.

Bibliography

(80)   A. B. Andreeva, K. N. Le, L. Chen, M. E. Kellman, C. H. Hendon, C. K. Brozek, Soft
Mode Metal-Linker Dynamics in Carboxylate MOFs Evidenced by Variable-Temperature
Infrared Spectroscopy *J. Am. Chem. Soc.* **142** (2020) 19291–19299.

§ 7. DISSERTATION SUPPLEMENT

7.1. Appendix I − Manuscript of Publication 1

Tunable Fulleretic Sodalite MOFs: Highly Efficient and Controllable Entrapment of C60 Fullerene via Mechanochemistry,

V. Martinez*[1], B. Karadeniz*[1], N. Biliškov[1], I. Lončarić[1], S. Muratović[1], D. Žilić[1], S. M. Avdoshenko[2], M. Roslova[3], A. A. Popov[2], K. Užarević[1]

[1] Ruđer Bošković Institute, Zagreb, Croatia [2] Leibniz IFW, Dresden, Germany
[3] Stockholm University, Stockholm, Sweden

Author contribution:

*V. M. and B. K. contributed equally as the first authors

V. M. and **B. K**. MOF design and synthesis, materials characterisation; **N. B.** quantitative and qualitative IR spectroscopy analysis; **I. L.** ASE simulations; **S. M.** and **D. Ž.** EPR measurements and data analysis; **S. M. A.** DFT and MD simulations; **M. R.** TEM analysis; **A. A. P.** idea conceptualisation; **K.U.** idea conceptualisation, funding acquisition

All authors contributed to the writing of the final manuscript.

CCC
RightsLink

A Sign in/Register   ⑦ ⚲

ACS Publications
Most Trusted. Most Cited. Most Read.

Tunable Fulleretic Sodalite MOFs: Highly Efficient and Controllable Entrapment of C60 Fullerene via Mechanochemistry

Author: Valentina Martinez, Bahar Karadeniz, Nikola Biliškov, et al

Publication: Chemistry of Materials

Publisher: American Chemical Society

Date: Dec 1, 2020

Copyright © 2020, American Chemical Society

Privacy - Terms

Tunable Fulleretic Sodalite MOFs: Highly Efficient and Controllable Entrapment of C_{60} Fullerene via Mechanochemistry

Valentina Martinez,[⊥] Bahar Karadeniz,[⊥] Nikola Biliškov, Ivor Lončarić, Senada Muratović, Dijana Žilić, Stanislav M. Avdoshenko, Maria Roslova, Alexey A. Popov,* and Krunoslav Užarević*

ACCESS | Metrics & More | Article Recommendations | Supporting Information

ABSTRACT: Encapsulation and confinement of fullerene guests in metal-organic frameworks (MOFs) lead to a novel class of crystalline fulleretic materials with unique physicochemical properties and a broad field of potential applications. The control over the amount of target guests confined in the MOF structure remains a significant challenge, which is particularly pronounced in the confinement of hardly accessible fullerene derivatives. The main strategies used in constructing fulleretic composites are limited by the solubility of components used and solvent versus guest competition for inhabitation of the framework voids. As mechanochemical procedures often overcome these issues, we developed here solvent-free processing by ball milling to gain control over the encapsulation of bulky and rigid C_{60}-fullerene into a sodalite MOF with large cages and narrow cage-apertures. A rapid, green, efficient, and stoichiometry-controlled mechanochemical processing afforded four model C_{60}@zeolitic-imidazolate framework 8 (ZIF-8) crystalline materials containing target 15, 30, 60, and 100 mol % of fullerene entrapped in the accessible cages of the model sodalite zeolitic-imidazolate framework 8 (ZIF-8), in stark contrast to the solution-based strategies that resulted in almost no loading. Varying the fullerene content affects the framework's vibrational properties, color and luminescence of the composites, and the electron-dose radiation stability. The computational and spectroscopic studies show that the fullerene is accommodated in the cage's center and that the cage-to-cage transport is a hardly feasible and energetically unfavored process. However, the fast release of C_{60} molecules from ZIF-8 can be effectively controlled by the pH. The entrapment of fullerene molecules in ZIF-8 resulted in their effective isolation even in higher loadings, paving the way to other tunable porous fulleretics containing single-molecule magnets or nanoprobes available on low scales.
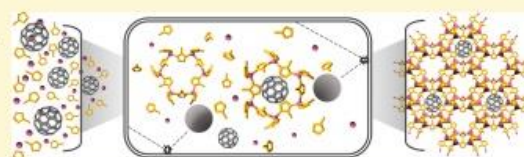
■ INTRODUCTION

Due to their unique molecular structure and electronic properties, buckminsterfullerene (C_{60}) and fullerene derivatives became one of the most important classes of functional materials in the fundamental and applied sciences, such as molecular electronics,[1−3] magnetic resonance imaging,[4] single-molecule magnetism,[5,6] tumor therapy,[7] catalysis,[8] gas storage,[9] and others. Electron-accepting property, hollow interior, and readiness for functionalization promote their potential application areas, which are especially emphasized in fullerenes functionalized at the exterior or interior side.[10,11] Combination of fullerene's intrinsic properties with the modular structures and chemical properties of metal nodes and walls of porous metal-organic frameworks (MOFs) opens a path toward a novel class of crystalline fulleretic materials with distinctive physicochemical properties and strong potential for application.[12,13] Structurally, MOFs could serve as stable, modular, and versatile matrices,[14−16] enabling spatial distribution and confinement of large guests like fullerenes.[17]

As in other porous materials, the primary strategies for encapsulation[18] of guests into MOFs are the in situ synthesis of the guest inside the cage, in situ growth of the framework in the presence of guests, and post-synthetic absorption (soaking)

of guests from the solution. Fullerenes were already considered for postsynthetic inclusion by soaking into MOFs with larger apertures, such as Zn-MOF-177,[14,19] and zirconium DUT-51[20] and NU-901.[21] This strategy, besides requiring an excess of fullerene and a suitable solvent, offers little control in the loading process, and allows the migration and potential egress of fullerene guest.[12,17,22] A particularly exciting example showing limitations in postsynthetic loading is the inclusion of C_{60} in the cobalt-based molecular sponge. The guests populated the channels exclusively, whereas the small cage-apertures prevented their inclusion in sizeable M_6L_4 cages.[23] The in situ formation of MOF in a solution containing fullerene was also reported for zirconium-based MOFs, UiO-67,[24] and PCN-222.[8] In all presented cases, the inclusion of fullerene to MOFs was accompanied by the increase in their stability,[25] conductivity,[21] and catalytic or photocatalytic

properties[24,26] and has also led to interesting spin structures in these fulleretic materials.[20] However, a general method for the encapsulation of fullerenes into MOFs is still a big challenge due to the low efficiency, solubility of fullerenes, and a need for a large excess of toluene or dichloromethane solvents. Another critical limiting factor is the competition with the solvent for cage inhabitation, which is particularly emphasized when working with costly and sparse metallofullerenes available at sub-milligram scales.[27−29]

Recently, mechanochemical reactions, widely used in other fields of materials chemistry,[30−36] have emerged as a particularly suitable technique for synthesis, transformation, and functionalization of MOFs,[37−39] with the examples of relevant MOFs as HKUST-1,[40−42] MOF-74,[43,44] zirconium carboxylate MOFs,[45−48] and various zeolitic-imidazolate frameworks (ZIFs).[49−51] Ball milling is best known for avoiding solvation and solubility issues, and atom efficiency. It was also used for the encapsulation of discrete organic molecules.[52−55] Even large flexible guests as enzymes[56] were successfully incorporated into MOFs' cavities by ball milling, enabling a pathway toward MOF biocomposites with improved stability and drug-release time.

Here, we describe a solid-state strategy for controllable encapsulation and immobilization of rigid and bulky buckminsterfullerene C_{60} molecules in the cages of the sodalite phase of ZIF-8[57] using mechanochemical agitation. The strategy relies on the formation of a sodalite framework around the solid template in a highly efficient and stoichiometry-controlled ion- and liquid-assisted grinding (ILAG)[58] procedure by ball milling. The ILAG procedure allowed for the use of simple, green, and abundant starting materials such as ZnO or ethanol. We have successfully prepared four C_{60}@ZIF-8 fulleretic materials with nominal targets 15, 30, 60, and 100 mol % of fullerene guests, relative to the number of cages available in the ZIF-8 structure (Scheme 1). This procedure, which is accomplishable at room

Scheme 1. Schematic Representation of the Ion- and Liquid-Assisted Grinding Procedure for Controllable Encapsulation of Fullerene Guests into Cavities of ZIF-8[a]
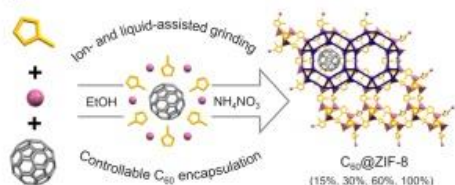
[a]The prepared fulleretic materials contain 15, 30, 60, and 100 mol % of fullerene relative to the maximum theoretical number of voids.

temperature (RT), is much faster and advantageous before both the solvothermal in situ loading and the postsynthetic soaking approach. The amount of fullerene guests habituating the cages of ZIF-8 has an impact on the vibrational properties of the metal-imidazolate framework and the luminescence of the prepared composites. Computational methods were used to estimate the fullerene's position in the framework and the possibility of fullerene transport through the framework. While the C_{60} immobilized in the sodalite framework remains captured when the composite is sonicated or stirred for a prolonged period, the fast release of the C_{60} is readily

accomplished by changing the pH. Spectroscopic data revealed that the efficient entrapment of fullerenes enables studies on "single-molecule" fullerene even in composites with a higher loading due to weak interactions of fullerene with other fullerenes or with the MOF walls.

■ RESULTS AND DISCUSSION

Zeolitic-imidazolate frameworks (ZIFs) are a subclass of MOFs formed by imidazole linkers and metal ions characterized by topologies similar to zeolites. Sodalite MOFs with large cages and small cage-apertures are well represented by zeolitic-imidazolate framework-8 (ZIF-8).[57] ZIF-8, one of the first commercially available MOFs, is often used, among other applications, for encapsulation of various organic molecules and enzymes for drug delivery and catalysis.[59−62] It was also one of the first MOF synthesized by ball milling.[49] At right milling conditions, ZIF-8 can transform into amorphous phase[50] or more stable (and less porous) katsenite and dia polymorphs,[63,64] but the sodalite phase is still considered as the most interesting form for application and composite preparation.

We were inspired by the recent work by Brekalo et al.,[65] showing how the topology in imidazole-based ZIF ($Zn(im)_2$) can be directed even to thermodynamically unstable forms by templating with $MeMeCH_2$ cavitands, in a process authors named the "shoe-last" principle. ZIF-8 was chosen as a host in our work due to the size, geometry, and hydrophobicity of the cavity that seemed particularly suitable for encapsulation and immobilization of C_{60} fullerene. It has large cages with a diameter of 11.6 Å, while the cage aperture is relatively small, only 3.4 Å in diameter.[57] Thus, with a diameter of ca. 6.8 Å,[66] C_{60} molecules can be comfortably accommodated in the ZIF-8 cavity. On the other hand, C_{60} should be efficiently immobilized as it is too large to pass through the cage aperture. We also expected that these small cage-apertures would prevent the preparation of C_{60}@ZIF-8 fulleretic materials from the solution by soaking procedure unless the cage aperture is flexible and rearranges to allow the entering and transport of fullerene through the MOF structure.

Synthesis of Fulleretic C_{60}@ZIF-8 Materials. The ILAG of zinc oxide, 2-methylimidazole (2-MeIm), and defined amounts of fullerene using ethanol and ammonium nitrate additives, resulted in rapid and tunable encapsulation of C_{60} in the ZIF-8 framework. The main idea was to avoid pushing the C_{60} molecules into the ZIF-8 cavities but rather to assemble the ZIF-8 framework around the fullerene template, without the need for dissolving the reactants, in particular fullerene. Partial encapsulation of C_{60} in ZIF-8 from an excess of fullerene was demonstrated recently in developing porous nitrogen-doped carbon anode for Li-ion batteries.[67] Herein, the loading of fullerene by ILAG was stoichiometry-controlled, and it required only traces of polar liquid additives as ethanol, in which the fullerene is insoluble, to facilitate the fulleretic formation. We designed the milling procedure in two steps. As it is well-established that ball milling is an excellent method for achieving a fast molecular diffusion in soft materials by breaking and recrystallizing the solid particles,[68] our initial step involved dry milling of ZnO, fullerene, and 2-methylimidazole in a ball mill operating at 30 Hz, for 10−15 min, to mix the reactants thoroughly. Powder X-ray diffraction (PXRD) analyses showed that no crystalline MOF was prepared at this stage (Figure S2a). In the second step, milling was stopped for a short period, ethanol and ammonium nitrate additives

were added to the milled reaction mixture, and milling was resumed for an additional 45 min. After the opening of the vessel, a dry purple microcrystalline powder was collected. This mechanochemical approach by ILAG required a simple work-up by washing with a small volume of toluene. Even in higher target ratios, the successful inclusion of fullerene guests could have been seen already during the washing. The products were sonicated during the washing procedure to remove the fullerene from ZIF-8 particles' surfaces, and even the initial wash-out was almost colorless (traces of fullerene color the toluene solution to intensive purple).

We have targeted four different C_{60}@ZIF-8 composites containing nominally 15, 30, 60, and 100 mol % of fullerene, relative to the maximum number of available cages in the structure of ZIF-8 (Cambridge Structural Database code VELVOY).[57] The purple color of C_{60}@ZIF-8 composites darkens with the increase in the fullerene content (Figure 1).

Figure 1. Different concentrations of C_{60} in mechanochemically prepared C_{60}@ZIF-8. From left to right: 0, 30, 60, and 100% C_{60}@ZIF-8, respectively.

One motivation for this work is developing a procedure for efficient encapsulation of rare and scarce endofullerenes, commonly available at sub-milligram levels. Thus, we also prepared C_{60}@ZIF-8 (30%) by capturing the sub-milligram amount of C_{60} (Figures S6 and S16). The EtOH and toluene filtrates were colorless, again proving the efficiency of the mechanochemical procedure (Figure S1). Guest-free ZIF-8 was prepared as a colorless microcrystalline solid in an identical ILAG procedure, only without adding the fullerene to the reaction mixture.

To test whether the C_{60} and 2-MeIm react in the first step, forming potentially complex species that would not be encapsulated, we performed several milling experiments mimicking the procedure for the preparation of C_{60}@ZIF-8 composites, only without the addition of zinc source. The analyses of the resulting purple product show only the amorphization of the reaction mixture, and the milling products are soluble in our standard washing procedure (Figures S5 and S15).

Interestingly, milling of the presynthesized ZIF-8 with C_{60} fullerene resulted in a very low encapsulation despite the increased molecular mobility and particle recrystallization resulting from the ball-milling procedure.[68] Our results show that mechanochemical treatment on the formed ZIF-8 framework, where the cages may get disassembled and recrystallized by ball milling to include the C_{60} template, resulted in very low loading, as evidenced from the color of the products and spectroscopic analysis. The products of the mechanochemical postsynthetic encapsulation attempts remained almost colorless after the washing, whereas the wash-outs were a deep purple. It can be concluded that for the inclusion of the rigid and large guests as C_{60} fullerene into sodalite MOFs, the in situ mechanochemical formation of the framework around the C_{60} template is a much better approach.

We also attempted to prepare C_{60}@ZIF-8 from the solution by postsynthetic soaking and in the solvothermal synthesis of the ZIF-8 in the presence of an excess of C_{60}, respectively. After a week of soaking of ZIF-8 in toluene containing an excess of fullerene, only a small amount of fullerene got encapsulated, which was evident from the sample's pale beige color and from the PXRD and IR analyses (Figures S4 and S8). In situ solvothermal synthesis of ZIF-8 with fullerene in the dimethylformamide (DMF)−toluene mixture at 120 °C also resulted in a low yield of C_{60}@ZIF-8 (Figure S4). The probable reason for such a low efficiency in encapsulation during solvothermal synthesis is the solvation and competition of the fullerene for the habitation of cages with the solvent molecules that are in vast excess, which is also suggested in spectroscopic analyses of fulleretic products (see Section S.3, Supporting Information (SI)).

PXRD Analysis. The absence of Bragg peaks characteristic of C_{60} confirms that ball milling yielded phase-pure C_{60}@ZIF-8 (Figure 2a), whereas the absence of Bragg peaks of ZnO reveals that the reaction was completed (Figure S2b). The encapsulation of C_{60} in ZIF-8 did not significantly influence the unit-cell parameters of the ZIF-8 structure; the position of the peaks is nearly identical to pure ZIF-8. Interestingly, the
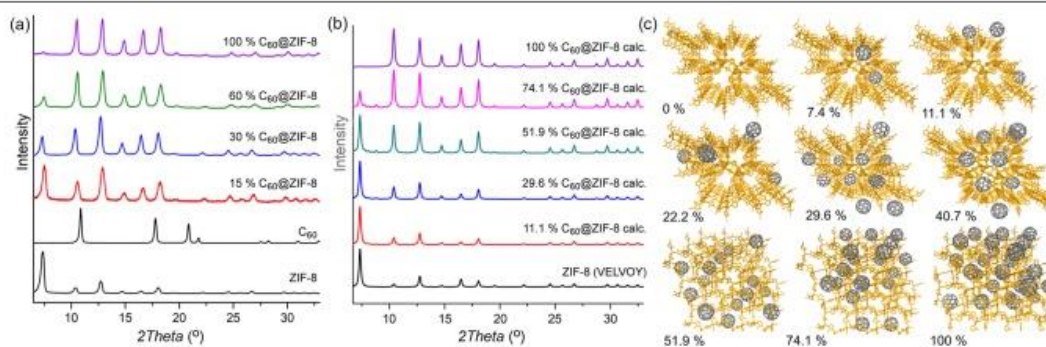
Figure 2. (a) Experimental PXRD data for the mechanochemically prepared ZIF-8 and the C_{60}@ZIF-8 composites; (b) calculated PXRD data for ZIF-8 containing randomly oriented fullerenes placed in the randomly chosen voids of 3 × 3 × 3 unit cells; (c) representation of randomly oriented fullerenes placed in the randomly chosen voids of 3 × 3 × 3 unit cell. Hydrogen atoms are omitted for clarity.

PXRD method can be used as a measure of loading of fullerene in this MOF. The relative intensity of peaks in the PXRD of the composites changes with an increase in the fullerene content, which can be used to estimate the encapsulation extent. In more detail, the intensity of a low angle (110) peak of ZIF-8, at $2\theta = 7.3°$, decreases[59,69−71] concurrently with the higher loading of C_{60}, whereas the intensity of the (200) peak at $2\theta = 10.3°$ increases gradually until it becomes stronger than the (211) peak at $2\theta = 12.7°$ (Figure 2a). For the estimation of loading success, (110) peak is the most suitable to serve as a probe of the encapsulation success, as the changes in intensity are the most pronounced. A significant reduction of the intensity of the (110) mirror plane, which is positioned in the center of the cage, results from modified electronic density in the ZIF-8 cages due to the inclusion of hollow C_{60}. To rationalize and confirm this finding, we have built the ZIF-8 3 × 3 × 3 unit cell with different amounts of disordered fullerenes in the cages, using the atomic simulation environment (ASE) (Figure 2c).[72] The simulated PXRDs of such structures show excellent agreement with the experimentally observed PXRD data (Figure 2b), confirming that the reduction in the intensity of the (110) peak is indeed a direct result of the guest inclusion. PXRD analysis also revealed a low degree of loading of fullerene in postsynthetic milling and solution strategies (Figures S3 and S4).

IR Spectroscopy. The IR spectrum of C_{60}[73,74] is dominated by two bands at 577 and 528 cm^{-1}, ascribed to the radial motion of carbon atoms (Figures 3 and S8). The other two bands, located at 1428 and 1182 cm^{-1}, are attributed to the tangential motion of carbon atoms; however, this pair of bands is highly overlapped by ZIF-8 features (see Figure S8, SI) in IR spectra of samples obtained by encapsulation and confining of C_{60} inside the ZIF-8 cages. On the other hand, the radial-motion bands do not overlap with any bands of ZIF-8 and so further in the text they serve as analytical markers. The IR spectrum of the activated ZIF-8 is in excellent agreement with previous reports (Figures 3a and S9).[57,75,76] The absorption bands for ZIF-8 at 3134 and 2929 cm^{-1} are due to the aromatic and aliphatic C−H stretch of imidazole, respectively. The band at 1583 cm^{-1} is attributed to the C=N stretch. The bands in the region of 1500−1350 cm^{-1} are assigned to various stretching vibrations of the imidazole ring. The in-plane deformations of the ring dominate the 1350−900 cm^{-1} region, while those in the 800−650 cm^{-1} region are associated with the out-of-plane bending of the ring. The band at 420 cm^{-1} is ascribed to the Zn−N stretch.

The 4000−2000 cm^{-1} region is not significantly affected by the encapsulation of C_{60} molecules inside the ZIF-8 framework. The changes are mostly located in the fingerprint region. At low C_{60} loadings (15% C_{60}@ZIF-8), the IR spectrum of ZIF-8 remains qualitatively more or less unaffected. However, higher loadings result in more noticeable spectral changes: (1) the envelope due to EtOH confined in the ZIF-8 cages, between 1280 and 1200 cm^{-1}, disappears and it is not present for 30% and higher loadings (Figures 3a and S12); (2) $\nu(CC)$ and $\nu(CN)$ bands at 1425 and 1458 cm^{-1}, respectively (Figure S10), change their relative intensity. The most evident is the change in their intensity ratio with $x(C_{60})$; (3) the $\delta(NH) + \delta(CN)$ combination band at 1380 cm^{-1} suffers a significant increase in intensity but it slowly decreases for $x(C_{60})$ over 30% (Figure S11); (4) the 780−720 cm^{-1} envelope consists of two bands, one due to the out-of-plane imidazole ring deformations at 760 cm^{-1} and the other due to the in-plane bending of the ring.
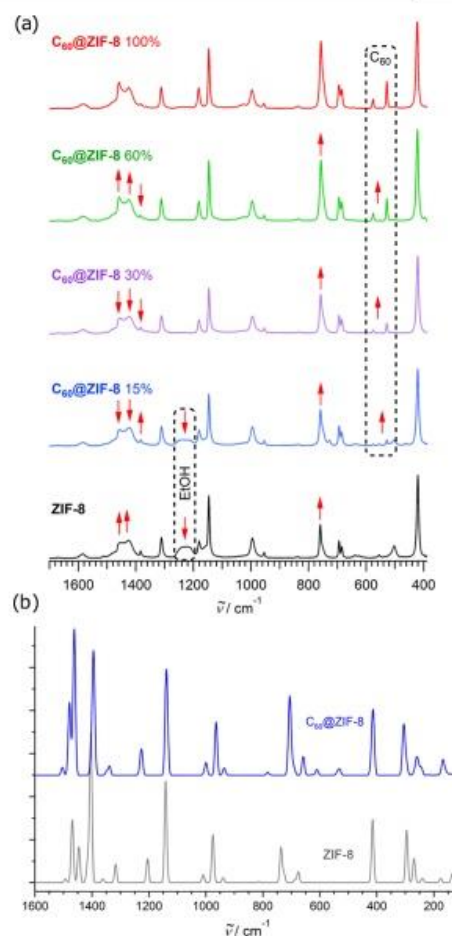
Figure 3. (a) Changes in the experimental IR spectra of ZIF-8 occurring due to encapsulation of C_{60}. Features due to the dynamic relation of C_{60} and EtOH are framed by dashed rectangles. (b) Density functional theory (DFT)-computed IR spectra of C_{60}@ZIF-8 and empty ZIF-8.

ring deformation at 750 cm^{-1} (Figure S13). While the in-plane deformation band remains unaffected, the out-of-plane contribution significantly increases in intensity; (5) the $\nu(ZnN)$ band shifts its position (Figure S14); and (6) C_{60} bands due to radial motions are located at 525 and 576 cm^{-1}, respectively.

Intensities of both C_{60} bands follow the second-order polynomial function of $x(C_{60})$, qualitatively the same as observed for pure C_{60} in the KBr matrix. A comparison of the gas-phase IR spectra of C_{60}[77] and the previously considered UV/vis spectra indicates no significant interaction between the ZIF-8 framework and fullerene molecule, so we could consider the encapsulated C_{60} as almost free-standing inside the cage. This is corroborated by the UV−vis measurements and molecular dynamics (MD) modeling discussed below.

The imidazole ring deformation bands change upon C_{60} encapsulation. This indicates that, although itself free-standing inside the cage, the encapsulated C_{60} molecule affects the

10631

dynamics of the imidazole linkers and the three-dimensional (3D) MOF framework. This is in line with intuitive expectations since these constituents define the ZIF-8 cavity, which is now occupied by the bulk spherical C_{60}. The intensity of the $\delta(NH) + \delta(CN)$ combination band at 1380 cm^{-1} initially significantly increases but it slowly decreases for C_{60} loadings over 30% (Figures 3 and S11). Density-functional-based tight-binding (DFTB)-based MD modeling indicates that the transport of the fullerene molecules along the cages is hardly possible. To allow C_{60} to move to the next cage, all six imidazole rings of the aperture should exhibit concerted rotation. For ZIF-8, such a concerted change in the position of imidazoles is a low-probability event that may account for the low loading of C_{60} in the standard soaking approach. Far-IR spectroscopy of the ZIF-8[78] indicates the corresponding gate-opening mode at 33.4 cm^{-1}. Although this mode is far from the reach of available instrumentation, in- and out-of-plane imidazole ring deformation modes are indirectly informative in this respect. Namely, while the in-plane imidazole ring deformation band at 750 cm^{-1} remains unaffected by C_{60} loading, the out-of-plane contribution at 760 cm^{-1} significantly increases in intensity (Figure S13), in line with the DFT findings obtained in this work at the Perdew–Burke–Ernzerhof (PBE)/projector augmented wave (PAW) level of theory (Figure 3b and SI). Additionally, both experiments and DFT clearly show intensification of the imidazole $(CH_3)C-N$ stretching modes around 1460 cm^{-1}. All of these findings indicate the increased amplitude of out-of-plane movements of the imidazole rings.

As previously mentioned, the solvation and competition of the fullerene with solvent molecules is a possible reason for the observed poor efficiency in C_{60} solvothermal encapsulation. The IR data revealed an interesting behavior of the broad 1280–1200 cm^{-1} envelope, which arises due to the EtOH confined inside the ZIF-8 cages, which completely disappears in fulleretic $C_{60}@ZIF$-8 materials with higher fullerene loading (Figure 3a and details in the Section S.3, SI).

The estimation of the C_{60} encapsulation efficiency was done by quantitative analysis of fullerene 528 and 577 cm^{-1} bands with respect to the standard crystalline C_{60} measured at the same conditions (Section S.3.2, Supporting Information). Intensities (and other spectral parameters) with respect to the C_{60} molar ratio are determined by fitting the 528 and 577 cm^{-1} bands, each band individually, to Lorentzian functions. For the 528 cm^{-1} band, fitting was done in the spectral range from 555 to 475 cm^{-1}, taking the ZIF-8 band at 504 cm^{-1} into consideration. Fitting of the 577 cm^{-1} band was done in the range from 610 to 550 cm^{-1}, taking the ZIF-8 band at 555 cm^{-1} into consideration. The corresponding bands for an equivalent amount of the C_{60} standards are considered in the same spectral ranges. The results are shown in Figure 4, while the details on the analysis are given in the SI (Section S.4.2). It can be concluded that C_{60} molecules are very efficiently encapsulated by the described mechanochemical strategy, reaching 95% efficiency at the highest loading. Postsynthetic loading by milling of fullerene and ZIF-8, and by soaking the ZIF-8 in the toluene solution containing an excess of fullerene, resulted in low loading, 2.0 and 1.7%, respectively (Figure 4), which is also evident from the color of the samples.

UV–Vis Spectroscopy. UV–vis spectroscopic studies of $C_{60}@ZIF$-8 in the visible range were performed to understand how the encapsulation in ZIF-8 affects the electronic properties of C_{60}. Powder samples were placed onto KBr
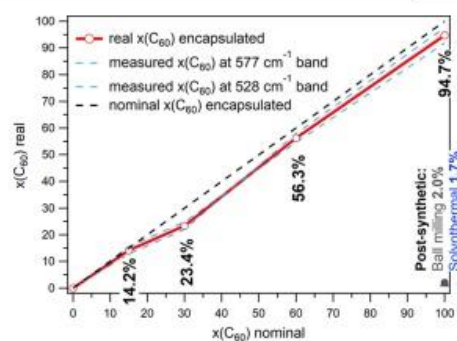
Figure 4. Efficiency of mechanochemical C_{60} encapsulation by ZIF-8. The postsynthetic loading attempts were done in excess of fullerene but resulted in low loading of ZIF-8 (black and blue points in the lower right corner).

substrates and measured with an Fourier transform infrared (FT-IR) microscope in the transmission mode; the solution was measured with a dispersive absorption spectrometer in a standard 1 cm quartz cell. Figure 5 compares the absorption
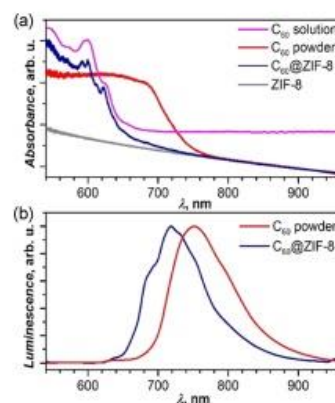
Figure 5. (a) Absorption spectra of ZIF-8, C_{60} powder, C_{60} solution in toluene, and $C_{60}@ZIF$-8 (100%) in the visible range. (b) Luminescence spectra of $C_{60}@ZIF$-8 and C_{60} powder, excitation with the laser with $\lambda = 515$ nm.

spectra of the powder samples of ZIF-8, C_{60}, and $C_{60}@ZIF$-8. As expected for the colorless powder, ZIF-8 does not absorb light in the visible range and thus should not interfere with the light absorption by the encapsulated fullerene. $C_{60}@ZIF$-8 exhibits the onset of the absorption near 740 nm, followed by the band with well-resolved features at 622, 611, 600, and 591 nm. An absorption spectrum of the C_{60} powder is substantially different from that of $C_{60}@ZIF$-8. The absorption onset of the fullerene powder is located at 780 nm, and the absorption band at shorter wavelengths is broad and almost featureless except for the relatively sharp inflection at 685 nm. Thus, encapsulation in ZIF-8 shifts electronic transitions of C_{60} to higher energy and makes the features better resolved. These differences can be explained by the dramatically reduced interactions between C_{60} molecules in $C_{60}@ZIF$-8, resulting in nearly single-molecule properties. Indeed, a spectrum similar to $C_{60}@ZIF$-8 is obtained for C_{60} in diluted solutions (see Figure
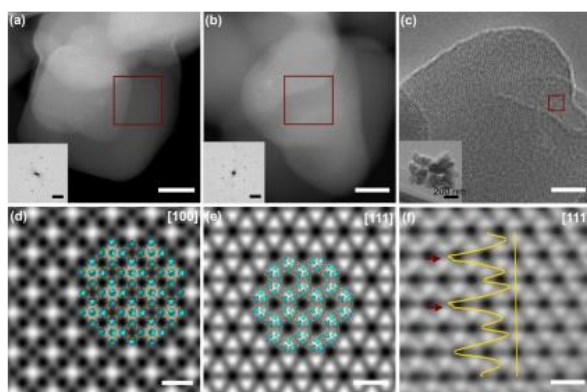
Figure 6. HAADF-STEM images of C_{60}@ZIF-8 along the [100] zone-axis (a), the [111] zone-axis (b). Insets show the fast Fourier transform (FFT) of the areas selected by red squares. (c) HRTEM image of C_{60}@ZIF-8 along the [111] zone-axis. The inset shows a typical low-resolution image of agglomerated particles. (d, e) Symmetry-imposed and lattice-averaged images along the [100] and [111] zone-axis, obtained using CRISP software,[84] with a structural model of ZIF-8 embedded. Images (d) and (e) are cropped to 5 × 5 unit cells and rotated by −125 and −61.3°, respectively, as compared to the areas outlined by red squares in images (a) and (b). In HAADF-STEM images, the contrast is approximately proportional to the square of the atomic number (Z); hence, the columns of the ZnN_4 tetrahedra (shown in cyan) are bright and the voids are dark. (f) A zoomed region of the specimen is outlined by the red square in Figure 6c. The intensity profile along the yellow line shows some minor changes in the contrast close to the center of a ZIF-8 cage, not visible in Figure 6e. The scale bar for all images in the upper row is 15 and −2 nm in the lower row.

5 for C_{60} in toluene and ref 79 for the spectrum in diluted hexane solution). Intermolecular interactions in crystalline C_{60} are comparably strong for the molecular crystal, leading to the significant dispersion of the highest occupied molecular orbital (HOMO)- and lowest unoccupied molecular orbital (LUMO)-derived bands and, therefore, to the broadening of the absorption spectrum.

The differences in the electronic states of C_{60} in the ZIF-8 matrix and the fullerene powder are further corroborated by their luminescence spectra (Figure 5b). C_{60}@ZIF-8 shows the luminescence band with the maximum at 718 nm and several vibronic features, whereas the maximum of the solid C_{60} luminescence is shifted to 750 nm. Furthermore, we found that the position of the peak in C_{60} powder depends on the sample morphology and excitation wavelength and shifts by 10−20 nm, whereas the spectrum of C_{60}@ZIF-8 is not affected by these measurement parameters or the load of C_{60} in ZIF-8. The fluorescence lifetime of C_{60}@ZIF-8 at room temperature is approximately 1.3 ns, and that of powder C_{60} is less than 1 ns. Thus, once again, we find that C_{60} entrapped in the ZIF-8 matrix shows different optical properties than the solid C_{60}. We can conclude that ZIF-8 appears to be a convenient matrix for the studies of almost "single-molecule" properties of fullerenes in the solid form without the need for substantial dilution.

Electron Spin Resonance (ESR) Spectroscopy. The presence of fullerene guests in the cages of ZIF-8 is confirmed additionally by ESR spectroscopy. Off-the-shelf fullerene shows a weak, sharp ESR line with a g-value around g = 2.002 and the peak-to-peak line width around $W_{pp} \approx 0.1$ mT, due to defects in the fullerene structure[80−83] (Figure S21). While pristine ZIF-8 does not show this signal, both ESR investigated C_{60}@ZIF-8 (15%) and C_{60}@ZIF-8 (100%) exhibit a similar but broader $W_{pp} \approx 0.2$ mT fullerene line (Figure S21). ESR is a very sensitive technique, and the fact that the signal of encapsulated C_{60} remains similar to that of the crystalline

fullerene reveals how mechanochemical treatment did not significantly damage the fullerene guests. Mechanochemistry looks like a reliable and suitable technique for fullerene loading. Importantly, no new paramagnetic defects were generated during the mechanochemical synthesis of C_{60}@ ZIF-8 (Figure S22).

High-Angle Annular Dark-Field Scanning Transmission Electron Microscopy (HAADF-STEM) and High-Resolution Transmission Electron Microscopy (HRTEM) Analyses. MOF materials are known to be highly unstable under electron beam irradiation. To date, only a few studies have reported TEM imaging of MOFs, including MIL-101,[85] MOF-5,[86] UiO-66,[87] and, very recently, ZIF-8.[88,89] The C_{60}@ ZIF-8 specimen was transferred to a lacey carbon grid by airflow. TEM experiments were carried out on a Themis Z (Thermo Fisher Scientific) microscope operated at 300 kV. We tested the C_{60}@ZIF-8 specimen at the liquid nitrogen temperature following the procedure by Li et al.;[88] however, no improvement in the resolution was gained and therefore the structure characterization described below has been conducted at noncryogenic conditions.

The crystals of C_{60}@ZIF-8 (100%) obtained by ball milling are typically ~70 ± 15 nm in size, nonuniformly shaped, and tend to agglomerate. Crystals with a square cross section and 90° angles between the surface facets commonly lie on the carbon support in the [100] zone-axis orientation (Figure 6a), and those having a triangular shape are close to the [111] zone-axis (Figure 6b). Although MOFs are often vulnerable under scanning transmission electron microscopy (STEM) conditions, it was possible to collect the images shown in Figure 6a,b using the high-angle annular dark-field scanning transmission electron microscopy (HAADF-STEM) settings and achieve a high resolution. It is worth noting that the pristine ZIF-8 immediately loses its crystallinity under STEM conditions while being illuminated with the same electron dose

as C_{60}@ZIF-8. While the fullerene loading did little to affect the thermal stability of the composites (Section S.7, SI), it leads to improved beam stability. This increase in stability can be considered as additional indirect evidence of filling the cages in the ZIF-8 structure and a particularly exciting feature of the C_{60}@ZIF-8 composites. The lattice parameter $a = 17.1$ Å, obtained from the fast Fourier transform (FFT) (insets in Figure 6a,b), is in agreement with the value reported for the pristine ZIF-8 in the literature ($a = 17.03$ Å, CSD code VELVOY)[57] and the experimental PXRD data (Figure 2a). The d-spacings up to 5.5 Å are resolvable from the FFT. Therefore, the individual ZnN_4 tetrahedra located at ~3.4 Å apart from each other cannot be distinguished. Imposing a projection symmetry ($P31m$ and $P4m$, correspondingly) on the lattice-averaged images results in a good match to the structural model of ZIF-8 along with both the [111] and [100] directions, thus providing additional proof that the ZIF-8 framework is retained during the C_{60}@ZIF-8 preparation by ball milling (Figure 6d,e). Since the contrast in HAADF-STEM is predominantly formed by the Zn metal centers (Figure 6a,b), we also took a high-resolution TEM (HRTEM) image of C_{60}@ZIF-8 viewed along the [111] zone axis (Figure 6c). The image has been both Fourier filtered and bandpass filtered to reduce random noise. At the given value of defocus, the HRTEM image has an inverted contrast: dark regions correspond to the cage space, whereas bright areas are formed by the Zn metal centers. The HRTEM image has additional features which have not been revealed and confirmed by HAADF-STEM experiments. Namely, for some thin areas of the specimen, an additional contrast was found approximately in the center of the ZIF-8 main channels, corresponding to the most energetically favorable position of the C_{60} molecule in the ZIF-8 framework, according to the calculated energy profile shown in Figure 7. Such a feature has been already reported as TEM evidence of CO_2 loading in ZIF-8.[88] Here, based on the collected TEM data alone, this contrast cannot be unambiguously attributed to the real fullerene position in the structure. However, this finding lays a path toward further investigations of the electron-dose-stable ZIF-8 composites and their local structure on the atomic level.

Molecular Dynamics Simulations. To get further insight into the location and dynamics of C_{60} molecules inside ZIF-8, molecular dynamics simulations were performed using a density-functional-based tight-binding (DFTB) method. The calculations showed that C_{60} could freely rotate and oscillate near the center of the cage. However, over the whole 250 ps trajectory with a Nosé−Hoover thermostat temperature of $T = 300$ K, we did not observe a single event of passing from one cage to another (Figure 7a and SI), indicating that the C_{60} migration through ZIF-8, if possible at all, must be very rare. Once C_{60} is encapsulated into a cage, it is likely to remain in that position. This contrasts with previous studies of the successful inclusion of small gases (N_2, CO_2) into empty ZIF-8. The previous reports talk about the "gate-opening" phenomenon in a relatively flexible structure of ZIF-8.[90−92] The methyl groups of 2-methylimidazole linkers spatially rearrange, ensuring the capture of gases bigger than the aperture.

Since the observation of a spontaneous movement of fullerene between the cages is not feasible on a reasonable time scale, the C_{60} molecule was dragged from one cage to another using distance constrain between a carbon atom in the fullerene cage and the center of the targeted cage. In contrast,
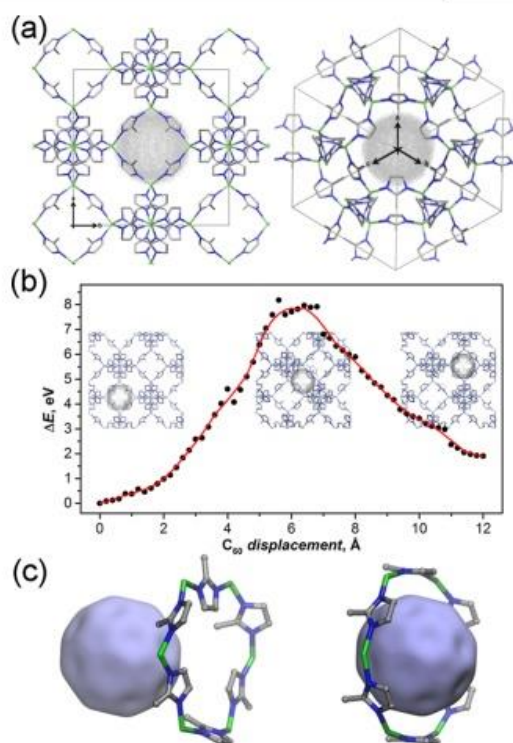
Figure 7. (a) DFTB-based molecular dynamics simulations of C_{60}@ZIF-8 at 300 K (left and right parts visualize two orientations of the structure). Gray dots show all positions of carbon atoms in the 250 ps trajectory. (b) DFTB-based energy profile and selected configuration of C_{60}@ZIF-8 obtained while dragging the C_{60} molecule from one cage to the neighboring cage through the larger aperture. (c) The structure of the aperture with two positions of C_{60}: in the middle of the cage (left) and in the moment of passing through the aperture (right). Hydrogen atoms and the rest of the ZIF-8 structure are omitted for clarity.

all other degrees of freedom were allowed to relax. Figure 7b shows the energy profile obtained in the course of such a trajectory (see SI for computational details and the full propagation path animation). The calculation reveals that the migration of C_{60} between the cages requires overcoming a substantial barrier of ca. 8 eV. Although the reliability of the DFTB approach in the precise estimation of the relative energies for this system is probably not very high, the prohibitively large barrier is another confirmation of the low loading efficiency in a solution soaking process or postsynthetic mechanochemical loading. The primary reason for a large energy demand can be well seen in Figure 7c, which compares the geometry of the aperture for two positions of the fullerene molecule, one in the center of the cage and another at the moment when C_{60} passes through the orifice. To let C_{60} pass through, all methylimidazole units should orient in a concerted manner parallel to the C_{60} surface, and the ring should expand by a considerable rearrangement of all N−Zn−N angles.

pH-Controlled Release of C_{60}. The releasing experiments also prove that C_{60} is effectively captured and immobilized in the sodalite framework. The fulleretics remain stable in neutral

pubs.acs.org/cm

or basic solutions (water/toluene mixtures) and do not release C_{60} upon sonication. However, C_{60} gets released almost immediately under acidic conditions (pH 2−4) (Figure 8), revealing that the releasing process can be controlled by the acidity of the environment, which one has to bear in mind in potential applications of C_{60}@ZIF-8 fulleretics. The sensitivity of ZIFs to the acidic environment is well studied,[93] and it is already used for the pH-controlled release of encapsulated drug molecules from MOF vehicles, such as 5-fluorouracil@ZIF-8.[94] Slow release of 5-fluorouracil from the ZIF-8 voids can be dramatically accelerated by lowering the pH of the slurry from 7.4 to 5.0, following the difference between the normal blood pH and the pH of cancer cells. The release of 5-fluorouracil was followed by the dissolution of the ZIF-8 structure, a degradation of the framework, and the increase of Zn^{2+} ions in the solution.[93,95]

Figure 8. Test tubes with C_{60}@ZIF-8 added to layered H_2O and toluene after the addition of (a) 0.5 mol dm^{-3} HCl (aq), and (b) 1 mol dm^{-3} KOH (aq). (c) C_{60}@ZIF-8 was initially dispersed in a basic solution of 1 mol dm^{-3} KOH (aq) and toluene was added subsequently. The releasing was only observed in (a).

CONCLUSIONS

To summarize, we have shown here how the mechanochemical ILAG approach leads to rapid, efficient, green, and controllable preparation of four tunable fulleretic materials, with specified amounts of C_{60}-fullerene guests. This mechanochemical strategy, involving cheap and easily accessible reactants such as ZnO and ethanol, proved superior to the solution synthetic and postsynthetic procedures. It avoided problems related to solubility, solvation, the competition of the target fullerene with the solvent molecules, and small cage-apertures. It allowed for a high level of stoichiometric-controlled loading of the buckminsterfullerene into the cages of ZIF-8. The confinement of C_{60} in the ZIF-8 cage does not influence the unit-cell parameters of ZIF-8, but increases the rigidity of the framework and improves the stability of fulleretic material toward the electron dose radiation. While the HAADF-STEM could not provide unambiguous proof on the fullerene's exact

position in the cages, the DFTB-based molecular dynamics studies indicate that the hollow fullerene is accommodated in the middle of the cage, which also rationalizes the changes in the IR and PXRD data observed upon encapsulation. Once entrapped, the fullerene is immobilized in one cage, and the transport of the fullerene through the network requires energy and substantial rearrangement in the aperture structure. The entrapped C_{60} molecules are in a weak interaction with the MOF wall and well isolated from oneother, even in high loading. This makes ZIF-8 a convenient matrix for the efficient immobilization of fullerene guests and achieving well-ordered, almost "single-molecule" properties of fullerenes in the solid form without substantial dilution. Due to high efficiency of the presented mechanochemical procedure, we aim to apply this mechanochemical strategy for entrapment of anisotropic and magnetic metallofullerenes available at sub-milligram scale to develop fulleretic materials with tunable content of magnetic centers, and to expand the interesting but poorly investigated field of fulleretic materials. We believe this strategy may prove general also for the stoichiometry-controlled confinement of other rigid nanoguests, such as polyoxometalates or metallic nanoparticles in MOF(s) with suitable structure and nature of the voids.

EXPERIMENTAL SECTION

Materials. ZnO, ammonium nitrate, and 2-methyl imidazole (MeIm) were obtained from Sigma-Aldrich. Ethanol (EtOH) was purchased from Grammol. Toluene was obtained from Sigma-Aldrich. Fullerene-C_{60} was supplied from TCI.

Mechanochemical Syntheses. *Mechanochemical Synthesis of ZIF-8.* ZIF-8 was synthesized according to the literature method.[49]

Mechanochemical Syntheses of C_{60}@ZIF-8 Materials. ZnO (40 mg, 0.491 mmol), 2-methyl imidazole (80.70 mg, 0.982 mmol), and C_{60} (9 mg (15%)) were placed into a Teflon jar with two stainless steel balls (7 mm). The mixture was neatly ground for 10 min at 30 Hz using IST-500 mixer mill, followed by further milling for 45 min by the addition of EtOH (45 μL) and 6 mg of NH_4NO_3. The resulting compound was washed first with EtOH and then with toluene, filtered, and air-dried. A purple compound was obtained and analyzed by PXRD, FTIR-attenuated total reflection (ATR), and thermogravimetric analysis (TGA). The quantity of C_{60} was calculated on the basis of the maximum number of voids in the ZIF-8 structure, which accounts for one-sixth of the ZIF-8 total quantity. The reaction was repeated using different ratios of C_{60} (18 mg, (30%), 36 mg (60%), 60 mg (100%)). Elemental analysis calculated (%) for ZIF-8 ($C_8H_{10}N_4Zn$); C:42.22, H: 4.43, N:24.62, found C:43.40, H: 5.11, N: 21.32. For 30% C_{60}@ZIF-8 ($C_{11}H_{10}N_4Zn$); C:50.11, H: 3.82, N:21.25, found C:49.00, H: 4.31, N: 19.82. For 100% C_{60}@ZIF-8 ($C_{18}H_{10}N_4Zn$); C:62.18, H: 2.90, N:16.11, found C:59.31, H: 3.88, N: 16.16.

Small-Scale Mechanochemical Synthesis of 30% C_{60}@ZIF-8 Material. ZnO (2 mg, 0.0245 mmol), 2-methyl imidazole (4 mg, 0.0491 mmol), and C_{60} (0.9 mg (30%)) were placed into a Teflon jar with two stainless steel balls (7 mm). The mixture was neatly ground for 10 min at 30 Hz using IST-500 mixer mill, followed by further milling for 45 min by the addition of EtOH (5 μL) and 0.4 mg of NH_4NO_3. The resulting compound was washed first with EtOH and then with toluene (following the procedure stated above), filtered, and air-dried. A purple compound was obtained and analyzed by PXRD and FTIR-ATR.

Neat Grinding of 2-Methyl Imidazole and C_{60}. 2-Methyl imidazole (25 mg, 0.306 mmol) and C_{60} (12.5 mg) were placed into a Teflon jar with two stainless steel balls (7 mm). The mixture was neatly ground for 1 h at 30 Hz using IST-500 mixer mill. The resulting product was analyzed by PXRD and FTIR-ATR. The milling product dissolves by washing with EtOH and toluene following the procedure given above.

ILAG of 2-Methyl Imidazole and C_{60}. 2-Methyl imidazole (25 mg, 0.306 mmol) and C_{60} (12.5 mg) were placed into a Teflon jar with two stainless steel balls (7 mm). The mixture was neatly ground for 15 min at 30 Hz using IST-500 mixer mill followed by further milling by the addition of NH_4NO_3 (3 mg) and 20 μL of EtOH. The resulting crude product was analyzed by PXRD and FTIR-ATR. The milling product was dissolved by washing with EtOH and toluene, following the procedure stated above.

ILAG of 2-Methyl Imidazole. 2-Methyl imidazole (25 mg, 0.306 mmol) and NH_4NO_3 (3 mg) were placed into a Teflon jar with two stainless steel balls (7 mm). EtOH (20 μL) was added and the mixture was milled for 30 min. The resulting product was analyzed by PXRD and FTIR-ATR.

Postsynthetic Method for the Encapsulation of C_{60} into Mechanochemically Synthesized ZIF-8. Mechanochemically synthesized ZIF-8 (15 mg) and 15 mg fullerene-C_{60} were placed into a Teflon jar with two stainless steel balls (7 mm). The mixture was milled for 45 min at 30 Hz using a IST-500 mixer mill. The resulting powder was washed with toluene three times (3 × 10 mL). A beige-colored solid was obtained and analyzed by PXRD and FTIR-ATR.

Solvothermal Synthesis of ZIF-8 and Postsynthetic Encapsulation of C_{60} by Soaking in Toluene Solution. $Zn(NO_3)_2 \cdot 6H_2O$ (108.70 mg, 0.365 mmol) and 2-methyl imidazole (60 mg, 0.730 mmol) were each dissolved in 5 mL of DMF. The prepared solutions were placed into a 20 mL Teflon-lined stainless steel autoclave. The mixture was then heated for 24 h at 120 °C. A white powder was precipitated, which was washed with DMF, air-dried, and analyzed by PXRD and FTIR-ATR. The resulting solid was then soaked for a week in toluene solution with an excess amount of C_{60} fullerene. A beige-colored solid obtained was analyzed by PXRD and FTIR-ATR.

One-Pot Solvothermal Synthesis of C_{60}@ZIF-8 Materials. $Zn(NO_3)_2 \cdot 6H_2O$ (108.70 mg, 0.365 mmol) and 2-methyl imidazole (60 mg, 0.730 mmol) were each dissolved in 5 mL of DMF. The prepared solutions and 8 mL of the toluene solution of C_{60} (25 mg, 0.0346 mmol) were placed into a 20 mL Teflon-lined stainless steel autoclave. The mixture was then autoclaved for 24 h at 120 °C. The obtained precipitate was light-colored while the mother liquid remained purple. It was subsequently washed several times with DMF and then with toluene. The beige-colored solid obtained was analyzed by PXRD and FTIR-ATR.

Activation of C_{60}@ZIF-8 Samples for IR Measurements. C_{60}@ZIF-8 samples were washed with EtOH three times and soaked in EtOH for 2 days; EtOH was changed three times a day. Afterward, they were left at 100 °C overnight.

Releasing Experiments. Test Tube 1. A suspension (5 g) of C_{60}@ZIF-8 in deionized H_2O (5 mL) was stirred at RT, while 0.5 mol dm^{-3} HCl (aq) was added dropwise. The resulting mixture was ultrasounded for a few seconds. When the color of the suspension started to turn brown, toluene was added to the mixture. The toluene phase turned purple immediately, which is the evidence of the successful release of fullerene C_{60}.

Test Tube 2. C_{60}@ZIF-8 (5 mg) was added to the mixed layer of deionized H_2O (5 mL) and toluene (5 mL) and stirred at RT, while 1 mol dm^{-3} KOH (aq) was added dropwise. The resulting mixture was ultrasounded for a few seconds. No color change was observed since C_{60} was unable to be released from the pores.

Test Tube 3. A suspension (5 g) of C_{60}@ZIF-8 in deionized H_2O (5 mL) was stirred at RT, while 1 mol dm^{-3} KOH (aq) was added dropwise. The resulting mixture was ultrasounded for a few seconds. When the color of the suspension started to turn brown, toluene was added to the resulting mixture. No color change was observed since C_{60} was unable to be released from the pores.

Powder X-ray Diffraction (PXRD). PXRD data for as-synthesized samples was analyzed using the PANalytical Aeris Research tabletop diffractometer, with Cu $K\alpha$ radiation (40 kV, 7.5 mA) in the Bragg Brentano geometry, with the sample mounted on a zero-background silicon plate.

FTIR Spectroscopy. Measurements were performed on a PerkinElmer Fourier transform infrared spectrometer Spectrum Two (PerkinElmer, Inc.) using Spectrum10 software (PerkinElmer, Inc.) in the transmittance mode by the KBr pellet technique and FTIR-ATR.

Vis−Near-Infrared (NIR) Absorption Spectroscopy. Absorption spectra of ZIF-8, C_{60}, and C_{60}@ZIF-8 powder samples in the visible range were measured with a Hyperion microscope attached to the Vertex FTIR spectrometer (Bruker). Powder samples were placed onto KBr single-crystal substrates, and the spectra were recorded in the transmission mode. The absorption spectrum of the fullerene solution in toluene was measured with a dispersive UV−vis−NIR spectrometer Shimadzu UV 3101PC.

Luminescence Spectroscopy. Steady-state luminescence spectra of powder samples were measured with a modular spectrometer of local design comprising Omicron PhoxX diode lasers for excitation (405, 488, 515 nm), Avantes AvaSpec HS1024x122TEC high-sensitivity fiber-optic spectrometer with TE-cooled back-thinned CCD detector (200−1000 nm), and an optical microscope of local design. Variable-temperature measurements were performed with a Janis ST-500 microscopy cryostat (temperatures down to 4 K). Luminescence lifetimes were measured by the time-correlated single-photon counting (TCSPC) technique using PicoQuant TimeHarp counter/timer and FluoFit software. Luminescence is excited by Omicron diode lasers modulated up to a frequency of 80 MHz (allowing the measurement of lifetimes longer than ~0.7 ns), time-resolved detection is performed by a PMA 192 PMT (Picoquant) in a visible range (250−850 nm).

ESR Spectroscopy. The electron spin resonance (ESR) or electron paramagnetic resonance (EPR) study was performed on powder samples in the range from room temperature down to 78 K using a Bruker Elexsys 580 FT/CW X-band spectrometer. The microwave frequency was around 9.7 GHz, the magnetic field modulation amplitude was 0.03 mT, and the modulation frequency was 100 kHz.

TGA Experiments. All TGA experiments were performed using a simultaneous thermal analyzer STA 6000 (PerkinElmer, Inc.) in alumina crucibles at a heating rate of 5 °C min^{-1} from 35 to 900 °C under nitrogen gas, and from 35 to 800 °C under oxygen gas, respectively, purging at a flow of 30 mL min^{-1}.

■ ASSOCIATED CONTENT

Ⓢ Supporting Information

The Supporting Information is available free of charge at https://pubs.acs.org/doi/10.1021/acs.chemmater.0c03796.

> Description of methods; powder X-ray diffraction (PXRD) analysis; infrared (IR) spectroscopy; luminescence spectroscopy; theoretical methods and models; ESR spectroscopy; TGA experiments (PDF)

> Animation of the transport of fullerene through the ZIF-8 structure (MP4)

■ AUTHOR INFORMATION

Corresponding Authors

Alexey A. Popov − *Leibniz Institute for Solid State and Materials Research (Leibniz IFW), 01069 Dresden, Germany;* ⊙ orcid.org/0000-0002-7596-0378; Email: A.Popov@ifw-dresden.de

Krunoslav Užarević − *Ruđer Bošković Institute, 10000 Zagreb, Croatia;* ⊙ orcid.org/0000-0002-7513-6485; Email: krunoslav.uzarevic@irb.hr

Authors

Valentina Martinez − *Ruđer Bošković Institute, 10000 Zagreb, Croatia*

Bahar Karadeniz − *Ruđer Bošković Institute, 10000 Zagreb, Croatia*

Nikola Biliškov − *Ruđer Bošković Institute, 10000 Zagreb, Croatia;* ⊙ orcid.org/0000-0002-6981-944X

Ivor Lončarić − *Ruđer Bošković Institute, 10000 Zagreb, Croatia*

Senada Muratović − *Ruđer Bošković Institute, 10000 Zagreb, Croatia;* ● orcid.org/0000-0001-5027-9191

Dijana Žilić − *Ruđer Bošković Institute, 10000 Zagreb, Croatia;* ● orcid.org/0000-0003-2387-0853

Stanislav M. Avdoshenko − *Leibniz Institute for Solid State and Materials Research (Leibniz IFW), 01069 Dresden, Germany*

Maria Roslova − *Department of Materials and Environmental Chemistry, Stockholm University, Stockholm SE-106 91, Sweden;* ● orcid.org/0000-0002-0607-0822

Complete contact information is available at:
https://pubs.acs.org/10.1021/acs.chemmater.0c03796

Author Contributions

[⊥]V.M. and B.K. contributed equally to this work.

Notes

The authors declare no competing financial interest.

■ REFERENCES

(1) Ortiz, M.; Cho, S.; Niklas, J.; Kim, S.; Poluektov, O. G.; Zhang, W.; Rumbles, G.; Park, J. Through-Space Ultrafast Photoinduced Electron Transfer Dynamics of a C 70-Encapsulated Bisporphyrin Covalent Organic Polyhedron in a Low-Dielectric Medium. *J. Am. Chem. Soc.* **2017**, *139*, 4286−4289.

(2) Guldi, D. M.; Illescas, B. M.; Atienza, C. M.; Wielopolski, M.; Martín, N. Fullerene for Organic Electronics. *Chem. Soc. Rev.* **2009**, *38*, 1587.

(3) Jeon, I; Ueno, H.; Seo, S.; Aitola, K.; Nishikubo, R.; Saeki, A.; Okada, H.; Boschloo, G.; Maruyama, S.; Matsuo, Y. Lithium-Ion Endohedral Fullerene (Li + @C 60) Dopants in Stable Perovskite Solar Cells Induce Instant Doping and Anti-Oxidation. *Angew. Chem., Int. Ed.* **2018**, *57*, 4607−4611.

(4) Ghiassi, K. B.; Olmstead, M. M.; Balch, A. L. Gadolinium-Containing Endohedral Fullerenes: Structures and Function as Magnetic Resonance Imaging (MRI) Agents. *Dalton Trans.* **2014**, *43*, 7346−7358.

(5) Chen, C.-H.; Krylov, D. S.; Avdoshenko, S. M.; Liu, F.; Spree, L.; Yadav, R.; Alvertis, A.; Hozoi, L.; Nenkov, K.; Kostanyan, A.; et al.

(6) Liu, F.; Wang, S.; Gao, C.-L.; Deng, Q.; Zhu, X.; Kostanyan, A.; Westerström, R.; Jin, F.; Xie, S.-Y.; Popov, A. A.; et al. Mononuclear Clusterfullerene Single-Molecule Magnet Containing Strained Fused-Pentagons Stabilized by a Nearly Linear Metal Cyanide Cluster. *Angew. Chem., Int. Ed.* **2017**, *56*, 1830−1834.

(7) Liu, Y.; Chen, C.; Qian, P.; Lu, X.; Sun, B.; Zhang, X.; Wang, L.; Gao, X.; Li, H.; Chen, Z.; et al. Gd-Metallofullerenol Nanomaterial as Non-Toxic Breast Cancer Stem Cell-Specific Inhibitor. *Nat. Commun.* **2015**, *6*, No. 5988.

(8) Zheng, D.-Y.; Chen, E.-X.; Ye, C.-R.; Huang, X.-C. High-Efficiency Photo-Oxidation of Thioethers over C 60 @PCN-222 under Air. *J. Mater. Chem. A* **2019**, *7*, 22084−22091.

(9) Gao, Y.; Wu, X.; Zeng, X. C. Designs of Fullerene-Based Frameworks for Hydrogen Storage. *J. Mater. Chem. A* **2014**, *2*, 5910−5914.

(10) Popov, A. A.; Yang, S.; Dunsch, L. Endohedral Fullerenes. *Chem. Rev.* **2013**, *113*, 5989−6113.

(11) Jin, P.; Li, Y.; Magagula, S.; Chen, Z. Exohedral Functionalization of Endohedral Metallofullerenes: Interplay between inside and Outside. *Coord. Chem. Rev.* **2019**, *388*, 406−439.

(12) Rice, A. M.; Dolgopolova, E. A.; Shustova, N. B. Fulleretic Materials: Buckyball- and Buckybowl-Based Crystalline Frameworks. *Chem. Mater.* **2017**, *29*, 7054−7061.

(13) Williams, D. E.; Dolgopolova, E. A.; Godfrey, D. C.; Ermolaeva, E. D.; Pellechia, P. J.; Greytak, A. B.; Smith, M. D.; Avdoshenko, S. M.; Popov, A. A.; Shustova, N. B. Fulleretic Well-Defined Scaffolds: Donor−Fullerene Alignment Through Metal Coordination and Its Effect on Photophysics. *Angew. Chem., Int. Ed.* **2016**, *55*, 9070−9074.

(14) Chae, H. K.; Siberio-Pérez, D. Y.; Kim, J.; Go, Y.; Eddaoudi, M.; Matzger, A. J.; O'Keeffe, M.; Yaghi, O. M. A Route to High Surface Area, Porosity and Inclusion of Large Molecules in Crystals. *Nature* **2004**, *427*, 523−527.

(15) Matsuzaki, S.; Arai, T.; Ikemoto, K.; Inokuma, Y.; Fujita, M. Networked-Cage Microcrystals for Evaluation of Host−Guest Interactions. *J. Am. Chem. Soc.* **2014**, *136*, 17899−17901.

(16) Brenner, W.; Ronson, T. K.; Nitschke, J. R. Separation and Selective Formation of Fullerene Adducts within an M II 8 L 6 Cage. *J. Am. Chem. Soc.* **2017**, *139*, 75−78.

(17) Meng, H.; Wang, C.; Wang, T.; Meng, H.; Wang, C.; Wang, T. Molecular Fullerenes Encapsulated in Metal-Organic Frameworks. *Gen. Chem.* **2018**, *4*, No. 180019.

(18) Cirujano, F. G.; Llabrés i Xamena, F. X. Metal Organic Frameworks as Nanoreactors and Host Matrices for Encapsulation. In *Organic Nanoreactors*; Sadjadi, S. B. T., Ed.; Elsevier: Boston, 2016; pp 305−340.

(19) Meng, H.; Zhao, C.; Nie, M.; Wang, C.; Wang, T. Changing the Hydrophobic MOF Pores through Encapsulating Fullerene C 60 and Metallofullerene Sc 3 C 2 @C 80. *J. Phys. Chem. C* **2019**, *123*, 6265−6269.

(20) Krylov, D. S.; Liu, F.; Brandenburg, A.; Spree, L.; Bon, V.; Kaskel, S.; Wolter, A. U. B.; Büchner, B.; Avdoshenko, S. M.; Popov, A. A. Magnetization Relaxation in the Single-Ion Magnet DySc 2 N@C 80: Quantum Tunneling, Magnetic Dilution, and Unconventional Temperature Dependence. *Phys. Chem. Chem. Phys.* **2018**, *20*, 11656−11672.

(21) Goswami, S.; Ray, D.; Otake, K.-i.; Kung, C.-W.; Garibay, S. J.; Islamoglu, T.; Atilgan, A.; Cui, Y.; Cramer, C. J.; Farha, O. K.; et al. A Porous, Electrically Conductive Hexa-Zirconium(IV) Metal−Organic Framework. *Chem. Sci.* **2018**, *9*, 4477−4482.

(22) García-Simón, C.; Costas, M.; Ribas, X. Metallosupramolecular Receptors for Fullerene Binding and Release. *Chem. Soc. Rev.* **2016**, *45*, 40−62.

(23) Inokuma, Y.; Arai, T.; Fujita, M. Networked Molecular Cages as Crystalline Sponges for Fullerenes and Other Guests. *Nat. Chem.* **2010**, *2*, 780−783.

Chemistry of Materials   pubs.acs.org/cm   Article

(24) Zheng, D.-Y.; Zhou, X.-M.; Mutyala, S.; Huang, X.-C. High Catalytic Activity of C 60 Pd n Encapsulated in Metal−Organic Framework UiO-67, for Tandem Hydrogenation Reaction. *Chem. − Eur. J.* **2018**, 24, 19141−19145.

(25) Li, H.; Hill, M. R.; Huang, R.; Doblin, C.; Lim, S.; Hill, A. J.; Babarao, R.; Falcaro, P. Facile Stabilization of Cyclodextrin Metal−Organic Frameworks under Aqueous Conditions via the Incorporation of C 60 in Their Matrices. *Chem. Commun.* **2016**, 52, 5973−5976.

(26) Md Pratik, S.; Gagliardi, L.; Cramer, C. J. Boosting Photoelectric Conductivity in Porphyrin-Based MOFs Incorporating C 60. *J. Phys. Chem. C* **2020**, 124, 1878−1887.

(27) Feng, Y.; Wang, T.; Li, Y.; Li, J.; Wu, J.; Wu, B.; Jiang, L.; Wang, C. Steering Metallofullerene Electron Spin in Porous Metal-Organic Framework. *J. Am. Chem. Soc.* **2015**, 15055.

(28) Avdoshenko, S. M.; Fritz, F.; Schlesier, C.; Kostanyan, A.; Dreiser, J.; Luysberg, M.; Popov, A. A.; Meyer, C.; Westerström, R. Partial Magnetic Ordering in One-Dimensional Arrays of Endofullerene Single-Molecule Magnet Peapods. *Nanoscale* **2018**, 10, 18153−18160.

(29) Meng, H.; Zhao, C.; Li, Y.; Nie, M.; Wang, C.; Wang, T. An Implanted Paramagnetic Metallofullerene Probe within a Metal−Organic Framework. *Nanoscale* **2018**, 10, 3291−3298.

(30) Friščić, T.; Mottillo, C.; Titi, H. M. Mechanochemistry for Synthesis. *Angew. Chem., Int. Ed.* **2020**, 59, 1018−1029.

(31) Do, J.-L.; Friščić, T. Mechanochemistry: A Force of Synthesis. *ACS Cent. Sci.* **2017**, 3, 13−19.

(32) James, S. L.; Adams, C. J.; Bolm, C.; Braga, D.; Collier, P.; Friščić, T.; Grepioni, F.; Harris, K. D. M.; Hyett, G.; Jones, W.; et al. Mechanochemistry: Opportunities for New and Cleaner Synthesis. *Chem. Soc. Rev.* **2012**, 41, 413−447.

(33) Tan, D.; Loots, L.; Friščić, T. Towards Medicinal Mechanochemistry: Evolution of Milling from Pharmaceutical Solid Form Screening to the Synthesis of Active Pharmaceutical Ingredients (APIs). *Chem. Commun.* **2016**, 52, 7760−7781.

(34) Friščić, T. Supramolecular Concepts and New Techniques in Mechanochemistry: Cocrystals, Cages, Rotaxanes, Open Metal−Organic Frameworks. *Chem. Soc. Rev.* **2012**, 41, 3493.

(35) Do, J.-L.; Friščić, T. Chemistry 2.0: Developing a New, Solvent-Free System of Chemical Synthesis Based on Mechanochemistry. *Synlett* **2017**, 28, 2066−2092.

(36) Boldyreva, E. Mechanochemistry of Inorganic and Organic Systems: What Is Similar, What Is Different? *Chem. Soc. Rev.* **2013**, 42, 7719.

(37) Stolar, T.; Užarević, K. Mechanochemistry: An Efficient and Versatile Toolbox for Synthesis, Transformation, and Functionalization of Porous Metal−Organic Frameworks. *CrystEngComm* **2020**, 22, 4511−4525.

(38) Julien, P. A.; Mottillo, C.; Friščić, F. Metal−Organic Frameworks Meet Scalable and Sustainable Synthesis. *Green Chem.* **2017**, 19, 2729−2747.

(39) Friščić, T.; Halasz, I.; Štrukil, V.; Eckert-Maksić, M.; Dinnebier, R. E. Clean and Efficient Synthesis Using Mechanochemistry: Coordination Polymers, Metal-Organic Frameworks and Metallodrugs. *Croat. Chem. Acta* **2012**, 85, 367−378.

(40) Yuan, W.; Garay, A. L.; Pichon, A.; Clowes, R.; Wood, C. D.; Cooper, A. I.; James, S. L. Study of the Mechanochemical Formation and Resulting Properties of an Archetypal MOF: Cu3(BTC)2 (BTC = 1,3,5-Benzenetricarboxylate). *CrystEngComm* **2010**, 12, 4063.

(41) Klimakow, M.; Klobes, P.; Thünemann, A. F.; Rademann, K.; Emmerling, F. Mechanochemical Synthesis of Metal−Organic Frameworks: A Fast and Facile Approach toward Quantitative Yields and High Specific Surface Areas. *Chem. Mater.* **2010**, 22, 5216−5221.

(42) Stolar, T.; Batzdorf, L.; Lukin, S.; Žilić, D.; Motillo, C.; Friščić, T.; Emmerling, F.; Halasz, I.; Užarević, K. In Situ Monitoring of the Mechanosynthesis of the Archetypal Metal−Organic Framework HKUST-1: Effect of Liquid Additives on the Milling Reactivity. *Inorg. Chem.* **2017**, 56, 6599−6608.

(43) Julien, P. A.; Užarević, K.; Katsenis, A. D.; Kimber, S. A. J.; Wang, T.; Farha, O. K.; Zhang, Y.; Casaban, J.; Germann, L. S.; Etter, M.; et al. In Situ Monitoring and Mechanism of the Mechanochemical Formation of a Microporous MOF-74 Framework. *J. Am. Chem. Soc.* **2016**, 138, 2929−2932.

(44) Ayoub, G.; Karadeniz, B.; Howarth, A. J.; Farha, O. K.; Đilović, I.; Germann, L. S.; Dinnebier, R. E.; Užarević, K.; Friščić, T. Rational Synthesis of Mixed-Metal Microporous Metal−Organic Frameworks with Controlled Composition Using Mechanochemistry. *Chem. Mater.* **2019**, 31, 5494−5501.

(45) Užarević, K.; Wang, T. C.; Moon, S.-Y.; Fidelli, A. M.; Hupp, J. T.; Farha, O. K.; Friščić, T. Mechanochemical and Solvent-Free Assembly of Zirconium-Based Metal−Organic Frameworks. *Chem. Commun.* **2016**, 52, 2133−2136.

(46) Karadeniz, B.; Howarth, A. J.; Stolar, T.; Islamoglu, T.; Dejanović, I.; Tireli, M.; Wasson, M. C.; Moon, S.-Y.; Farha, O. K.; Friščić, T.; et al. Benign by Design: Green and Scalable Synthesis of Zirconium UiO-Metal−Organic Frameworks by Water-Assisted Mechanochemistry. *ACS Sustainable Chem. Eng.* **2018**, 6, 15841−15849.

(47) Fidelli, A. M.; Karadeniz, B.; Howarth, A. J.; Huskić, I.; Germann, L. S.; Halasz, I.; Etter, M.; Moon, S.-Y.; Dinnebier, R. E.; Stilinović, V.; et al. Green and Rapid Mechanosynthesis of High-Porosity NU- and UiO-Type Metal−Organic Frameworks. *Chem. Commun.* **2018**, 54, 6999−7002.

(48) Karadeniz, B.; Žilić, D.; Huskić, I.; Germann, L. S.; Fidelli, A. M.; Muratović, S.; Lončarić, I.; Etter, M.; Dinnebier, R. E.; Barišić, D.; et al. Controlling the Polymorphism and Topology Transformation in Porphyrinic Zirconium Metal−Organic Frameworks via Mechanochemistry. *J. Am. Chem. Soc.* **2019**, 141, 19214−19220.

(49) Beldon, P. J.; Fábián, L.; Stein, R. S.; Thirumurugan, A.; Cheetham, A. K.; Friščić, T. Rapid Room-Temperature Synthesis of Zeolitic Imidazolate Frameworks by Using Mechanochemistry. *Angew. Chem., Int. Ed.* **2010**, 49, 9640−9643.

(50) Bennett, T. D.; Cao, S.; Tan, J. C.; Keen, D. A.; Bithell, E. G.; Beldon, P. J.; Friscic, T.; Cheetham, A. K. Facile Mechanosynthesis of Amorphous Zeolitic Imidazolate Frameworks. *J. Am. Chem. Soc.* **2011**, 133, 14546−14549.

(51) Friščić, T.; Halasz, I.; Beldon, P. J.; Belenguer, A. M.; Adams, F.; Kimber, S. A. J.; Honkimäki, V.; Dinnebier, R. E. Real-Time and in Situ Monitoring of Mechanochemical Milling Reactions. *Nat. Chem.* **2013**, 5, 66−73.

(52) Souza, B. E.; Rudić, S.; Titov, K.; Babal, A. S.; Taylor, J. D.; Tan, J.-C. Guest−Host Interactions of Nanoconfined Anti-Cancer Drug in Metal−Organic Framework Exposed by Terahertz Dynamics. *Chem. Commun.* **2019**, 55, 3868−3871.

(53) Gao, P.; Shi, X.; Xu, X.; Wei, W. Versatile and Efficient Mechanochemical Synthesis of Crystalline GuestCzeolitic Imidazolate Framework Complexes by in Situ Host− Guest Nanoconfinement. *Cryst. Growth Des.* **2018**, 18, 5845−5852.

(54) Orellana-Tavra, C.; Marshall, R. J.; Baxter, E. F.; Lázaro, I. A.; Tao, A.; Cheetham, A. K.; Forgan, R. S.; Fairen-Jimenez, D. Drug Delivery and Controlled Release from Biocompatible Metal−Organic Frameworks Using Mechanical Amorphization. *J. Mater. Chem. B* **2016**, 4, 7697−7707.

(55) Glembockyte, V.; Frenette, M.; Mottillo, C.; Durantini, A. M.; Gostick, J.; Štrukil, V.; Friščić, T.; Cosa, G. Highly Photostable and Fluorescent Microporous Solids Prepared via Solid-State Entrapment of Boron Dipyrromethene Dyes in a Nascent Metal−Organic Framework. *J. Am. Chem. Soc.* **2018**, 140, 16882−16887.

(56) Wei, T.-H.; Wu, S.-H.; Huang, Y.-D.; Lo, W.-S.; Williams, B. P.; Chen, S.-Y.; Yang, H.-C.; Hsu, Y.-S.; Lin, Z.-Y.; Chen, X.-H.; et al. Rapid Mechanochemical Encapsulation of Biocatalysts into Robust Metal−Organic Frameworks. *Nat. Commun.* **2019**, 10, No. 5002.

(57) Park, K. S.; Ni, Z.; Cote, A. P.; Choi, J. Y.; Huang, R.; Uribe-Romo, F. J.; Chae, H. K.; O'Keeffe, M.; Yaghi, O. M. Exceptional Chemical and Thermal Stability of Zeolitic Imidazolate Frameworks. *Proc. Natl. Acad. Sci. U.S.A.* **2006**, 103, 10186−10191.

(58) Friščić, T.; Reid David, G.; Halasz, I.; Stein Robin, S.; Dinnebier Robert, E.; Duer Melinda, J. Ion- and Liquid-Assisted Grinding: Improved Mechanochemical Synthesis of Metal−Organic Frameworks Reveals Salt Inclusion and Anion Templating. *Angew. Chem., Int. Ed.* 2010, 49, 712−715.

(59) Zheng, H.; Zhang, Y.; Liu, L.; Wan, W.; Guo, P.; Nyström, A. M.; Zou, X. One-Pot Synthesis of Metal-Organic Frameworks with Encapsulated Target Molecules and Their Applications for Controlled Drug Delivery. *J. Am. Chem. Soc.* 2016, 138, 962−968.

(60) Liédana, N.; Galve, A.; Rubio, C.; Téllez, C.; Coronas, J. CAF@ZIF-8: One-Step Encapsulation of Caffeine in MOF. *ACS Appl. Mater. Interfaces* 2012, 4, 5016−5021.

(61) Zhao, Y.; Ni, X.; Ye, S.; Gu, Z.-G.; Li, Y.; Ngai, T. A Smart Route for Encapsulating Pd Nanoparticles into a ZIF-8 Hollow Microsphere and Their Superior Catalytic Properties. *Langmuir* 2020, 36, 2037−2043.

(62) Malkar, R. S.; Yadav, G. D. Synthesis of Cinnamyl Benzoate over Novel Heteropoly Acid Encapsulated ZIF-8. *Appl. Catal., A* 2018, 560, 54−65.

(63) Katsenis, A. D.; Puškarić, A.; Štrukil, V.; Mottillo, C.; Julien, P. A.; Užarević, K.; Pham, M.-H.; Do, T.-O.; Kimber, S. A. J.; Lazić, P.; et al. In Situ X-Ray Diffraction Monitoring of a Mechanochemical Reaction Reveals a Unique Topology Metal-Organic Framework. *Nat. Commun.* 2015, 6, No. 6662.

(64) Akimbekov, Z.; Katsenis, A. D.; Nagabhushana, G. P.; Ayoub, G.; Arhangelskis, M.; Morris, A. J.; Friščić, T.; Navrotsky, A. Experimental and Theoretical Evaluation of the Stability of True MOF Polymorphs Explains Their Mechanochemical Interconversions. *J. Am. Chem. Soc.* 2017, 139, 7952−7957.

(65) Brekalo, I; Kane, C. M.; Ley, A. N.; Ramirez, J. R.; Friščić, T.; Holman, K. Travis. Use of a "Shoe-Last" Solid-State Template in the Mechanochemical Synthesis of High-Porosity RHO-Zinc Imidazolate. *J. Am. Chem. Soc.* 2018, 140, 10104−10108.

(66) Goel, A.; Howard, J. B.; Vander Sande, J. B. Size Analysis of Single Fullerene Molecules by Electron Microscopy. *Carbon* 2004, 42, 1907−1915.

(67) Guan, J.; Zhong, X.; Chen, X.; Zhu, X.; Li, P.; Wu, J.; Lu, Y.; Yu, Y.; Yang, S. Expanding Pore Sizes of ZIF-8-Derived Nitrogen-Doped Microporous Carbon: Via C60 Embedding: Toward Improved Anode Performance for the Lithium-Ion Battery. *Nanoscale* 2018, 10, 2473−2480.

(68) Lukin, S.; Tireli, M.; Stolar, T.; Barišić, D.; Blanco, M. V.; di Michiel, M.; Užarević, K.; Halasz, I. Isotope Labeling Reveals Fast Atomic and Molecular Exchange in Mechanochemical Milling Reactions. *J. Am. Chem. Soc.* 2019, 141, 1212−1216.

(69) Yan, Q.; Lin, Y.; Kong, C.; Chen, L. Remarkable CO2/CH4 Selectivity and CO2 Adsorption Capacity Exhibited by Polyamine-Decorated Metal−Organic Framework Adsorbents. *Chem. Commun.* 2013, 49, 6873.

(70) Liang, J.; Nuhnen, A.; Millan, S.; Breitzke, H.; Gvilava, V.; Buntkowsky, G.; Janiak, C. Encapsulation of a Porous Organic Cage into the Pores of a Metal−Organic Framework for Enhanced CO2 Separation. *Angew. Chem., Int. Ed.* 2020, 59, 6068−6073.

(71) Esken, D.; Turner, S.; Wiktor, C.; Kalidindi, S. B.; Van Tendeloo, G.; Fischer, R. A. GaN@ZIF-8: Selective Formation of Gallium Nitride Quantum Dots inside a Zinc Methylimidazolate Framework. *J. Am. Chem. Soc.* 2011, 133, 16370−16373.

(72) Hjorth Larsen, A.; Jørgen Mortensen, J.; Blomqvist, J.; Castelli, I. E.; Christensen, R.; Dulak, M.; Friis, J.; Groves, M. N.; Hammer, B.; Hargus, C.; et al. The Atomic Simulation Environment—a Python Library for Working with Atoms. *J. Phys.: Condens. Matter* 2017, 29, No. 273002.

(73) Țucureanu, V.; Matei, A.; Avram, A. M. FTIR Spectroscopy for Carbon Family Study. *Crit. Rev. Anal. Chem.* 2016, 46, 502−520.

(74) Schettino, V.; Pagliai, M.; Ciabini, L.; Cardini, G. The Vibrational Spectrum of Fullerene C 60. *J. Phys. Chem. A* 2001, 105, 11192−11196.

(75) He, M.; Yao, J.; Liu, Q.; Wang, K.; Chen, F.; Wang, H. Facile Synthesis of Zeolitic Imidazolate Framework-8 from a Concentrated Aqueous Solution. *Microporous Mesoporous Mater.* 2014, 184, 55−60.

(76) Jafari, S.; Ghorbani-Shahna, F.; Bahrami, A.; Kazemian, H. Effects of Post-Synthesis Activation and Relative Humidity on Adsorption Performance of ZIF-8 for Capturing Toluene from a Gas Phase in a Continuous Mode. *Appl. Sci.* 2018, 8, No. 310.

(77) Nemes, L.; Ram, R. S.; Bernath, P. F.; Tinker, F. A.; Zumwalt, M. C.; Lamb, L. D.; Huffman, D. R. Gas-Phase Infrared Emission Spectra of C60 and C70. Temperature-Dependent Studies. *Chem. Phys. Lett.* 1994, 218, 295−303.

(78) Ryder, M. R.; Civalleri, B.; Bennett, T. D.; Henke, S.; Rudić, S.; Cinque, G.; Fernandez-Alonso, F.; Tan, J.-C. Identifying the Role of Terahertz Vibrations in Metal-Organic Frameworks: From Gate-Opening Phenomenon to Shear-Driven Structural Destabilization. *Phys. Rev. Lett.* 2014, 113, No. 215502.

(79) Leach, S.; Vervloet, M.; Després, A.; Bréheret, E.; Hare, J. P.; John Dennis, T.; Kroto, H. W.; Taylor, R.; Walton, D. R. M. Electronic Spectra and Transitions of the Fullerene C60. *Chem. Phys.* 1992, 160, 451−466.

(80) Pace, M. D.; Christidis, T. C.; Yin, J. J.; Milliken, J. EPR of a Free Radical in Fullerene, C60: Effect of Molecular Oxygen. *J. Phys. Chem. A* 1992, 96, 6855−6858.

(81) Stankowski, J.; Piekara-Sady, L.; Kempiński, W.; Huminiecki, O.; Sczaniecki, P. B. EPR of Graphite and Fullerenes. *Fullerene Sci. Technol.* 1997, 5, 1203−1217.

(82) Paul, P.; Kim, K.-C.; Sun, D.; Boyd, P. D. W.; Reed, C. A. Artifacts in the Electron Paramagnetic Resonance Spectra of C 60 Fullerene Ions: Inevitable C 120 O Impurity. *J. Am. Chem. Soc.* 2002, 124, 4394−4401.

(83) Konchits, A. A.; Shanina, B. D.; Krasnovyd, S. V.; Burya, A. I.; Kuznetsova, O. Y. Paramagnetic Properties of Fullerene-Derived Nanomaterials and Their Polymer Composites: Drastic Pumping Out Effect. *Nanoscale Res. Lett.* 2017, 12, No. 475.

(84) Hovmöller, S. CRISP: Crystallographic Image Processing on a Personal Computer. *Ultramicroscopy* 1992, 41, 121−135.

(85) Lebedev, O. I.; Millange, F.; Serre, C.; Van Tendeloo, G.; Férey, G. First Direct Imaging of Giant Pores of the Metal−Organic Framework MIL-101. *Chem. Mater.* 2005, 17, 6525−6527.

(86) Wiktor, C.; Turner, S.; Zacher, D.; Fischer, R. A.; Van Tendeloo, G. Imaging of Intact MOF-5 Nanocrystals by Advanced TEM at Liquid Nitrogen Temperature. *Microporous Mesoporous Mater.* 2012, 162, 131−135.

(87) Zhu, L.; Zhang, D.; Xue, M.; Li, H.; Qiu, S. Direct Observations of the MOF (UiO-66) Structure by Transmission Electron Microscopy. *CrystEngComm* 2013, 15, 9356−9359.

(88) Li, Y.; Wang, K.; Zhou, W.; Li, Y.; Vila, R.; Huang, W.; Wang, H.; Chen, G.; Wu, G.-H.; Tsao, Y.; et al. Cryo-EM Structures of Atomic Surfaces and Host-Guest Chemistry in Metal-Organic Frameworks. *Matter* 2019, 1, 428−438.

(89) Zhu, Y.; Ciston, J.; Zheng, B.; Miao, X.; Czarnik, C.; Pan, Y.; Sougrat, R.; Lai, Z.; Hsiung, C.-E.; Yao, K.; et al. Unravelling Surface and Interfacial Structures of a Metal−Organic Framework by Transmission Electron Microscopy. *Nat. Mater.* 2017, 16, 532−536.

(90) Fairen-Jimenez, D.; Moggach, S. A.; Wharmby, M. T.; Wright, P. A.; Parsons, S.; Düren, T. Opening the Gate: Framework Flexibility in ZIF-8 Explored by Experiments and Simulations. *J. Am. Chem. Soc.* 2011, 133, 8900−8902.

(91) Haldoupis, E.; Watanabe, T.; Nair, S.; Sholl, D. S. Quantifying Large Effects of Framework Flexibility on Diffusion in MOFs: CH4 and CO2 in ZIF-8. *ChemPhysChem* 2012, 13, 3449−3452.

(92) García-Simón, C.; Colomban, C.; Çetin, Y. A.; Gimeno, A.; Pujals, M.; Ubasart, E.; Fuertes-Espinosa, C.; Asad, K.; Chronakis, N.; Costas, M.; et al. Complete Dynamic Reconstruction of C60, C70, and (C59N)2 Encapsulation into an Adaptable Supramolecular Nanocapsule. *J. Am. Chem. Soc.* 2020, 142, 16051−16063.

(93) Gao, S.; Hou, J.; Deng, Z.; Wang, T.; Beyer, S.; Buzanich, A. G.; Richardson, J. J.; Rawal, A.; Seidel, R.; Zulkifli, M. Y.; et al. Improving

Dissertation supplement

the Acidic Stability of Zeolitic Imidazolate Frameworks by Biofunctional Molecules. *Chem* **2019**, *5*, 1597−1608.

(94) Sun, C.-Y.; Qin, C.; Wang, X.-L.; Yang, G.-S.; Shao, K.-Z.; Lan, Y.-Q.; Su, Z.-M.; Huang, P.; Wang, C.-G.; Wang, E.-B. Zeolitic Imidazolate Framework-8 as Efficient PH-Sensitive Drug Delivery Vehicle. *Dalton Trans.* **2012**, *41*, 6906−6909.

(95) Zhuang, J.; Kuo, C.-H.; Chou, L.-Y.; Liu, D.-Y.; Weerapana, E.; Tsung, C.-K. Optimized Metal−Organic-Framework Nanospheres for Drug Delivery: Evaluation of Small-Molecule Encapsulation. *ACS Nano* **2014**, *8*, 2812−2819.

57

7.2.   Appendix II − Supplementary Information for Publication 1

Supporting Information

Tunable fulleretic sodalite MOFs: highly efficient and controllable entrapment of C$_{60}$ fullerene via mechanochemistry

Valentina Martinez,[¥,a] Bahar Karadeniz,[¥,a] Nikola Biliškov,[a] Ivor Lončarić,[a] Senada Muratović,[a] Dijana Žilić,[a] Stanislav M. Avdoshenko,[b] Maria Roslova,[c] Alexey A. Popov,*[b] and Krunoslav Užarević *[a]

[a] Ruđer Bošković Institute, 10000 Zagreb, Croatia

[b] Leibniz Institute for Solid State and Materials Research (Leibniz IFW), 01069 Dresden, Germany

[c] Department of Materials and Environmental Chemistry, Stockholm University, Stockholm SE-106 91, Sweden

Table of Contents

S.1 Experimental section

Figure S1. Toluene waste after washing (left), solid 30% C_{60}@ZIF-8 (right).

2

S.2 Powder X-ray diffraction (PXRD) Analysis
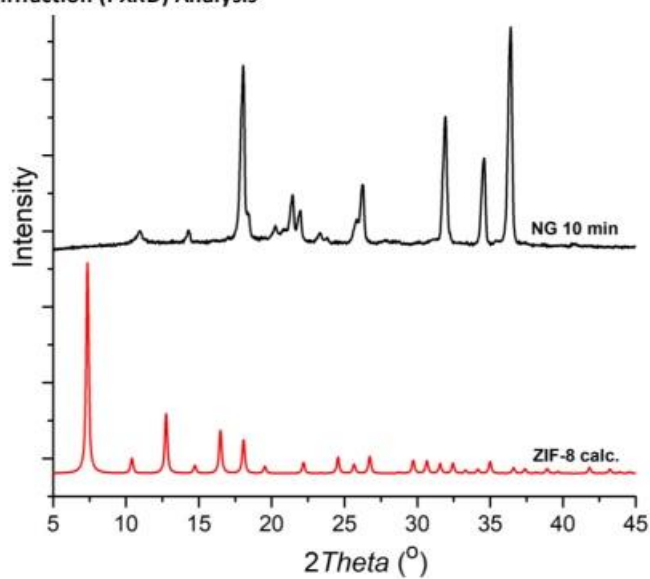
(a)
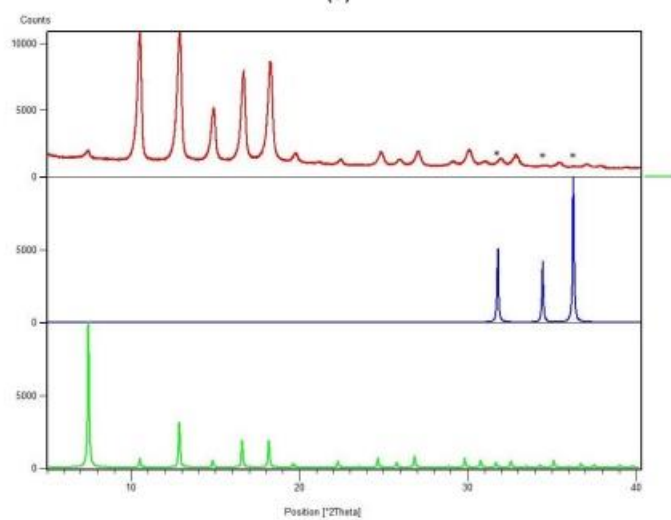
(b)

Figure S2: PXRD data of (a) The product after neat grinding of mixture of ZnO, 2-MeIm, and fullerene for 10 minutes; and (b) a product of ILAG loading of fullerene (red) shows no traces of ZnO (asterisk) and fullerene, only the pure ZIF-8 phase. Green is the calculated diffractogram for the deposited ZIF-8 structure (CSD code VELVOY), and blue is the PXRD of ZnO.

3
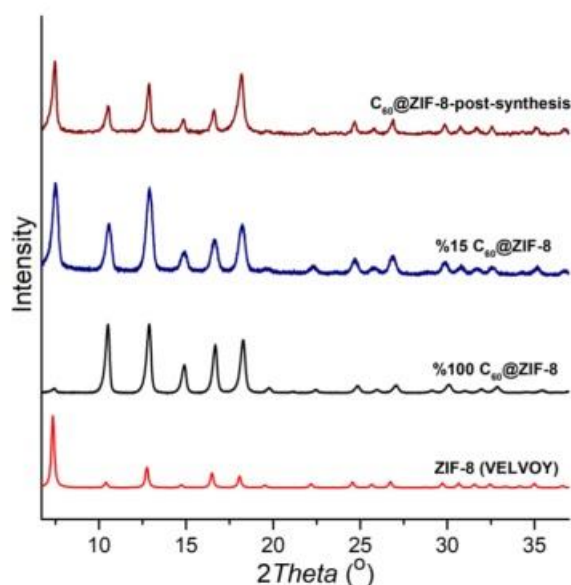
Figure S3. PXRD data of red: ZIF-8 (VELVOY), black: 100% C₆₀@ZIF-8, navy: 15% C₆₀@ZIF-8, brown: C₆₀@ZIF-8 by mechanochemical post-synthetic method
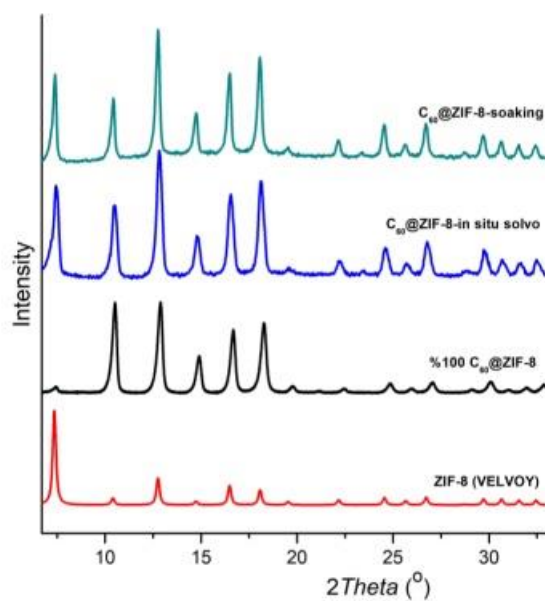
Figure S4. PXRD data of red: ZIF-8 (VELVOY), black: 100% C₆₀@ZIF-8, blue: C₆₀@ZIF-8 by in situ solvothermal synthesis, green: post-synthetic encapsulation of C₆₀ by soaking in toluene solution.

4
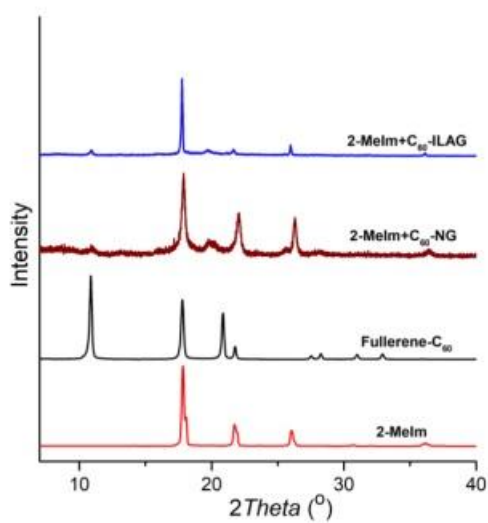
Figure S5. PXRD data of red: 2-methyl imidazole, black: Fullerene C_{60}, brown: attempted NG reaction of 2-methyl imidazole and C_{60}, blue: attempted ILAG reaction of 2-methyl imidazole and C_{60}.
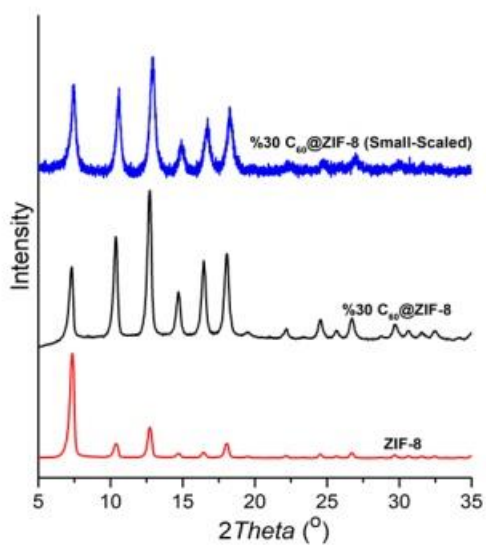
Figure S6. PXRD data of mechanochemically prepared red: ZIF-8, black: 30% C_{60}@ZIF-8, blue: small-scaled 30% C_{60}@ZIF-8.

5

S.3 Infrared (IR) spectroscopy

S.3.1 Qualitative analysis

To confirm the formation of ZIF-8, as well as to confirm encapsulation of fullerene in ZIF-8 framework, IR spectra of prepared KBr pellets were examined. First, one should understand IR spectra of the constituents, which are fullerene C_{60} and 2-methylimidazole (2MeIM) as a main building block of the ZIF-8 metal-organic framework. IR spectrum of fullerene[2,3] is dominated by two main bands, found at 577 and 528 cm^{-1}, ascribed to radial motion of its carbon atoms. Fullerene is fully characterized by the other two bands at 1428 and 1182 cm^{-1}, attributed to a tangential motion of carbon atoms. IR spectrum of 2MI is fully assigned by Arivazhagan et al.[4] The comparison of 2MI and ZIF-8 IR spectra is given in Figure S7, which provides a basis for a tentative assignation of ZIF-8 IR bands, as given in Table S1.
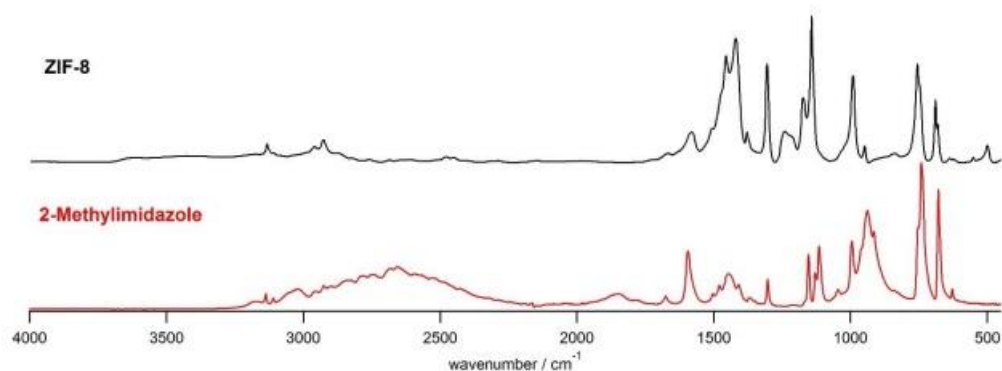
Figure S7. IR spectra of 2-methylimidazole and ZIF-8.

Table S1. The comparison of experimental IR spectra of 2MI and ZIF-8.

2MeIm[a]	ZIF-8	Assignation
3173	3177	$\nu(NH)$
3136	3129	$\nu(CH)$
3110		$\nu_s(CH_3)$
3019	2960	$\nu(CH_3)$ out-of-plane
2925	2929	$\nu_s(CH_2)$
2898	2868	$\nu_{as}(CH_2)$
3000-2200		$\nu(NH)$ hydrogen bonded
1853		a combination envelope
1672	1672	$\nu(C=N)$
1595	1583	$\nu(CN)$
1503		$\delta(CH_3)$
1478	1482	$\nu(CN)$

6

1445	1459	$\nu(CN)$
1407	1424	$\nu(CC)$
1370	1383	$\delta(NH)+ \delta(CN)$
1303	1309	$\delta(ring)+\delta(CC)$
	1246	Confined EtOH
1209	1216	Confined EtOH
1169		$\delta(CH_3)$
1153	1178	$\delta(CH_3)$
1129	1147	$\gamma(CH_3)$
1114		$\rho(CH_2)+\delta(CN)$
1046		$\gamma(NH)+ \gamma(CH)$
996	995	$\rho(CH_3)$ in-plane
962		$\rho(CH_3)$ out-of-plane
937	954	$\gamma(CH)+ \gamma(CC)$
914		$\gamma(NH)$
840	843	$\gamma(CH)$
753	760	$\gamma(CH)+ \gamma(CN)$
740	751	$\delta(CC)+\delta(CN)$
678	695	$\nu(CCH_3)$
653	685	$\tau(ring)$
627	641	$\gamma(CH)+ \gamma(CC)$
	555	
	503	
420	422	$\nu(ZnN)$

[a][M. Arivazhagan, S. Manivel, S. Jeyavijayan, R. Meenakshi, *Spectrochim. Acta A*, **134** (2015) 493-450]

[b]n - stretching; s - symmetric; as - antisymmetric; δ - in-plane deformation; γ - out-of-plane deformation; ρ- rocking; τ- torsion

Now, we consider changes in IR spectra due to the encapsulation of C_{60} molecules inside ZIF-8 framework. Due to overlap of bands corresponding to tangential motion modes of C_{60} with bands belonging to C_{60}@ZIF-8 samples only the ones ascribed to radial motion are used (Figure S8).

7
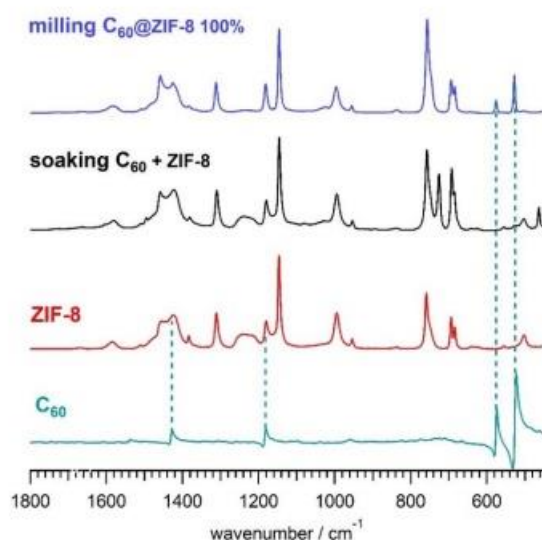
Figure S8. IR spectra of green: C_{60} fullerene, red: ZIF-8, black: C_{60}+ZIF-8 by post-synthesis, blue: 100 % C_{60}@ZIF-8 by one-pot mechanochemistry

A broad envelope in the 1280-1200 cm^{-1} range completely disappears for C_{60} loadings over 15%. The origin of this envelope is resolved by comparing the spectra for ZIF-8 prepared in different conditions, as shown in Figure S9. For this reason, ZIF-8 was synthesized in following ways: 1. solvothermally from $Zn(NO_3)_2$ in DMF. After the synthesis the sample was washed with toluene; 2. solvothermally from $Zn(NO_3)_2$ in DMF. After the synthesis the sample was washed with EtOH; 3. LAG ball milling from ZnO with EtOH; 4. LAG ball milling from ZnO with MeOH; 5. ILAG ball milling from ZnO using EtOH and NH_4NO_3 (the method used for preparation of here considered samples); 6. ILAG ball milling of the mixture of C_{60} (15% with respect of the ZIF-8 precursors) from ZnO using EtOH and NH_4NO_3 (the method used for preparation of here considered samples).

It is evident that this spectral feature is present exclusively in cases of ZIF-8 prepared in the presence of ethanol (EtOH). While it is visible in the nascent ZIF-8 prepared by ILAG using EtOH, this feature is almost unnoticeable in mechanochemically prepared 30% C_{60}@ZIF-8. It could not be detected for greater C_{60} loadings (Figures 3a in the manuscript and S12). In solution, the EtOH molecule acts as a hydrogen bond donor for electron pairs of the N atoms of imidazole rings, which may cause stronger binding with respect of C_{60} which, together with the vast excess of solvent molecules in solvothermal synthesis, may reduce the loading of fullerene guests. This is further corroborated by evidence from the ν(Zn–N) band. For neat ZIF-8 and low C_{60} loadings, it consists of two bands, one peaking at 422 and another at 416 cm^{-1}. The 416 cm^{-1} contribution rapidly decreases in intensity and completely disappears for $x(C_{60})$ = 30%. On the other hand, the intensity of the 422 cm^{-1} band is unaffected by C_{60} loading, but it is narrowed. It is important to note that for ZIF-8 prepared from DMF, only 422 cm^{-1} contribution is observed (SI). This indicates that, for ZIF-8 prepared in the presence of EtOH, the Zn-N moiety is in interaction with EtOH, possibly through hydrogen bonding. The same supramolecular interaction is absent in the presence of C_{60}, thus setting the Zn-N vibrator free. That being so, in solution strategies, an excess of EtOH prevents substantial loading of C_{60}. However, in LAG and ILAG conditions, EtOH is present in amounts much lower than C_{60} enabling the C_{60} molecules to efficiently compete for the inhabitation of ZIF-8 cages.

8

Figure S9. Comparison of the ZIF-8 samples prepared by different methods. The 1280-1200 cm^{-1} feature is present exclusively when EtOH was used in the synthetic process.

The fullerene bands are located at the same positions for neat C$_{60}$, and unaffected by amount of the encapsulated C$_{60}$ inside the ZIF-8 framework. Gas-phase IR spectra of C$_{60}$ show the corresponding bands at 528 and 576 cm^{-1}, respectively. Here observed bandwidths are also very similar to those for gas-phase samples.[5] Altogether, this shows that there is no significant interaction between ZIF-8 framework and fullerene molecule, so it is free standing inside the cage. ZIF-8 does not absorb light in the visible range – so all the features come from C$_{60}$. The lowest-energy absorption of C$_{60}$ powder is rather broad absorption, the onset is near 760 nm. C$_{60}$@ZIF-8 sample shows different absorption pattern. It is better resolved and is shifted to higher energy. Again, like in luminescence spectra, these differences may be attributed to considerable interactions between C$_{60}$ molecules in the fullerene solid (there should be some dispersion in the electronic bands) and the absence of such interactions in C$_{60}$@ZIF-8 samples. This suggestion is

9

further verified by comparison to C_{60} spectrum measured in solution (i.e. C_{60} molecules are also non-interacting), which is very similar to the spectrum of C_{60}@ZIF-8. In brief, C_{60} in C_{60}@ZIF-8 shows electronic properties of the single molecule not affected by intermolecular interaction.

C_{60} encapsulation-induced changes in IR spectrum of the ZIF-8 are mainly limited to the features due to the deformations of the imidazole ring. This indicates that embedding of C_{60} molecule significantly affects the dynamics of the imidazole moiety, which is in line with intuitive expectations, since these moieties define the dimensions of the ZIF-8 cavity, now occupied by bulk spherical C_{60}.

The envelope attributed to $\nu(ZnN)$ mode consists of two bands for ZIF-8, one at 422 cm^{-1} and another at 416 cm^{-1}. The 416 cm^{-1} contribution rapidly decreases in intensity and completely disappears for $x(C_{60}) = 30\%$. Simultaneously, the intensity of the 422 cm^{-1} band remains constant, but it is narrowed. This indicates that Zn-N moiety is in some interaction with its surrounding for empty ZIF-8, which is broken by encapsulation of C_{60}, making the Zn-N vibrator free.
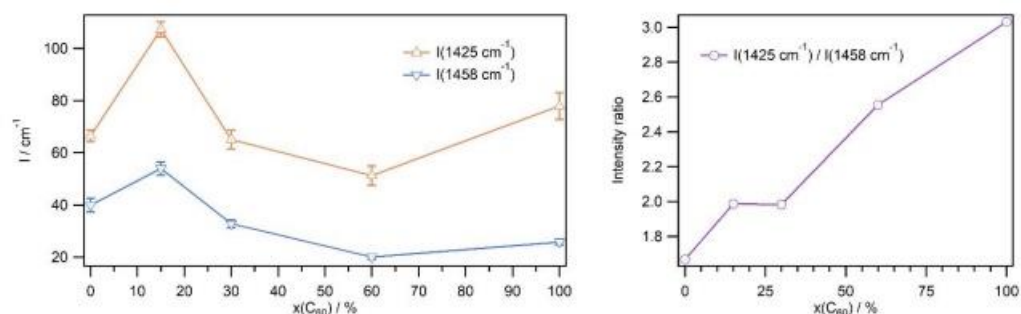
Figure S10. Intensity of the $\nu(CC)$ and $\nu(CN)$ band, respectively, and their ratio. Error bars represent standard deviations of intensity of the band as obtained by fitting to Lorentzian function.
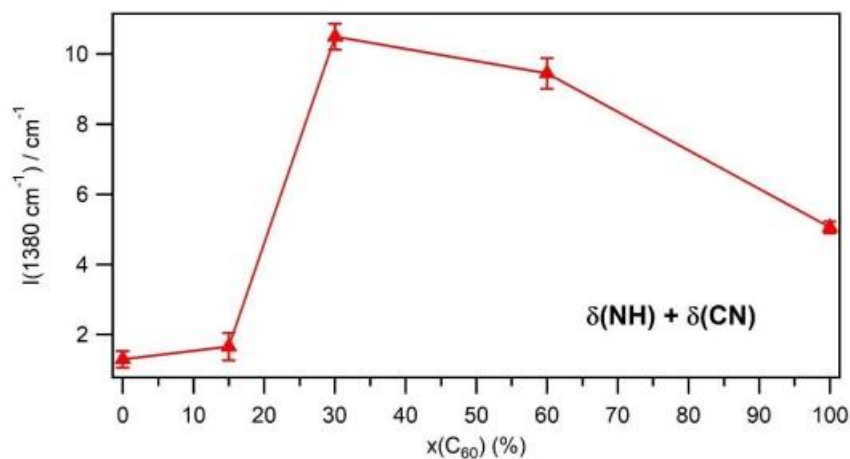
Figure S11. Intensity of the $\delta(NH) + \delta(CN)$ combination band. Error bars represent standard deviations of intensity of the band as obtained by fitting to Lorentzian function.

10
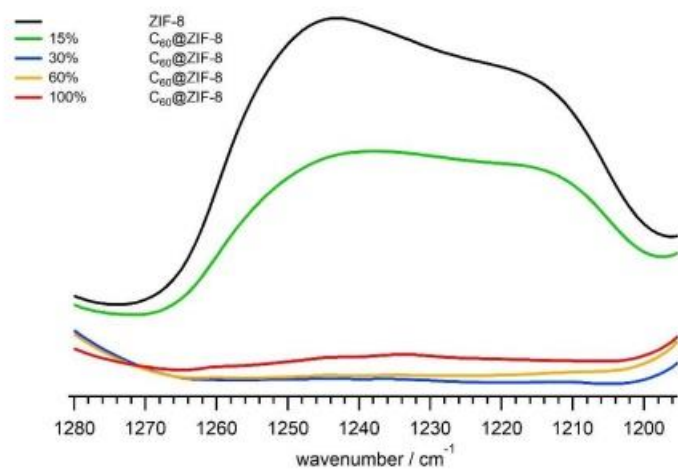
Figure S12. Envelope in the 1280-1200 cm^{-1} range due to the EtOH confined inside the ZIF-8 pores.
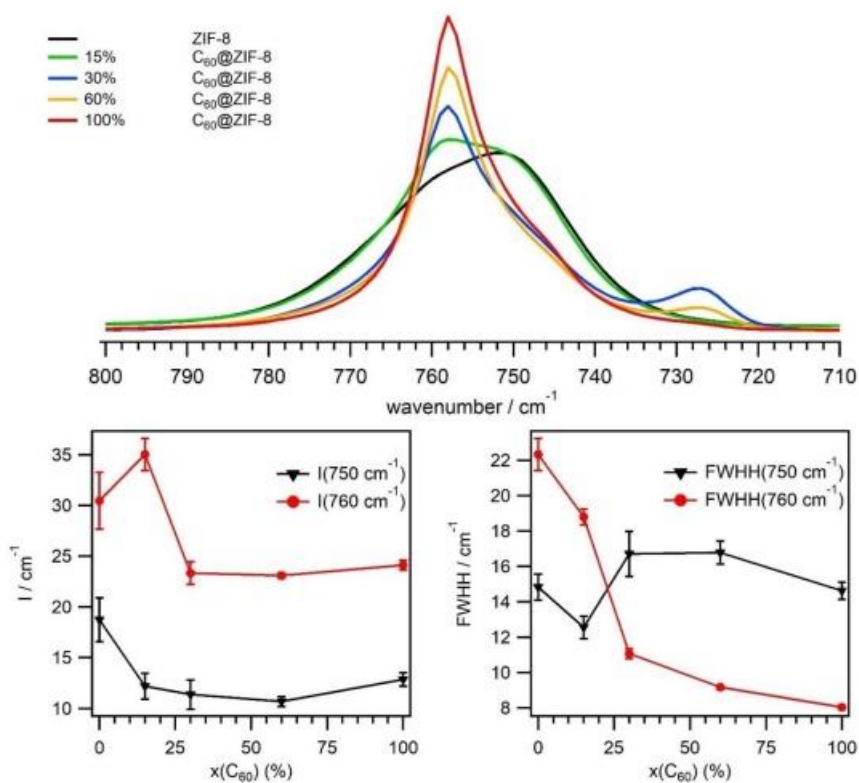
Figure S13. Intensity and full width at half height of the in-plane and out-of-plane deformation, respectively, of the imidazole ring. Error bars represent standard deviations of the corresponding parameters as obtained by fitting to Lorentzian function.

11
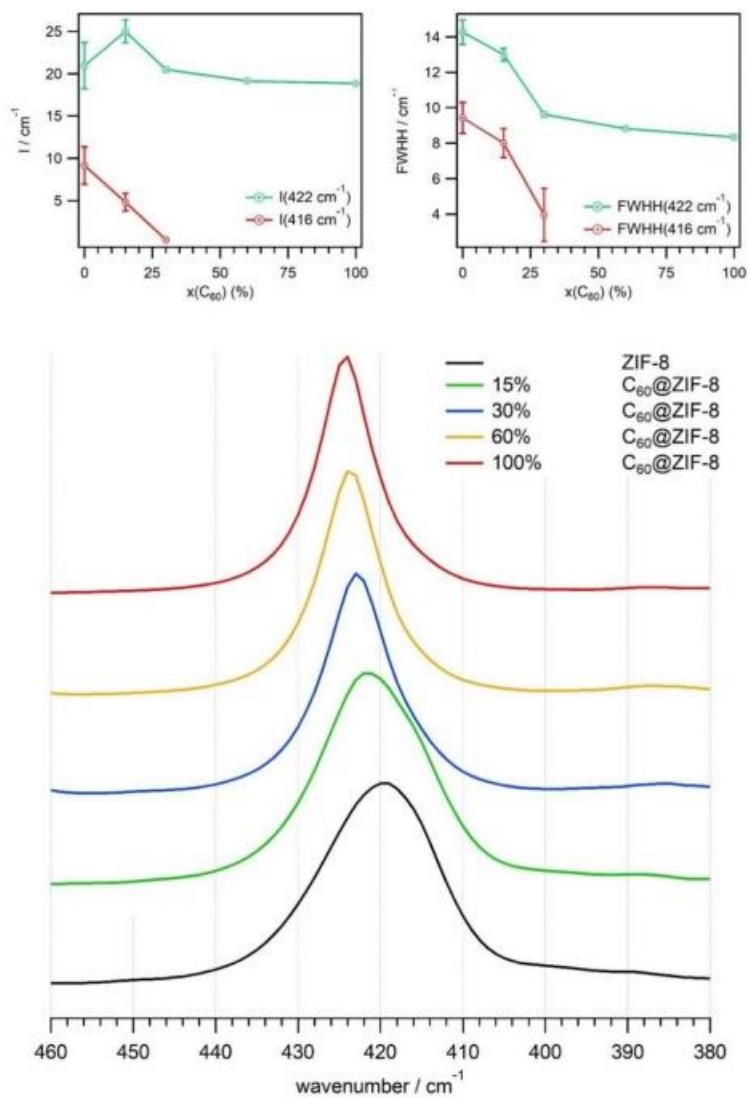
Figure S14. IR absorption due to the v(ZnN) vibrational mode.

12
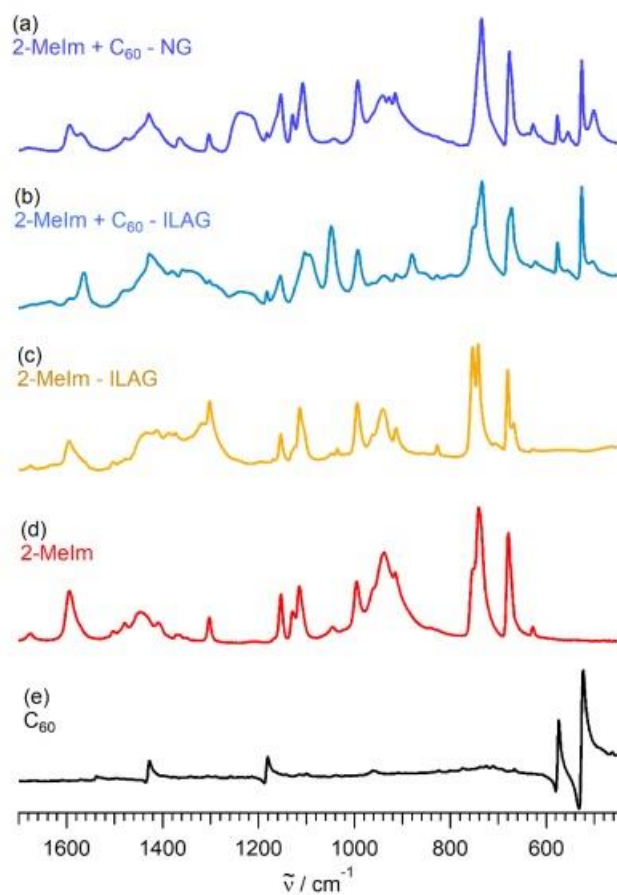
Figure S15. IR spectra of black: Fullerene C_{60}, red: 2-methyl imidazole, orange: attempted ILAG reaction of 2-methyl imidazole, blue: attempted ILAG reaction of 2-methyl imidazole and C_{60}, violet: attempted NG reaction of 2-methyl imidazole and C_{60}.

13
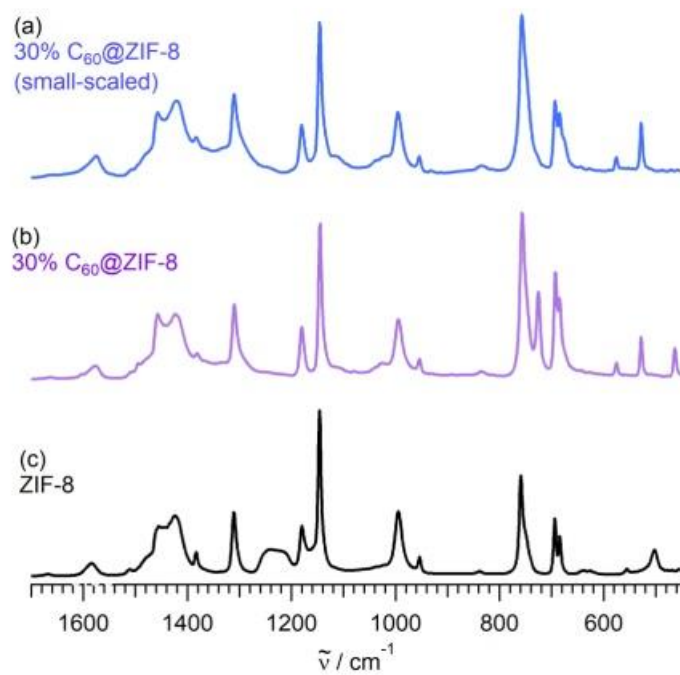
Figure S16. IR spectra of mechanochemically-synthesized black: ZIF-8, violet: 30% C_{60}@ZIF-8, blue: small-scaled 30% C_{60}@ZIF-8.

S.3.2 Quantitative analysis

The amounts of KBr and ZIF-8, fullerene (C_{60}) or fullerene encapsulated ZIF-8 (C_{60}@ZIF-8) used for pellet preparation are given in the Table S2. Each spectrum was recorded across the range of 4000-350 cm^{-1} with the spectral resolution of 1 cm^{-1}. IR spectra were subsequently examined to study amount of C_{60} encapsulated in ZIF-8.

Table S2. The preparation of pellets for the FT-IR spectroscopy

Sample	m(C_{60} or ZIF-8 sample)/ mg	m(KBr)/mg*
C_{60}_30%	0.42	102.58
C_{60}_60%	0.72	102.28
C_{60}_100%	1.05	101.95
ZIF-8	3	100
C_{60}@ZIF-8_15%	3	100
C_{60}@ZIF-8_30%	3	100
C_{60}@ZIF-8_60%	3	100
C_{60}@ZIF-8_100%	3	100

*Sufficient for the preparation of pellets with a total weight of 103 mg. C_{60}: fullerene; C_{60}@ZIF-8: fullerene encapsulated ZIF-8

To obtain calibration curve, approximate fullerene content in 30 %, 60 % and 100 % C_{60}@ ZIF-8 were calculated and relative amounts of corresponding free fullerene, were mixed with powdered KBr, previously dried at 100°C in an oven to constant weight, to prepare the 103 mg pellets. The powders were mixed and ground in an agate mortar to obtain a homogeneous mixture. Thereafter, this mixture was compressed with a mechanical press for one minute under the pressure of 10 bar to obtain translucent pellets.

Previously dried empty ZIF-8 sample, as well as four C_{60}@ZIF-8 samples, containing 15%, 30 %, 60 % and 100 % of C_{60}, were made into KBr pellets following the same procedure. In order to obtain 103 mg pellets, 3 mg of ZIF-8 or C_{60}@ZIF-8 samples were taken and diluted with 100 mg of powdered KBr.

In order to determine efficiency of encapsulation of C_{60} into the ZIF-8 matrix, we selected 528 and 577 cm^{-1} bands. These bands are well isolated from the rest of the spectral features, as well as well separated to each other (Figure S17), allowing a highly accurate measurement of spectral parameters. As seen from Figure S17, 528 cm^{-1} band is partially overlapped by 504 cm^{-1} feature of ZIF-8, but this does not affect the results.

15
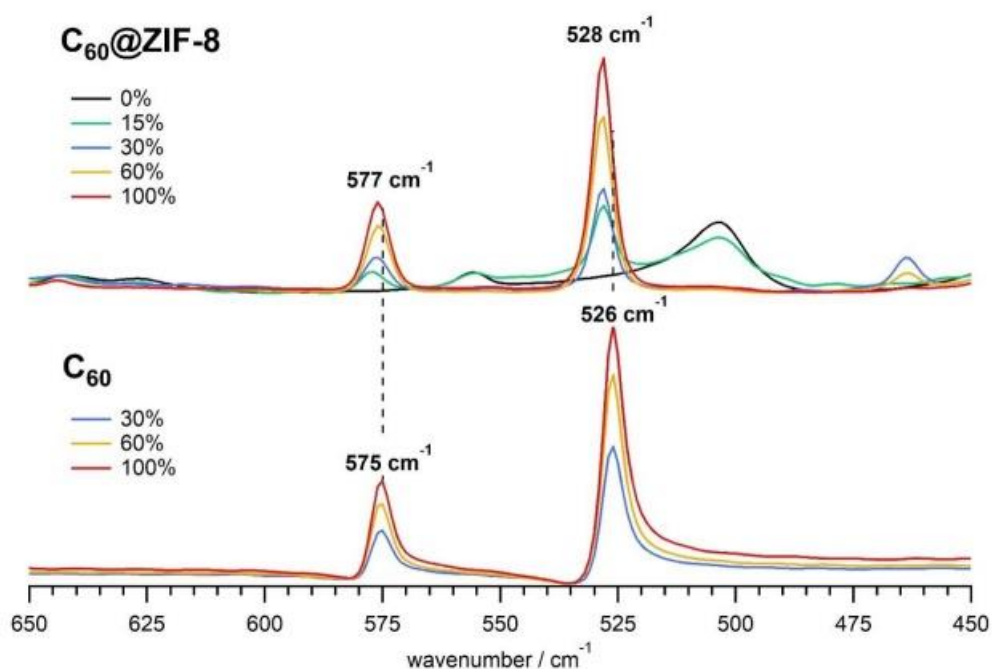
Figure S17. Changes in IR spectra (region 650-450 cm^{-1}) upon loading of fullerene.

Intensities (and other spectral parameters) with respect of C_{60} molar ratio were determined by fitting the 528 and 577 cm^{-1} bands, each band individually, to Lorentzian functions. For 528 cm^{-1} band, fitting was done in the spectral range from 555 to 475 cm^{-1}, taking the ZIF-8 504 cm^{-1} into consideration. Fitting of the 577 cm^{-1} band was done in the range from 610 to 550 cm^{-1}, taking the ZIF-8 555 cm^{-1} into consideration. The corresponding bands for equivalent amount of neat C_{60} are considered in the same spectral ranges. The results are given in Table S3 and Figure S18.

Table S3. Intensities of the fullerene 528 and 577 cm^{-1} band, respectively, as obtained by fitting them to Lorentzian shape functions.

Nominal $x(C_{60})$ / %	C_{60}		C_{60}@ZIF-8	
	526 cm^{-1}	575 cm^{-1}	528 cm^{-1}	577 cm^{-1}
15	1.30 ± 0.11	0.49 ± 0.12	1.35 ± 0.05	0.38 ± 0.03
30	2.38 ± 0.12	0.99 ± 0.14	1.97 ± 0.03	0.73 ± 0.03
60	3.84 ± 0.12	1.49 ± 0.14	3.49 ± 0.05	1.44 ± 0.04
100	4.88 ± 0.18	1.94 ± 0.20	4.49 ± 0.06	1.89 ± 0.05

16
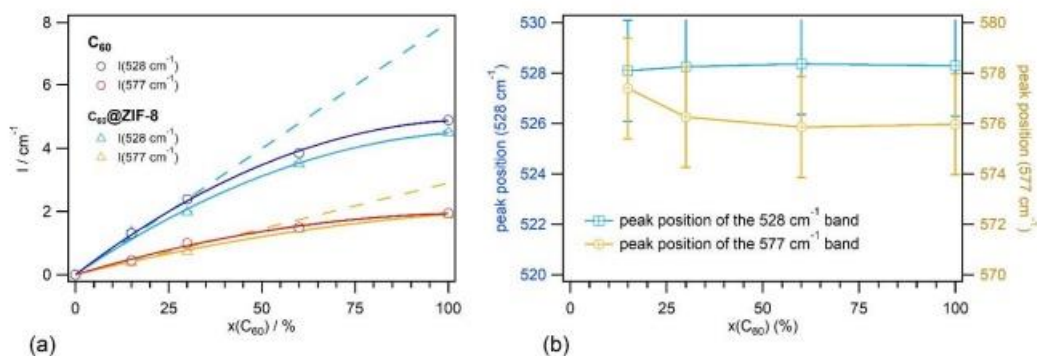
Figure S18. (a) Intensities and (b) peak positions of the characteristic fullerene bands. Error bars for intensities represent standard deviations of the intensity as obtained by fitting to Lorentzian function, while the error bars for peak positions represent the resolution of the recorded IR spectra.

Now, the intensities of fullerene bands at 528 and 577 cm^{-1} are fitted to second-order polynomial function of the form:

$$I = ax(C_{60}) + bx^2(C_{60})$$

The obtained fitting parameters are given in Table S4.

Table S4. Second-order fitting parameters for intensities of fullerene bands.

	C_{60}		C_{60}@ZIF-8	
	a	*b*	*a*	*b*
I(528 cm^{-1})	0.090 ± 0.002	-0.00041 ± 2.5·10^{-5}	0.080 ± 0.006	-0.00035 ± 6.3·10^{-5}
I(577 cm^{-1})	0.035 ± 0.002	-0.00016 ± 2.4·10^{-5}	0.029 ± 0.002	-0.00001 ± 2.4·10^{-5}

Figure S18 a shows comparison of intensities of the neat C_{60} with those for the corresponding bands for encapsulated C_{60}, together with fitting of these data to second-order polynomial functions. It is evident that the behavior of encapsulated C_{60} is very similar to neat C_{60}. The expected behavior for is given by dashed lines, but in both cases C_{60} significantly deviates from linear behavior with respect of molar ratio.

For these reasons, in order to finally determine the encapsulation efficiency of C_{60} inside the ZIF-8 pores, we compared the molar ratio dependent intensities of neat with respect to encapsulated C_{60}. Thus, the encapsulation efficiency f_{Enc} for corresponding band $\tilde{v}$ is calculated as:

$$f_{Enc}(\tilde{v}) = \left[1 - \frac{I_{neat}(x(C_{60})) - I_{enc}(x(C_{60}))}{I_{neat}(x(C_{60}))}\right] x(C_{60})$$

where $I_{neat}(x(C_{60}))$ and $I_{enc}(x(C_{60}))$ represent intensity of neat and encapsulated C_{60}, respectively, for given nominal molar ratio $x(C_{60})$.

17

S.4.Luminescence spectroscopy
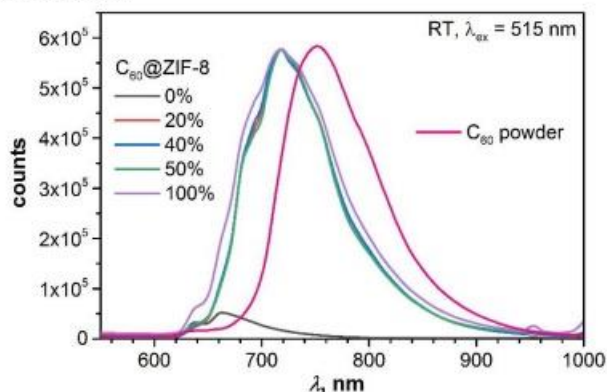
Figure S19. Luminescence spectra of C_{60}@ZIF-8 samples with different C_{60} loading and the spectrum of C_{60} powder. Room temperature, excitation at 515 nm, all spectra are normalized to have similar intensity (absolute intensities are not comparable, i.e. we do not know if quantum yield is changing).

The interactions between C_{60} molecules in solid C_{60} and their absence in the ZIF-8 encapsulated fullerene changes the exciton properties. Comparison of the luminescence spectra of C_{60}@ZIF-8 and C_{60} samples reveals an evident shift of encapsulated C_{60} luminescence to higher energy, suggesting almost isolated C_{60} molecules inside ZIF-8 cages.(Figure S19) The measured fluorescence lifetime of C_{60} itself is less than 1 ns (the set-up used in the measurement has the limit of ~0.7 ns), while for C_{60}@ZIF-8 it is increased to 1.4 ns and it seems to be independent on the load. Temperature dependent luminescence spectra show constant fluorescence lifetimes down to liquid He temperatures (4 K). However, while the spectra of the C_{60} powder is significantly intensified by cooling, the intensity of the C_{60}@ZIF-8 spectra is only slightly increased. This points to the decrease of interaction with other C_{60} neighbors in C_{60}@ZIF-8, thus indicating mutual isolation of C_{60} molecules due to the encapsulation in ZIF-8 matrix.
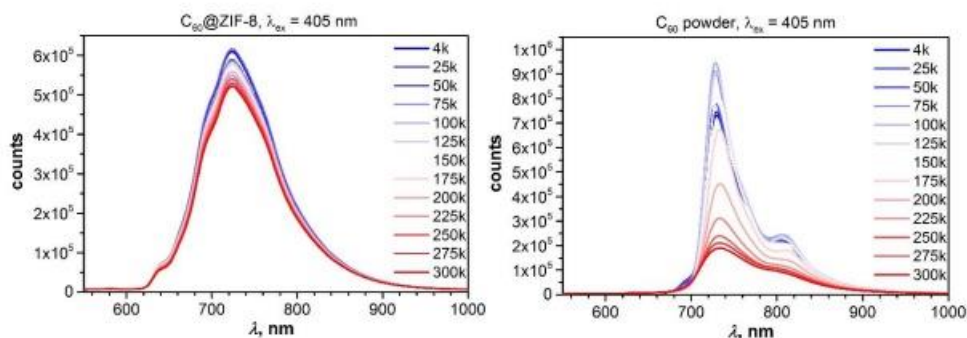
Figure S20. Luminescence spectra of C_{60}@ZIF-8 (50%) and the spectrum of C_{60} powder measured at different temperatures, excitation at 405 nm. Spectra of C_{60} powder seem to be different with different excitation wavelength, whereas those of C_{60}@ZIF-8 are only slightly changing.

18

S.5 Theoretical methods and models

Two theoretical frameworks were employed for the different computational tasks according to their computational needs and time efficiency. Density functional based tight-binding (DFTB) model[6] was used for the molecular dynamic propagation of ZIF-8 and C_{60}@ZIF-8 (Figure 7a in the main text) and potential energy scan (PES) along the C_{60} motion between the centers of two pores (Figure 7b,c in the main text). Density functional theory (DFT) at PBE level of theory was used for the computations of harmonic vibrational spectra of ZIF-8 and C_{60}@ZIF-8 (Figure 3b).

DFTB calculations were performed using DFTB+ code (*ver. 20.1*) and the Slater-Koster parameters 3ob-3-1-CC optimized for organic and biological systems.[7,8] The dynamic trajectories propagated for 250ps with the time step of 0.5 fs within the canonical (NVT) ensemble, using the Nosé−Hoover thermostat set at T=300 K for temperature control. The PES profile for C_{60} "leap" between two consequent pores was obtained by using constraint optimization techniques. In this run, the distance between the front carbon of the cage and the central point of the targeted-pore was changed step-wise and remained fixed at the optimization, while all other degrees of freedom were optimized down to the gradient of 10^{-3} eV/Å. **Animation** (animation.mp4) shows the geometrical changes along this reaction path.

For the ZIF-8 and C_{60}@ZIF-8 structures well-optimized at the DFT/PBE level of theory, dynamic matrixes and Born effective charges were computed using the plane-wave basis set and the projector augmented wave method with energy cutoffs recommended by VASP5.1 developers.[9,10,11,12] The results of the density functional perturbation theory (DFTP) computations were used to estimate IR frequencies and intensities in the dipole approximation for periodic systems (Figure 3b in the main text).[13,14]

19

S.6 ESR spectroscopy

The presence of fullerene guests in the cages of ZIF-8 is confirmed also by ESR spectroscopy. Off-the-shelf fullerene shows weak sharp ESR line with g-value around $g = 2.002$ and peak-to-peak line-width around $W_{pp} \approx 0.1$ mT, due to defects in fullerene structure,[9–12] as could be seen in Figure S21 a. While pristine ZIF-8 does not show this signal (Figure S21 b), both investigated C_{60}@ZIF-8 (15%) and C_{60}@ZIF-8 (100%) clearly exhibit the similar but broader fullerene line with $W_{pp} \approx 0.2$ mT (Figures S21 c and d). Stronger line intensity of C_{60}@ZIF-8 (100%) compared to weaker line intensity of C_{60}@ZIF-8 (15%) agrees with different mol% of fullerene in ZIF-8.
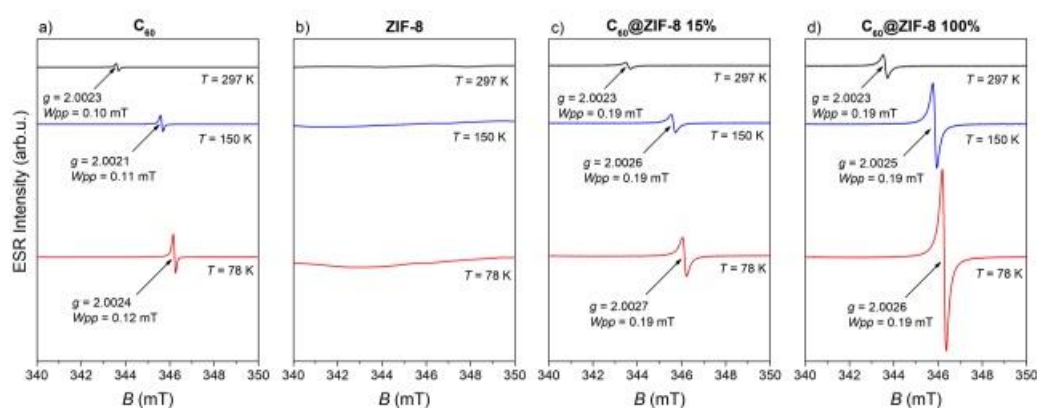
Figure S21. Comparison of the ESR spectra for a) C_{60}, b) ZIF-8, c) C_{60}@ZIF-8 (15%) and d) C_{60}@ZIF-8 (100%) at indicated temperatures.

In order to check does synthesis of C_{60}@ZIF-8 produce some additional paramagnetic signal, ESR spectra of investigated samples were recorded also in the broader magnetic field range 0-800 mT (Figure S22). In the spectrum of pristine ZIF-8, a weak and broad background signal is visible (Figure S22b), probably due to presence of small amount of paramagnetic impurities. The same background line is presented in C_{60}@ZIF-8 (15%) and C_{60}@ZIF-8 (100%), as can be seen in Figure S22 c and d, respectively. However, no additional lines (beside fullerene line) are presented in C_{60}@ZIF-8 confirming that during the synthesis no new paramagnetic defects were generated.

20
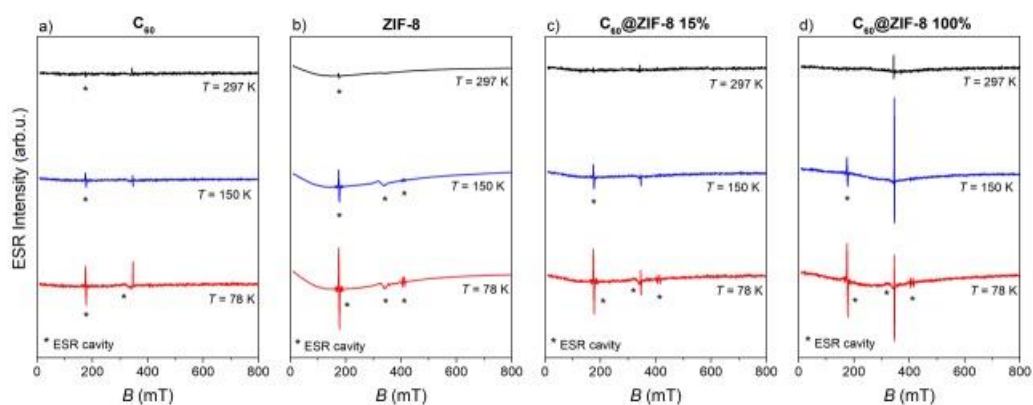
Figure S22. ESR spectra recorded in the magnetic field range 0-800 mT for a) C_{60}, b) ZIF-8, c) C_{60}@ZIF-8 (15%) and d) C_{60}@ZIF-8 (100%) at indicated temperatures. The lines labelled with asterisks originate from the ESR cavity.

S.7 TGA experiments
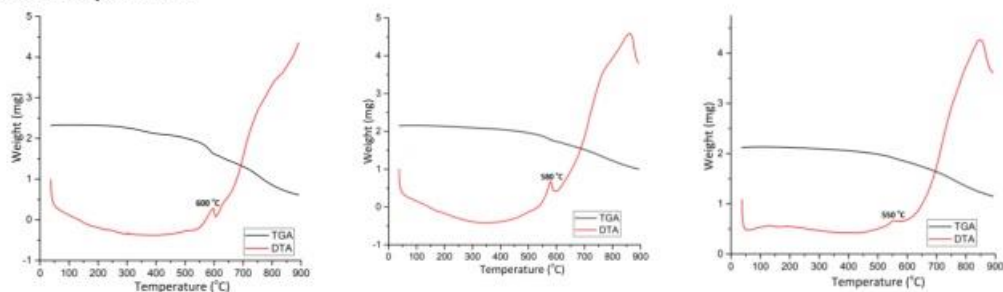
Figure S23. TGA-DTA data collected under N_2, heating rate 5 $^\circ$C/min for (from left to right): ZIF-8, 30% C_{60}@ZIF-8, and 100% C_{60}@ZIF-8. Endotherm was set to point upwards for all experiments.
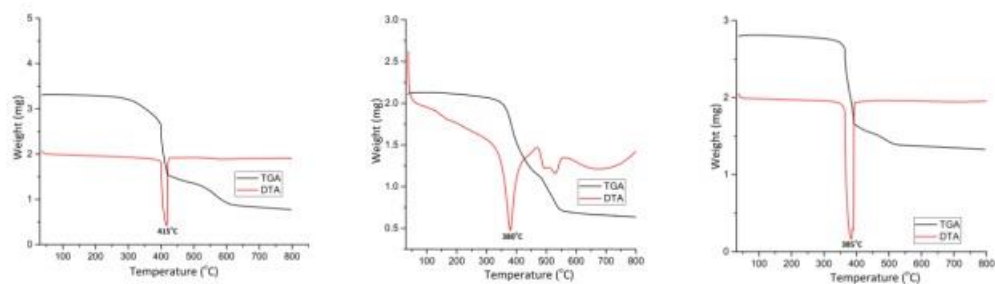
Figure S24. TGA-DTA data collected under O_2, heating rate 5 $^\circ$C/min for (from left to right): ZIF-8, 30% C_{60}@ZIF-8, and 100% C_{60}@ZIF-8. Endotherm was set to point upwards for all experiments.

22

References

(1)   Beldon, Patrick J.; Fábián, László; Stein, Robin S.; Thirumurugan, A.; Cheetham, Anthony K.; Friščić, Tomislav. Rapid Room-Temperature Synthesis of Zeolitic Imidazolate Frameworks by Using Mechanochemistry. *Angew. Chem. Int. Ed.* **2010**, *49* (50), 9640–9643. https://doi.org/10.1002/anie.201005547.

(2)   Țucureanu, Vasilica; Matei, Alina; Avram, Andrei Marius. FTIR Spectroscopy for Carbon Family Study. *Crit. Rev. Anal. Chem.* **2016**, *46* (6), 502–520. https://doi.org/10.1080/10408347.2016.1157013.

(3)   Schettino, Vincenzo; Pagliai, Marco; Ciabini, Lucia; Cardini, Gianni. The Vibrational Spectrum of Fullerene C 60. *J. Phys. Chem. A* **2001**, *105* (50), 11192–11196. https://doi.org/10.1021/jp012874t.

(4)   Arivazhagan, M.; Manivel, S.; Jeyavijayan, S.; Meenakshi, R. Vibrational Spectroscopic (FTIR and FT-Raman), First-Order Hyperpolarizablity, HOMO, LUMO, NBO, Mulliken Charge Analyses of 2-Ethylimidazole Based on Hartree–Fock and DFT Calculations. *Spectrochim. Acta Part A Mol. Biomol. Spectrosc.* **2015**, *134*, 493–501. https://doi.org/10.1016/j.saa.2014.06.108.

(5)   Nemes, Laszlo; Ram, Ram S.; Bernath, Peter F.; Tinker, Frank A.; Zumwalt, Michael C.; Lamb, Lowell D.; Huffman, Donald R. Gas-Phase Infrared Emission Spectra of C60 and C70. Temperature-Dependent Studies. *Chem. Phys. Lett.* **1994**, *218* (4), 295–303. https://doi.org/10.1016/0009-2614(93)E1488-3.

(6)   Porezag, D.; Frauenheim, Th.; Köhler, Th.; Seifert, G.; Kaschner, R. Construction of Tight-Binding-like Potentials on the Basis of Density-Functional Theory: Application to Carbon. *Phys. Rev. B* **1995**, *51* (19), 12947–12957. https://doi.org/10.1103/PhysRevB.51.12947.

(7)   Hourahine, B.; Aradi, B.; Blum, V.; Bonafé, F.; Buccheri, A.; Camacho, C.; Cevallos, C.; Deshaye, M. Y.; Dumitrică, T.; Dominguez, A.; et al. DFTB+, a Software Package for Efficient Approximate Density Functional Theory Based Atomistic Simulations. *J. Chem. Phys.* **2020**, *152* (12), 124101. https://doi.org/10.1063/1.5143190.

(8)   Gaus, Michael; Goez, Albrecht; Elstner, Marcus. Parametrization and Benchmark of DFTB3 for Organic Molecules. *J. Chem. Theory Comput.* **2013**, *9* (1), 338–354. https://doi.org/10.1021/ct300849w.

(9)   Perdew, John P.; Burke, Kieron; Ernzerhof, Matthias. Generalized Gradient Approximation Made Simple. *Phys. Rev. Lett.* **1996**, *77* (18), 3865–3868. https://doi.org/10.1103/PhysRevLett.77.3865.

(10) Kresse, G.; Hafner, J. Ab Initio Molecular Dynamics for Liquid Metals. *Phys. Rev. B* **1993**, *47* (1), 558–561. https://doi.org/10.1103/PhysRevB.47.558.

(11) Kresse, G.; Joubert, D. From Ultrasoft Pseudopotentials to the Projector Augmented-Wave Method. *Phys. Rev. B* **1999**, *59* (3), 1758–1775. https://doi.org/10.1103/PhysRevB.59.1758.

(12) Hafner, Jürgen. Ab-Initio Simulations of Materials Using VASP: Density-Functional Theory and Beyond. *J. Comput. Chem.* **2008**, *29* (13), 2044–2078. https://doi.org/10.1002/jcc.21057.

(13) Giannozzi, Paolo; Baroni, Stefano. Vibrational and Dielectric Properties of C 60 from Density-functional Perturbation Theory. *J. Chem. Phys.* **1994**, *100* (11), 8537–8539. https://doi.org/10.1063/1.466753.

(14) Karhánek, David; Bučko, Tomáš; Hafner, Jürgen. A Density-Functional Study of the Adsorption of Methane-Thiol on the (111) Surfaces of the Ni-Group Metals: II. Vibrational Spectroscopy. *J. Phys. Condens. Matter* **2010**, *22* (26), 265006. https://doi.org/10.1088/0953-8984/22/26/265006.

7.3.   Appendix III− Manuscript of Publication 2

Low-Dimensional Magnetism in Multivariate Copper/Zinc MOF-74 Materials Formed via Different Mechanochemical Methods

S. Muratović[1], V. Martinez[1], B. Karadeniz[1], D. Pajić[2], I. Brekalo[1], M. Arhangelskis[3], M. Mazaj[4], G. Mali[4], M. Etter[5], T. Friščić[6], Y. Krupskaya[7], V. Kataev[7], D. Žilić[1], K. Užarević[1]

[1] Ruđer Bošković Institute, Zagreb, Croatia [2] Department of Physics, Faculty of Science, Zagreb, Croatia
[3] University of Warsaw, Warsaw, Poland [4] National Institute of Chemistry, Ljubljana, Slovenia
[5] DESY, Hamburg, Germany [6] McGill University, Montreal, Canada [7] Leibniz IFW, Dresden, Germany

Author contribution:

*S. M. and V. M. contributed equally as the first authors

S. M. X-band EPR and HF-EPR measurements and data analysis; **V. M.** and **B. K.** MOF design and synthesis, materials characterisation, in-situ synchrotron study; **D. P.** SQUID measurements and analysis; **I. B.** and **M. A.** PXRD structure solution; **M. M.** SEM-EDAX analysis; **G. M.** ssNMR measurements and analysis; **M. E.** synchrotron data integration; **T. F.** idea conceptualisation; **Y. K.** magnetisation measurements analysis; **V. K.** magnetisation measurements analysis; **D. Ž.** idea conceptualisation, funding acquisition; **K. U.** idea conceptualisation, funding acquisition

All authors contributed to the writing of the final manuscript.

CCC
RightsLink

ACS Publications
Most Trusted. Most Cited. Most Read

Low-Dimensional Magnetism in Multivariate Copper/Zinc MOF-74 Materials Formed via Different Mechanochemical Methods

Author: Senada Muratović, Valentina Martinez, Bahar Karadeniz, et al

Publication: Inorganic Chemistry

Publisher: American Chemical Society

Date: Nov 1, 2022

Copyright © 2022, American Chemical Society

BACK   CLOSE WINDOW

Privacy - Terms

Inorganic Chemistry

Low-Dimensional Magnetism in Multivariate Copper/Zinc MOF-74 Materials Formed via Different Mechanochemical Methods

Senada Muratović,[∇] Valentina Martinez,[∇] Bahar Karadeniz, Damir Pajić, Ivana Brekalo, Mihails Arhangelskis, Matjaž Mazaj, Gregor Mali, Martin Etter, Tomislav Friščić, Yulia Krupskaya, Vladislav Kataev, Dijana Žilić,* and Krunoslav Užarević*

ACCESS | Metrics & More | Article Recommendations | Supporting Information

ABSTRACT: MOF-74 is an archetypal magnetic metal−organic framework (MOF) family, with metal nodes bridged by 2,5-dioxido-1,4-benzenedicarboxylic acid (H_4dobdc) and arranged into one of the simplest representations of the 1D Ising magnetic model. Recently, a novel mechano-synthetic approach opened a pathway toward a series of bimetallic multivariate (1:1) M1M2-MOF-74 materials, with the uniform distribution of metal cations in the oxometallic chains, offering a unique opportunity to investigate low-dimensional magnetism in these heterometallic MOFs. We explore here how different mechanochemical procedures affect the interaction between the metal nodes of the model system of three multivariate copper(II)/zinc(II)-MOF-74 materials, two of which were obtained through a template-controlled procedure, and the third one was obtained by recently developed mechanical MOF-alloying combined with subsequent accelerated aging. While the three Cu/Zn-MOF-74 products have almost identical powder X-ray diffraction (PXRD) diffractograms and Fourier transform infrared spectra, they differ significantly in their magnetic properties, as revealed through detailed magnetization and X-band and multifrequency high-field electron spin resonance measurements. The magnetic results of the three multivariate Cu/Zn-MOF-74s were compared to the properties of the monometallic Cu-MOF-74, which shows antiferromagnetic intrachain and weaker ferromagnetic interchain interactions. Energy-dispersive X-ray spectroscopy/scanning electron microscopy and solid-state nuclear magnetic resonance spectroscopy helped rationalize the observed differences in magnetization, and *in situ* synchrotron PXRD monitoring of template-controlled MOF formation revealed different reaction pathways when using the zinc or copper intermediates, involving even the fleeting occurrence of a rare MOF-74 polymorph.
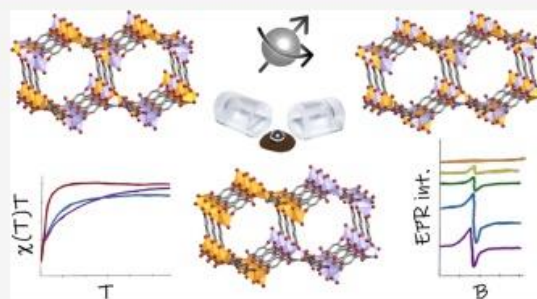
■ INTRODUCTION

Thirty years after their discovery, metal−organic frameworks (MOFs), porous coordination polymers comprised of metal nodes bridged by organic molecules, are still widely considered "novel" materials as this field remains one of the fastest developing and studied fields in materials chemistry, taking many new directions concerning the composition of MOFs and their applicability.[1−5] One of the subfields that attract significant attention are multivariate MOF materials containing diverse metal nodes in the MOF structure, but these materials are still scarce.[6−8] Such disparity in the multivariate-MOF classes stems from the difficulty in controlling the uniformity of distribution and the relative ratio of the respective metal-node constituents in the two main conventional solvothermal approaches, postsynthetic metal exchange, and direct synthesis.[9] Postsynthetic exchange relies on the soaking of monometallic MOF in a solution containing the salt of the other metal(s), usually for a period of days to weeks.[10,11] The literature on thermodynamic and kinetic factors governing the

process is still limited, and the process is hard to control.[12,13] In the direct synthesis approach, MM-MOFs are built from solutions containing linkers and multiple metal salts. While there are several studies where a significant degree of control of metal content in MM-MOFs was obtained through careful choice of the metal source and synthetic/crystallite growth conditions, the inclusion of a respective metal is most often serendipitous.[14−16] This is mostly expected, and many factors such as the nature of the metal cation (such as the acidity, charge, softness, and radius), solvent effects (solubility, pH, and solvation), and the thermodynamics of the process must
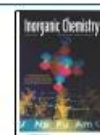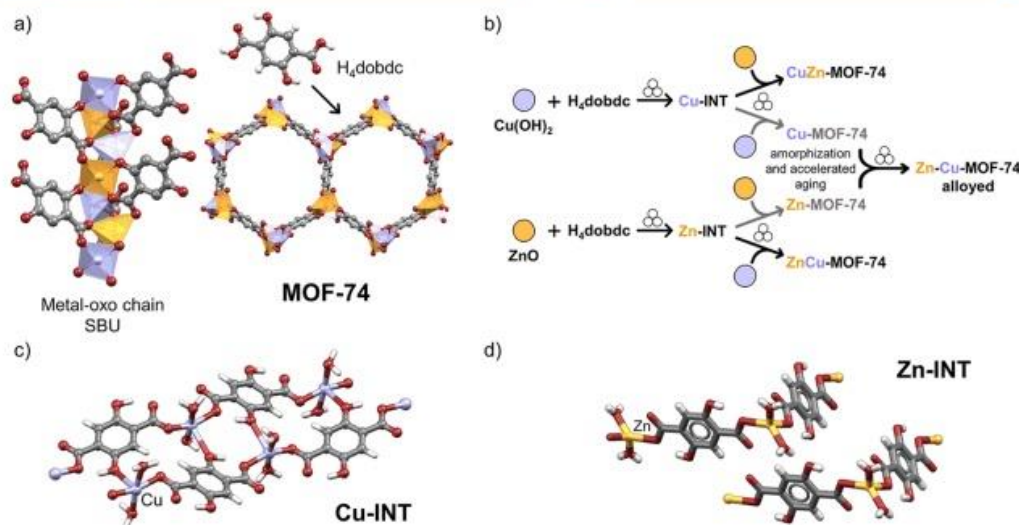
Figure 1. (a) Representation of the idealized crystal structure of MM-MOF-74, and its constituents. The H_4dobdc linker bridges metal-oxo chains to form the MOF-74 structure with hexagonal channels along the *c*-axis. H atoms of SBU and MOF are omitted for clarity. (b) Schematic representation of the mechanochemical synthesis of binary multivariate Cu/Zn MOF-74 materials examined in this study. (c) Structure of $[Cu(H_2dobdc)(H_2O)_2]_n$ (Cu-INT) prepared in this study. (d) Structure of $[Zn(H_2dobdc)(H_2O)_2]_n$ (Zn-INT) CCDC code: ODIPOH.[17,18] Color code: copper, blue; zinc, yellow; carbon, grey; oxygen, red; and hydrogen, light grey.

be taken into account to introduce a higher degree of control into processing.[7]

A particularly important target for multivariate MM-MOFs is the MOF-74 family, also known as CPO-27.[19] From the first reports, these chemically stable MOFs, characterized by large channels (12 Å diameter) and open metal sites, stood out on account of their outstanding properties.[2,20] In MOF-74, the metal cations are ordered in the 1D metal-oxo chain secondary building units (SBUs), bridged by 2,5-dioxido-1,4-benzenedicarboxylate anions ($dobdc^{4-}$) to form an $M_2(dobdc)$ MOF with hexagonal channels in a honeycomb arrangement (Figure 1a). They are highly modular, and several monometallic M-MOF-74 are known (M = Mg, Zn, Cd, Co, Mn, Fe, Ni, and Cu),[21-23] providing an ideal platform for the preparation of mixed metal phases. It is expected that these materials may have unique properties stemming from the synergistic effect between the two metals coupled closely in the 1D oxometallic chain. However, initial attempts at making mixed metal MOF-74 (MM-MOF-74) materials through postsynthetic metal exchange showed that the replacement of the metal cation is not straightforward, and the reported transmetallation efficiency was low.[24] Nevertheless, even with a low inclusion of the second metal, the obtained materials expressed large advances in their catalytic properties and chemical stability.[7]

Conversely, the direct solvothermal synthesis approach yielded MM-MOF-74 materials with up to 10 different metals incorporated in the framework,[25] but with significant inhomogeneity both in the ratio and distribution of the metal nodes, yielding crystallites with different compositions in the same product. The same group recently reported a series of binary MM-MOF-74 materials incorporating Co, Cd, Pb, and Mn, where atom probe tomography was used to tackle the issue of the local distribution of metals in MM-MOFs. It was shown that the occurrence and distribution of metal nodes largely depended on the type of the metal incorporated, and

the temperature of the synthesis.[26] It follows that, while the metal-oxo chains in MOF-74 can accommodate different metals in close vicinity—making them a prime target for MM-MOF synthesis—current synthetic approaches lack the needed control and tunability to truly realize the potential of these materials. Therefore, overcoming the limitations of conventional synthetic procedures and the dependence of MM-MOF-74 assembly on judicious choice of metals may have a transformative impact on the field of multivariate MOFs.

Two interesting synthetic alternatives to MM-MOFs rely on mechanochemical processing. The first one is mechanical alloying.[27] Here, the authors dry milled a mixture containing a pair of monometallic MOFs until no Bragg peaks were detectable by powder X-ray diffraction (PXRD). The amorphous matrix was then exposed to water vapors in an accelerated aging process[28] to obtain crystalline Al/Gd (1,4-naphthalenedicarboxylate). The alloying method was tested for several other archetypal MOFs, including MOF-74, ZIF-8, and HKUST-1. The results showed that the success of alloying largely depends on several parameters, including the ionic radii, coordination preferences, charge, electronegativity of the metal nodes, and the MOF topology. The other mechanochemical method is a two-step process involving monometallic coordination intermediates and ditopic ligands. To the best of our knowledge, it presents the only chemically controlled approach toward MM-MOFs reported to date, where the different reactivity of the functional groups on the ligand leads to controllable coordination and positioning of the two metals in the framework. This two-step mechanochemical strategy circumvented the issues related to solution synthesis, yielding a series of 12 porous, stable, and well-defined 1:1 binary MM-MOF-74 materials with pairs of main and transition metals.[29] In the first step, the first metal and H_4dobdc formed a precursor $[M(H_2dobdc)(solvent)]_n$ through coordination of the reactive carboxylate groups, while the second metal

activated the remaining phenolic groups to form highly porous and stable binary MM-MOF-74 products upon further milling, where the position of a particular metal is defined by the order of coordination. From this series, only one MOF has been tested for the real-world application so far. Though the monometallic zinc or copper MOF-74 materials were inactive, the mixed metal ZnCu-MOF-74 showed dramatically increased catalytic activity toward the selective catalytic formation of methanol from carbon dioxide based on a synergistic action among the zinc and copper nodes.[30]

As one of unique potential applications, the MM-MOF-74 allows for the systematic study of low-dimensional magnetism in multimetallic systems. These porous magnets have an advantage compared to inorganic materials, such as oxides and polymers, as the targeted synthesis leads to better control of the spatial arrangement and separation of magnetic centers and chains, which are much sought after for advanced applications. Metal nodes are organized into infinite and efficiently separated 1D chains, making MOF-74 probably the simplest realization of the 1D Ising model.[31] Until now, the magnetic properties of Fe-, Co-, and Ni-MOF-74 were studied, revealing a plethora of interesting phenomena such as solvent-exchange induced switching from ferromagnetic (FM) to an anti-ferromagnetic (AFM) state, metamagnetism, spin-crossover, and so forth.[20,32−38] To the best of our knowledge, only three heterometallic MOF-74 were studied, none with a defined metal distribution. Rubio-Giménez and coworkers studied the spontaneous magnetization of Ni-MOF-74 upon iron doping $(Ni_{1−x}Fe_x$-MOF-74, x = 4 or 6%)[35] The Zhao group investigated $Co_xFe_{1−x}$-MOF-74 for its catalytic activity with only electron spin resonance (ESR) spectra presented,[39] and recently, $Co_xNi_{1−x}$-MOF-74, where x = 0.752, 0.458, and 0.233, were reported.[40]

Here, we present the magnetic properties of three different binary multivariate MM-MOF-74 materials comprised of zinc(II) and copper(II) nodes in a 1:1 ratio (Figure 1b) prepared by different mechanochemical approaches and from different polymeric precursors. As the magnetic properties of monometallic Cu-MOF-74 are unknown, we first thoroughly characterized Cu-MOF-74, followed by the preparation of two bimetallic Cu/Zn materials by a template-controlled approach. Two different coordination M(H₂dobdc) polymers, [Cu-(H₂dobdc)(H₂O)₂]ₙ (Cu-INT) (Figure 1c) and [Zn-(H₂dobdc)(H₂O)₂]ₙ (Zn-INT) (Figure 1d), were used as the precursors in the preparation of CuZn-MOF-74 and ZnCu-MOF-74, respectively. A third mixed metal MOF, Zn/Cu-MOF-74-alloyed, was prepared by mechanical amorphization and then aging of the 1:1 mixture of monometallic Zn-MOF-74 and Cu-MOF-74 in methanol vapors. All products are highly crystalline, with similar PXRD diffractograms (Figures S2−S5) and Fourier transform infrared (FTIR) spectra (Figures S10−S13), and the similar molar ratio of two metals in the bulk sample was observed using flame atomic absorption spectroscopy (AAS). However, they show significant differences in their ESR spectra and static magnetization properties. ^{13}C magic angle spinning nuclear magnetic resonance (^{13}C MAS NMR) spectra, together with the scanning electron microscopy with energy-dispersive X-ray spectroscopy (EDAX/SEM) and *in situ* synchrotron PXRD monitoring[41,42] of the mechanochemical formation of MOFs, were used for estimating the local ordering of the metal nodes in the chains and the rationalization of differences in magnetic properties of the three materials.

■ RESULTS

In order to determine the magnetic properties of the monometallic Cu-MOF-74 and to see how copper dilution with zinc and distribution within the framework affect the magnetic properties of multivariate MOF-74 materials, we prepared Cu-MOF-74 by an adapted, recently described procedure.[30] Next, we prepared three multivariate MOF-74 materials that differ in synthetic pathways. The ZnCu-MOF-74 material was prepared in a step-wise manner following a previously described procedure.[29] In the first step, ZnO and H₄dobdc were milled together to form Zn-intermediate (Zn-INT, CCDC code: ODIPOH)[17,18] followed by introducing copper hydroxide in the second step, where the MOF-74 framework assembles upon further milling. The mechanochemical synthesis of the CuZn-MOF-74 material was designed in an analogous way, preparing the Cu-INT in the first step and adding ZnO in the second step, resulting in a crystalline CuZn-MOF-74 material. For the preparation of Zn/Cu-MOF-74-alloyed, a 1:1 mixture of crystalline Zn-MOF-74 and Cu-MOF-74 was milled, then dried and amorphized according to a recently described procedure.[30] The crystalline Zn/Cu-MOF-74-alloyed phase was obtained by aging of the amorphous mixture in methanol vapors. The details of the synthesis can be found in Section 1.1 of Supporting Information. The different prepared phases of three MM-MOF-74 are indistinguishable by PXRD (Figure 2a) and their FTIR spectra closely match (Figure 2b). In the spectra of MOF-74 materials, the free carboxyl group stretching band of H₄dobdc ligand around 1640 cm$^{−1}$ disappeared and was replaced by bands around 1550 and 1366 cm$^{−1}$, which correspond to the asymmetric and symmetric stretching of the coordinated carboxyl group, respectively, while the phenolic group stretching band shifted to 1246 cm$^{−1}$.[43] A certain amount of methanol remaining in the pores is manifested by a band at about 1025 cm$^{−1}$.[44] The molar ratio of the two metals in MM-MOF-74 materials is approximately 1:1, established on the basis of flame AAS and EDAX/SEM (Table S2).

While the Zn-INT, used in the preparation of ZnCu-MOF-74, was previously reported,[17,18] the Cu-INT detected in the first step of the two-step synthesis of CuZn-MOF-74 did not correspond to any known copper−H₄dobdc complex.[18] All attempts at solution synthesis and single crystal preparation of Cu-INT were unsuccessful due to its partial transformation into Cu-MOF-74 (Figure S1). The crystal structure of Cu-INT was, therefore, determined from room temperature PXRD data (Table S1), with the composition Cu(dobdc)(H₂O)₂ obtained through TGA analysis (Figures S7 and S8). The Cu-INT structure consists of square-pyramidally coordinated copper atoms, with two water molecules and two different dobdc molecules occupying the equatorial positions in a trans conformation, and a third dobdc molecule coordinated in the axial position (Figures 1c and S9a). Importantly, each dobdc molecule bridges three different copper centers, two through each carboxylic group (non-chelating, equatorial binding of Cu) and one through one of the hydroxyl groups (axial position of Cu). This is markedly distinct from both the previously reported Cu(dobdc)(H₂O)₂ compound (CCDC code: KUSNAQ)[18] and Zn-INT, where the hydroxyl groups of dobdc are uncoordinated, and the ligand is bound in a quasi-tetrahedral coordination (Figures 1d and S9b). For the full description of the Cu-INT crystal structure and the details of
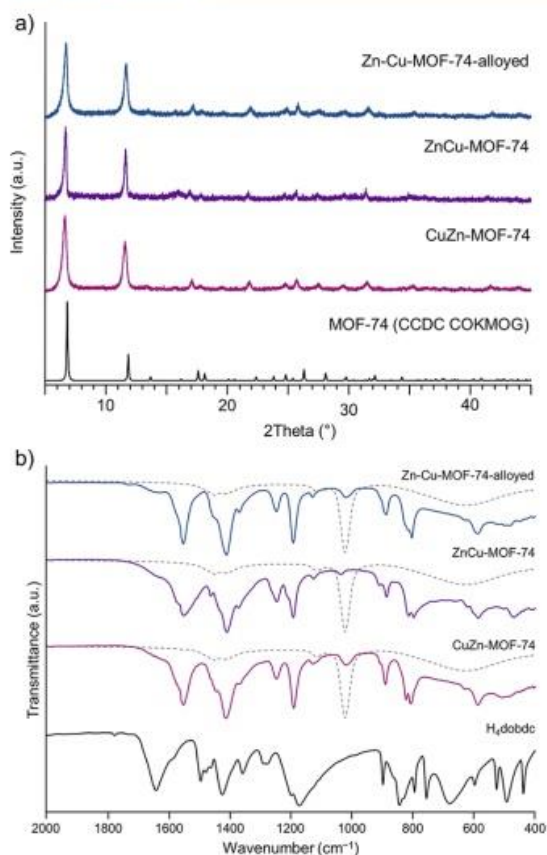
Figure 2. (a) PXRD patterns of mechanochemically synthesized bimetallic copper/zinc MOF-74 materials (Cu Kα radiation) compared to the simulated pattern of MOF-74 (CCDC code: COKMOG);[18,21] (b) FTIR spectra of mechanochemically synthesized bimetallic copper/zinc MOF-74 materials compared to the ligand H_4dobdc. Additional bands in the spectra are from residual MeOH (dashed line).

the structure solution, see Section 2.2 in Supporting Information.

■ MAGNETIC CHARACTERIZATION

Monometallic Cu-MOF-74 Sample. *ESR Study.* The temperature dependence of the X-band ESR and HF-ESR spectra of Cu-MOF-74 are shown in Figure 3a,b, respectively. The frequency *versus* resonance field dependence obtained in the HF-ESR measurements at $T = 4$ K is presented in the inset to Figure 3b together with characteristic HF-ESR spectra. The analysis of the spectral shape reveals that it is composed of two contributions, one corresponding to noninteracting, purely paramagnetic, and other corresponding to magnetically coupled spin species. With this assumption, the X-band spectrum at 10 K was successfully simulated by using the EasySpin software,[45] assuming spin-Hamiltonian with Zeeman and hyperfine terms

$$\mathbf{H} = \mu_B \mathbf{B} \cdot \mathbf{g} \cdot \mathbf{S} + \mathbf{S} \cdot \mathbf{A} \cdot \mathbf{I} \tag{1}$$
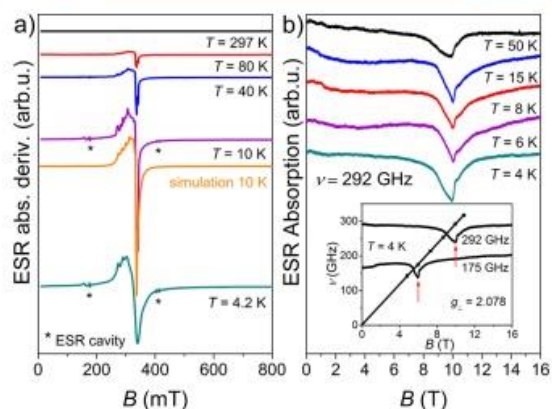
Figure 3. Temperature dependence of (a) X-band ESR spectra of the Cu-MOF-74 complex together with the simulated spectrum at 10 K and (b) HF-ESR spectra of this complex. The frequency *vs* resonance field diagram at 4 K for prominent points labeled by red arrows is shown in the inset to (b) together with exemplary HF-ESR spectra. Asterisks in panel (a) mark parasitic signals from the ESR cavity.

where $\mathbf{B}$ is the applied magnetic field, $\mathbf{g}$ is the g-tensor, $\mathbf{S}$ is the electron spin operator for copper spin ($S = 1/2$), μ_B is Bohr magneton, $\mathbf{A}$ is the hyperfine tensor, and $\mathbf{I}$ is the nuclear spin operator for copper ($I = 3/2$). Both copper species in Cu-MOF-74 can be simulated with the same spin-Hamiltonian parameters: $\mathbf{g} = [2.07\ 2.36]$ and $\mathbf{A} = [0\ 400]$ MHz but with different line-widths of assumed Lorentzian lines, one broader and one narrower for coupled and paramagnetic species, respectively. The used parameters of the simulation are given in Table S3, while the simulated spectrum at 10 K is presented in Figure 3a.

Magnetization Study. The field dependence of the magnetization $M(H)$ of Cu-MOF-74 at the lowest measured temperature of 1.8 K is shown in Figure 4a. Even at the highest applied field of 7 T, $M(H)$ is far from the expected saturation value $M_{sat} = ng\mu_B S$ (n is the number of magnetic moments per mole),[46] indicating a significant AFM interaction between the Cu spins in Cu-MOF-74. Namely, for one Cu(II) ion in a formula unit with $g = 2.171$ taken as the powder averaged g-factor $<g> = \sqrt{1/3(g_\parallel^2 + 2g_\perp^2)}$ from ESR results, M_{sat} should amount to 1.086 μ_B, but a much smaller value of 0.12 μ_B is observed.

This conclusion is corroborated on the quantitative level by the analysis of the temperature dependence of the magnetic susceptibility $\chi(T)$, presented in Figure 4b. Fitting of the $\chi(T)$ curve (in the range 100−300 K) with the Curie−Weiss law[47]

$$\chi = C/(T - \Theta) + \chi_0 \tag{2}$$

yields the Weiss temperature $\Theta \approx -55$ K and the Curie constant $C \approx 0.57$ erg K/(G^2 mol) (Table 1). Here, χ_0 is the temperature independent susceptibility. This value of C is somewhat larger than the expected Curie constant of the noninteracting Cu spins, $C = (n\mu_B^2 g^2 S(S + 1))/(3k_B) = 0.442$ erg K/(G^2 mol), where k_B is the Boltzmann constant.[46] Such an overestimate may be related to the large value of Θ, comparable to the temperatures of the fitting range, while, strictly speaking, eq 2 is applicable at T $\gg \Theta$, only. Indeed, the product $\chi(T)T$,
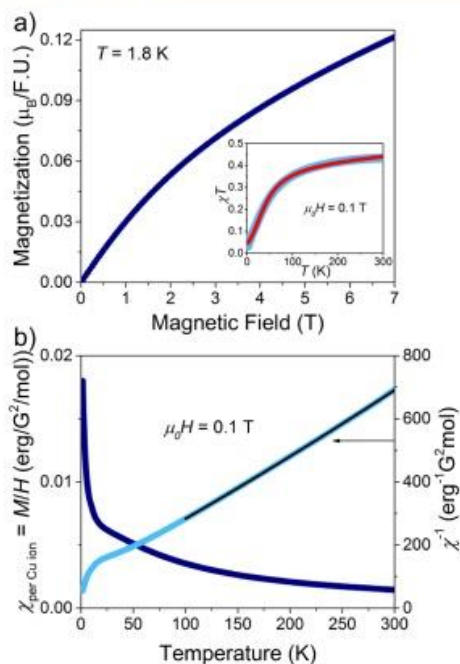
Figure 4. (a) Field dependence of the magnetization $M(H)$ of Cu-MOF-74 at $T = 1.8$ K. The inset shows the temperature dependence of the product $\chi(T)T$ in units of erg K/(G^2 mol). Red solid line represents the fit to the extended Bonner–Fisher model for $S = 1/2$ according to eqs S1 and S2. (b) Temperature dependence of the magnetic susceptibility $\chi(T)$ of Cu-MOF-74 and of its inverse $\chi^{-1}(T)$ measured in a field of 0.1 T. The black solid line is the fit to the Curie–Weiss law given by eq 2. The fitting results are presented in Table 1.

plotted in the inset to Figure 4a, is very small at low temperatures, as expected for the strong AFM coupling, and gradually increases to its temperature-independent limit $\chi(T)T \approx C$ by approaching room temperature, where it gives a more realistic estimate of $C \approx 0.433$ erg K/(G^2 mol).

Considering the chain structure of Cu-MOF-74 and the AFM type of the $M(H)$ and $\chi(T)$ dependences, the $\chi T(T)$ curve was fitted in the entire temperature range to the AFM spin-chain Bonner–Fisher model, including the interchain mean field correction eqs S1–S3.[48,49]

The fit result plotted as the red solid line in Figure 4a inset yielded the nearest neighbor intrachain AFM exchange constant $J \approx -57$ K and the residual inter-chain coupling $j \approx 7.5$ K. Also, the fit requires adding a Curie term C/T to

account for paramagnetic Cu ions around 9%. Such a significant amount of the "paramagnetic" Cu sites may originate from the boundaries of the nanometer-sized crystallites, usual for mechanochemical synthesis, and is in agreement with the value of 10% obtained from the ESR simulations (Table S3).

Bimetallic Cu/Zn-MOF-74 Samples. *ESR Study.* Experimental X-band ESR spectra of CuZn-MOF-74, ZnCu-MOF-74, and Zn/Cu-MOF-74-alloyed at different temperatures are shown in Figure 5a together with their simulations at $T = 10$ K made on the basis of the spin-Hamiltonian (eq 1) and under the assumption of the presence of a two-component spin system in these materials, similar to the analysis in the previous section. The spin-Hamiltonian parameters $g = [2.07\ 2.36]$ and $A = [0\ 400]$ MHz appeared to be the same as those used for the simulation of the Cu-MOF-74 ESR spectra, but with the different weights of the spectral components, linewidths, and g-strain values (Table S3).

The temperature dependence of the HF-ESR spectra of the investigated MOF samples is presented in Figure 5b. Lowering the temperature results in an increase of the spectral intensity, as expected, while the shape, width, and position of the lines do not change. The HF-ESR spectrum of ZnCu-MOF-74 exhibits a typical powder pattern with a peak and a shoulder corresponding to $g_\perp$ and $g_\parallel$, respectively. In contrast, the spectra of CuZn-MOF-74 and Zn/Cu-MOF-74-alloyed are single Lorentzian-shaped lines pointing at the presence of significant AFM interactions in these compounds, resulting in a well-known exchange narrowing effect.[50,51] These observations are in agreement with the magnetic susceptibility data (see below) and obtained Weiss parameters given in Table 1. The more narrow line of Zn/Cu-MOF-74-alloyed indicates a stronger AFM interaction, as compared to CuZn-MOF-74. The frequency dependence of the HF-ESR spectra of the mixed-metals MOFs was recorded at $T = 4$ K at several chosen frequencies from 142 to 317 GHz. The frequency *versus* resonant magnetic field diagram, together with the selected spectra, are shown in Figure S17 of SI. From this dependence, the approximate values of the g-factors were determined, and their values are presented in the insets of the respective graphs.[52–54]

Magnetization Study. The field dependence of the magnetization $M(H)$ of CuZn-MOF-74, ZnCu-MOF-74, and Zn/Cu-MOF-74-alloyed recorded at 1.8 K are shown in Figure 6a. The $M(H)$ curve of Cu-MOF-74, discussed in the previous section, is plotted in the same graph for comparison. One can notice that all three $M(H)$-curves of the mixed compounds are mutually different and also are very different from that of Cu-MOF-74. At the maximum magnetic field of 7 T, the magnetization is far from the saturation for all compounds

Table 1. Parameters of the Fit to the Curie–Weiss Law eq 2, Extended Bonner–Fisher Model eqs S1–S3, and Bleaney–Bowers Dimer Model eqs S4 and S5[a]

sample	temp. range Curie–Weiss	C (erg K/(G^2 mol))	Θ (K)	J/k_B (K)	j/k_B (K)	paramag. species %
Cu-MOF-74	100–300 K	0.5710(5)	−54.5(1)	−56.8(2)	7.5(3)	9.06(5)
CuZn-MOF-74	50–300 K	0.5150(3)	−18.70(5)	−36.0(3)	13.3(4)	33.5(1)
ZnCu-MOF-74	50–300 K	0.5050(2)	−1.81(3)	−11.19(1)		37.59(4)
Zn-Cu-MOF-74-alloyed	50–300 K	0.4660(1)	−19.51(1)			

[a]For details, see the main text and Supporting Information.
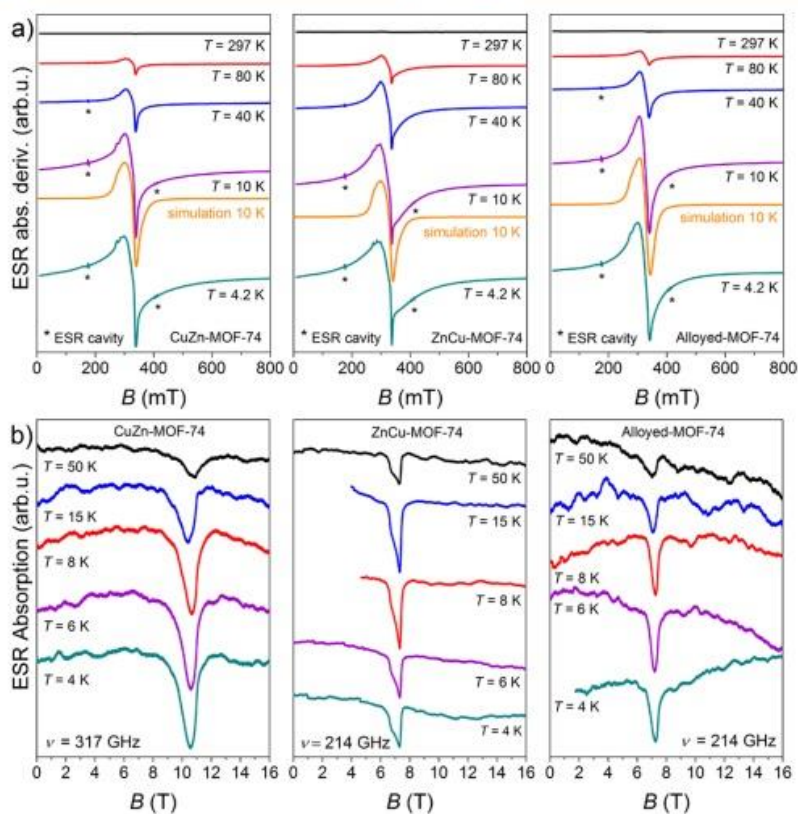
Figure 5. Temperature dependence of the ESR spectra of CuZn-MOF-74, ZnCu-MOF-74, and Zn-Cu-MOF-74-alloyed complexes. (a) X-band spectra together with the simulated spectra at 10 K. (b) HF-ESR spectra. Asterisks in panel (a) mark parasitic signals from the ESR cavity.
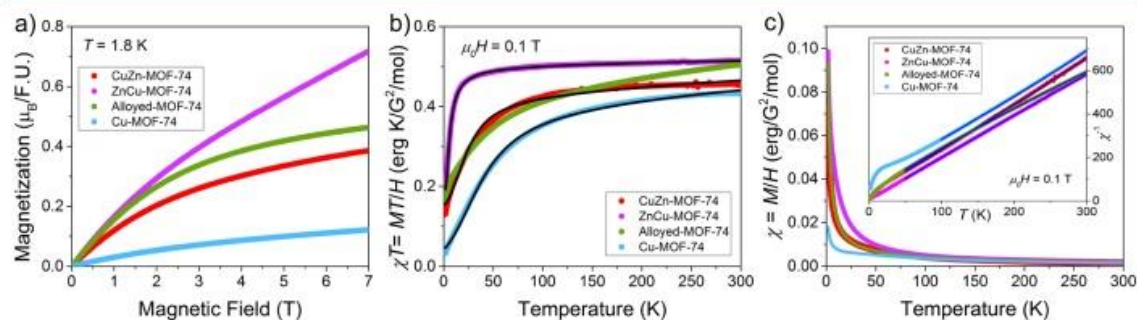
Figure 6. (a) Field dependence of the magnetization $M(H)$ of the mixed CuZn-MOF-74, ZnCu-MOF-74, and Zn/Cu-MOF-74-alloyed samples and of the monometallic Cu-MOF-74 at $T = 1.8$ K. (b) Temperature dependence of the magnetic susceptibility, $\chi(T)$, multiplied by T measured in a field of 0.1 T for the same samples. Black solid lines represent the fit to the extended Bonner–Fisher model for Cu-MOF-74 and CuZn-MOF-74 samples and the Bleaney–Bowers model for the ZnCu-MOF-74 sample. (c) Temperature dependence of $\chi(T)$ (main panel) and of its inverse $\chi^{-1}(T)$ (inset) of the same samples in a field of 0.1 T. Blue solid lines in the inset are the fits to the Curie–Weiss law according to eq 2.

pointing at the presence of significant AFM interactions in these materials.

It is interesting to note that the magnetization is lowest for the Cu-MOF-74 sample although it has two times more copper ions per formula unit as compared to mixed samples. This is in fact expected since, in Cu-MOF-74, the majority of the Cu ions are coupled into AFM spin-chains and only a small fraction remains "free", giving rise to the paramagnetic Curie

contribution to the sample's magnetization and susceptibility at low temperatures. The nonmagnetic dilution in the mixed MOF-74 systems increases the amount of paramagnetic spins, as compared to the monometallic version, and yields larger magnetization. If the Cu and Zn ions in a 1:1 proportion would randomly occupy the metal sites in the structure, all three $M(H)$ curves should overlap. It is clear from Figure 6a that this is not the case. Obviously, a random distribution is

not achieved in the mixed samples and, depending on the synthetic route, various types of spin clustering may take place, which is also reflected in a distinct behavior of the magnetic susceptibility $\chi(T)$.

The temperature dependence of the product $\chi(T)T$ and $\chi(T)$ for all three mixed samples are presented in Figure 6b,c, respectively, along with the respective curves for the monometallic Cu-MOF-74 sample, scaled by a factor of 0.5 to account for the presence of two copper ions in the formula unit. The high temperature part (50−300 K) of the $\chi(T)$ dependence can be fitted to the Curie−Weiss law (eq 2), as shown in the inset to Figure 6c, with the parameters listed in Table 1. The weakening of the average AFM interactions due to nonmagnetic dilution is reflected in the reduction of the Weiss temperature Θ. Still, the numbers obtained should be considered only as an order of magnitude estimate due to the complexity of the spin structures in the mixed compounds, as discussed below.

At room temperature, the product χT for the mixed ZnCu-MOF-74 and Zn/Cu-MOF-74-alloyed complexes exceeds the ideal value $\chi(T)T \approx C = 0.442$ erg K/(G² mol) expected for an equal amount of the Cu and Zn ions, suggesting the slight excess of the magnetic Cu ions in these samples. As the EDAX/SEM and AAS analyses (Table S2) both show almost identical metal composition in all samples, this difference likely stems from the unequal composition of the guests in pores of these molecular sponges, where the water and methanol may exchange, thus slightly changing the molar mass of materials and influencing the absolute values of magnetic susceptibility.

As discussed in the previous section, a strong reduction of the product $\chi(T)T$ at low temperatures for the monometallic Cu-MOF-74 sample is due to a significant AFM interaction between the majority of the Cu ions arranged into the spin-chains, whereas noninteracting, paramagnetic Cu ions are present in a relatively small amount of 9−10% only. An appreciable increase of $\chi(T)T$ at low T for the mixed samples indicates fragmentation of the AFM spin-chains into shorter segments and a corresponding increase of the concentration of uncompensated spins up to 30−40%, in agreement with the values obtained from ESR simulations ∼30% (Table S3).

Theoretical Models. In addition to the standard Curie−Weiss model used, by comparing the shapes of the $\chi(T)T$ curves, it is possible to derive some qualitative conclusions on the feasible spin arrangements in the mixed compounds. The $\chi(T)T$ dependence for CuZn-MOF-74 is most similar to that for Cu-MOF-74. This suggests that the synthetic route of CuZn-MOF-74 is as follows: first the Cu ions form the AFM spin-chains, which the Zn ions then break into segments of different lengths. In contrast, it seems that the synthetic route of ZnCu-MOF-74 is as follows: first, the nonmagnetic Zn chains are formed, and then, Cu ions break their continuity, yielding spin monomers (paramagnetic centers), spin dimers, or some short spin-chain segments.

In view of the various types of the Cu/Zn site disorder present in the mixed CuZn-MOF-74 and ZnCu-MOF-74 complexes, it is not feasible to define a unique microscopic spin interaction model, which would enable a unified fitting of the measured susceptibility curves of these compounds. The magnetic behavior of the CuZn-MOF-74 complex is qualitatively closest to its monometallic counterpart, Cu-MOF-74, suggesting applicability of the extended AFM spin-chain Bonner−Fisher model to CuZn-MOF-74 (eqs S1−S3). Indeed, its $\chi(T)T$ dependence can be reasonably well fitted to

this model, yielding the intrachain exchange constant $J \approx -36$ K and the positive inter-chain exchange constant $j \approx 13$ K (Figure 6b). This result shows that the AFM interaction within the chain segments is weakened in comparison to Cu-MOF-74, and there is an appreciable effective FM interaction between these segments.

The $\chi T(T)$ curve for ZnCu-MOF-74 is more reminiscent of that for spin dimers and, in fact, the Bleaney−Bowers AFM dimer model (eqs S4 and S5) nicely reproduces the experimental dependence with the intradimer exchange constant $J \approx -11$ K (Figure 6b).[49,55] Nevertheless, the presence of more extended spin clusters, for example, trimers and tetramers, in this compound cannot be excluded.

The alloyed compound shows a completely different magnetic behavior as compared with both ZnCu- and CuZn-MOF-74. Presumably, the Cu-based spin system of this compound is composed of spin-chain fragments with a distribution of the superexchange interaction strengths, and therefore, a reasonable physical model here could not be performed. An indication for that is a continuous increase of the product $\chi(T)T$ even above the room temperature, despite a rather small value of Θ derived from the Curie−Weiss fit (Table 1). This behavior above 100 K is very similar to the behavior of Cu-MOF-74 curve, but disagreement between these two curves could be seen in the low-temperature region, due to different magnetic compositions.

■ SOLID-STATE NMR

Solid-state NMR spectroscopy can often provide additional insight into the local structure of solids; therefore, ¹³C MAS NMR spectra of CuZn-MOF-74, ZnCuMOF-74, and Zn/Cu-MOF-74-alloyed were recorded and compared to the spectra of pure crystalline Cu-MOF-74 and Zn-MOF-74 (Figure 7). The spectra of CuZn-MOF-74 and ZnCuMOF-74 are very similar to one another. They both show a high, sharp signal of methanol molecules at about 50 ppm, and a large number of broad signals with isotropic shifts ranging from about −100 to 700 ppm. Large positive and negative isotropic shifts are typical for carbon nuclei in close proximity to paramagnetic centers. The fact that the signals do not appear only at shifts characteristic for either Cu-MOF-74 or Zn-MOF-74 suggests that carbon nuclei within these two samples experience many different environments—most probably because the dobdc linkers of the MOF-74 framework connect not only the metal nodes of a single type but also the metal nodes of two different types (i.e., dobdc linkers can be bound to various numbers of Cu and Zn centers). In other words, the large number of signals and the spread of their isotropic chemical shifts suggest that in CuZn-MOF-74 and ZnCuMOF-74, copper and zinc atoms are mixed within the frameworks on the (sub)-nanometer scale.

The ¹³C MAS NMR spectrum of Zn/Cu-MOF-74-alloyed is different from the spectra of the above-described mixed-metal samples and strongly suggests that the alloyed sample is a physical mixture of Cu-MOF-74 and Zn-MOF-74 particles or is built of large copper-based and zinc-based domains. In the spectrum of Zn/Cu-MOF-74-alloyed, we can see strong sharp signals at 174, 157, 128, and 126 ppm, which are typical for neat Zn-MOF-74, and broad signals at about 500 and −60 ppm, which very much resemble the signals of neat Cu-MOF-74. The signal of the C3 carbon nuclei, which can be found at 90 ppm in the spectrum of neat Cu-MOF-74, is shifted in the spectrum of the alloyed sample and overlaps with the sharp
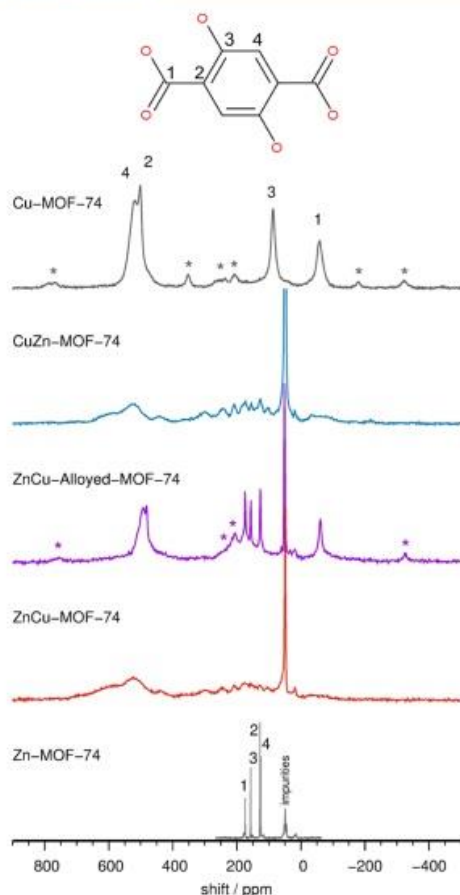
Figure 7. ¹³C MAS NMR spectra of mixed-metal CuZn-MOF-74, ZnCu-MOF-74, and Zn-Cu-MOF-74-alloyed compared to the spectra of neat Cu-MOF-74 and Zn-MOF-74. Assignment of the carbon NMR signals of Zn-MOF-74 is based on the solution spectrum of H₂dobdc, whereas the assignment of the carbon NMR signals of Cu-MOF-74 is based on ¹³C spin-lattice relaxation measurements and density functional theory-based calculations of hyperfine coupling constants.[56] Asterisks denote spinning sidebands.

signal of the zinc-based particles and the spinning sidebands of the signals of the copper-based particles in the range between 170 and 210 ppm. Taking into account that Zn/Cu-MOF-74-alloyed contains a large amount of methanol molecules or methoxy species, such a shift is not surprising—even subtle changes of the local environment of copper centers can lead to notable changes in the magnitude of the hyperfine coupling between the unpaired electrons of Cu(II) and the ¹³C nuclei and thus in the isotropic shift of these nuclei.

■ EDAX/SEM ANALYSIS

Elemental maps obtained by EDAX/SEM analysis indicate homogenous distribution of Cu and Zn throughout the selected areas of the CuZn-MOF-74 and ZnCu-MOF-74 samples, respectively (Figures S14 and S15), with Cu/Zn molar ratios of approximately 0.95 in both cases (Table S2). On the other hand, in spite of slightly lower Zn content (Cu/Zn = 1.03), the agglomerates of Zn/Cu-MOF-74-alloyed

sample contain some Zn-rich domains/grains, implying lower homogeneity of the distributed metal cations (Figure S16). These results are in line with the metal ratios determined in bulk samples using flame AAS.

Real-Time *in situ* Monitored Syntheses. To gain insight into the mechanism of mechanochemical synthesis of copper/zinc MOF-74 materials and to rationalize the observed differences in the magnetic properties of these materials, as well as the differences compared to monometallic Cu-MOF-74, we designed several real-time *in situ* PXRD monitoring experiments and carried them out at the Deutsches Elektronen-Synchrotron (DESY), described in SI. For *in situ* PXRD monitoring experiments, pre-prepared intermediates Zn-INT and Cu-INT were used to not only closely mimic the two-step synthetic route but also simplify the studied system.

ZnCu-MOF-74. In situ PXRD monitoring of the synthesis of ZnCu-MOF-74 was performed by milling Zn-INT and Cu(OH)₂ in a 1:1 stoichiometric ratio with the addition of a small amount of MeOH. Intensities of the reflections of the reactants decrease within the first few minutes of milling. The reflections of MOF-74 appear 6 min from the onset of milling, along with those of UTSA-74,[57] a recently discovered high-temperature MOF-74 polymorph. This phase forms jointly with the MOF-74 phase and transforms to pure ZnCu-MOF-74 after an additional 10 min of milling (Figure 8a).

CuZn-MOF-74. Next, CuZn-MOF-74 was prepared by milling Cu-INT and ZnO in a 1:1 stoichiometric ratio, with the addition of a small amount of MeOH. Within 5 min from the start of milling, the reflections of MOF-74 start to appear, and after 10 min, the peaks of Cu-INT disappear completely (Figure 8b). Unlike Cu-INT, the consumption of ZnO is gradual and slower, and the reflections of ZnO are detectable for further 15 min after milling (Figure S18).

Zn/Cu-MOF-74-one-step. To establish the reactivity and affinity of the two metal sources for the binding to H₄dobdc, we explored the mechanochemical formation of zinc/copper MOF-74 by performing the milling of ZnO, Cu(OH)₂, and H₄dobdc in a 1:1:1 stoichiometric ratio with the addition of small amounts of H₂O and MeOH. During the first minute of the synthesis, a new phase is detected. MOF-74 reflections are observed after 8 min milling, and after 25 min, MOF-74 is the only observable crystalline phase (Figure 8c). We identified the unknown phase to be a mixture of three copper H₂dobdc complexes: *cis*-[Cu(H₂dobdc)(H₂O)₂] (CCDC code: KUS-NAQ),[18] *trans*-[Cu(H₂dobdc)(H₂O)₂] (Cu-INT, identified in this study), and a copper complex with H₂dobdc (of yet unknown structure) that can be prepared by milling Cu(OH)₂ and H₄dobdc in a 1:1 stoichiometric ratio using excess MeOH as a liquid additive (Figure S19).

■ DISCUSSION

Mechanochemical procedures are now well known for their high level of stoichiometric control and the ability to open pathways toward unique products, as was also the case with the bimetallic MOF-74 materials.[29] *In situ* PXRD monitoring shows that the Zn-INT to ZnCu-MOF-74 transformation occurs as a multistep process through the transient UTSA-74 phase[57] (Figure 8a). The reaction happens without any observable transformation of the Zn-INT to Cu-INT phase, indicating that the copper did not exchange the zinc from the carboxylate sites. Together with the results of solid-state NMR and magnetic studies, one can assume that this process includes the incorporation of copper atoms at available free metal sites,
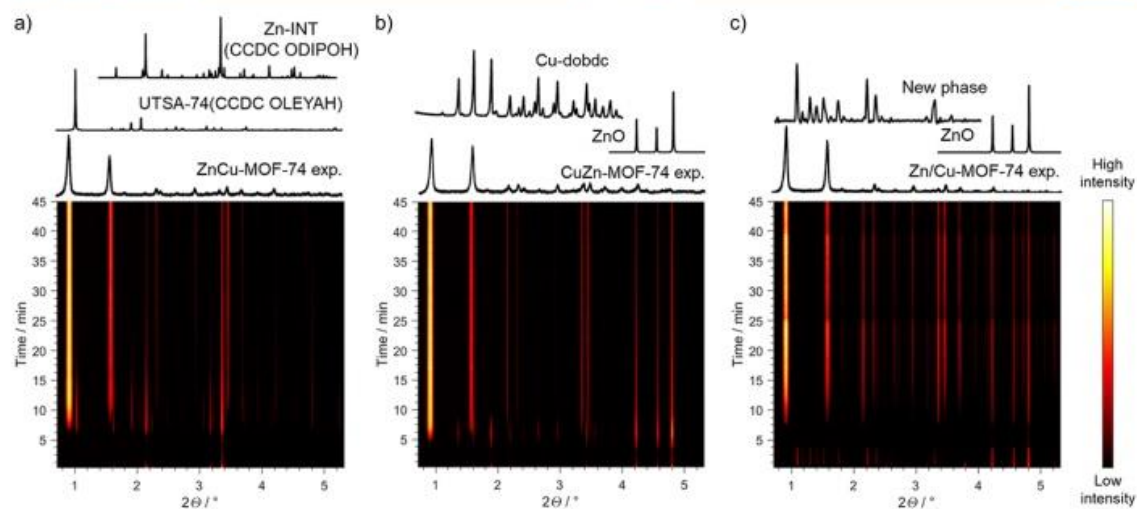
Figure 8. (a) Time-resolved diffractograms from the in situ and real-time monitoring of the synthesis of ZnCu-MOF-74 from $[Zn(H_2dobdc)(H_2O)_2]$ and $Cu(OH)_2$ by LAG (MeOH). (b) Time-resolved diffractograms for the synthesis of CuZn-MOF-74 from $[Cu(H_2dobdc)(H_2O)_2]$ and ZnO by LAG (MeOH). (c) Time-resolved diffractograms for the synthesis of Zn/Cu-MOF-74 from ZnO, $Cu(OH)_2$, and H_4dobdc by LAG (H_2O, MeOH). Diffraction patterns of observed crystalline phases are given on the top. X-ray beam: $E \approx 60$ keV, $\lambda = 0.20735$ Å.

leading to a homogeneous distribution of copper nodes in the oxo-chains of the MOF and the most paramagnetic-like behavior in comparison with the remaining two materials.

The slower consumption of ZnO in the formation of CuZn-MOF-74 from the Cu-INT, compared to the MOF-74 formation (Figures 8b and S18), is indicative of a process where the copper(II) nodes from the Cu-INT partially react into the Cu-MOF-74, as was already observed during the crystallization of Cu-INT in methanol, unlike the zinc analogue. The higher reactivity of the Cu(II) for the dobdc ligand is corroborated by the monitoring of the formation of copper/zinc MOF-74 from the mixture of ZnO and $Cu(OH)_2$, where different copper intermediate phases are formed (Figures 8c and S19). The different reactivity and affinity of two metals for the dobdc ligand, and the unique structure of the Cu-INT, where even the less reactive phenolic groups coordinate the copper node, may explain the differences between the different structures of the oxometallic chains and the magnetic properties of the three tested copper/zinc MOFs. The higher reactivity of copper, even for phenolic groups, will induce the formation of longer chains containing exclusively the copper nodes for the CuZn-MOF-74. The efficient dispersion of copper nodes in the ZnCu-MOF-74 results in higher magnetization than Cu-MOF-74, despite ZnCu-MOF-74 containing half the copper(II) nodes. It reveals that the copper is not exchanging the zinc node coordinated to carboxylate. It rather coordinates the remaining phenolic groups, leading to the observed magnetic properties of the ZnCu-MOF-74.

Another exciting observation is the short occurrence of the fleeting UTSA-74 polymorph, which is most likely a mixed-metal phase. UTSA-74 emerged only in a few instances until now, showing new and exciting properties compared to MOF-74. The possibility to form the mixed-metal UTSA-74 may expand the application potential for these two MOF polymorphs.

■ CONCLUSIONS

The presented magnetic analysis shows that magnetically active nodes can be efficiently dispersed in the bimetallic copper/zinc-MOF-74 material, leading to the different magnetic properties, as compared to the monometallic Cu-MOF-74. Cu-MOF-74 can be described, using the extended Bonner−Fisher model, as AFM copper chains ($J \approx -57$ K) with weaker interchain ferromagnetic interaction ($j \approx 7.5$ K). This is an interesting result as all the other known magnetic MOFs-74, Co-MOF-74, Fe-MOF-74, and Ni-MOF-74, containing nodes with spin higher than 1/2, have ferromagnetically coupled metal ions inside the oxo-chains, while the interchain interactions are AFM.[20,32,37,38] Small changes in spin states and magnetic anisotropy, as well as subtle structural changes, led to substantially different magnetic behaviors. Combined with the open coordination sites on the metal nodes present in the 1D oxometallic chains, this makes the MOF-74 family a particularly interesting platform for the investigation of low-dimensional magnetism in MOFs.

Although mixed-metal MOFs have almost indistinguishable PXRD and FTIR, different magnetic behaviors reveal different interactivity of copper(II) and zinc(II) ions inside MOF structures. CuZn-MOF-74, obtained *via* the new complex Cu-INT, can be described as a combination of isolated paramagnetic copper species and longer copper−copper associations; CuZn-MOF-74 can be described similar to monometallic Cu-MOF-74 using the extended Bonner−Fisher model but with the reduced strength of intrachain coupling ($J \approx -36$ K) and FM interchain interaction ($j \approx 13$ K). On the other hand, ZnCu-MOF-74, obtained *via* the Zn-INT complex, can be described as a combination of well-isolated paramagnetic copper species and short copper dimers fitted by the Bleaney−Bowers model ($J \approx -11$ K). According to magnetic, EDAX/SEM, and SS NMR results, the alloyed sample seemed to be predominantly a physical mixture of Cu-MOF-74 and Zn-MOF-74 domains, with mixed phases on the grain

interfaces. Our results also show that the application of MOFs as real system magnets will be in part complicated by the hard-to-control content of the pores. The dynamic exchange of the solvent in pores with the atmosphere will influence the absolute magnetization values due to the change in the molar mass of the compound.

Performing real-time *in situ* synchrotron PXRD monitored synthesis, the obtained difference is rationalized with different copper *versus* zinc reactivity and the affinity of the copper or zinc toward the functional groups of the ligand. Although the mechanochemical procedure offers an unprecedented level of control in the synthesis of bimetallic MOFs from monometallic coordination polymers, the synthetic process still relies on the nature and affinity of the chemical species at hand. The experimentalist must take into account, in the future design and production of bimetallic MOF-74 materials, not only parameters such as the structure of the coordination polymer reactant and the reactivity of the metal nodes for the particular binding group on the ligand but also the order in which the two metals are added into the reaction. In the presented case, zinc is strongly bound in Zn-INT, resulting in an efficient dispersion and isolation of paramagnetic copper nodes added in the second synthetic step. On the other hand, the high reactivity of Cu(II) for H_4dobdc leads to the formation of directly bound longer copper-chain clusters in the formed material and different magnetic properties.

We will now focus on determining magnetic properties for new bimetallic MOF-74 materials containing pairs of paramagnetic centers such as Co(II), Mn(II), Fe(II), Ni(II), and Cu(II) to explore the magnetic properties in these materials stemming from close contacts and interactions between centers with different spin states. We also aim to tune the synthetic parameters toward the stabilization of the bimetallic UTSA-74 polymorph, which would present a particularly interesting class of magnetic compounds.

■ ASSOCIATED CONTENT

ⓈI Supporting Information

The Supporting Information is available free of charge at https://pubs.acs.org/doi/10.1021/acs.inorgchem.2c02898.

> Additional experimental details, materials and methods, PXRD, TGA, FTIR, AAS, EDAX/SEM, magnetization and ESR results (PDF)

Accession Codes

CCDC 2174976 contains the supplementary crystallographic data for this paper. These data can be obtained free of charge via www.ccdc.cam.ac.uk/data_request/cif, or by emailing data_request@ccdc.cam.ac.uk, or by contacting The Cambridge Crystallographic Data Centre, 12 Union Road, Cambridge CB2 1EZ, UK; fax: +44 1223 336033.

■ AUTHOR INFORMATION

Corresponding Authors

Dijana Žilić − *Ruđer Bošković Institute, 10000 Zagreb, Croatia;* ⦾ orcid.org/0000-0003-2387-0853; Email: dijana.zilic@irb.hr

Krunoslav Užarević − *Ruđer Bošković Institute, 10000 Zagreb, Croatia;* ⦾ orcid.org/0000-0002-7513-6485; Email: krunoslav.uzarevic@irb.hr

Authors

Senada Muratović − *Ruđer Bošković Institute, 10000 Zagreb, Croatia;* ⦾ orcid.org/0000-0001-5027-9191

Valentina Martinez − *Ruđer Bošković Institute, 10000 Zagreb, Croatia*

Bahar Karadeniz − *Ruđer Bošković Institute, 10000 Zagreb, Croatia*

Damir Pajić − *Faculty of Science, Department of Physics, University of Zagreb, 10000 Zagreb, Croatia;* ⦾ orcid.org/0000-0002-4907-7290

Ivana Brekalo − *Ruđer Bošković Institute, 10000 Zagreb, Croatia;* ⦾ orcid.org/0000-0002-0309-5610

Mihails Arhangelskis − *Faculty of Chemistry, University of Warsaw, 02-093 Warsaw, Poland;* ⦾ orcid.org/0000-0003-1150-3108

Matjaž Mazaj − *National Institute of Chemistry, SI-1001 Ljubljana, Slovenia;* ⦾ orcid.org/0000-0003-3196-9079

Gregor Mali − *National Institute of Chemistry, SI-1001 Ljubljana, Slovenia;* ⦾ orcid.org/0000-0002-9012-2495

Martin Etter − *Deutsches Elektronen-Synchrotron DESY, D-22607 Hamburg, Germany*

Tomislav Friščić − *McGill University, Montreal, Quebec H3A 0B8, Canada;* ⦾ orcid.org/0000-0002-3921-7915

Yulia Krupskaya − *Leibniz IFW Dresden, D-01069 Dresden, Germany*

Vladislav Kataev − *Leibniz IFW Dresden, D-01069 Dresden, Germany;* ⦾ orcid.org/0000-0003-2147-2616

Complete contact information is available at:
https://pubs.acs.org/10.1021/acs.inorgchem.2c02898

Author Contributions

Notes

The authors declare no competing financial interest.

■ ACKNOWLEDGMENTS

Dissertation supplement

■ REFERENCES

(1) Li, H.; Eddaoudi, M.; O'Keeffe, M.; Yaghi, O. M. Design and synthesis of an exceptionally stable and highly porous metal-organic framework. *Nature* **1999**, *402*, 276−279.

(2) Rosi, N. L.; Kim, J.; Eddaoudi, M.; Chen, B.; O'Keeffe, M.; Yaghi, O. M. Rod Packings and Metal−Organic Frameworks Constructed from Rod-Shaped Secondary Building Units. *J. Am. Chem. Soc.* **2005**, *127*, 1504−1518.

(3) Zhou, H.-C.; Long, J. R.; Yaghi, O. M. Introduction to Metal-Organic Frameworks. *Chem. Rev.* **2012**, *112*, 673−674.

(4) Mínguez Espallargas, G.; Coronado, E. Magnetic functionalities in MOFs: from the framework to the pore. *Chem. Soc. Rev.* **2018**, *47*, 533−557.

(5) Thorarinsdottir, A. E.; Harris, T. D. Metal-Organic Framework Magnets. *Chem. Rev.* **2020**, *120*, 8716−8789.

(6) Abednatanzi, S.; Gohari Derakhshandeh, P. G.; Depauw, H.; Coudert, F.-X.; Vrielinck, H.; Van Der Voort, P.; Leus, K. Mixed-metal metal-organic frameworks. *Chem. Soc. Rev.* **2019**, *48*, 2535−2565.

(7) Masoomi, M. Y.; Morsali, A.; Dhakshinamoorthy, A.; Garcia, H. Mixed-Metal MOFs: Unique Opportunities in Metal-Organic Framework (MOF) Functionality and Design. *Angew. Chem., Int. Ed.* **2019**, *58*, 15188−15205.

(8) Viciano-Chumillas, M.; Liu, X.; Leyva-Pérez, A.; Armentano, D.; Ferrando-Soria, J.; Pardo, E. Mixed component metal-organic frameworks: Heterogeneity and complexity at the service of application performances. *Coord. Chem. Rev.* **2022**, *451*, 214273.

(9) Guo, W.; Xia, W.; Cai, K.; Wu, Y.; Qiu, B.; Liang, Z.; Qu, C.; Zou, R. Kinetic-Controlled Formation of Bimetallic Metal-Organic Framework Hybrid Structures. *Small* **2017**, *13*, 1702049.

(10) Kalaj, M.; Cohen, S. M. Postsynthetic Modification: An Enabling Technology for the Advancement of Metal-Organic Frameworks. *ACS Cent. Sci.* **2020**, *6*, 1046−1057.

(11) Santaclara, J. G.; Olivos-Suarez, A. I.; Gonzalez-Nelson, A.; Osadchii, D.; Nasalevich, M. A.; van der Veen, M. A.; Sheveleva, F.; Veber, A. M.; Fedin, S. L.; Murray, M. V.; Hendon, A. T.; Walsh, C. H.; Gascon, A.; Gascon, J. Revisiting the Incorporation of Ti(IV) in UiO-type Metal-Organic Frameworks: Metal Exchange versus Grafting and Their Implications on Photocatalysis. *Chem. Mater.* **2017**, *29*, 8963−8967.

(12) Garai, B.; Bon, V.; Krause, S.; Schwotzer, F.; Gerlach, M.; Senkovska, I.; Kaskel, S. Tunable Flexibility and Porosity of the Metal-Organic Framework DUT-49 through Postsynthetic Metal Exchange. *Chem. Mater.* **2020**, *32*, 889−896.

(13) Lalonde, M.; Bury, W.; Karagiaridi, O.; Brown, Z.; Hupp, J. T.; Farha, O. K. Transmetalation: routes to metal exchange within metal-organic frameworks. *J. Mater. Chem. A* **2013**, *1*, 5453−5468.

(14) Nouar, F.; Devic, T.; Chevreau, H.; Guillou, N.; Gibson, E.; Clet, G.; Daturi, M.; Vimont, A.; Grenèche, J. M.; Breeze, M. I.; Walton, R. I.; Llewellyn, P. L.; Serre, C. Tuning the breathing behaviour of MIL-53 by cation mixing. *Chem. Commun.* **2012**, *48*, 10237−10239.

(15) Caskey, S. R.; Matzger, A. J. Selective Metal Substitution for the Preparation of Heterobimetallic Microporous Coordination Polymers. *Inorg. Chem.* **2008**, *47*, 7942−7944.

(16) Wang, Y.; Bredenkötter, B.; Rieger, B.; Volkmer, D. Two-dimensional metal-organic frameworks (MOFs) constructed from heterotrinuclear coordination units and 4,4'-biphenyldicarboxylate ligands. *Dalton Trans.* **2007**, 689−696.

(17) Ghermani, N. E.; Morgant, G.; d'Angelo, J.; Desmaële, D.; Fraisse, B.; Bonhomme, F.; Dichi, E.; Sgahier, M. Covalently bonded infinite zigzag chain structure in a novel Zn(II) complex of 2,5-dihydroxy-1,6-benzenedicarboxylic acid. *Polyhedron* **2007**, *26*, 2880−2884.

(18) Groom, C. R.; Bruno, I. J.; Lightfoot, M. P.; Ward, S. C. The Cambridge Structural Database. *Acta Crystallogr.* **2016**, *72*, 171−179.

(19) Li, H.; Yang, Z.; Lu, S.; Su, L.; Wang, C.; Huang, J.; Zhou, J.; Tang, J.; Huang, M. Nano-porous bimetallic CuCo-MOF-74 with coordinatively unsaturated metal sites for peroxymonosulfate activation to eliminate organic pollutants: Performance and mechanism. *Chemosphere* **2021**, *273*, 129643.

(20) Dietzel, P. D. C.; Morita, Y.; Blom, R.; Fjellvåg, H. An In Situ High-Temperature Single-Crystal Investigation of a Dehydrated Metal-Organic Framework Compound and Field-Induced Magnetization of One-Dimensional Metal-Oxygen Chains. *Angew. Chem., Int. Ed.* **2005**, *44*, 6354−6358.

(21) Queen, W. L.; et al. Comprehensive study of carbon dioxide adsorption in the metal-organic frameworks M2(dobdc) (M = Mg, Mn, Fe, Co, Ni, Cu, Zn). *Chem. Sci.* **2014**, *5*, 4569−4581.

(22) Xiao, T.; Liu, D. The most advanced synthesis and a wide range of applications of MOF-74 and its derivatives. *Microporous Mesoporous Mater.* **2019**, *283*, 88−103.

(23) Lee, K.; Howe, J. D.; Lin, L.-C.; Smit, B.; Neaton, J. B. Small-Molecule Adsorption in Open-Site Metal-Organic Frameworks: A Systematic Density Functional Theory Study for Rational Design. *Chem. Mater.* **2015**, *27*, 668−678.

(24) Sun, D.; Sun, F.; Deng, X.; Li, Z. Mixed-Metal Strategy on Metal-Organic Frameworks (MOFs) for Functionalities Expansion: Co Substitution Induces Aerobic Oxidation of Cyclohexene over Inactive Ni-MOF-74. *Inorg. Chem.* **2015**, *54*, 8639−8643.

(25) Wang, H.; Deng, J.; Furukawa, H.; Gándara, H.; Cordova, F.; Peri, K. E.; Yaghi, D.; Yaghi, O. M. Synthesis and Characterization of Metal-Organic Framework-74 Containing 2, 4, 6, 8, and 10 Different Metals. *Inorg. Chem.* **2014**, *53*, 5881−5883.

(26) Ji, Z.; Li, T.; Yaghi, O. M. Sequencing of metals in multivariate metal-organic frameworks. *Science* **2020**, *369*, 674−680.

(27) Panda, T.; Horike, S.; Hagi, K.; Ogiwara, N.; Kadota, K.; Itakura, T.; Tsujimoto, M.; Kitagawa, S. Mechanical Alloying of Metal-Organic Frameworks. *Angew. Chem., Int. Ed.* **2017**, *56*, 2413−2417.

(28) Cliffe, C.; Mottillo, J. .; Stein, R. S.; Bučar, R. S.; Friščić, D.-K.; Friščić, T. Accelerated aging: a low energy, solvent-free alternative to solvothermal and mechanochemical synthesis of metal-organic materials. *Chem. Sci.* **2012**, *3*, 2495−2500.

(29) Ayoub, G.; Karadeniz, B.; Howarth, A. J.; Farha, O. K.; Ðilović, I.; Germann, L. S.; Dinnebier, R. E.; Užarević, K.; Friščić, T. Rational Synthesis of Mixed-Metal Microporous Metal-Organic Frameworks with Controlled Composition Using Mechanochemistry. *Chem. Mater.* **2019**, *31*, 5494−5501.

(30) Stolar, T.; Prašnikar, A.; Martinez, V.; Karadeniz, B.; Bjelić, A.; Mali, G.; Friščić, T.; Likozar, B.; Užarević, K. Scalable Mechanochemical Amorphization of Bimetallic Cu−Zn MOF-74 Catalyst for Selective CO2 Reduction Reaction to Methanol. *ACS Appl. Mater. Interfaces* **2021**, *13*, 3070−3077.

(31) Canepa, P.; Chabal, Y. J.; Thonhauser, T. When metal organic frameworks turn into linear magnets. *Phys. Rev. B: Condens. Matter Mater. Phys.* **2013**, *87*, 094407.

(32) Bloch, E. D.; Queen, W. L.; Krishna, R.; Zadrozny, J. M.; Brown, C. M.; Long, J. R. Hydrocarbon Separations in a Metal-Organic Framework with Open Iron(II) Coordination Sites. *Science* **2012**, *335*, 1606−1610.

(33) Kim, H.; Park, J.; Jung, Y. The binding nature of light hydrocarbons on Fe/MOF-74 for gas separation. *Phys. Chem. Chem. Phys.* **2013**, *15*, 19644−19650.

(34) Park, J.; Kim, H.; Jung, Y. Origin of Selective Guest-Induced Magnetism Transition in Fe/MOF-74. *J. Phys. Chem. Lett.* **2013**, *4*, 2530−2534.

(35) Rubio-Giménez, V.; Waerenborgh, J. C.; Clemente-Juan, J. M.; Martí-Gastaldo, C. Spontaneous Magnetization in Heterometallic NiFe-MOF-74 Microporous Magnets by Controlled Iron Doping. *Chem. Mater.* **2017**, *29*, 6181−6185.

(36) Son, K.; Kim, J. Y.; Schütz, G.; Kang, S. G.; Moon, H. R.; Oh, H. Coordinated Molecule-Modulated Magnetic Phase with Metamagnetism in Metal-Organic Frameworks. *Inorg. Chem.* **2019**, *58*, 8895−8899.

(37) Son, K.; Kim, R. K.; Kim, S.; Schütz, G.; Choi, K. M.; Oh, H. Metal Organic Frameworks as Tunable Linear Magnets. *Phys. Status Solidi A* **2020**, *217*, 1901000.

93

(38) Muratović, S.; Karadeniz, B.; Stolar, T.; Lukin, S.; Halasz, I.; Herak, M.; Mali, G.; Krupskaya, Y.; Kataev, V.; Žilić, D.; Užarević, K. Impact of dehydration and mechanical amorphization on the magnetic properties of Ni(ii)-MOF-74. *J. Mater. Chem. C* **2020**, *8*, 7132−7142.

(39) Zhao, X.; Pattengale, B.; Fan, D.; Zou, Z.; Zhao, Y.; Du, J.; Huang, J.; Xu, C. Mixed-Node Metal-Organic Frameworks as Efficient Electrocatalysts for Oxygen Evolution Reaction. *ACS Energy Lett.* **2018**, *3*, 2520−2526.

(40) Mukoyoshi, M.; Maesato, M.; Kawaguchi, S.; Kubota, Y.; Cho, K.; Kitagawa, Y.; Kitagawa, H. Systematic Tuning of the Magnetic Properties in Mixed-Metal MOF-74. *Inorg. Chem.* **2022**, *61*, 7226−7230.

(41) Lukin, S.; Germann, L. S.; Friščić, T.; Halasz, I. Toward Mechanistic Understanding of Mechanochemical Reactions Using Real-Time In Situ Monitoring. *Acc. Chem. Res.* **2022**, *55*, 1262−1277.

(42) Užarević, K.; Halasz, I.; Friščić, T. Real-Time and In Situ Monitoring of Mechanochemical Reactions: A New Playground for All Chemists. *J. Phys. Chem. Lett.* **2015**, *6*, 4129−4140.

(43) Hadjiivanov, K. I.; Panayotov, D. A.; Mihaylov, M. Y.; Ivanova, E. Z.; Chakarova, K. K.; Andonova, S. M.; Drenchev, N. L. Power of Infrared and Raman Spectroscopies to Characterize Metal-Organic Frameworks and Investigate Their Interaction with Guest Molecules. *Chem. Rev.* **2021**, *121*, 1286−1424.

(44) Flores, J. G.; Sánchez-González, E.; Gutiérrez-Alejandre, A.; Aguilar-Pliego, J.; Martínez, A.; Jurado-Vázquez, T.; Lima, E.; González-Zamora, E.; Díaz-García, M.; Sánchez-Sánchez, M.; Ibarra, I. A. Greener synthesis of Cu-MOF-74 and its catalytic use for the generation of vanillin. *Dalton Trans.* **2018**, *47*, 4639−4645.

(45) Stoll, S.; Schweiger, A. EasySpin, a comprehensive software package for spectral simulation and analysis in EPR. *J. Magn. Reson.* **2006**, *178*, 42−55.

(46) Blundell, S. *Magnetism in Condensed Matter*; Oxford University Press: Oxford, U.K., 2006.

(47) Spaldin, N. A. *Magnetic Materials Fundamentals and Applications*; Cambridge University Press: Cambridge, U.K., 2013.

(48) Bonner, J. C.; Fisher, M. E. Linear Magnetic Chains with Anisotropic Coupling. *Phys. Rev.* **1964**, *135*, A640−A658.

(49) Kahn, O. *Molecular Magnetism*; Wiley-VCH Inc., 1993.

(50) Anderson, P. W.; Weiss, P. R. Exchange Narrowing in Paramagnetic Resonance. *Rev. Mod. Phys.* **1953**, *25*, 269−276.

(51) Anderson, P. W. A Mathematical Model for the Narrowing of Spectral Lines by Exchange or Motion. *J. Phys. Soc. Jpn.* **1954**, *9*, 316−339.

(52) Žilić, D.; Androš, L.; Krupskaya, Y.; Kataev, V.; Büchner, B. Magnetic anisotropy of Cr(III) ions in polymeric oxalate complexes as revealed by HF-ESR spectroscopy. *Appl. Magn. Reson.* **2015**, *46*, 309−321.

(53) Žilić, D.; Molčanov, K.; Jurić, M.; Habjanič, J.; Rakvin, B.; Krupskaya, Y.; Kataev, V.; Wurmehl, S.; Büchner, B. 3D oxalate-based coordination polymers: Relationship between structure, magnetism and color, studied by high-field ESR spectroscopy. *Polyhedron* **2017**, *126*, 120−126.

(54) Dubraja, L. A.; Jurić, M.; Popović, J.; Pajić, D.; Krupskaya, Y.; Kataev, V.; Büchner, B.; Žilić, D. Magneto-structural correlations in oxalate-bridged Sr(II)Cr(III) coordination polymers: structure, magnetization, X-band, and high-field ESR studies. *Dalton Trans.* **2018**, *47*, 3992−4000.

(55) Bleaney, B.; Bowers, K. D. Anomalous Paramagnetism of Copper Acetate. *Proc. R. Soc. London, Ser. A* **1952**, *214*, 451.

(56) Mali, G.; Mazaj, M. Hyperfine Coupling Constants in Cu-Based Crystalline Compounds: Solid-State NMR Spectroscopy and First-Principles Calculations with Isolated-Cluster and Extended Periodic-Lattice Models. *J. Phys. Chem. C* **2021**, *125*, 4655−4664.

(57) Luo, F.; Yan, C.; Dang, L.; Krishna, R.; Zhou, W.; Wu, H.; Dong, X.; Han, Y.; Hu, T.-L.; O'Keeffe, M.; Wang, L.; Luo, M.; Lin, R.-B.; Chen, B. UTSA-74: A MOF-74 Isomer with Two Accessible Binding Sites per Metal Center for Highly Selective Gas Separation. *J. Am. Chem. Soc.* **2016**, *138*, 5678−5684.

7.4.   Appendix IV− Supplementary Information for Publication 2

Supporting Information

for

Low-dimensional magnetism in multivariate copper/zinc MOF-74 materials formed via different mechanochemical methods

by

Senada Muratović,[‡,△] Valentina Martinez,[‡,△] Bahar Karadeniz,[‡] Damir Pajić,[¶]
Ivana Brekalo,[‡] Mihails Arhangelskis,[§] Matjaž Mazaj,[‖] Gregor Mali,[‖] Martin
Etter,[⊥] Tomislav Friščić,[#] Yulia Krupskaya,[@] Vladislav Kataev,[@] Dijana Žilić,[*,‡]
Krunoslav Užarević[*,‡]

[‡] *Ruđer Bošković Institute, Bijenička cesta 54, 10000 Zagreb, Croatia.*
[¶] *University of Zagreb, Faculty of Science, Department of Physics, Bijenička cesta 32, 10000
Zagreb, Croatia.*
[§] *Faculty of Chemistry, University of Warsaw, 1 Pasteura St, 02-093 Warsaw, Poland.*
[‖] *National Institute of Chemistry, Hajdrihova 19, SI-1001 Ljubljana, Slovenia.*
[⊥] *Deutsches Elektronen-Synchrotron DESY, Notkestraße 85, D-22607 Hamburg, Germany.*
[#] *McGill University, Montreal, Quebec H3A 0B8, Canada*
[@] *Leibniz IFW Dresden, Helmholtzstrasse 20, D-01069 Dresden, Germany.*
[△] *equally contributing first authors*

E-mail: dijana.zilic@irb.hr, krunoslav.uzarevic@irb.hr

Contents

List of Figures

S3

List of Tables

S4

S1 Materials and methods

S1.1 Synthesis

ZnO, $Cu(OH)_2$ and 2,5-dihydroxy-1,4-benzenedicarboxylic acid (H_4dobdc) were obtained from Sigma-Aldrich. Methanol (MeOH) was purchased from Lach-ner.

If not stated otherwise mechanochemical milling syntheses were performed using an IST-500 (InSolido Technologies) vibratory ball mill at 30Hz in 14 mL of poly(methyl methacrylate) (PMMA) jars and with one 4 g (10 mm) ss ball.

Mechanochemical synthesis of Cu-MOF-74

220 mg (1.11 mmol) of H_4dobdc and 216.68 mg (2.22 mmol) of $Cu(OH)_2$ were placed into a 14 mL PMMA jar along with 360 μL of MeOH and the reaction mixture was milled for 30 minutes to form the brown product.

Mechanochemical synthesis of ZnCu-MOF-74

First, 220 mg (1.11 mmol) of H_4dobdc and 90.38 mg (1.11 mmol) of ZnO were placed into a 14 mL PMMA jar with one 4 g (10 mm) stainless steel ball. Then 100 μL of H_2O was added and the reaction mixture was milled for 15 minutes to form a zinc intermediate. Next, 108.34 mg (1.11 mmol) of $Cu(OH)_2$ was added along with 150 μL of MeOH and the reaction mixture was milled for 60 minutes to form the brown ZnCu-MOF-74.

Mechanochemical synthesis of CuZn-MOF-74

First, 220 mg (1.11 mmol) of H_4dobdc and 108.34 mg (1.11 mmol) of $Cu(OH)_2$ were placed into a 14 mL PMMA jar with one 4 g (10 mm) stainless steel ball. Then 110 μL of MeOH was added and the reaction mixture was milled for 15 minutes to form a copper intermediate. Next, 90.38 mg (1.11 mmol) of ZnO was added along with 150 μL of MeOH and the reaction mixture was milled for 30 minutes to form the brown CuZn-MOF-74.

Mechanochemical synthesis of zinc-copper MOF-74 alloyed

Zn-MOF-74 and Cu-MOF-74 used for alloying were synthesized according to the literature.[5,6] 160 mg of Zn-MOF-74 and 158 mg of Cu-MOF-74 were placed into a 14 mL PMMA jar with two 1.98 g (8 mm) stainless steel balls. Then 100 μL of MeOH was added and the reaction mixture was milled for 15 minutes at 30 Hz. Amorphous material was attained by drying the milling product overnight at 150°C then neat grounding it in a PMMA jar with one 4 g ss ball for 90 minutes at 30 Hz. Finally, the crystalline phase was recovered by the exposure of the amorphized product to vapours of MeOH at 45°C for 9 days.

The crystalline MOF-74 products were washed three times with a small volume of MeOH, then filtered and dried, analyzed by powder X-ray diffraction (PXRD) and FTIR-ATR and subjected to further analyses.

Zn-INT 220 mg (1.11 mmol) of H_4dobdc and 90.38 mg (1.11 mmol) of ZnO were placed into a 14 mL PMMA jar with one 4 g (10 mm) stainless steel ball. Then 200 μL of H_2O was added and the reaction mixture was milled for 15 minutes to form beige product.

Cu-INT 220 mg (1.11 mmol) of H_4dobdc and 108.34 mg (1.11 mmol) of $Cu(OH)_2$ were placed into a 14 mL PMMA jar with one 4 g (10 mm) stainless steel ball. Then 220 μL of MeOH was added and the reaction mixture was milled for 15 minutes to form turquoise product.

Intermediates were washed three times with a small volume of distilled water, then filtered and dried.

S1.2   PXRD

Powder X-ray diffraction (PXRD) data was collected by Panalytical Aeris Research tabletop powder X-ray diffractometer, with CuK_α radiation (40 kV, 7.5 mA) in Bragg-Bretano geometry, with the sample mounted on zero background silicon plate. The data were collected in the range of 5-50°. The step size was 0.005°with a time per step of 8 s.

S1.3   TGA analysis

Thermogravimetric (TGA) experiments were performed on a Simultaneous thermal analyzer (STA) 6000 (PerkinElmer, Inc.) in alumina crucibles at 5°C min^{-1} heating rate from 40 °C to 950 °C under oxygen gas purging at the flow of 30 mL min^{-1}.

S1.4   Structure determination from PXRD data

The crystal structure of Cu-INT was determined from room temperature (RT) PXRD data collected in an analogous way to S1.2, except the range used was 5-80°, and the step size was 0.005°with a time per step of 550 s.

The powder pattern was indexed using DICVOL06, as implemented in the program EXPO v1.21.09, resulting in the *Pbcn* space group with the following unit cell parameters: a = 14.7903(6) Å, b = 6.9442(3) Å, c = 21.651(1) Å. Pawley refinement, simulated annealing structure solution and Rietveld refinement were performed using TOPAS Academic 6. First, Pawley refinement was used to refine unit cell parameters, peak shape parameters (pseudo-Voigt function) and background Chebyshev polynomial terms.

The optimal values for unit cell, peak shape and background polynomials found in Pawley refinement were fixed during the Simulated Annealing structure solution. The position and orientation of the rigid body fragment representing the dobdc ligand molecule, along with a Cu atom and two oxygen atoms representing water molecules (composition determined from TGA analysis (Figure S7), were allowed to vary along with the overall scale factor (Fig. S6a).

Once a satisfactory structural model was found, Rietveld refinement was performed. During the refinement procedure all previously constrained parameters (unit cell, peak shape and background) were allowed to refine. At this stage hydrogen atoms were added to water molecules in the positions ensuring the most reasonable hydrogen bonding pattern (Fig. S6b).

S1.5   FTIR spectroscopy

Measurements were performed on a PerkinElmer Fourier transform infrared spectrometer Spectrum Two (PerkinElmer,Inc.) using Spectrum10 software (PerkinElmer, Inc.) in transmittance mode by FTIR-ATR technique.

S1.6   Flame AAS

Flame atomic absorption spectroscopy (AAS) analysis was carried out on Perkin Elmer AAnalyst 200 Atomic Absorption Spectrometer with air/acetylene burner head and hollow cathode lamp for Cu and Zn, respectively. ZnCu-MOF-74 and CuZn-MOF-74 were dissolved using aqua regia and

diluted with deionized water (DI) to a total volume of 50 mL in a volumetric flask. Solutions were then diluted with DI to meet linearity response range for a given element. Standards for calibration were prepared by diluting Fluka (Cu) and AlfaAesar (Zn) 1000 ppm standard solutions.

S1.7   EDAX/SEM

Elemental maps of the investigated samples were obtained by energy dispersive X-ray analysis (EDAX) on a Thermo Fisher Verios 4G HP field-emission scanning electron microscope (FEG-SEM) using Aztec Live Ultim Max EDS detection/analysis system (Oxford Instruments).

S1.8   Magnetic susceptibility analysis

Temperature- and field dependences of the susceptibility and magnetization, respectively, were measured in the temperature range 1.8–300 K and in magnetic fields up to 7 T using a commercial SQUID (superconducting quantum interferometer device) VSM (vibrating sample magnetometer), model MPMS3 from Quantum Design. The powder samples were cooled down from room temperature down to 1.8 K without applied magnetic field, then the magnetization curves $M(H)$ were measured by ramping the field from 0 to 7 T and back to 0 T. After that a field of 0.1 T was applied and the susceptibility temperature dependence $\chi(T)$ was measured upon heating the sample. During the fits the susceptibility data were corrected for a small sample and instrumental dependent offset.

S1.9   ESR spectroscopy

X-band ESR/EPR measurements were performed on a Bruker Elexsys 580 FT/CW X-band spectrometer at a frequency around 9.7 GHz. Magnetic field modulation amplitude was 0.5 mT and the modulation frequency was 100 kHz. HF-ESR study was carried out on a home-made spectrometer based on Vector Network Analyzer that uses 16 T magnetocryostat.[7] HF-ESR spectra of the samples were recorded at several selected frequencies from 142 GHz up to 317 GHz in the temperature range 4–50 K.

S1.10   Solid-state NMR

Solid-state ^{13}C magic-angle spinning (MAS) NMR spectra were recorded on a 600 MHz Varian VNMRS spectrometer equipped with a 1.6 mm HXY Varian MAS probe. The spectra of copper-containing samples were obtained with a Hahn echo sequence. The duration of the 90- and 180-degree pulses was 2 and 4 μs, respectively, and the interpulse delay was equal to one rotation period. MAS frequencies of 38 and 40 kHz were used. Repetition delay between consecutive scans was 100 ms, and the number of scans was between 600,000 and 800,000. The ^{1}H–^{13}C cross-polarization (CP) MAS NMR spectrum of Zn-MOF-74 was recorded at a MAS frequency of 32 kHz using a ramp during the 5 ms CP block and high-power XiX proton decoupling during acquisition. The repetition delay was 2 s, and the number of scans was 3200. All ^{13}C shifts are reported relative to the position of the ^{13}C signal of tetramethylsilane.

S7

S1.11 In-situ synchrotron PXRD monitoring

In-situ synchrotron PXRD monitoring was performed at the P02.1 beamline (X-ray beam: $E \approx 60$ keV, $\lambda = 0.20735$ Å) at PETRA III, DESY. Diffraction data was collected on a VAREX XRD4343CT area detector, with exposure time of 10 s. Millings were conducted using a modified IST-636 (In-Solido Technologies) vibratory ball mill operating at 30 Hz, controlled remotely from outside of the experimental hutch.

Real-time in-situ monitored synthesis of ZnCu-MOF-74 starting from Zn-INT

259.8 mg (0.87 mmol) of Zn-INT [$Zn(H_2dobdc)(H_2O)_2$] and 85.20 mg (0.87 mmol) of $Cu(OH)_2$ were placed into separate parts of 14 mL PMMA jar with one 4 g (10 mm) stainless steel ball along with 170 μL of MeOH and milled for 45 minutes.

Real-time in-situ monitored synthesis of CuZn-MOF-74 starting from Cu-INT

328.37 mg (1.11 mmol) of Cu-INT ($Cu(H_2dobdc)(H_2O)_2$) and 90.38 mg (1.11 mmol) of ZnO were placed into separate parts of 14 mL PMMA jar with one 4 g (10 mm) stainless steel ball along with 200 μL of MeOH and milled for 45 minutes.

Real-time in-situ monitored synthesis of Zn/Cu-MOF-74 in one step

90.38 mg (1.11 mmol) of ZnO and 108.34 mg (1.11 mmol) of $Cu(OH)2$ along with 100μL of H_2O and 220 mg (1.11 mmol) of H_4dobdc with 250μL MeOH were placed into separate parts of 14 mL PMMA jar with one 4 g (10 mm) stainless steel ball and the reaction mixture was milled for 45 minutes.

S2   Results

S2.1   PXRD
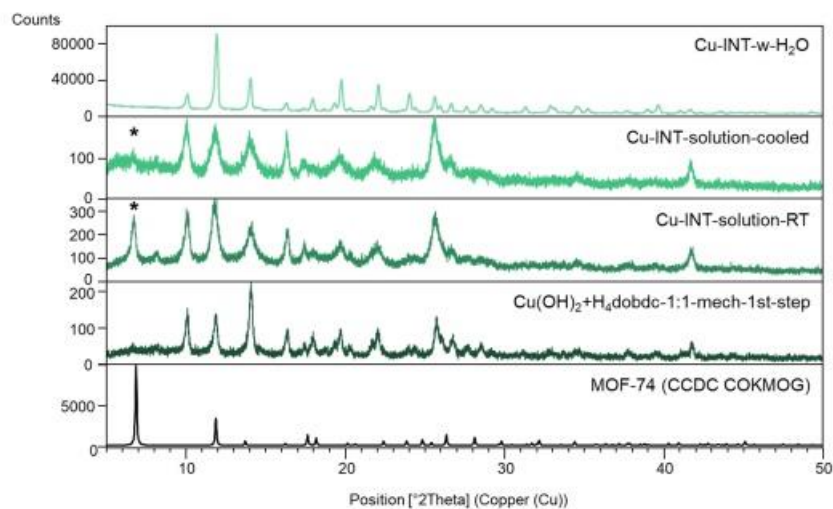
Figure S1: PXRD patterns of copper intermediate phase (Cu-INT) detected in the first step in the step-wise synthesis of CuZn-MOF-74 (Cu(OH)$_2$+H$_4$dobdc-1:1-mech-1st-step), Cu-INT solution preparation attempts at RT (Cu-INT-solution-RT) and 4°C (Cu-INT-solution-cooled) that resulted in partial transformation to MOF-74 phase, and mechanochemically prepared Cu-INT washed with water(Cu-INT-w-H$_2$O) compared to the simulated pattern of Cu-MOF-74 (CCDC code: COK-MOG). Observed MOF-74 reflexes are marked with asterisks.
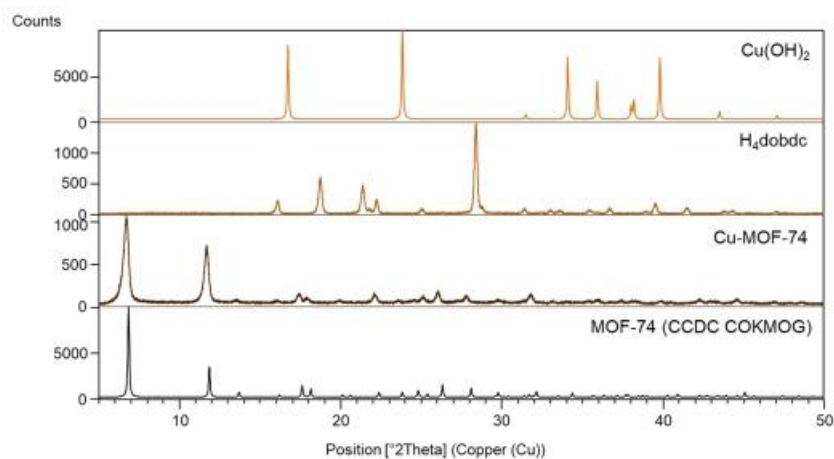
Figure S2: PXRD patterns of reactants $Cu(OH)_2$ and H_4dobdc, and Cu-MOF-74 product compared to the simulated pattern of Cu-MOF-74 (CCDC code: COKMOG)[1,2].
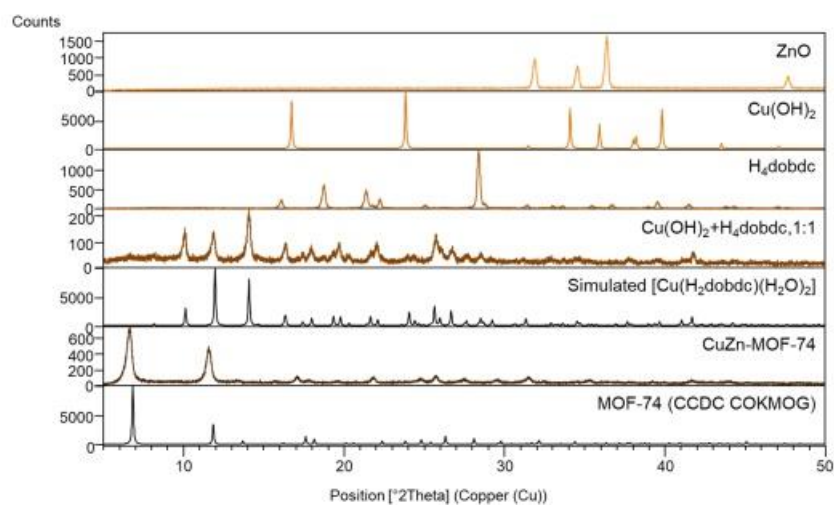
Figure S3: PXRD patterns of reactants ZnO, $Cu(OH)_2$ and H_4dobdc, first step intermediate $[Cu(H_2dobdc)(H_2O)_2]$ and CuZn-MOF-74 product compared to the simulated patterns of $[Cu(H_2dobdc)(H_2O)_2]$ and Cu-MOF-74 (CCDC code: COKMOG)[1,2].

S10
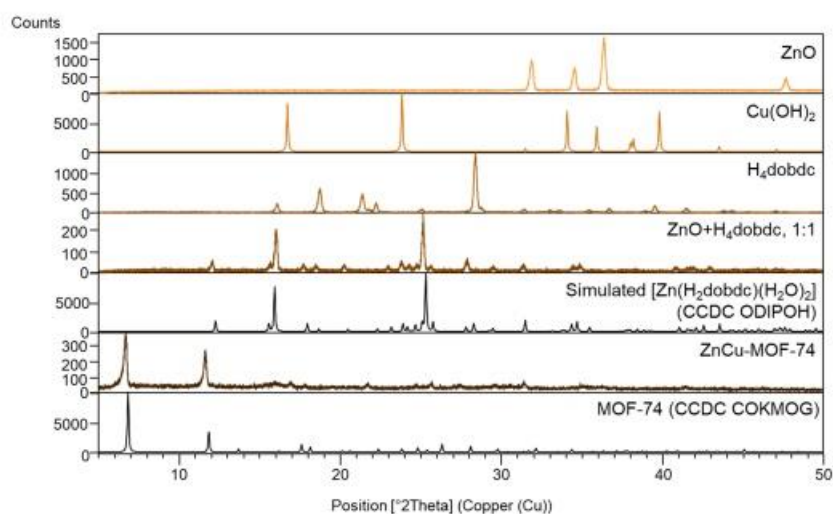
Figure S4: PXRD patterns of reactants ZnO, Cu(OH)$_2$ and H$_4$dobdc, first step intermediate [Zn(H$_2$dobdc)(H$_2$O)$_2$] and ZnCu-MOF-74 product compared to the simulated patterns of [Zn(H$_2$dobdc)(H$_2$O)$_2$] and Cu-MOF-74 (CCDC code: COKMOG)[1,2].
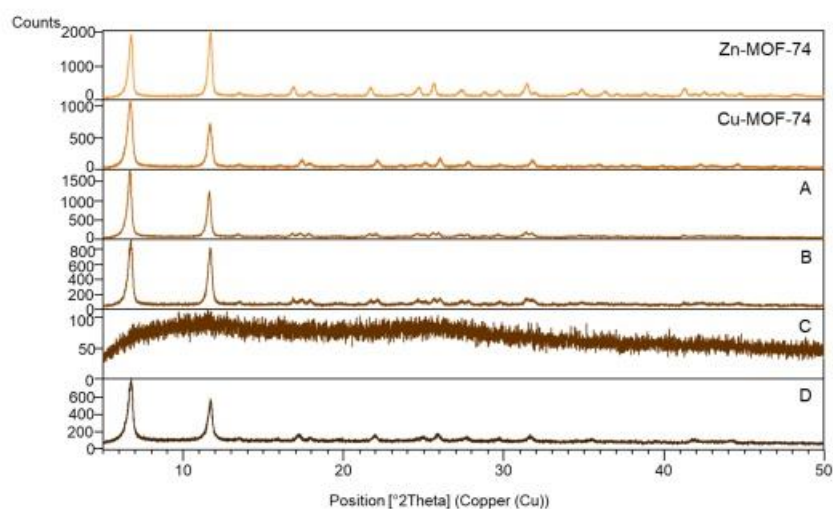
Figure S5: PXRD patterns of Zn-MOF-74 and Cu-MOF-74, and stages of their alloying into Zn-Cu-MOF-74-alloyed. Two MOFs were milled (A), dried overnight at 150°C (B) then neat ground-amorphized (C) and lastly exposed to methanol vapours for 9 days to regain crystallinity (D).

S2.2 Structure solution from PXRD data

Cu-INT crystallizes in the *Pbcn* space group with the following unit cell parameters: $a = 14.7903(6)$ Å, $b = 6.9442(3)$ Å, $c = 21.651(1)$ Å (Fig. S9 e). The structure consists of square-pyramidally coordinated copper atoms, with two water molecules and two different dobdc molecules occupying the equatorial positions in a trans conformation, and a third dobdc molecule coordinated in the axial position (Fig. S9a). Each dobdc molecule bridges three different copper centers, two through each carboxylic group (non-chelating, equatorial binding of Cu), and one through one of the hydroxyl groups (axial position of Cu). This is markedly distinct from both the other previously reported [Cu(H$_2$dobdc)(H$_2$O)$_2$] compound (CCDC code: KUSNAQ)[2], and Zn-INT. In both structures, the hydroxyl groups of dobdc are uncoordinated, the ligand is bound in a quasi-tetrahedral coordination (Fig. S9b). In Cu-INT, the square-pyramidal Cu atoms connect into Cu-dobdc chain dimers (dCu-Cu(chain) = 10.869 Å, dCu-Cu(bridge1) = 5.800 Å, dCu-Cu(bridge2) = 7.573 Å, Fig. S9 c), which then connect through hydrogen bonding of coordinated water molecules, and uncoordinated oxygen atoms of carboxylic dobdc groups (Fig. S9 d).

Table S1: Crystallographic table for the Cu-INT crystal structure obtained through structure solution from PXRD data.

	Cu-INT
Formula	Cu(C$_8$H$_4$O$_2$)(H$_2$O)$_2$
M_r (g mol^{-1})	295.69
Crystal system	orthorhombic
a/Å	14.7903(6)
b/Å	6.9442(3)
c/Å	21.651(1)
α (°)	90
β (°)	90
γ (°)	90
V/Å^3	2223.7(2)
Z	8
Space group	*Pbcn*
ρ_c (g cm^{-3})	1.7664
Radiation type	CuK_α
$F(000)$	1192
R_{wp}	0.086
R_p	0.059
R_{Bragg}	0.064
χ^2	7.174
CCDC number	2174976
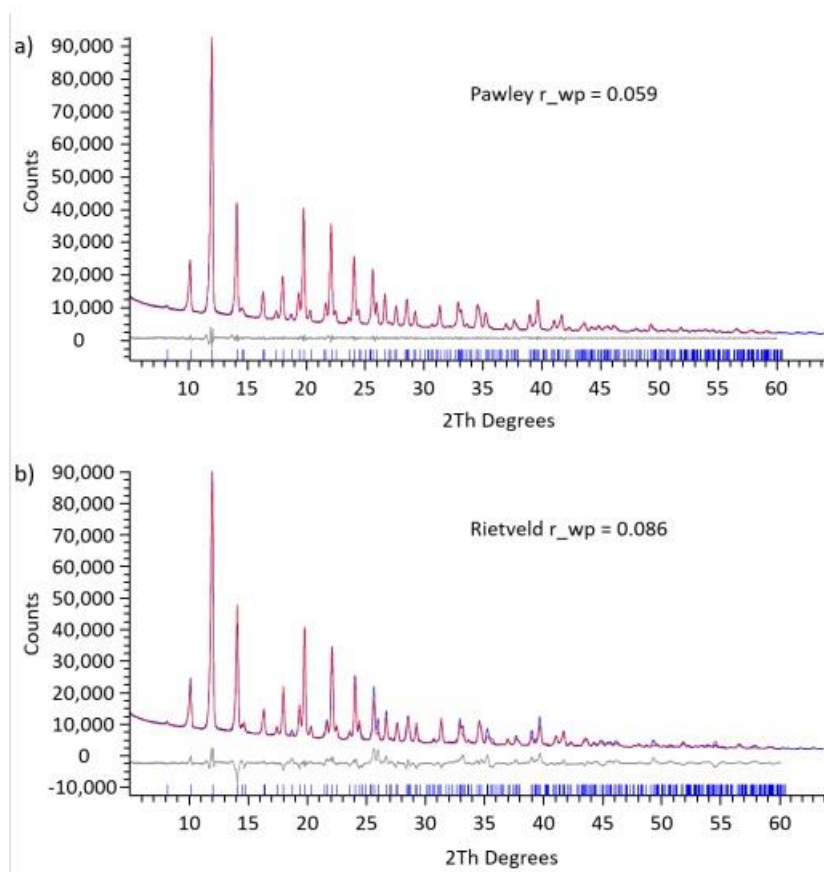
Figure S6: Graphical results of the a) Pawley, and b) Rietveld refinement of Cu-INT, with the corresponding r_{wp} values. The experimental PXRD patterns are drawn in blue, the simulated patterns in red, and the difference curve in grey. The predicted peak positions obtained by indexing are shown by dark blue bars.

S13
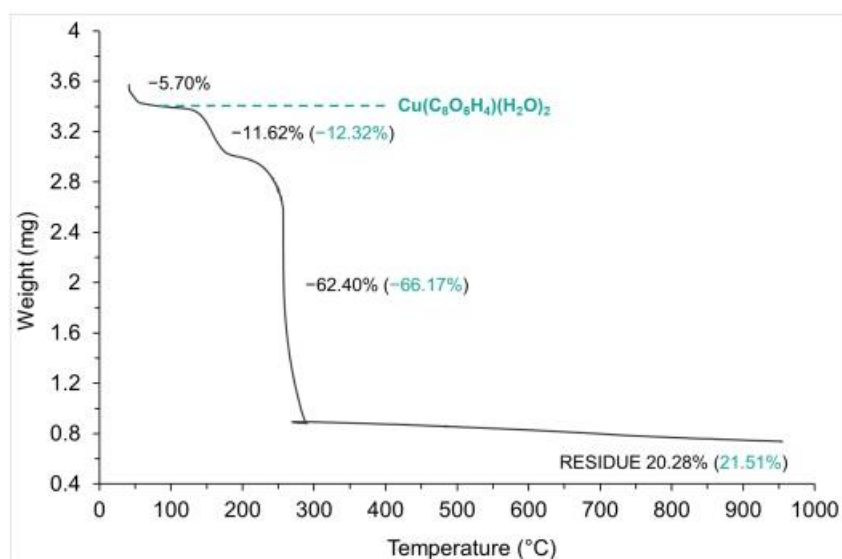
Figure S7: Thermogram of Cu-INT. After the initial mass loss, attributed to the solvent remnants from the synthesis and post-synthetic processing, Cu-INT decomposed in two steps. Mass loss in the first step can be attributed to coordinated water molecules and the second to the decomposition of the organic moiety. Theoretical mass losses and solid residue percentage calculated according to Cu-INT composition $[Cu_2dobdc)(H_2O)_2]$ are shown in teal.
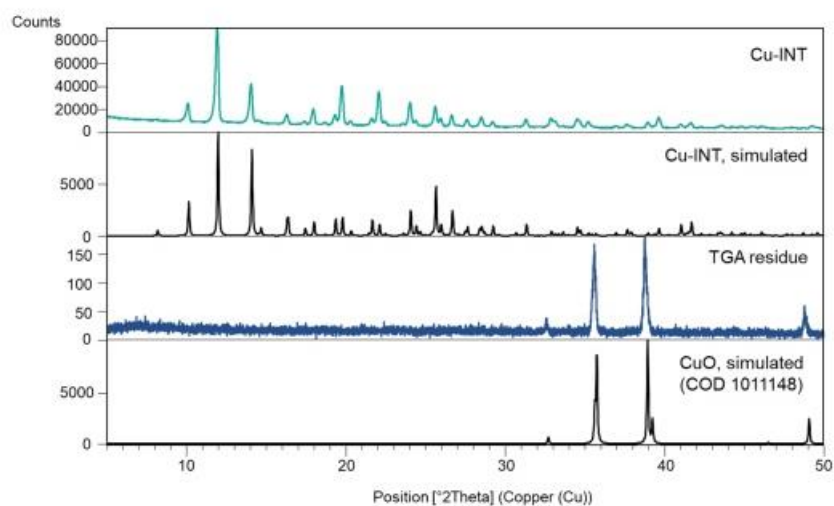
Figure S8: PXRD patterns of copper intermediate analyzed by TGA and solid residue after the analysis compared to the simulated patterns of $[Cu_2dobdc)(H_2O)_2]$ and CuO (COD code: 1011148)[3,4]
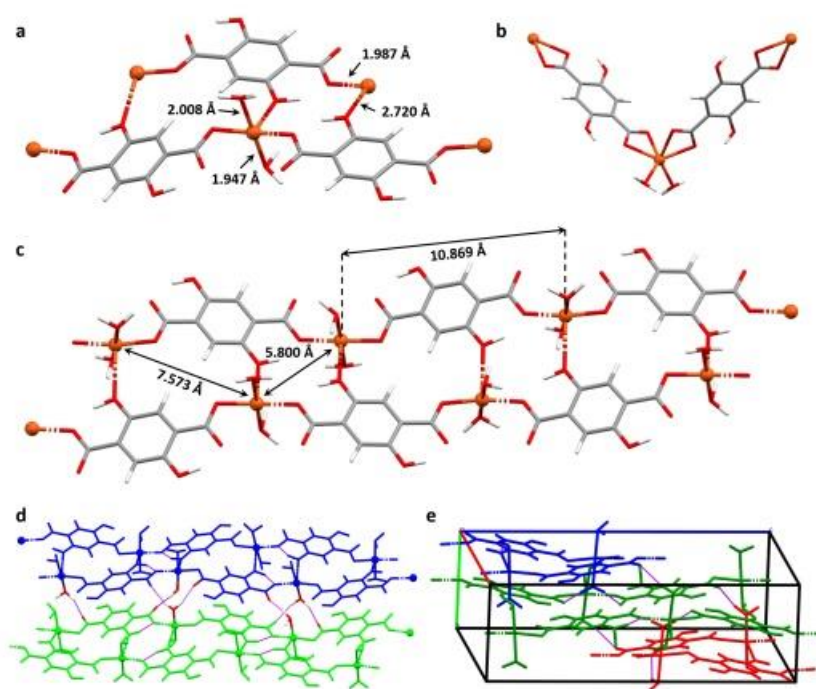
Figure S9: The crystal structure of Cu-INT. a) first coordination sphere of each copper atom, b) first coordination sphere of a copper atom in the structure of KUSNAQ[2] Cu-dobdc complex, c) the double chain of Cu-INT, d) hydrogen bonding between two double-chains of Cu-INT, e) unit cell of Cu-INT. Dashed purple lines represent hydrogen bonds, spheres represent copper atoms.

S16

S2.3 FTIR spectroscopy
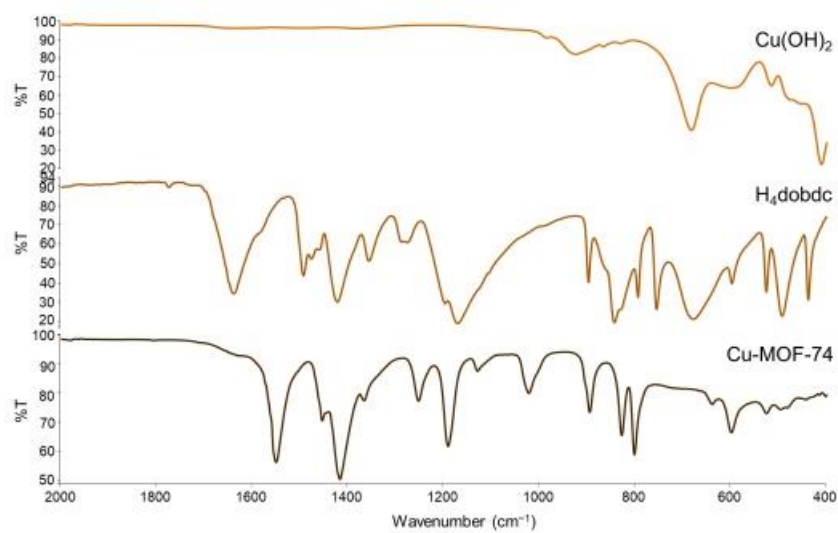
Figure S10: FTIR-ATR data of product, Cu-MOF-74 of liquid-assisted grinding of $Cu(OH)_2$ with H_4dobdc, compared to starting materials.
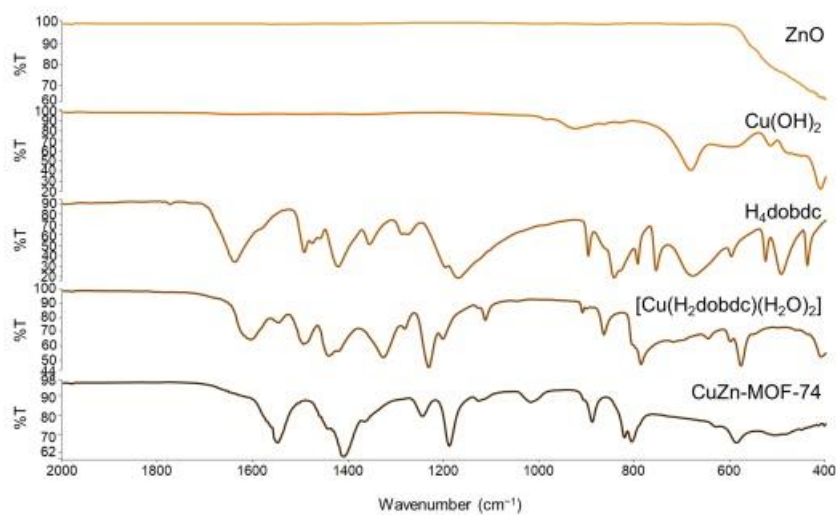
Figure S11: FTIR-ATR data of the first step intermediate, [Cu(H$_2$dobdc)(H$_2$O)$_2$] and final product, CuZn-MOF-74 of liquid-assisted grinding of ZnO and Cu(OH)$_2$ with H$_4$dobdc, compared to starting materials.
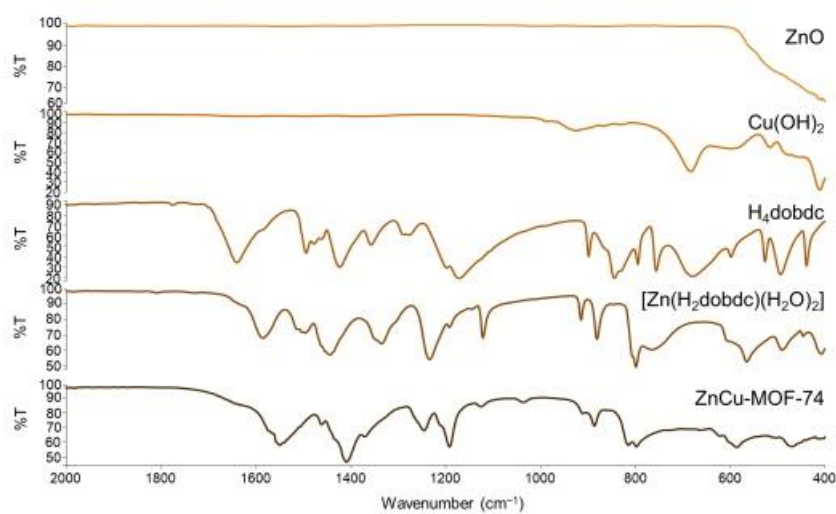
Figure S12: FTIR-ATR data of the first step intermediate, [Zn(H$_2$dobdc)(H$_2$O)$_2$] and final product, ZnCu-MOF-74 of liquid-assisted grinding of ZnO and Cu(OH)$_2$ with H$_4$dobdc, compared to starting materials.
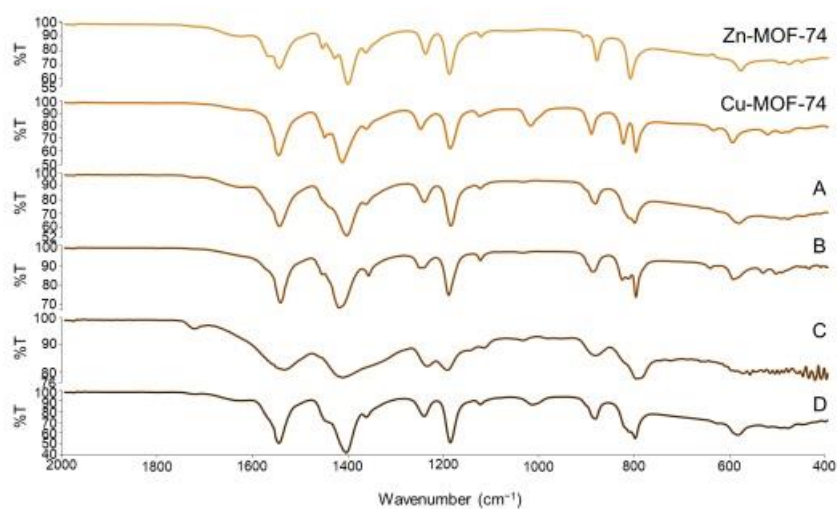
Figure S13: FTIR-ATR data of Zn-MOF-74 and Cu-MOF-74, and product of their milling (A) that was subsequently dried at 150°C (B) then amorphized by neat-grinding (C) and finally exposed to methanol vapours for 9 days to regain crystallinity and form Zn-Cu-MOF-74-alloyed (D).

S19

S2.4   Flame AAS and EDAX/SEM analyses

Table S2: Ratio of Cu and Zn metal within the investigated copper/zinc MM-MOF-74 samples based on EDAX/SEM mapping and Flame AAS analyses.

Sample	EDAX/SEM		AAS
	Cu/Zn (weight ratio)	Cu/Zn (molar ratio)	Cu/Zn (molar ratio)
CuZn-MOF-74	0.92 ± 0.01	0.95 ± 0.01	0.97 ± 0.01
ZnCu-MOF-74	0.91 ± 0.01	0.94 ± 0.01	1.03 ± 0.01
Zn-Cu-MOF-74-alloyed	1.00 ± 0.01	1.03 ± 0.01	N/A
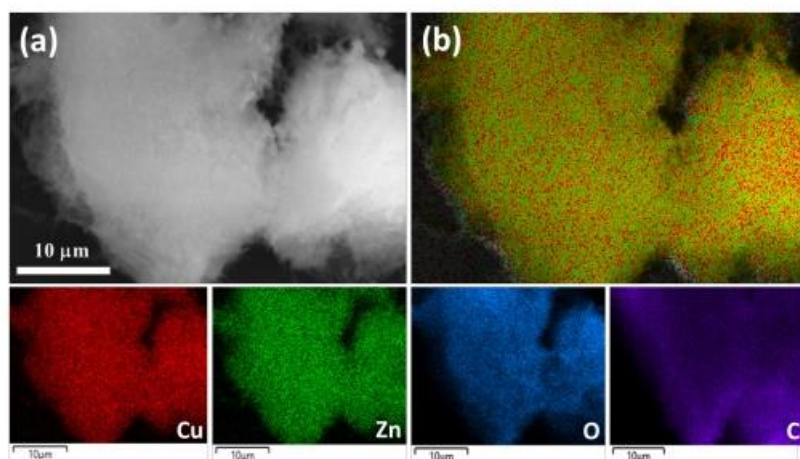
Figure S14: a) Scanning electron micrograph of the investigated area used for EDS analysis for CuZn-MOF-74 sample; b) corresponding colour overlay map with the Cu (red), Zn (green), O (blue) and C (purple) elemental distribution.
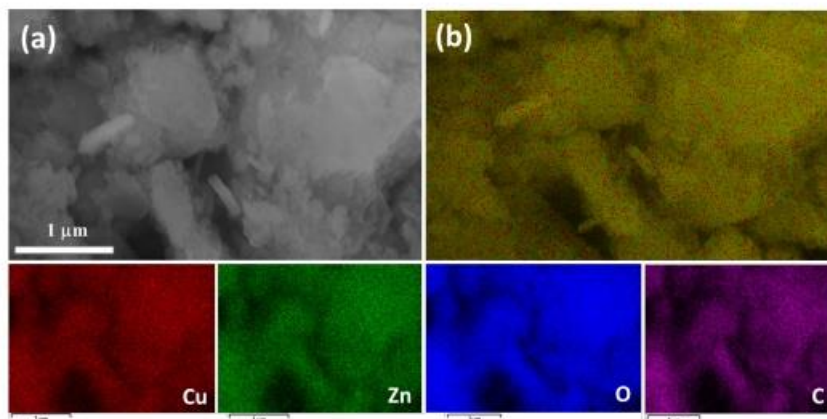
Figure S15: a) Scanning electron micrograph of the investigated area used for EDS analysis for ZnCu-MOF-74 sample; b) corresponding colour overlay map with the Cu (red), Zn (green), O (blue) and C (purple) elemental distribution.
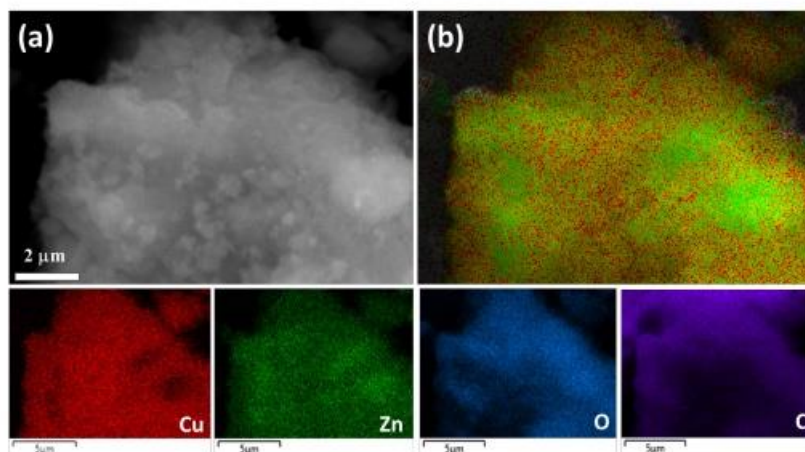
Figure S16: a) Scanning electron micrograph of the investigated area used for EDS analysis for Zn-Cu-MOF-74-alloyed sample; b) corresponding colour overlay map with the Cu (red), Zn (green), O (blue) and C (purple) elemental distribution.

S21

S2.5 Magnetic susceptibility analysis

The Bonner-Fisher formula is given by:[8]

$$\chi_{chain} = \frac{N_A \mu_B^2 g^2}{k_B T} \frac{0.25 + 0.074975x + 0.075235x^2}{1 + 0.9931x + 0.172135x^2 + 0.757825x^3}, \tag{S1}$$

where $x = |J|/k_B T$, and thereafter additionally modified with the mean field correction (like in Ref. 9)

$$\chi = \frac{\chi_{chain}}{1 - \frac{zj}{N_A \mu_B^2 g^2} \chi_{chain}}, \tag{S2}$$

where $z = 3$ is number of the nearest neighbour spin-chains. Total susceptibility, with the correction due to paramagnetic impurities and background, is fitted by:

$$\chi_{total} = r(C/T) + (1-r)\chi + D, \tag{S3}$$

where r is the molar fraction of noncoupled species and D is the background contribution.

The Bleaney-Bowers formula is given by:[8]

$$\chi = \frac{N_A \mu_B^2 g^2}{k_B T (3 + exp(-J/k_B T))}. \tag{S4}$$

With the correction for paramagnetic impurities and background, the total susceptibility is fitted by:

$$\chi_{total} = F(r(C/T) + (1-r)\chi) + D. \tag{S5}$$

Here F is the fraction of experimental / theoretical copper content, where theoretical copper content for ZnCu-MOF-74 is 50%. Due to 50% copper ions in ZnCu-MOF-74, factor 2 is removed in the numerator of the eq. S4.

S2.6 ESR spectroscopy

Table S3: The spin-Hamiltonian parameters used for the simulation of X-band ESR spectra of the investigated samples. Lorentzian lineshapes were used for the all simulations.

Compound	$g_\perp$	$g_\parallel$	$A_\perp$ (MHz)	$A_\parallel$ (MHz)	g-strain	l_w (mT)	Weight
Cu-MOF-74	2.07	2.36	0	400	0 0 0	2	0.10
	2.07	2.36	0	400	0 0 0	12	0.90
CuZn-MOF-74	2.07	2.36	0	400	0.05 0 0	11	0.32
	2.07	2.36	0	400	0.25 0 0	20	0.68
ZnCu-MOF-74	2.07	2.36	0	400	0.07 0 0	9	0.29
	2.07	2.36	0	400	0.31 0 0	14	0.71
Zn-Cu-MOF-74-alloyed	2.07	2.36	0	400	0.13 0 0	9	0.30
	2.07	2.36	0	400	0.16 0 0	20	0.70
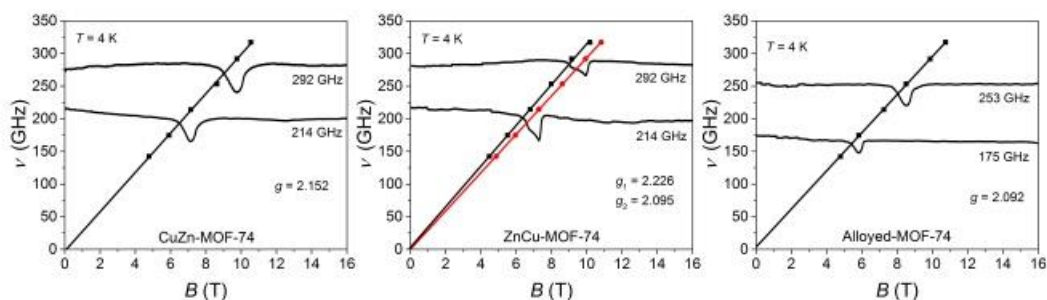
Figure S17: Frequency vs. resonance field dependencies of the prominent spectral points with two selected spectra of CuZn-MOF-74, ZnCu-MOF-74 and Alloyed-MOF-74 samples, measured at different frequencies at $T = 4$ K.

S23

S2.7 In-situ synchrotron PXRD monitoring
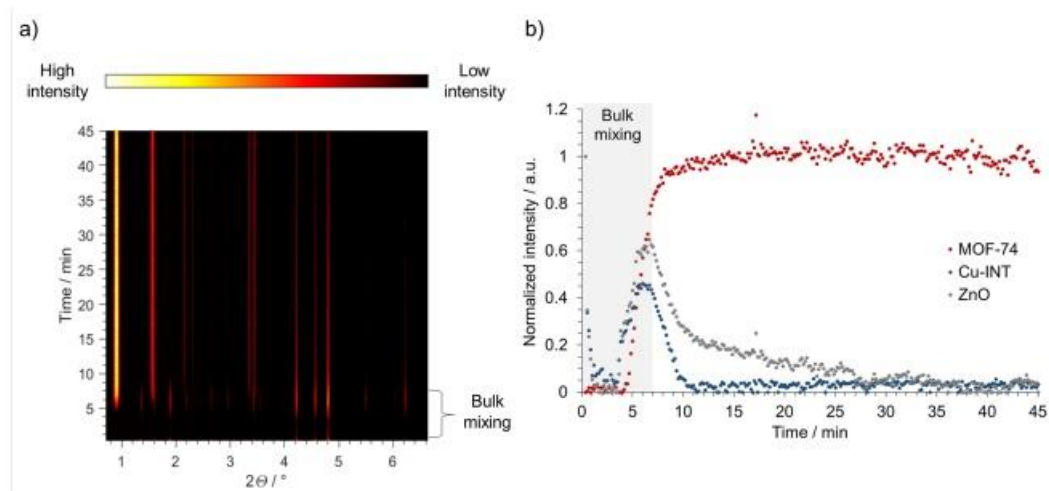
Figure S18:   a) Time-resolved diffractograms for the synthesis of CuZn-MOF-74 from [Cu(H$_2$dobdc)(H$_2$O)$_2$] and ZnO by LAG (MeOH). Fading of the reactants Bragg reflections within first 5 minutes of the reaction can be ascribed to uneven distribution of material in the jar caused by it sticking on the balls and jar walls. After this period distribution is getting more even and at 7 min from the reaction onset, reaction mixture looks evenly distributed. b) Changes in the normalized integrated peak intensity of the most prominent Bragg reflections of MOF-74 (2Θ = 0.92°), Cu-INT (2Θ = 1.88°) and ZnO (2Θ = 6.21°), over the course of the reaction. Mixing period is shown in grey. In case of ZnO we chose less prominent reflection because more prominent ones overlap with MOF-74 Bragg reflections.
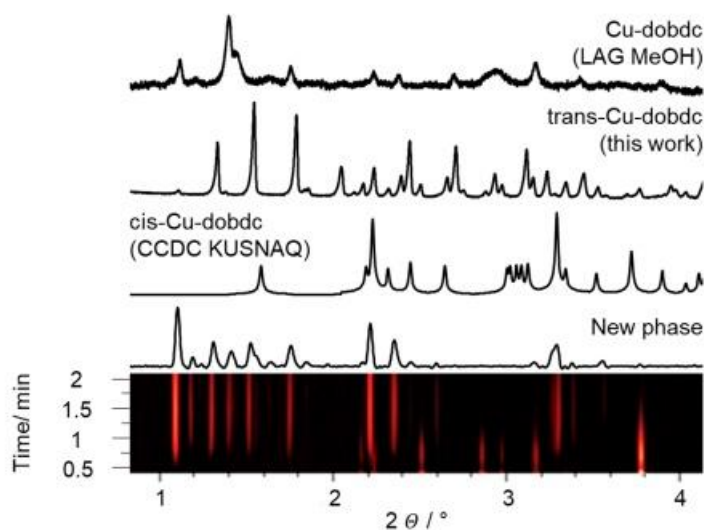
Figure S19: Time-resolved diffractograms for the first 2.5 minutes of the Zn/Cu-MOF-74 one step synthesis displaying mixed intermediate phase consisting of different Cu-H_2dobdc complexes.

References

[1] W. L. Queen, M. R. Hudson, E. D. Bloch, J. A. Mason, M. I. Gonzalez, J. S. Lee, D. Gygi, J. D. Howe, K. Lee, T. A. Darwish, M. James, V. K. Peterson, S. J. Teat, B. Smit, J. B. Neaton, J. R. Long and C. M. Brown, *Chem. Sci.*, 2014, **5**, 4569–4581.

[2] C. R. Groom, I. J. Bruno, M. P. Lightfoot and S. C. Ward, *Acta Crystallogr.*, 2016, **B72**, 171–179.

[3] G. Tunell, E. Posnjak and C. Ksanda, *Z. fur Krist. Cryst. Mater.*, 1935, **90**, 120–142.

[4] A. Vaitkus, A. Merkys and S. Gražulis, *J. Appl. Crystallogr.*, 2021, **54**, 661–672.

[5] P. A. Julien, K. Užarević, A. D. Katsenis, S. A. J. Kimber, T. Wang, O. K. Farha, Y. Zhang, J. Casaban, L. S. Germann, M. Etter, R. E. Dinnebier, S. L. James, I. Halasz and T. Friščić, *J. Am. Chem. Soc.*, 2016, **138**, 2929–2932.

[6] T. Stolar, A. Prašnikar, V. Martinez, B. Karadeniz, A. Bjelić, G. Mali, T. Friščić, B. Likozar and K. Užarević, *ACS Appl. Mater. Interfaces*, 2021, **13**, 3070–3077.

[7] C. Golze, A. Alfonsov, R. Klingeler, B. Büchner, V. Kataev, C. Mennerich, H.-H. Klauss, M. Goiran, J.-M. Broto, H. Rakoto, S. Demeshko, G. Leibeling and F. Meyer, *Phys. Rev. B*, 2006, **73**, 224403.

[8] O. Kahn, *Molecular Magnetism*, Wiley-VCH Inc., 1993.

[9] P. Šenjug, J. Dragović, F. Torić, I. Lončarić, V. Despoja, K. Smokrović, E. Topić, I. Đilović, M. Rubčić and D. Pajić, *Materials*, 2021, **14**, 1–19.

7.5.   Appendix V − Manuscript of Publication 3

Scalable Mechanochemical Amorphization of Bimetallic Cu−Zn MOF-74 Catalyst for Selective CO₂ Reduction Reaction to Methanol

T. Stolar*[1], A. Prašnikar*[2], V. Martinez[1], B. Karadeniz[1], A. Bjelić[2], G. Mali[2], T. Friščić[3], B. Likozar[2], K. Užarević[1]

[1] Ruđer Bošković Institute, Zagreb, Croatia [2] National Institute of Chemistry, Ljubljana, Slovenia
[3]McGill University, Montreal, Canada

Author contribution:

*T.S. and A.P. contributed equally as first authors

T.S., V.M. and **B.K** MOF design and synthesis, amorphisation and material characterisation; **A.P. and A.B.** catalysis and catalytic analysis; **G.M.** ssNMR measurements and analysis, funding acquisition; **T.F.** idea conceptualisation; **B.L.** catalysis and catalytic analysis, funding acquisition; **K.U.** idea conceptualisation, funding acquisition

All authors contributed to the writing of the final manuscript.

CCC
RightsLink

Scalable Mechanochemical Amorphization of Bimetallic Cu–Zn MOF-74 Catalyst for Selective CO2 Reduction Reaction to Methanol

Tomislav Stolar,[||] Anže Prašnikar,[||] Valentina Martinez, Bahar Karadeniz, Ana Bjelić, Gregor Mali, Tomislav Friščić, Blaž Likozar,* and Krunoslav Užarević*

ACCESS | 📊 Metrics & More | 📄 Article Recommendations | 🆘 Supporting Information

ABSTRACT: Selective catalytic reduction of CO_2 to methanol has tremendous importance in the chemical industry. It mitigates two critical issues in the modern society, the overwhelming climate change and the dependence on fossil fuels. The most used catalysts are currently based on mixed copper and zinc phases, where the high surface of active copper species is a critical factor for the catalyst performance. Motivated by the recent breakthrough in the controllable synthesis of bimetallic MOF-74 materials by ball milling, we targeted to study the potential of ZnCu-MOF-74 for catalytic CO_2 reduction. Here, we tested whether the nanosized channels decorated with readily accessible and homogeneously distributed Zn and Cu metal sites would be advantageous for the catalytic CO_2 reduction. Unlike the inactive monometallic Cu-MOF-74, ZnCu-MOF-74 shows moderate catalytic activity and selectivity for the methanol synthesis. Interestingly, the postsynthetic mechanochemical treatment of desolvated ZnCu-MOF-74 resulted in amorphization and a significant increase in both the activity and selectivity of the catalyst despite the destruction of the well-ordered and porous MOF-74 architecture. The results emphasize the importance of defects for the MOF catalytic activity and the potential of amorphous MOFs to be considered as heterogeneous catalysts. Scanning electron microscopy (SEM), X-ray powder diffraction (XRD) and ^{13}C magic angle-spinning nuclear magnetic resonance (MAS NMR) were applied to establish quantitative structure–reactivity relationships. The apparent activation energy of rate reaction kinetics has indicated different pathway mechanisms, primarily through reverse water–gas shift (RWGS). Prolonged time on stream productivity, stability and deactivation were assessed, analysing the robustness or degradation of metal–organic framework nanomaterials. Scalable MOF production processes are making the latter more appealing within emerging industrial decarbonisation, in particular for carbon capture and utilisation (CCU) or hydrogen carrier storage. Acknowledging scale, the costs of fabrication are paramount.

KEYWORDS: *mechanochemistry, ball-milling, MOF-catalyzed methanol production, bimetallic MOF-74, amorphous MOF, CO_2 hydrogenation*
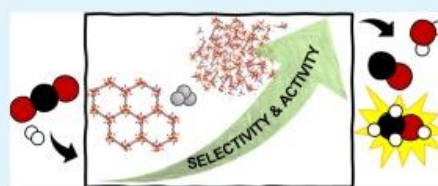
■ INTRODUCTION

Extensive usage of fossil fuels for the production of energy has led to huge amounts of anthropogenic CO_2 emissions. This represents one of the greatest problems facing our society and a pressing need to close the carbon cycle. Therefore, it is of tremendous interest to develop chemical processes that would use carbon dioxide as a feed stock and convert it to useful products. One example of such a value-added reaction is catalytic hydrogenation of CO_2, which can nonselectively result in methanol synthesis *via* hydrogenation, CO through reverse-water gas shift (RWGS) reaction, CH_4 through CO_2 methanation, or hydrocarbons by a combination of CO_2 reduction with Fischer–Tropsch reactions.[1] Among them, methanol is especially important because it is a bulk commercial chemical and is used as a versatile C_1 source in the chemical industry. If methanol can be efficiently synthesized from atmospheric CO_2, it not only mitigates greenhouse gas emissions but can also be used as a biofuel, hence the origin of the term "methanol economy".[2] One of the most used industrial

catalysts for methanol synthesis are the ones based on mixed copper/zinc oxide materials, such as $Cu/ZnO/Al_2O_3$.[3] $Cu/ZnO/Al_2O_3$ (CuZnAl) denotes a family of catalysts comprised of Cu and ZnO nanoparticles (NPs), with at least 50 mol % of Cu metal content in the mixture. The spherical Cu NPs in the industrial catalyst are in a close contact with ZnO NPs. The two types of NPs form aggregates with the moderately high surface area of the active Cu NPs. Although the exact role of Cu and ZnO constituents is still debated, a large body of evidence confirms that ZnO dramatically increases the intrinsic activity of the copper catalyst, a phenomenon better known as Cu–ZnO synergy.[3–7] Furthermore, Al_2O_3 is the most commonly used
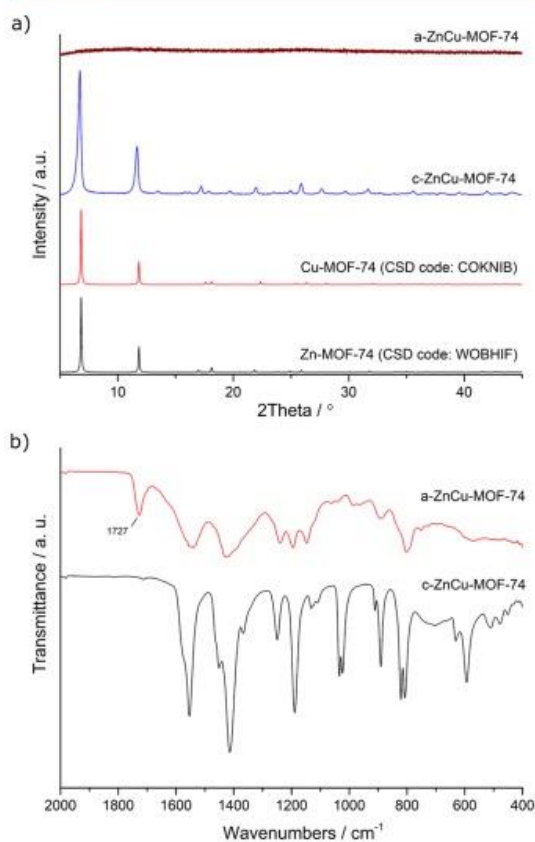
Figure 2. (a) PXRD patterns of mechanochemically synthesized c-ZnCu-MOF-74 and a-ZnCu-MOF-74 compared to monometallic Zn-MOF-74 and Cu-MOF-74; (b) FTIR spectra of mechanochemically synthesized c-ZnCu-MOF-74 and a-ZnCu-MOF-74. A new band that appears in a-ZnCu-MOF-74 at 1727 cm^{-1} is highlighted.

and vacuum dried. The resultant compound was analyzed by powder X-ray diffraction (PXRD) and FTIR−ATR and subjected to further analyses described in the main text.

Solid-state ^{13}C magic-angle spinning (MAS) NMR spectra were recorded on a 600 MHz Varian VNMRS spectrometer equipped with a 1.6 mm HXY Varian MAS probe. MAS frequencies ranged between 32 and 40 kHz. The spectra of copper-containing samples were obtained with a Hahn echo sequence. The durations of 90 and 180° pulse were 2 and 4 μs, respectively, and the interpulse delay was equal to one rotation period. Repetition delay between consecutive scans was 100 ms, and the number of scans was 800,000. The ^{1}H−^{13}C cross-polarization (CP) MAS NMR spectrum of Zn-MOF-74 was recorded at a MAS frequency of 32 kHz using a ramp during 5 ms CP block and high-power XiX proton decoupling during acquisition. The repetition delay was 2 s, and the number of scans was 3200. All ^{13}C shifts are reported relative to the position of the ^{13}C signal of tetramethylsilane.

Scanning electron microscopy (SEM) was performed on SUPRA35 VP (Carl Zeiss) coupled with an energy-dispersive X-ray spectroscopy (EDS) detector Inca 400 (Oxford Instruments). The samples were coated by 3 nm of Au using a calibrated precision etching and coating system, Gatan 682.

N$_2$ physisorption was used to obtain specific surface areas and other parameters. Measurements were performed on Micromeritics ASAP

2020, with degassing at 150 °C for 20 h with 50 mg of sample. The BET surface area and pore volume were determined using adsorption data.

Catalytic tests were performed in a parallel reactor system with online gas composition analysis using gas chromatography (Agilent 490 Micro GC, TCD detectors equipped with CP-Molsieve and PoraPlot U columns). The gas mixture with a ratio H$_2$/CO$_2$ = 3 was prepared by mixing H$_2$ (99.999%, Messer) and CO$_2$ (99.999%, Messer). Samples (200 mg) were mixed with SiC (1 g, 300 μm) to ensure sufficient thermal conductivity and uniform gas flow. Mixtures were then inserted into packed bed reactors and pre-reduced at 230 °C for 12 h in pure H$_2$ at 1 bar. The catalytic tests were performed between 160 and 230 °C, 20 bar, and flow 33,000 NmL/g$_{cat}$h. Commercial CuZnAl catalyst HiFuel W230 (particle sizes 240−400 μm) was used as a reference for methanol synthesis.

■ RESULTS AND DISCUSSION

Mechanochemistry, that is, chemical reactivity in the solid state induced by mechanical action,[26,27] emerged recently as a sustainable method for the rapid and green production[24,28] of several functional MOFs.[29−32] These mechanochemical procedures were developed without using bulk solvents and applicable even in a continuous production on pilot scales using a twin-screw extrusion.[33,34] Moreover, the mechanochemical procedures offer a unique level of selectivity and control. An efficient mechanochemical preparation of bimetallic MOFs is demonstrated by either (a) milling together already synthesized MOFs in a mechanochemical alloying approach[35,36] or (b) using a bottom-up approach where bimetallic MOFs are synthesized in a stepwise manner starting from inorganic sources and organic ligands thus gaining a control over the metal stoichiometric ratio and minimizing solvent consumption.[20]

As evidenced from Figure 2a, a-ZnCu-MOF-74 lacks long-range crystal ordering and exhibits a broad PXRD pattern absent of characteristic Bragg peaks. FTIR spectra of c-ZnCu-MOF-74 show sharp signals that broaden and shift upon amorphization. However, the most notable difference is the appearance of a new band at 1727 cm^{-1} which is assigned to the stretching vibration of the uncoordinated carbonyl group. This suggests that the amorphization proceeds *via* partial breakage of the node-linker carboxylate bonds, thus creating a defective coordination sphere around copper and zinc nodes. The recent theoretical study has shown that the linker-metal bonds in MOF-74 materials are dynamic and can brake under certain conditions.[37] Similar observations of the appearance of the uncoordinated carbonyl group were also recently described in the case of mechano-chemical amorphization of Ni-MOF-74, where the amorphization led to spin-crossover and significant drop in magnetization.[25] Furthermore, there seems to be a correlation between the mechanochemical amorphization and the introduction of defects as observed by Bennett et al. in zirconia-based MOFs.[38]

The established BET surface area of the here prepared bimetallic c-ZnCu-MOF-74 is about 660 m^2/g, which is slightly lower than the reference (910 m^2/g).[20] There is a large difference in porosity between the crystalline and amorphous samples (Figure 3). The surface area of a-ZnCu-MOF-74 is 250 times lower than the surface area of c-ZnCu-MOF-74 (2.6 m^2/g). Also, the pore volume of materials drops from 0.56 cm^3/g in c-ZnCu-MOF-74 to 0.029 cm^3/g after the mechanochemical treatment. Mechanochemical incorporation of defects to activated c-ZnCu-MOF-74 thus leads to the fast collapse of the open and porous MOF-74 structure, as already observed for Ni- and Zn-MOF-74.[25]

The difference in guest accommodation properties for two materials is also visible from thermogravimetric analysis (TGA).
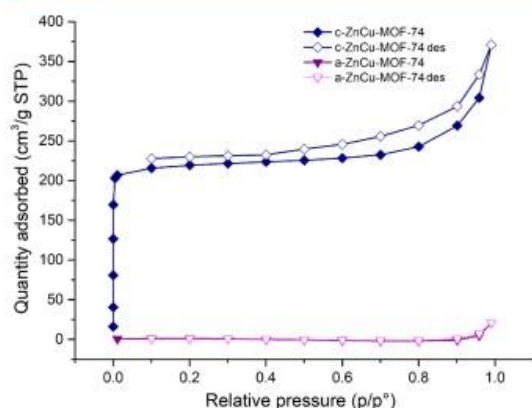
Figure 3. Nitrogen adsorption−desorption isotherms measured at 77 K for crystalline and amorphous ZnCu-MOF-74 catalysts prepared by mechanochemical processing.

The initial mass loss in c-ZnCu-MOF-74 starts almost immediately upon heating, denoting the loss of MeOH and water guests from the channels (Figures S7 and S8). Amorphous a-ZnCu-MOF-74 exhibits a less pronounced step in the same temperature region due to the presence of a limited amount of guests in the collapsed MOF structure. Both materials show similar decomposition profiles in the range of 400−900 °C,

indicating that the collapse of the long-range ordering had little effect on the thermal stability of ZnCu-MOF-74 materials.

In order to probe local ordering of metals in c-ZnCu-MOF-74 and a-ZnCu-MOF-74 solid catalysts, we utilized solid-state nuclear magnetic resonance spectroscopy.[39,40] As evident from Figure 4, neither the ^{13}C MAS NMR spectrum of c-ZnCu-MOF-74 nor the spectrum of a-ZnCu-MOF-74 is a simple sum of the spectra of Zn-MOF-74 and Cu-MOF-74. This indicates that the two bimetallic samples are not mixtures of two single-metal phases and are not composed only of single-metal domains. The ^{13}C MAS NMR spectra of c-ZnCu-MOF-74 and a-ZnCu-MOF-74 are rather similar but not identical to one another. They both exhibit several narrow signals in the range between 0 and 240 ppm and several broad signals in the range between 0 and 800 ppm. The narrow signals belong to carbon atoms in diamagnetic amorphous species. In the spectrum of a-ZnCu-MOF-74, the signals at 18, 45, 52, and 178 ppm belong to PMMA, an impurity introduced by milling, whereas the signals at 123, 155, and 170 ppm belong to domains of amorphous Zn-MOF-74. There is an additional narrow signal present at about 213 ppm, which might correspond to the unbound and deprotonated −COO[−] groups of the linker molecules. The broad signals belong to carbon atoms, which are close to paramagnetic Cu centers. Strong hyperfine coupling among the unpaired electronic spins of copper ions and nuclear spins of ^{13}C nuclei gives rise to huge shifts and broadening of these signals. The number, the positions, and the widths of the broad signals of c-ZnCu-MOF-74 and a-ZnCu-MOF-74 are different from those in the
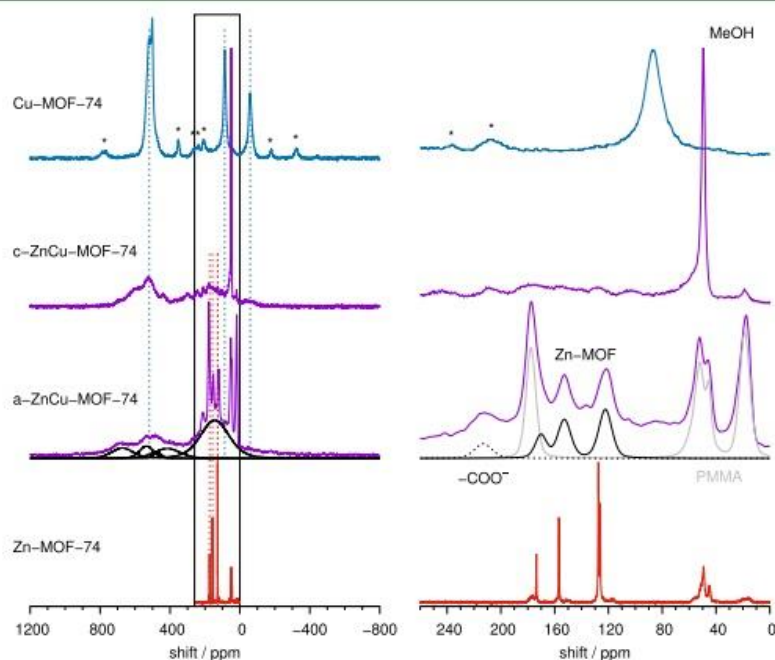

Figure 4. ^{13}C MAS NMR spectra of c-ZnCu-MOF-74 and a-ZnCu-MOF-74, compared to the corresponding spectra of the crystalline Zn-MOF-74 and Cu-MOF-74. The left panel shows full spectra; asterisks above the spectrum of Cu-MOF-74 mark the spinning sidebands; in the spectrum of a-ZnCu-MOF-74 individual broad contributions, as identified by the spectral deconvolution, are shown by black solid lines; red and blue vertical dotted lines mark the positions of the ^{13}C signals of Zn-MOF-74 and Cu-MOF-74, respectively. The right panel shows only a selected part of the spectra; contributions of MeOH, Zn-MOF-74 domains, PMMA impurities, and potential −COO[−] groups are denoted.

spectrum of the pure crystalline Cu-MOF-74. This strongly suggests that Zn and Cu atoms are partially well-dispersed and "intimately" mixed within the two mixed-metal frameworks, giving rise to a number of different chemical environments for the nearby carbon atoms. As already mentioned, ^{13}C MAS NMR spectra of c-ZnCu-MOF-74 and a-ZnCu-MOF-74 are somewhat different from one another. In the spectrum of the crystalline material, we can notice a strong, sharp signal of MeOH, which is not present in the spectrum of the amorphous material. More interestingly, the spectra of the two bimetallic samples exhibit differences also in the broad signals resonating in the range between 300 and 800 ppm; these complies with the results of the IR analysis indicating that the connectivity of Zn and Cu within the frameworks of the crystalline and amorphous ZnCu-MOF-74 is somewhat different.

Mechanochemical synthesis afforded the c-ZnCu-MOF-74 material particles with an irregular shape and a broad size ranging from 10 to 80 nm (Figure 5a,b). Based on the performed
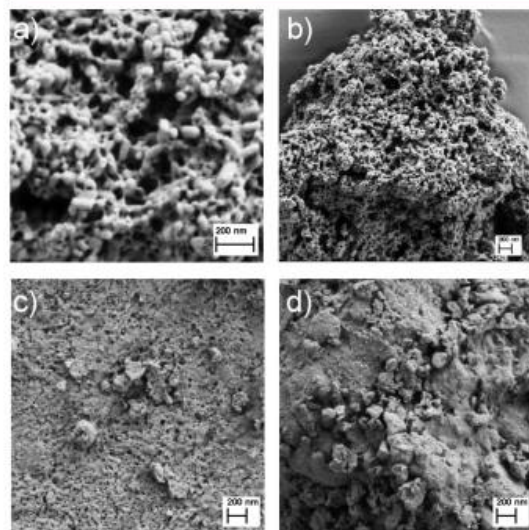
Figure 5. (a) SEM micrographs for (a,b) crystalline ZnCu-MOF-74; (c) amorphous ZnCu-MOF-74; and (d) amorphous ZnCu-MOF-74 after catalysis.

SEM−EDS analysis, both the crystalline and amorphous ZnCu-MOF-74 materials have homogeneous distribution and similar loading of copper and zinc metals on the surface (Figures S9−S11). The crystalline sample exhibits a hierarchical structure of separated porous MOF particles thus showing potential for excellent gas transport properties. On the other hand, amorphization changes the catalyst morphology and the a-ZnCu-MOF-74 material consists of smaller particles of an average size of 5−30 nm, which are dispersed without much agglomeration (Figure 5c). This arrangement may assist in allowing the direct access of gases to Cu- and Zn-based phases on the catalyst surface. After the catalytic process, the amorphous particles form conglomerates with a diameter of 50−200 nm, which again consisted of nanosized MOF particles (Figure 5d).

During CO_2 reduction using MOF samples, we observed a formation of H_2O, CO, and MeOH. Compared to the

monometallic Cu-MOF-74 catalyst, the activity toward MeOH synthesis increased by 4−6 times when using the bimetallic c-ZnCu-MOF-74 (Figure 6). It is already established that zinc
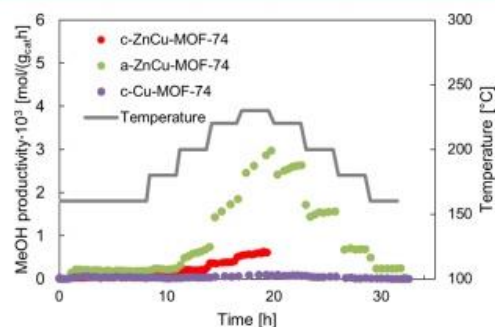

Figure 6. Evolution of MeOH molar productivity during the catalytic experiments.

increases the binding energy of the reaction intermediates on the Cu surface in commercial catalysts, causing the formation of more active catalytic sites by lowering activation energy of critical elementary steps toward MeOH.[3] One important factor for the activity of the commercial CuZnAl catalyst is the high surface area of active copper species achieved by dispersion in the ZnO/Al_2O_3 matrix. We expected here the crystalline and highly porous c-ZnCu-MOF-74 to readily compete with the commercial CuZnAl catalyst. However, the observed catalytic methanol production rise further when using amorphous a-ZnCu-MOF-74, with a collapsed structure and very low porosity (Figure 6). The activity of a-ZnCu-MOF-74 even increases during the catalytic test at 230 °C. The MeOH molar fraction increased in 2 h by 1, 5, and 21% for Cu, c-ZnCu, and a-ZnCu(-MOF-74) at 230 °C, respectively. A large increase of the MeOH synthesis rate with a-ZnCu-MOF-74 is highly likely due to the lack of rigid structure, active metal sites on disordered MOF surfaces, and the sintering of Cu particles, which all cause a MeOH TOF increase.[41,42] The change of the reaction rate was much lower when catalytic tests were repeated by lowering the temperature down to 160 °C (Figure 6). Overall, the c-ZnCu-MOF-74 sample activity increased by 4−7 fold after amorphization. The surface area of a-ZnCu-MOF-74 is about 250-times lower than the one of the crystalline sample which points to the fact that for this industrial setup, the introduction of defects in the MOF catalyst enables the creation of more active sites for MeOH synthesis and plays more important role than the well-ordered and porous MOF architecture. The PXRD analysis of the catalyst after the catalytic cycle reveals traces of copper NPs in the amorphous matrix (Figure S12).

The impact of the catalyst structure and composition on the catalytic properties was examined using the Arrhenius plot (Figure 7). The concentration of MeOH and CO of the last four stable points at a single temperature step was averaged and plotted. The CO concentration below 10^{-3}% could not be determined due to experimental limitations. The apparent activation energies (E_a) were determined at temperatures below 200 °C to avoid mistakes due to the possible mass transfer limitation or proximity to equilibrium. Due to the high gas flow rate (WHSV = 33,000 $NmL/g_{cat}h$), the CO_2 conversion at the highest conversion of the MOF is low (0.9% for a-ZnCu-MOF-74). Therefore, the decrease of the MeOH productivity due to
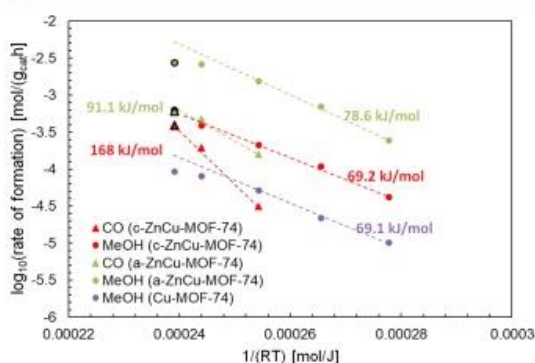
Figure 7. Comparison of the catalytic activities of different MOFs. E_a is determined in the low temperature range to avoid an apparent decrease of E_a due to reaction proximity to chemical equilibrium. The circled points with the black line indicates points that did not reach the steady state.

the proximity to the chemical equilibrium at high temperature is not expected. It is observed that at higher temperatures, the log of the rate of MeOH formation for a-ZnCu-MOF-74 and Cu-MOF-74 deviates from linear Arrhenius correlation, indicating intraparticle mass transfer limitation.[43,44] Artificial linear correlation at $T > 200$ °C is observed for c-ZnCu-MOF-74 because the data points obtained are from the part of the catalytic tests where the temperature is increased, causing morphology change and increased activity. The apparent activation energy and preexponential factor of CO_2 to CO reaction (RWGS) are much higher for c-ZnCu-MOF-74 in comparison to the a-ZnCu-MOF-74 catalyst, pointing to a large difference in the reaction mechanism. The rate of competitive RWGS reaction of the crystalline sample increases nearly up to the rate of MeOH synthesis at 230 °C.

The Table 1 contains E_a, pre-exponential factors A, and the rates of MeOH and CO synthesis (r), including comparison with the commercial CuZnAl catalyst. It is observed that the activation energy for methanol synthesis catalyzed by MOF samples is similar to the one when using the CuZnAl catalyst. The catalytic properties for CO formation of a-ZnCu-MOF-74 sample are very special with a large difference in the value of apparent activation energy (91.1 kJ/mol) comparing to the CuZnAl sample (149 kJ/mol). This could occur due to a difference in the exposure of the terminal crystal plane of Cu since apparent energy for CO formation varies from 78 kJ/mol on Cu(110) to 135 kJ/mol on polycrystalline Cu, while it is significantly more constant for MeOH synthesis where it varies between 67 and 77 kJ/mol for Cu(110) and polycrystalline Cu, respectively.[45]

The selectivity toward MeOH therefore increases by defects introduced into the bimetallic MOF structure (Figure 8),
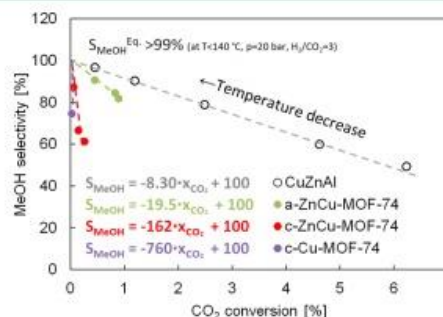

Figure 8. MeOH selectivity (S_{MeOH}) at the same CO_2 conversion (x_{CO_2}) increases in order: Cu-MOF-74 < c-ZnCu-MOF-74 < a-ZnCu-MOF-74 < CuZnAl. Commercial CuZnAl catalyst is, as expected, objectively more selective at certain catalyst activity. a-ZnCu-MOF-74 displays significantly higher selectivity than crystalline c-ZnCu-MOF-74. MeOH selectivity converges to 100% at zero CO_2 conversion as expected by the chemical equilibrium by decreasing the temperature below 140 °C as determined using Gaseq.[46]

allowing copper phase agglomeration, which is also in line with the conclusions about the basis for activity of the industrial CuZnAl catalyst. The performance enhancing parameters in the CuZnAl system are the presence of the Cu surface plane steps by increasing the Cu particle size[41,42] and strong metal-support interaction which enables high degree of Cu substitution with Zn atoms and consequently favorable binding of reaction intermediates.[3,47] Addition of Zn to the c-Cu-MOF-74 increases MeOH synthesis selectivity by 4.7 times which is a consequence of incorporation of Zn into the active Cu phase. The amorphization of c-ZnCu-MOF-74 decreases the surface area but also reduces the particle sizes and changes the coordination sphere of the metal nodes in MOF-74, thus increasing the MeOH selectivity by a factor of 8.3. Separated Cu atoms or small Cu clusters in the crystalline MOF tend to promote the competitive RWGS reaction, while the amorphization leads to the promotion of methanol synthesis.

■ CONCLUSIONS

To summarize, unlike the monometallic Cu-MOF-74, bimetallic crystalline ZnCu-MOF-74 prepared by the mechanochemical procedure shows activity for the catalytic reduction of CO_2 to methanol. Mechanochemical treatment of the activated and degassed crystalline ZnCu-MOF-74 results in the formation of amorphous and non-porous a-ZnCu-MOF-74 with similar distribution of heterometal nodes as in the crystalline phase.

Table 1. Values of E_a, A, and r Parameters for MeOH and CO Formation at 200 °C[a]

sample	MeOH			CO		
	E_a*	log(A)**	r(200 °C)**	E_a*	log(A)**	r(200 °C)**
a-ZnCu-MOF-74	78.6	5.9	1.6×10^{-3}	91.1	6.3	1.1×10^{-4}
c-ZnCu-MOF-74	69.2	4.0	2.2×10^{-4}	168	14.0	3.2×10^{-5}
c-Cu-MOF-74	69.1	3.3	5.0×10^{-5}	na	na	na
CuZnAl	62.8	4.8	7.4×10^{-3}	149	13.8	2.0×10^{-3}

[a]*unit kJ/mol, ** unit mol/(g_{cat}h).

The spectroscopic analyses show that the coordination sphere of the nodes is changed upon amorphization, most likely due to breaking of carboxylate—metal bonds. The catalyst activity is significantly higher for the amorphous ZnCu-MOF-74 than the crystalline counterpart due to the additional active sites formed during the amorphization. More importantly, the selectivity of process changes upon amorphization of c-ZnCu-MOF-74. In reaction catalyzed by amorphous ZnCu-MOF-74, the selectivity toward methanol formation is comparable even to the industrial $Cu/ZnO/Al_2O_3$ benchmark. For the methanol synthesis reaction, the introduction of defects *via* amorphization thus seems to be more important than the catalyst porosity, revealing that the CO_2 reduction is conducted on the surface of the MOF catalyst. Our future work will be directed toward exploiting the potential of mechanochemical MOF transformations[28] for expanding the portfolio of catalytically active non-conventional MOF materials.

■ ASSOCIATED CONTENT

Ⓢ Supporting Information

The Supporting Information is available free of charge at https://pubs.acs.org/doi/10.1021/acsami.0c21265.

Characterization data (PXRD, IR, DSC, TGA, and SEM) for all new compounds (PDF)

■ AUTHOR INFORMATION

Corresponding Authors

Blaž Likozar − *National Institute of Chemistry, SI-1001 Ljubljana, Slovenia;* ⦿ orcid.org/0000-0001-7226-4302; Email: blaz.likozar@ki.si

Krunoslav Užarević − *Ruđer Bošković Institute, 10000 Zagreb, Croatia;* ⦿ orcid.org/0000-0002-7513-6485; Email: krunoslav.uzarevic@irb.hr

Authors

Tomislav Stolar − *Ruđer Bošković Institute, 10000 Zagreb, Croatia;* ⦿ orcid.org/0000-0002-9824-4462

Anže Prašnikar − *National Institute of Chemistry, SI-1001 Ljubljana, Slovenia*

Valentina Martinez − *Ruđer Bošković Institute, 10000 Zagreb, Croatia*

Bahar Karadeniz − *Ruđer Bošković Institute, 10000 Zagreb, Croatia*

Ana Bjelić − *National Institute of Chemistry, SI-1001 Ljubljana, Slovenia*

Gregor Mali − *National Institute of Chemistry, SI-1001 Ljubljana, Slovenia;* ⦿ orcid.org/0000-0002-9012-2495

Tomislav Friščić − *Ruđer Bošković Institute, 10000 Zagreb, Croatia; McGill University, H3A 0B8 West Montréal, Québec, Canada;* ⦿ orcid.org/0000-0002-3921-7915

Complete contact information is available at: https://pubs.acs.org/10.1021/acsami.0c21265

Author Contributions

‖T.S. and A.P. contributed equally.

Notes

The authors declare the following competing financial interest(s): Krunoslav Užarević is a share-holder in InSolido Technologies.

■ REFERENCES

(1) Porosoff, M. D.; Yan, B.; Chen, J. G. Catalytic reduction of CO_2 by H_2 for synthesis of CO, methanol and hydrocarbons: challenges and opportunities. *Energy Environ. Sci.* **2016**, *9*, 62−73.

(2) Goeppert, A.; Czaun, M.; Jones, J.-P.; Surya Prakash, G. K.; Olah, G. A. Recycling of carbon dioxide to methanol and derived products − closing the loop. *Chem. Soc. Rev.* **2014**, *43*, 7995−8048.

(3) Behrens, M.; Studt, F.; Kasatkin, I.; Kuhl, S.; Havecker, M.; Abild-Pedersen, F.; Zander, S.; Girgsdies, F.; Kurr, P.; Kniep, B.-L.; Tovar, M.; Fischer, R. W.; Norskov, J. K.; Schlogl, R. The Active Site of Methanol Synthesis over $Cu/ZnO/Al_2O_3$ Industrial Catalysts. *Science* **2012**, *336*, 893−897.

(4) Huš, M.; Dasireddy, V. D. B. C.; Štefančič, N. S.; Likozar, B. Mechanism, kinetics and thermodynamics of carbon dioxide hydrogenation to methanol on $Cu/ZnAl_2O_4$ spinel-type heterogeneous catalysts. *Appl. Catal., B* **2017**, *207*, 267−278.

(5) An, B.; Zhang, J.; Cheng, K.; Ji, P.; Wang, C.; Lin, W. Confinement of Ultrasmall Cu/ZnO_x Nanoparticles in Metal-Organic Frameworks for Selective Methanol Synthesis from Catalytic Hydrogenation of CO_2. *J. Am. Chem. Soc.* **2017**, *139*, 3834−3840.

(6) Huš, M.; Kopač, D.; Likozar, B. Catalytic Hydrogenation of Carbon Dioxide to Methanol: Synergistic Effect of Bifunctional Cu/perovskite Catalysts. *ACS Catal.* **2019**, *9*, 105−116.

(7) Gaikwad, R.; Reymond, H.; Phongprueksathat, N.; Rudolf von Rohr, P.; Urakawa, A. From CO or CO_2?: space-resolved insights into high-pressure CO_2 hydrogenation to methanol over $Cu/ZnO/Al_2O_3$. *Catal. Sci. Technol.* **2020**, *10*, 2763−2768.

(8) Kurtz, M.; Wilmer, H.; Genger, T.; Hinrichsen, O.; Muhler, M. Deactivation of Supported Copper Catalysts for Methanol Synthesis. *Catal. Lett.* **2003**, *86*, 77−80.

(9) Prašnikar, A.; Pavlišič, A.; Ruiz-Zepeda, F.; Kovač, J.; Likozar, B. Mechanisms of Copper-Based Catalyst Deactivation during CO_2 Reduction to Methanol. *Ind. Eng. Chem. Res.* **2019**, *58*, 13021−13029.

(10) Gascon, J.; Corma, A.; Kapteijn, F.; Llabrés i Xamena, F. X. Metal Organic Framework Catalysis: Quo vadis? *ACS Catal.* **2014**, *4*, 361−378.

(11) Yang, D.; Gates, B. C. Catalysis by Metal Organic Frameworks: Perspective and Suggestions for Future Research. *ACS Catal.* **2019**, *9*, 1779−1798.

(12) Chen, L.; Wang, H.-F.; Li, C.; Xu, Q. Bimetallic metal−organic frameworks and their derivatives. *Chem. Sci.* **2020**, *11*, 5369−5403.

(13) Abednatanzi, S.; Gohari Derakhshandeh, P.; Depauw, H.; Coudert, F.-X.; Vrielinck, H.; Van Der Voort, P.; Leus, K. Mixed-metal metal−organic frameworks. *Chem. Soc. Rev.* **2019**, *48*, 2535−2565.

(14) Rosi, N. L.; Kim, J.; Eddaoudi, M.; Chen, B.; O'Keeffe, M.; Yaghi, O. M. Rod Packings and Metal-Organic Frameworks Constructed from Rod-Shaped Secondary Building Units. *J. Am. Chem. Soc.* **2005**, *127*, 1504−1518.

(15) Dietzel, P. D. C.; Panella, B.; Hirscher, M.; Blom, R.; Fjellvåg, H. Hydrogen adsorption in a nickel based coordination polymer with open metal sites in the cylindrical cavities of the desolvated framework. *Chem. Commun.* **2006**, 959−961.

(16) Rowsell, J. L. C.; Yaghi, O. M. Effects of Functionalization, Catenation, and Variation of the Metal Oxide and Organic Linking Units on the Low-Pressure Hydrogen Adsorption Properties of Metal-Organic Frameworks. *J. Am. Chem. Soc.* **2006**, *128*, 1304−1315.

(17) Botas, J. A.; Calleja, G.; Sánchez-Sánchez, M.; Orcajo, M. G. Effect of Zn/Co ratio in MOF-74 type materials containing exposed metal sites on their hydrogen adsorption behaviour and on their band gap energy. *Int. J. Hydrogen Energy* **2011**, *36*, 10834−10844.

(18) Jiao, Y.; Morelock, C. R.; Burtch, N. C.; Mounfield, W. P.; Hungerford, J. T.; Walton, K. S. Tuning the Kinetic Water Stability and Adsorption Interactions of Mg-MOF-74 by Partial Substitution with Co or Ni. *Ind. Eng. Chem. Res.* **2015**, *54*, 12408−12414.

(19) Wang, L. J.; Deng, H.; Furukawa, H.; Gándara, F.; Cordova, K. E.; Peri, D.; Yaghi, O. M. Synthesis and Characterization of Metal-Organic Framework-74 Containing 2, 4, 6, 8, and 10 Different Metals. *Inorg. Chem.* **2014**, *53*, 5881−5883.

(20) Ayoub, G.; Karadeniz, B.; Howarth, A. J.; Farha, O. K.; Đilović, I.; Germann, L. S.; Dinnebier, R. E.; Užarević, K.; Friščić, T. Rational Synthesis of Mixed-Metal Microporous Metal-Organic Frameworks with Controlled Composition Using Mechanochemistry. *Chem. Mater.* **2019**, *31*, 5494−5501.

(21) Rungtaweevoranit, B.; Baek, J.; Araujo, J. R.; Archanjo, B. S.; Choi, K. M.; Yaghi, O. M.; Somorjai, G. A. Copper Nanocrystals Encapsulated in Zr-based Metal-Organic Frameworks for Highly Selective CO$_2$ Hydrogenation to Methanol. *Nano Lett.* **2016**, *16*, 7645−7649.

(22) Kobayashi, H.; Taylor, J. M.; Mitsuka, Y.; Ogiwara, N.; Yamamoto, T.; Toriyama, T.; Matsumura, S.; Kitagawa, H. Charge transfer dependence on CO$_2$ hydrogenation activity to methanol in Cu nanoparticles covered with metal−organic framework systems. *Chem. Sci.* **2019**, *10*, 3289−3294.

(23) Gutterød, E. S.; Lazzarini, A.; Fjermestad, T.; Kaur, G.; Manzoli, M.; Bordiga, S.; Svelle, S.; Lillerud, K. P.; Skúlason, E.; Øien Ødegaard, S.; Nova, A.; Olsbye, U. Hydrogenation of CO2 to Methanol by Pt Nanoparticles Encapsulated in UiO-67: Deciphering the Role of the Metal−Organic Framework. *J. Am. Chem. Soc.* **2020**, *142*, 999−1009.

(24) Julien, P. A.; Mottillo, C.; Friščić, T. Metal−organic frameworks meet scalable and sustainable synthesis. *Green Chem.* **2017**, *19*, 2729−2747.

(25) Muratović, S.; Karadeniz, B.; Stolar, T.; Lukin, S.; Halasz, I.; Herak, M.; Mali, G.; Krupskaya, Y.; Kataev, V.; Žilić, D.; Užarević, K. Impact of dehydration and mechanical amorphization on the magnetic properties of Ni(II)-MOF-74. *J. Mater. Chem. C* **2020**, *8*, 7132−7142.

(26) James, S. L.; Adams, C. J.; Bolm, C.; Braga, D.; Collier, P.; Friščić, T.; Grepioni, F.; Harris, K. D. M.; Hyett, G.; Jones, W.; Krebs, A.; Mack, J.; Maini, L.; Orpen, A. G.; Parkin, I. P.; Shearouse, W. C.; Steed, J. W.; Waddell, D. C. Mechanochemistry: opportunities for new and cleaner synthesis. *Chem. Soc. Rev.* **2012**, *41*, 413−447.

(27) Friščić, T.; Do, J.-L. Chemistry 2.0: Developing a New, Solvent-Free System of Chemical Synthesis Based on Mechanochemistry. *Synlett* **2017**, *28*, 2066−2092.

(28) Stolar, T.; Užarević, K. Mechanochemistry: an efficient and versatile toolbox for synthesis, transformation, and functionalization of porous metal−organic frameworks. *CrystEngComm* **2020**, *22*, 4511−4525.

(29) Pichon, A.; James, S. L. An array-based study of reactivity under solvent-free mechanochemical conditions—insights and trends. *CrystEngComm* **2008**, *10*, 1839.

(30) Beldon, P. J.; Fábián, L.; Stein, R. S.; Thirumurugan, A.; Cheetham, A. K.; Friščić, T. Rapid Room-Temperature Synthesis of Zeolitic Imidazolate Frameworks by Using Mechanochemistry. *Angew. Chem., Int. Ed.* **2010**, *49*, 9640−9643.

(31) Julien, P. A.; Užarević, K.; Katsenis, A. D.; Kimber, S. A. J.; Wang, T.; Farha, O. K.; Zhang, Y.; Casaban, J.; Germann, L. S.; Etter, M.; Dinnebier, R. E.; James, S. L.; Halasz, I; Friščić, T. In Situ Monitoring and Mechanism of the Mechanochemical Formation of a Microporous MOF-74 Framework. *J. Am. Chem. Soc.* **2016**, *138*, 2929−2932.

(32) Užarević, K.; Wang, T. C.; Moon, S.-Y.; Fidelli, A. M.; Hupp, J. T.; Farha, O. K.; Friščić, T. Mechanochemical and solvent-free assembly of zirconium-based metal−organic frameworks. *Chem. Commun.* **2016**, *52*, 2133−2136.

(33) Crawford, D.; Casaban, J.; Haydon, R.; Giri, N.; Mcnally, T.; James, S. L. Synthesis by extrusion: continuous, large-scale preparation of MOFs using little or no solvent. *Chem. Sci.* **2015**, *6*, 1645−1649.

(34) Karadeniz, B.; Howarth, A. J.; Stolar, T.; Islamoglu, T.; Dejanović, I.; Tireli, M.; Wasson, M. C.; Moon, S.-Y.; Farha, O. K.; Friščić, T.; Užarević, K. Benign by Design: Green and Scalable Synthesis of Zirconium UiO-MetalOrganic Frameworks by Water-Assisted Mechanochemistry. *ACS Sustainable Chem. Eng.* **2018**, *6*, 15841.

(35) Panda, T.; Horike, S.; Hagi, K.; Ogiwara, N.; Kadota, K.; Itakura, T.; Tsujimoto, M.; Kitagawa, S. Mechanical Alloying of Metal−Organic Frameworks. *Angew. Chem., Int. Ed.* **2017**, *56*, 2413−2417.

(36) Lee, J.-S. M.; Fujiwara, Y.-I.; Kitagawa, S.; Horike, S. Homogenized Bimetallic Catalysts from Metal−Organic Framework Alloys. *Chem. Mater.* **2019**, *31*, 4205−4212.

(37) Andreeva, A. B.; Le, K. N.; Chen, L.; Kellman, M. E.; Hendon, C. H.; Brozek, C. K. Soft Mode Metal-Linker Dynamics in Carboxylate MOFs Evidenced by Variable-Temperature Infrared Spectroscopy. *J. Am. Chem. Soc.* **2020**, *142*, 19291−19299.

(38) Bennett, T. D.; Todorova, T. K.; Baxter, E. F.; Reid, D. G.; Gervais, C.; Bueken, B.; Van de Voorde, B.; De Vos, D.; Keen, D. A.; Mellot-Draznieks, C. Connecting defects and amorphization in UiO-66 and MIL-140 metal−organic frameworks: a combined experimental and computational study. *Phys. Chem. Chem. Phys.* **2016**, *18*, 2192−2201.

(39) Mali, G.; Mazaj, M.; Arčon, I.; Hanžel, D.; Arčon, D.; Jagličić, Z. Unraveling the Arrangement of Al and Fe within the Framework Explains the Magnetism of Mixed-Metal MIL-100(Al,Fe). *J. Phys. Chem. Lett.* **2019**, *10*, 1464−1470.

(40) Brunner, E.; Rauche, M. Solid-state NMR spectroscopy: An advancing tool to analyse structure and properties of metal-organic frameworks. *Chem. Sci.* **2020**, *11*, 4297.

(41) van den Berg, R.; Prieto, G.; Korpershoek, G.; van der Wal, L. I.; van Bunningen, A. J.; Lægsgaard-Jørgensen, S.; de Jongh, P. E.; de Jong, K. P. Structure sensitivity of Cu and CuZn catalysts relevant to industrial methanol synthesis. *Nat. Commun.* **2016**, *7*, 13057.

(42) Karelovic, A.; Galdames, G.; Medina, J. C.; Yévenes, C.; Barra, Y.; Jiménez, R. Mechanism and structure sensitivity of methanol synthesis from CO$_2$ over SiO$_2$-supported Cu nanoparticles. *J. Catal.* **2019**, *369*, 415−426.

(43) Graaf, G. H.; Scholtens, H.; Stamhuis, E. J.; Beenackers, A. A. C. M. Intra-particle diffusion limitations in low-pressure methanol synthesis. *Chem. Eng. Sci.* **1990**, *45*, 773−783.

(44) Froment, G.; Bischoff, K.; De Wilde, J. *Chemical Reactor Analysis and Design*, 3rd ed.; John Wiley & Sons, Inc., 2010.

(45) Yoshihara, J.; Campbell, C. T. Methanol Synthesis and Reverse Water−Gas Shift Kinetics over Cu(110) Model Catalysts: Structural Sensitivity. *J. Catal.* **1996**, *161*, 776−782.

(46) Morley, C. *Gaseq v. 0.79.* 2005; www.gaseq.co.uk (accessed on 1.5.2019).

(47) Kuld, S.; Thorhauge, M.; Falsig, H.; Elkjaer, C. F.; Helveg, S.; Chorkendorff, I.; Sehested, J. Quantifying the promotion of Cu catalysts by ZnO for methanol synthesis. *Science* **2016**, *352*, 969−974.

128

Supporting Information for:

Mechanochemical amorphization of bimetallic MOF-74 catalyst for selective hydrogenation of CO_2 to methanol

Tomislav Stolar,[†,¶] Anže Prašnikar,[‡,¶] Valentina Martinez,[†] Bahar Karadeniz,[†] Ana Bjelić,[‡] Gregor Mali,[‡] Tomislav Friščić,[†,§] Blaž Likozar,[*,‡] and Krunoslav Užarević[*,†]

[†]*Ruđer Bošković Institute, Bijenička cesta 54, 10000 Zagreb, Croatia*

[‡]*National Institute of Chemistry, Hajdrihova 19, SI-1001 Ljubljana, Slovenia*

[¶]*These authors contributed equally*

[§]*McGill University, 801 Sherbrooke St. West Montréal, Québec H3A 0B8*

E-mail: blaz.likozar@ki.si; krunoslav.uzarevic@irb.hr

List of Figures

Materials

ZnO, Cu(OH)$_2$ and 2,5-dihydroxyterephtalic acid (H$_4$dhta) were obtained from Sigma-Aldrich. Methanol was purchased from Lach-ner.

Powder X-ray Diffraction (PXRD) analysis

PXRD data for all samples was analyzed by Panalytical Aeris Research tabletop X-ray diffractometer, with CuK_α radiation (40 kV, 7.5 mA) in Bragg-Bretano geometry, with the sample mounted on zero background silicon plate.

As it can be seen in Figures S1 and S2 resultant materials are of good crystallinity and phase pure. In the Figure S3 we can notice the change in PXRD pattern of ZnCu-MOF-74 upon desolvation and subsequent amorphization by neat grinding.
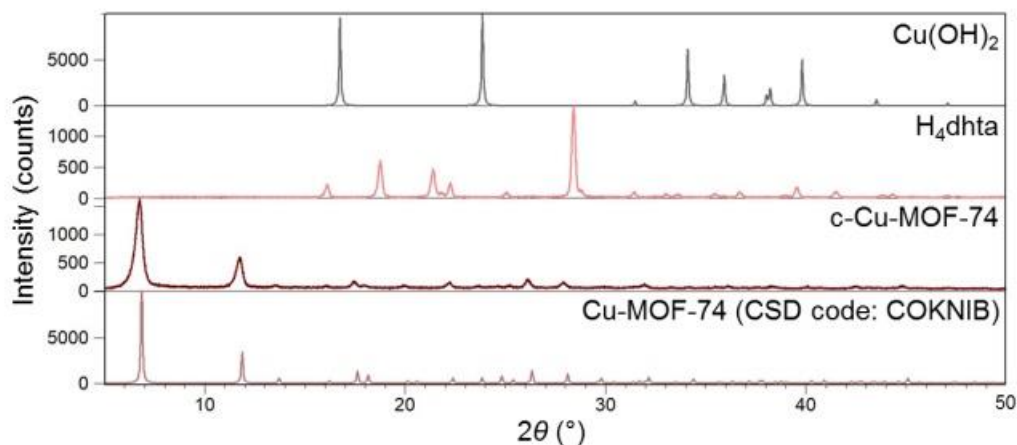
Figure S1: PXRD data for c-Cu-MOF-74, compared to the starting materials Cu(OH)$_2$ and H$_4$dhta and the calculated Cu-MOF-74 (CSD code COKNIB)

S3
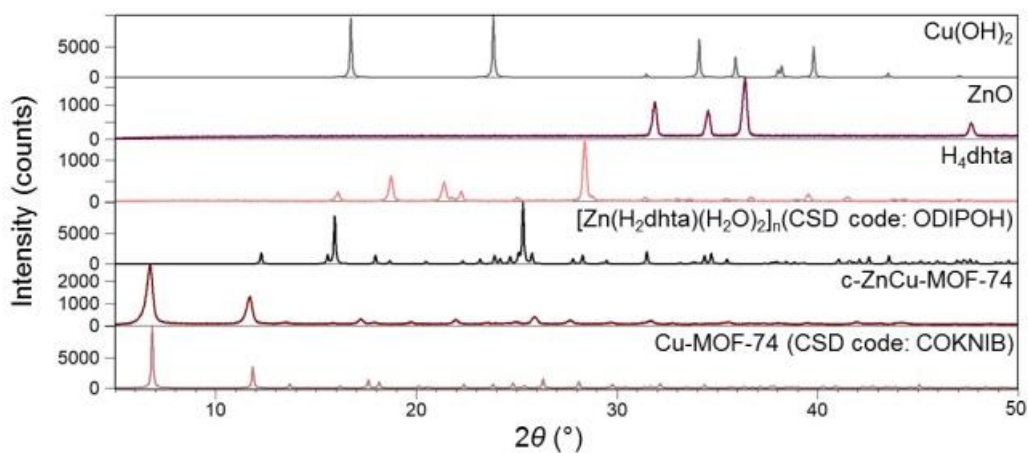
Figure S2: PXRD data for c-ZnCu-MOF-74, compared to the starting materials Cu(OH)$_2$, ZnO and H$_4$dhta as well as to the calculated intermediate structure [Zn(H$_2$dhta)(H$_2$O)]$_n$ (CSD code ODIPOH) and calculated Cu-MOF-74 (CSD code COKNIB)
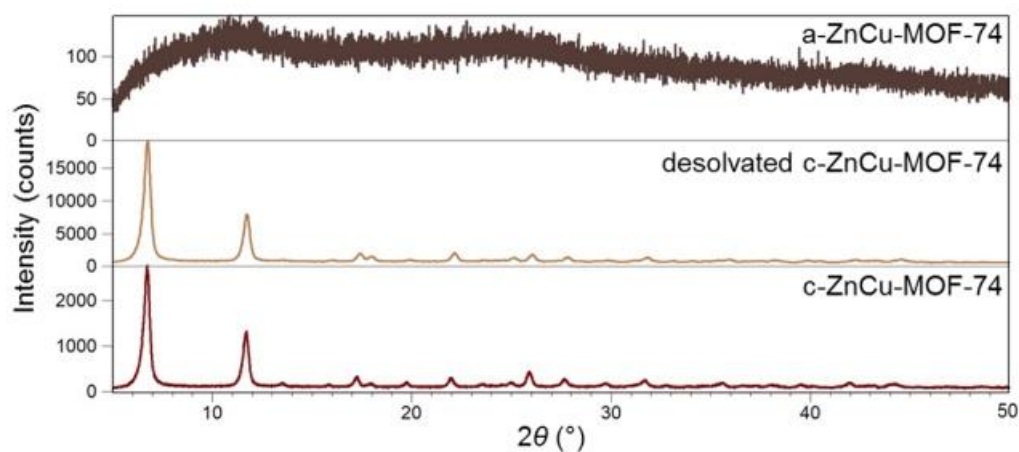

Figure S3: PXRD data for c-ZnCu-MOF-74, desolvated c-ZnCu-MOF-74 and a-ZnCu-MOF-74.

S4

Infrared Spectroscopy

Measurements were performed on a PerkinElmer Fourier transform infrared spectrometer Spectrum Two (PerkinElmer,Inc.) using Spectrum10 software (PerkinElmer, Inc.) in transmittance mode by FTIR-ATR technique.
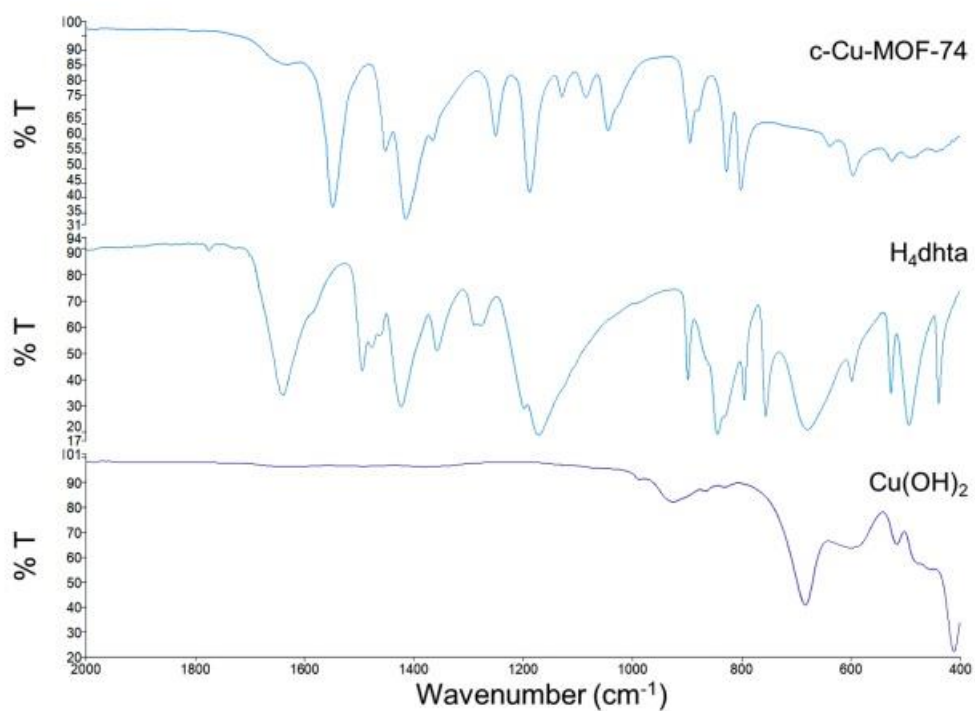
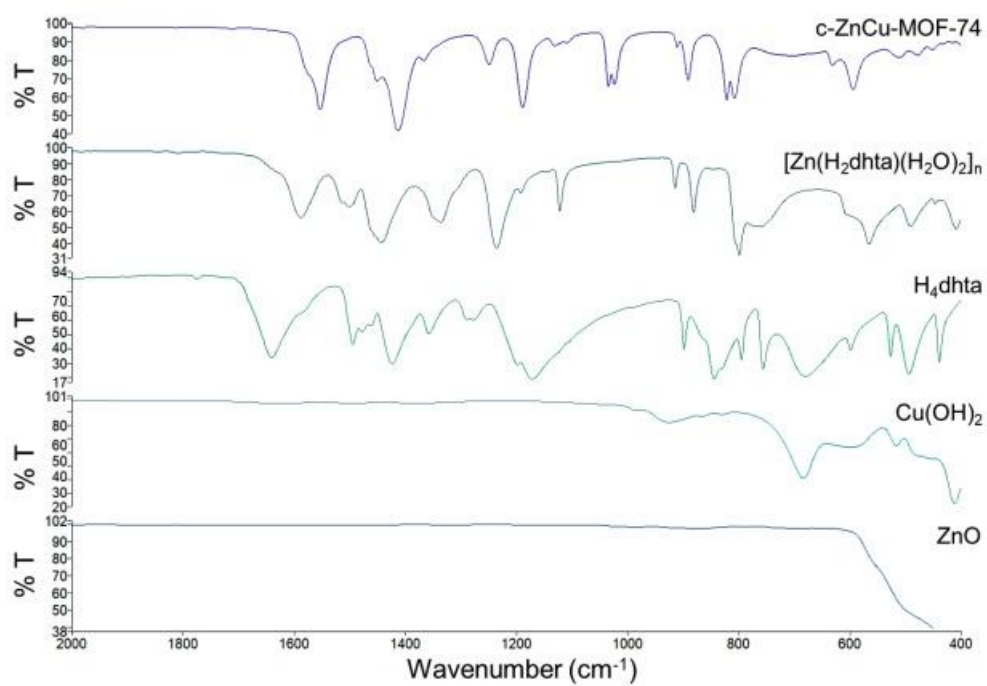Figure S4: FTIR-ATR data for Cu-MOF-74, compared to the starting materials $Cu(OH)_2$ and H_4dhta

Figure S5: FTIR-ATR data for c-ZnCu-MOF-74, compared to the starting materials $Cu(OH)_2$, ZnO and H_4dhta, and the intermediate phase $[Zn(H_2dhta)(H_2O)]_n$
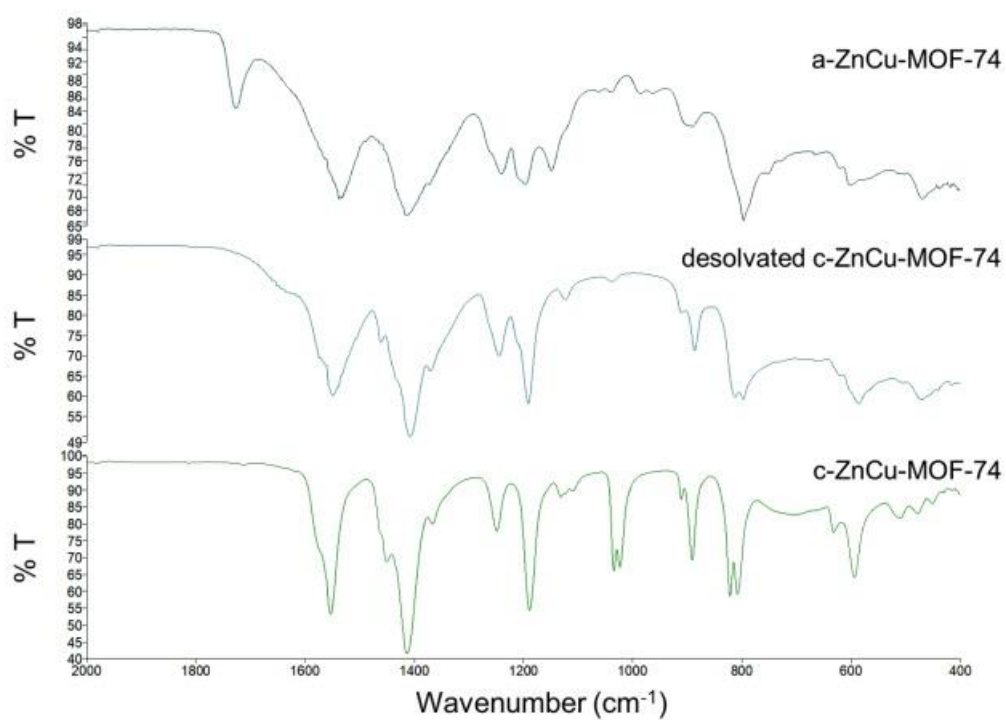
Figure S6: FTIR-ATR data for c-ZnCu-MOF-74, desolvated c-ZnCu-MOF-74, distinguished by the absence of characteristic methanol peak around 1020 cm^{-1} and a-ZnCu-MOF74 with additional peak around 1727 cm^{-1} assigned to the free carboxyl group

S7

Thermal Analysis (DSC & TGA)

TGA and DSC experiments were performed by Simultaneous thermal analyzer (STA) 6000 (PerkinElmer,Inc.) in alumina crucibles at $10°C$ min^{-1} heating rate from $35°C$ to $950°C$ under nitrogen gas purging at flow of 30 mL min^{-1}.
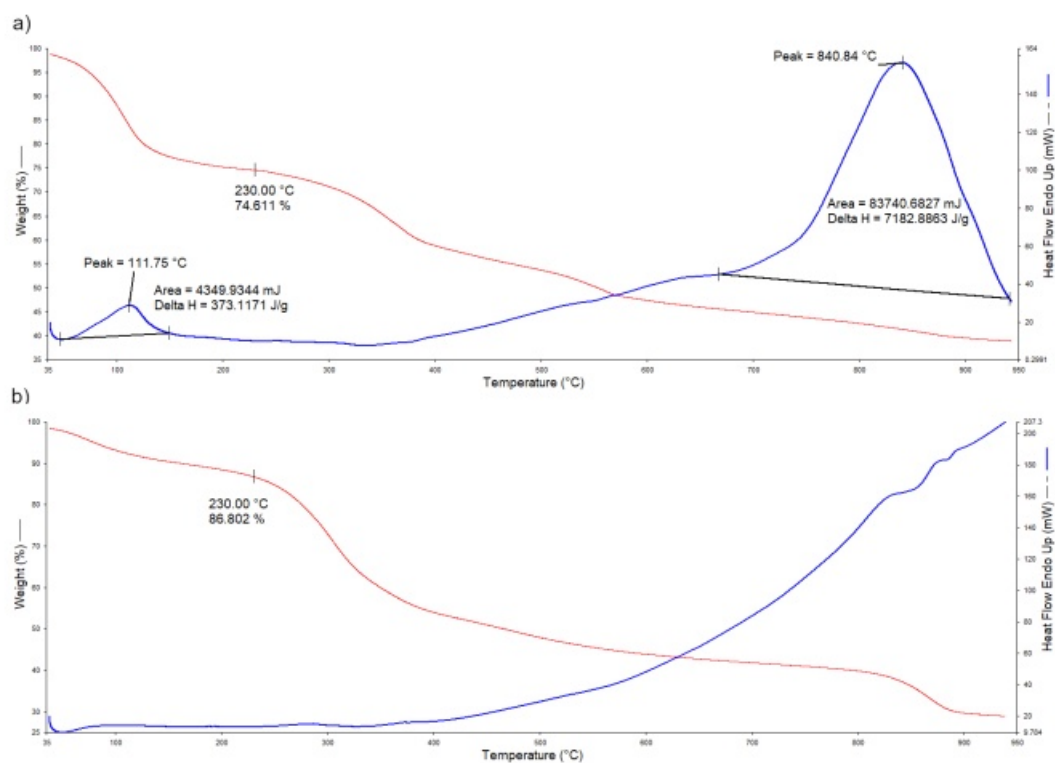

Figure S7: Simultaneous TGA (red coloured) and DSC (blue coloured) traces for: (a) c-ZnCu-MOF-74 and (b) a-ZnCu-MOF-74.
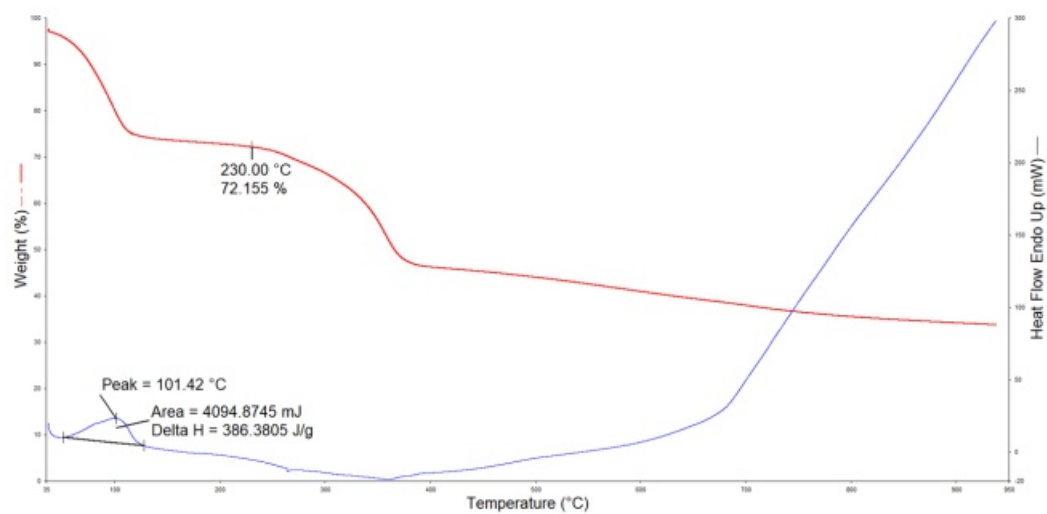
S8

Figure S8: Simultaneous TGA (red coloured) and DSC (blue coloured) traces for c-Cu-MOF-74

SEM-EDS

In the Figures S9 - S11 given below, we can observe the uniform dispersion of Zn and Cu over all MOF samples. The analyses were performed at 20 kV using 60 μm aperture and 5 minute exposure time. Note that the Cu and Zn distributions do not even change after the catalytic test as observed in Figure S11.
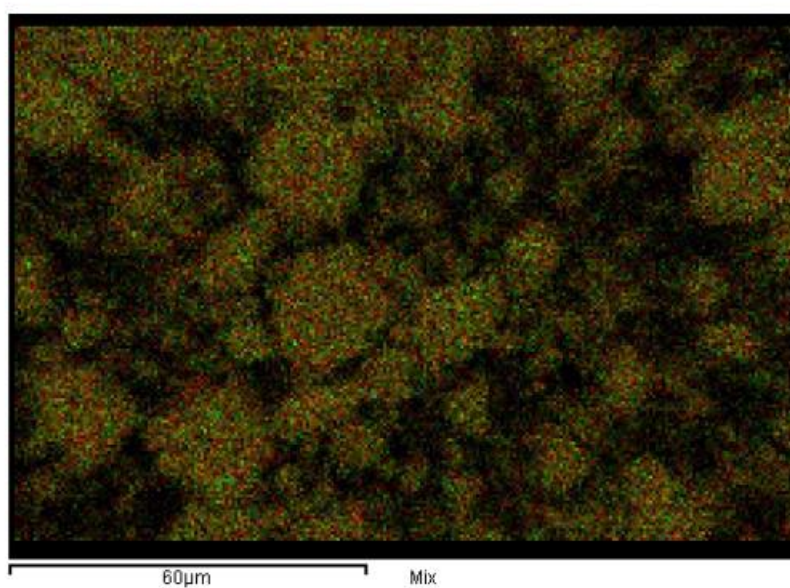

Figure S9: SEM-EDS micrographs of crystalline ZnCu-MOF-74. Green color represents Zn and red Cu.
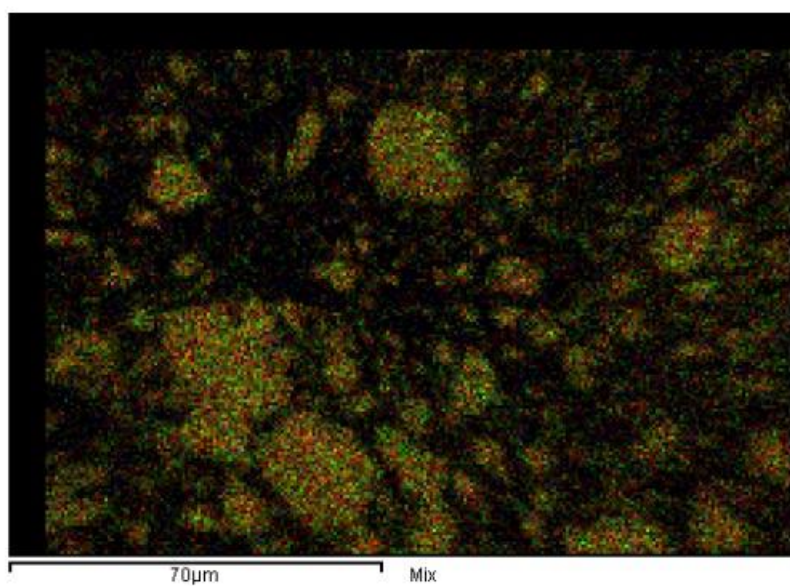
S10

Figure S10: SEM-EDS micrographs of amorphous ZnCu-MOF-74. Green color represents Zn and red Cu.
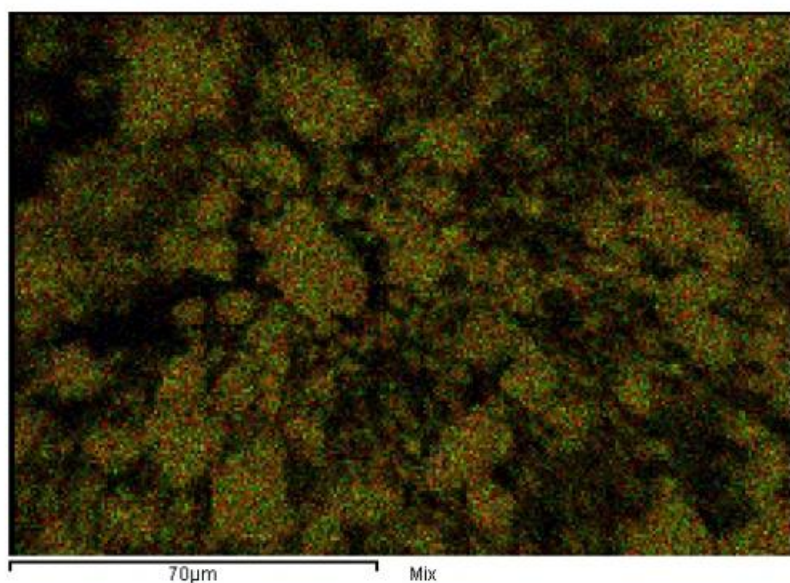

Figure S11: SEM-EDS micrographs of amorphous ZnCu-MOF-74 after catalysis. Green color represents Zn and red Cu.
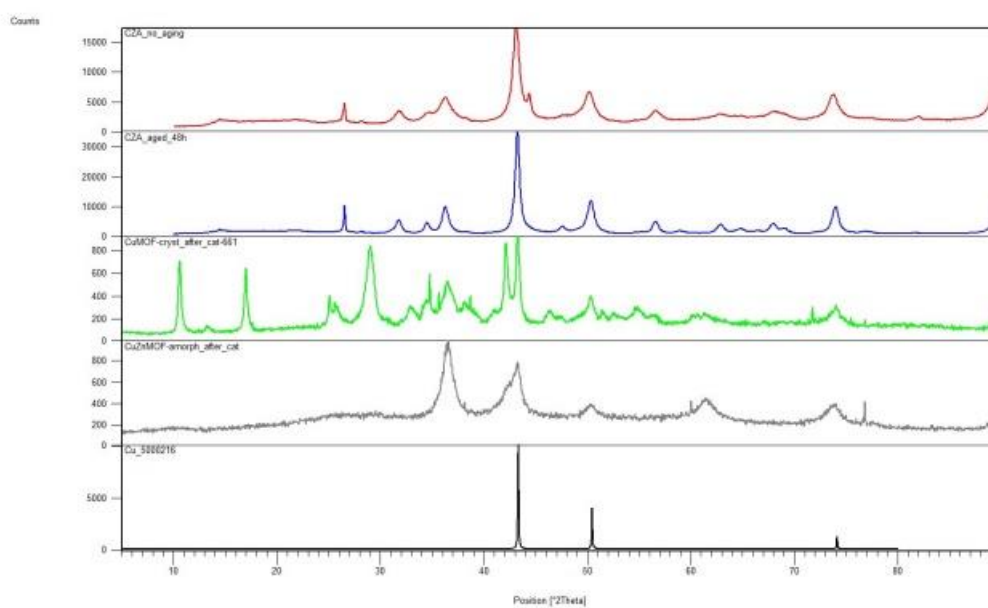
S11

Figure S12: PXRD of used catalysts after catalysis.

§ 8. CURRICULUM VITAE

Valentina Martinez, ████████████████████████████ completed her primary and secondary education in her hometown. In 2013, she enrolled in undergraduate studies in Chemistry at the Faculty of Science, University of Zagreb, and after completing them in 2017, she enrolled in graduate studies at the same institution. During her graduate studies, she conducted her Master's research under the supervision of Prof Vladimir Stilinović, PhD, in the group of Prof Dominik Cinčić, PhD. She completed her graduate studies in 2019 and, in the same year, enrolled in doctoral studies in Chemical Engineering and Applied Chemistry at the Faculty of Chemical Engineering and Technology, University of Zagreb. From December 2019 to December 2023, she was employed in the Laboratory for Applied and Sustainable Chemistry, Division of Physical Chemistry, Ruđer Bošković Institute. There, she worked under the supervision of Krunoslav Užarević, Scientific Adviser, PhD and collaborated on 2 research projects (PZS-2019-02-4129, IP-2020-02-4702), and mentored 2 students. Throughout her doctoral studies, she participated in 12 scientific conferences and co-authored 1 review paper and 8 scientific papers cited in the WoS and CC databases. Notably, 3 of those scientific papers received the RBI annual award for best publications (in 2020, 2021 and 2022).

List of publications:

*first author or co-first author

9) C. Ye, G. I. Lampronti, L. N. McHugh, C. Castillo-Blas, A. Kono, C. Chen, G. P. Robertson, L. A. V. Nagle-Cocco, W. Xu, S. D. Stranks, **V. Martinez**, I. Brekalo, B. Karadeniz, K. Užarević, W. Xue, P. Kolodzeiski, C. Das, P. Chater, D. A. Keen, S. E. Dutton, T. D. Bennett *Chem. Sci*. 15 (2024) 7198-7205; doi: 10.1039/D4SC00905C

8). N. Jakupec, K. J. Ardila-Fierro, **V. Martinez**, I. Halasz, J. Volavšek, G. Algara-Siller, M. Etter, V. Valtchev, K. Užarević, A. Palčić *ACS Sustainable Chem. Eng.* **12** (2024) 5220-5228; doi: 10.1021/acssuschemeng.3c08477

7) **V. Martinez***, T. Stolar*, B. Karadeniz, I. Brekalo, K. Užarević *Nat Rev Chem* **7** (2023), 51–65; doi: 10.1038/s41570-022-00442-1

6) S. Muratović*, **V. Martinez***, B. Karadeniz, D. Pajić, I. Brekalo, M. Arhangelskis, M. Mazaj, G. Mali, M. Etter, T. Friščić, Y. Krupskaya, V. Kataev, D. Žilić, K. Užarević *Inorg. Chem.* **61** (2022) 18181–18192; doi: 10.1021/acs.inorgchem.2c02898

5) I. Brekalo, **V. Martinez**, B. Karadeniz, P. Orešković, D. Drapanauskaite, H. Vriesema, R. Stenekes, M. Etter, I.Dejanović, J. Baltrusaitis, K. Užarević *ACS Sustainable Chem. Eng.* **10** (2022) 6743–6754; doi: 10.1021/acssuschemeng.2c00914

4) **V. Martinez***, N. Bedeković, V. Stilinović, D. Cinčić *Crystals* **11** (2021) 699; doi:10.3390/cryst11060699

3) T. Stolar, A. Prašnikar, **V. Martinez**, B. Karadeniz, A. Bjelić, G. Mali, T. Friščić, B. Likozar, K. Užarević *ACS Appl. Mater. Interfaces* **13** (2021) 3070–3077; doi: 10.1021/acsami.0c21265

2) **V. Martinez***, B. Karadeniz*, N. Biliškov, I. Lončarić, S. Muratović, D. Žilić, S. M. Avdoshenko, M. Roslova, A. A. Popov, K. Užarević *Chem. Mater.* **32** (2020) 10628–10640; doi: 10.1021/acs.chemmater.0c03796

1) N. Bedeković, **V. Martinez**, E. Topić, V. Stilinović, D. Cinčić *Materials* **13** (2020) 2370; doi: 10.3390/ma13102370

CroRIS ID: 36096; WoS ResearcherID: ABB-4791-2021 ORCID: 0000-0001-7918-9843